NUMERIC MODELLING OF WATER HAMMER EFFECTS IN PENSTOCKS

by
Dominic Bernard

A thesis submitted to the University of Ottawa
in partial fulfillment of the requirements for
Masters of Applied Science in Civil Engineering

Department of Civil Engineering
Faculty of Engineering
University of Ottawa

Dedicated to *Maxime Thibaudeau* who taught me to believe and *Lauren Michaels* who followed me in my dreams.

NOTE: This page is for M.A.Sc.
THE UNIVERSITY OF OTTAWA-FACULTY OF GRADUATE STUDIES

C E R T I F I C A T E O F E X A M I N A T I O N

Examining Board
Dr. Dan Palermo
Dr. Majid Mohammadian
Dr. Elena Dragomirecu
Advisors
Dr. Magdi Mohareb
Dr. Ioan Nistor

The thesis by
Dominic Bernard
entitled
Numeric Modelling of Water Hammer Effects in Penstocks
is accepted in partial fulfillment
of the requirements of the degree of
Master of Applied Science (Civil Engineering)
in the
Department of Civil Engineering

Date: 04/12/2013

Dr. Beatriz Martin-Perez
Chairperson of Examining Board

ABSTRACT

Water hammer represents a complex hydraulic phenomenon with significant consequences on the proper functioning and safety of operation for pipe and conduit systems. The complexity and intricate physics of water hammer translated into significant difficulties associated firstly, with finding a proper solution for understanding the mechanism of its occurrence and, secondly, relating to proposing technically and economically viable design methods and devices that would help reduce and mitigate water hammer effects. In this context, the present thesis deals with the numerical modeling of the transient behaviour of water pipe segments. Following an extensive literature review of the state-of-the-art on the water hammer mechanisms and past work on experimental, analytical and numerical analysis of this phenomenon, a three dimensional numerical model of the water hammer in a pipe which considers the fluid-structure interaction (FSI) is developed using a Finite Element Method – Finite Volume Method (FEM-FVM) technique. Structural and fluid computational results based on rapid and slow gate closure scenarios are compared with existing closed-form solutions of the water hammer.

A parametric study is also performed on a simply supported pipe segment to determine the influence of various design parameter. A systematic sensitivity analysis was conducted and a ranking mechanism was established for the importance of each parameter on the fluid fields and structural response. A first comparative analysis is conducted on horizontally and vertically bent elevated pipe segments to quantify the influence of the bend angle on the results. A second comparative analysis is performed on a horizontally bent segment buried in soil to determine the influence of the pipe interaction with the soil on the response.

It is observed that the thickness, span, initial velocity and bend angle had a significant impact on the pressure and structural response. The presence of soil was observed to have a significant benefit in decreasing the von-Mises stresses.

ACKNOWLEDGEMENTS

Dreams and accomplishments can't be achieved without help from others. This help can be either moral, technical or financial.

I did my master to discover and understand. I would have never guessed I would also have been taught how to organize my thoughts, defend my ideas and present them. For all the hours we spent discussing together, I am sincerely grateful to both of my supervisors *Dr. Magdi Mohareb and Dr. Ioan Nistor.*

For all the moral support you gave me throughout those years. For all the times you understood my late working night and my really early mornings. I definitely owe a lot to my best friend and partner in life *Lauren Michaels.*

For their precious encouragement and understanding that I couldn't always be present in the past two years, I want to thank all my family members and their significant others. My mum *Lynda Fecteau*, my dad *Paul Bernard, Anne-Marie Bernard, Guillaume and Léonard Bureau* and *Alexandre Bernard, Marie-Claude Cossette.*

A dream can't be accomplished without the financial aspect. I owe a big thanks to *Denis Roy* from BPR-Tetratech in believing that a partnership project would benefit for the industry sector as well as the academic sector.

For our little adventures that changed the seriousness of life and enjoying philosophical discussions, I would like to thank *Andrew Lutowicz, Better Mae Glen, Nicolas Cormier.*

A healthy mind in a healthy body (Mens sana in corpore sano). I want to give a big thank to Swing Dynamite and my two dedicated dance partners *Cathy Jones* and *Kimberly Maria Kroeker* that help me to develop the artistic side of my brain.

TABLE OF CONTENT

LIST OF TABLES

LIST OF FIGURES

LIST OF SYMBOLS

$\forall_m$	Total Volume of the liquid/vapor mixture, m^3
$\forall_v$	Volume of vapor, m^3
a_c	Velocity of pressure wave, m/s
a_{c1}	Velocity of the pressure wave at section 1, m/s
a_{c2}	Velocity of the pressure wave at section 2, m/s
a_s	Velocity of stress wave, m/s
a_x	Acceleration of the water, m/s^2
A^*	Non-dimensional constant for the weighted function model
A_g	Cross-sectional area of the gate opening, m^2
A_p	Area of the pipe, m^2
α	Inclination angle, $^\circ$
α_v	Void fraction vapor within a fluid
B	Effective gate opening
B^*	Non-dimensional constant for the weighted function model
B_0	Effective gate opening at $t = 0$
$B1$	Location on the section pipe 1
$B2$	Location on the section pipe 2
β	Horizontal bend angle, °
c_1	Constant function of the boundary conditions of the pipe
C^*	Shear Decay coefficient
C_a	Constant used in the characteristic method
C_d	Coefficient of discharge through the gate
C_n	Constant used in the characteristic method

C_p	Constant used in the characteristic method
C_n	Courant Number
$C1$	Location on the section pipe 1
$C2$	Location on the section pipe 2
χ	Vertical bend angle, °
D_{po}	Pipe outside diameter, m
D_p	Pipe inner diameter, m
δ_{max}	Maximal deflection, m
Δt	Time increment, s
Δx	Length increment, m
e	Practical Pipe Thickness, m
e_c	Pipe's thickness with a corrosion allowance, m
e_{min}	Pipe's minimal thickness requirement, m
e_t	Theoretical pipe's thickness, m
E	Young Modulus, GPa
$f(t+\frac{x}{a_c})$	Reflected wave travelling from the reservoir to the gate, m
$F\left(t-\frac{x}{a_c}\right)$	Pressure wave travelling from the gate to the reservoir, m
FS	Security factor
f	Water hammer amplification factor
g	Gravity, m/s^2
h	Head ratio, m/m
h_a	Transient Pressure caused by the water hammer, m
H	Pressure head, m
H_0	Static pressure head at the pipe's outlet, m

H_A, H_B, H_P	Head computed at points A,B,P with the characteristic method, m
dH	Pressure head changed in the pipe, m
	Input parameter
I_p	Inertia of the Pipe, m^4
k	Bulk modulus of the water, Pa
κ_o	Bulk Modulus of the water at an absolute pressure $P_{abs} = 101.3kPa$ and a reference temperature $T_{ref} = 20^\circ C$
k_B	Brunone's empirical factor
K	Increase factor
K_S	Subgrade Modulus
l_{el}	Element longitudinal length, m
L_1	Straight segment at inlet, m
L_2	Curved segment, m
L_3	Straight segment at outlet, m
L_D	Dynamic equation in the characteristic method
L_C	Continuity equation in the characteristic method
L_p	Length of the pipe, m
ΔL_{pe}	Variation of the pipe's length caused by the elasticity of the wall, m
ΔL_{pw}	Variation of the pipe's length caused by the compressibility of the water, m
ΔL_{pt}	Total variation of the pipe's length, m
L_x	Length between the position x_1 and the inlet boundary condition, m
λ	Arbitrary constant used for the characteristic method

m_w	Mass of the water, kg
M_b	Moment induced by the bending, $kN \cdot m$
O	Value of an output field
p	Pressure, Pa
P_{abs}	Absolute Pressure, Pa
P_{ref}	Reference Pressure, Pa
ρ_1	Pipe line constant for section 1
ρ_2	Pipe line constant for section 2
ρ_A	Allievi's characteristic parameter
ρ_s	Steel's density, kg/m^3
ρ_w	Water's density, kg/m^3
ρ_{w0}	Density of the water at an absolute pressure $P_{abs} = 101.3kPa$ and a reference temperature $T_{ref} = 20^\circ C$
Q	Flow rate, m^3/s
Q_0	Initial flow rate, m^3/s
Q_{P1}	Positive Characteristic Equation
Q_{P2}	Negative Characteristic Equation
Q_A, Q_B, Q_P	Flow computed at pt. A,B,P (Characteristic method), m^3/s
r_i	Pipe inner radius, m
r_o	Pipe outside radius, m
r_m	Pipe middle radius, m
R	Input value of the reference case
Δr_m	Radius changed in the pipe, m
ϑ	Constant for the rigid water column theory

S_y	Yield strength, *MPa*
S_u	Ultimate strength, *MPa*
S_p	Pipe section modulus, m^3
SI	Sensitivity Index
σ_b	Bending stress, *MPa*
σ_e	Stress induced by the expansion joint, *MPa*
σ_f	Allowable stress, *MPa*
σ_h	Hoop Stress, *MPa*
σ_k	Allowable stress factored, *MPa*
σ_l	Longitudinal Stress, *MPa*
σ_{vm}	von-Mises stress, *MPa*
σ_u	Allowable stress induced by the ultimate strength, *MPa*
σ_y	Allowable stress induced by the yield strength, *MPa*
t	Time, *s*
T	Time for gate closure, *s*
T_{ref}	Reference Temperature, $^{\circ}C$
T_e	Linear force, kN/m
τ	Ratio of effective gate opening
τ_w	Friction term, *N*
τ_{ws}	Quasi-Steady Friction term, *N*
τ_{wu}	Discrepancy between Numerical and Experimental Friction term, N
u	Radial displacement, m
μ	Poisson's Coefficient
v	Longitudinal displacement, m
Δv_p	Variation of pipe volume, m^3

Δv_w	Variation of water volume, m^3
V	Velocity of water, m/s
V'	Difference between initial and final velocities, m/s
V_0	Initial velocity of water at the gate, m/s
v	Velocity ratio, $(m/s)/(m/s)$
x	Longitudinal direction of the pipe, m
x_1	Location where the pressure is computed
dX	Element length, m
δx	Change in the longitudinal length, m
ψ	Non-dimensional historical time
$\hbar$	Hoop displacement, m
w_b	Bending distributed force, kN/m
w_l	Longitudinal distributed force, kN/m
w_s	Distributed force induced by the steel's weight, kN/m
w_t	Total distributed force induced by the weight, kN/m
w_w	Distributed force induced by the water's weight, kN/m
W_a	Weighted function model of transient friction for flows in smooth pipe
ω	Specific weight of water measured in, N/m^3
ξ	Damping ratio
Ψ	Value of an output field O based on an input parameter I
Ψ_R	Variation Criterion
Z	Elevation point, m

CHAPTER 1-INTRODUCTION

1.1 Description of the Problem

In the context of economic growth in Canada and increasing of energy prices, the construction of high head hydropower plants considered unprofitable up until recently, are now being contemplated by the hydropower industry. High head hydraulic resources are associated with smaller turbines and reduced construction costs. However, the long distance from the water source to the power plant increases the installation cost of the steel piping system involved.

Penstocks can stretch from a few hundred meters to a few kilometres. From the intake to the power plant, the penstock changes directions either horizontally or vertically to follow the topography and thus involves a number of bends. Penstocks can be either elevated or buried. The behaviour of elevated penstocks is relatively well understood and design guidelines have been developed for these systems. In contrast, a proper prediction of the response of buried penstocks necessitates the modelling of the interaction with surrounding soil and involves additional complexities. Within this context, this project focuses on the analysis of buried penstock systems by incorporating the soil-penstock interaction.

Under operating conditions, penstocks are subjected to high pressures induced by the high head. Under these high pressures, penstock bends are subject to a significant thrust force. Several details have been proposed to resist the thrust force. Of these, the use of heavy anchor concrete blocks of buried penstock bends is intended to provide reactions to the thrusts, and thus controlling the penstock displacements. The construction of concrete blocks in steep terrain is associated with high costs that decrease the profitability of a hydropower project. Within this context, a new method which avoids the use of anchor thrust blocks has recently been used in the Bear Creek Hydro Generation project. This alternative is significantly more economical, but its behaviour is less understood than the more conventional anchored detail.

Throughout the operating life of a hydropower plant, when the power demand on the electricity grid is subject to sudden drops, the generator is let free of the resisting load.

Without loads, the flow provided to the turbine increases its speed. In order to avoid the turbine reaching excessive speeds, it is necessary to quickly close the wicket gates to control the flow. The rapid decrease of flow rate causes a shock wave known as a "water hammer" which creates a pressure increase followed by a vacuum within the penstock.

This study aims to develop an integrated penstock-fluid-soil finite element model capable of predicting the dynamic response of pipe bends under water hammer effects caused by sudden gate closures. The model will then be used to conduct a parametric study on the effect of a water hammer on penstock response. Comparisons with and without soil configurations will be conducted.

1.2 Objectives

The thesis is organized logically so the reader can follow the student thoughts process. Each chapter presents an analysis and its results are used for subsequent chapters. Each analysis responds to a particular objective. The below objectives are achieved in a chronological order throughout the chapters.

1. Effectuate a pre design of an elevated straight segment using a reference case from the Bear Creek Hydro Project.
2. Carry out static and transient analyses comparing pre design results with numerical fluid-structure interaction results.
3. Conduct a numerical parametric analysis of an elevated straight segment studying the effect of design parameters on the water hammer phenomenon and the structure of the penstock.
4. Perform dynamic analyses comparing horizontal and vertical bend segments with a straight segment.
5. Compare dynamic analyses of an elevated bend with a buried bend.

1.3 Scope of the study

The present study numerically reproduces the well known and documented phenomenon called the water hammer using a finite element method [ANSYS-CFX]. Fluid-structure interaction simulations are used to recreate the effect of the fluid on pipe structure and vice-versa when a water hammer occurs.

The study first validates the numerical model through a comparison of the analytical and numerical analyses. Using parametric study, it then determines the influence of the design parameters on the simulated water hammer. A comparison between different bend curvatures is then made to study its effect on the water hammer and the von-Mises stress. Lastly, it determines the influence of surrounding soil on the bend stress due to its thrust force.

Results of the latter validate the new method used for minimizing the von-Mises stress at buried bends without the use of anchor blocks.

1.4 Thesis Outline

The present section is intended to give the reader a short overview of each chapter.

In Chapter 2, the background information, literature on theoretical knowledge and current research is reviewed. The classical model of the water hammer is first presented and different methods of its computation are overviewed.

In Chapter 3, a classical design of an elevated straight penstock segment is presented. Calculations are made using real data taken from an existing case located at the Bear Creek Hydro Project, BC. Analytical results are discussed and will form the base of a comparison with numerical results.

In Chapter 4, the mechanism of a Fluid-Structure Interaction (FSI) simulation is explained and a fluid-structure interaction model using design parameters from chapter 3 is developed in ANSYS-CFX and presented in details to the reader. Fluid and structural properties and boundary conditions, meshing choices, type of analysis and solver controls are explained and commented. Steady-state and transient simulations of the elevated straight segment are used as a reference case.

In Chapter 5, a steady-state and transient analyses are conducted on the model developed in Chapter 4 for both rapid and slow gate closure cases. Fluid and structural numerical results for both cases are presented and compared to the analytical ones. Results from the slow gate closure case will serve as a reference case for the parametric study performed in the next chapter.

In Chapter 6, a parametric study that analyses the influence of each design parameter on the fluid and structural response is performed. A sensitivity analysis on the importance of every parameter closes the chapter.

In Chapter 7, fluid-structure interaction models for a horizontal and vertical bends are developed. Transient analyses for different curvature angles are performed. Fluid and structural results are compared to a straight segment and discussed.

Chapter 8, a fluid-structure interaction model of a buried bend segment is developed. Transient analyses for different subgrade reaction modulus are conducted and compared to each other. Discussion about the results validates the new method used for minimizing the von-Mises stress at buried bends.

In conclusion, Chapter 9 summarizes the work accomplished in each chapter, concludes about their important questions and gives recommendations for future work.

CHAPTER 2 – LITERATURE AND THEORY REVIEW

2.1 Objectives

This chapter intends to overview the previous work done on the water hammer field by multiple researchers and to give a background theory to people who are new to the field.

Section 2.2 gives a historical literature review starting with the early work on the water hammer done by Joukowsky (1900) until the current work on the effect of fluid-structure interaction on the water hammer done by Tissjeling (2008).

Section 2.3 presents the rigid and elastic water column theory assumptions and, from the mass and momentum conservation equations, develops its equations.

Section 2.4 presents three methods used to resolve the partial differential equation system developed for the elastic water column theory in Section 2.3

2.2 Literature Review

2.2.1 Early physical model for water hammer

In the late nineteenth century, world industrialisation and urbanization created a need for electrical power. As a primary source of power, hydroelectricity became an important field of study within the industry and science sectors. Among many different types of studies, the water hammer phenomenon and its control became important subjects studied in turbo machinery laboratories. Experimental works from contemporaries von Kries (1883) in Freibourg, Germany and Joukowski (1900) in Moscow, Russia defined the basis of the current water hammer theory. Their investigation on the water hammer, impressive for their clarity and maturity in theory and experiment (Tijsseling, 2007), allowed them to formulate the fundamental equation in the water hammer theory, relating the pressure with the velocity variation for an instantaneous valve closure.

$$\Delta p = \rho_w a_c \Delta v \tag{2.1}$$

where ρ_w is the density of the water and a_c is the speed of sound in a fluid contained in a cylindrical pipe of circular cross section. The variable a_c, defined in Korteweg (1878),

accounts for the water compressibility k, the pipe wall elasticity E and the pipe geometry e, D_p, c_1.

$$a_c = \sqrt{\frac{k}{\rho_w(1+\frac{D_p k c_1}{eE})}} \qquad (2.2)$$

2.2.2 Analytical and Graphical method of resolution

Unsteady flow through close conduits is described by the dynamic and continuity equations and transformed in a hyperbolic first-order partial differential equations system. In these equations, the longitudinal position x and the time t are the two independent variables and the pressure H and the velocity V are the two dependent variables. The equations derivation is shown in Section 2.3.2 and well explained in Parmakian (1963). Allievi (1902) was the first to develop a mathematical tool that analytically solve the system and find the pressure values for each timestep and location in a one dimensional thin-walled pipe model for any linear flow variations. Allievi (1913) presented the general theory of water hammer based on his previous mathematical tool. The generalization was achieved by the introduction of the characteristic parameter ρ_A that absorbs structural and fluid element of a conduit.

$$\rho_A = \frac{a_c V_0}{2gH_0} \qquad (2.3)$$

where V_0 is the initial velocity and the H_0 is the static pressure at the valve. Monographs based on ρ_A, provided in the work, have long been used to determine the transient pressure for reservoir-pipe-valve systems. Gibson (1920) discussion considered the effect of the net head on the water hammer phenomenon. A method of resolution and an analytical integration is presented. Results are compared to those of Allievi (Fig.2.1). Jaeger (1933) developed the Allievi general theory for particular cases. Analytical methods of resolution for systems with more than one conduit, thick-walled pipe conduit, concrete covered conduit and system with surge tanks were developed. Analytical methods based on the Allievi theory provide a general understanding of the water hammer phenomenon, but formulae obtained from it are restrained to only few cases. The

methods neglect the friction and the second-order terms contained in the hyperbolic partial differential equations system. They do not allow a solution for problems with many characteristic parameters ρ_A, give a solution for the pressure field only and consider the flow reduction linear for a valve closure.

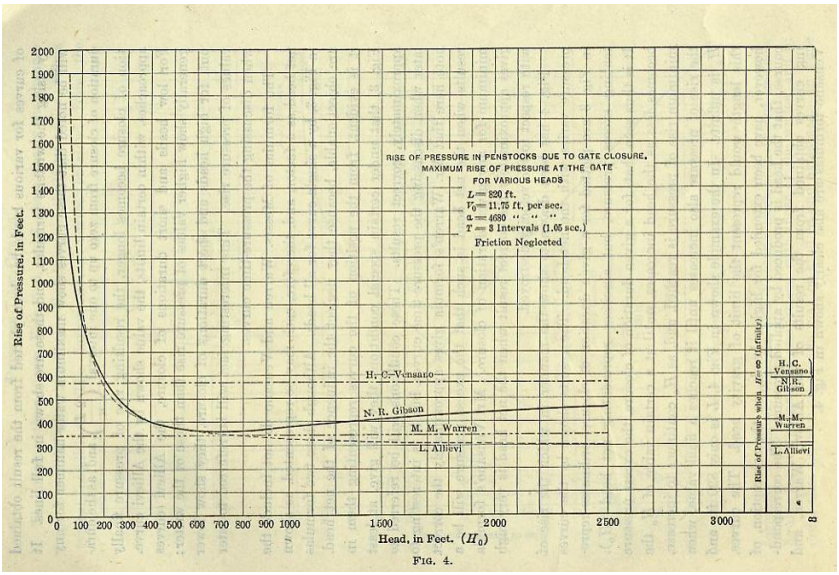

Figure 2. 1 - Comparison of Allievi results to Gibson (1920)

Graphical methods were introduced to palliate analytical methods limitations. Schnyder (1936) and Bergeron (1935) graphical methods gave a pressure and velocity fields for every timestep at any location in a one-dimensional thin-walled pipe model for any type of valve closures. Parmakian (1963) presented Schnyder-Bergeron graphical method that suits for systems with many characteristic parameters ρ_A, hydraulic losses and compound pipes. The graphical method gives an accurate and rapid solution for simple pipe systems. However, it became rapidly overwhelming for complex pipe systems that include many hydraulic equipments and branches. Numerical methods implemented in computer codes addressed this problem.

2.2.3 Numerical methods of resolution

The introduction of digital computers in the early sixties had allowed the hyperbolic partial differential equations system to be solved with numerical methods. Gray (1953) was the first to use the Eularian method of characteristic (MOC) that computes H and V for every Δt and Δx. The method allowed him to determine the order of approximation

made when the effect of friction, kinetic energy and change in waveform are neglected. Lister (1960) compared two MOC discretization methods: the method of specified time intervals or fixed-grid method (Fig.2) and the method of characteristic grid. She found out that the fixed-grid method was much easier to compute giving the analyst full control over the grid selection. For its accuracy, simplicity, numerical efficiency and programming simplicity, the MOC discretized with the fixed-grid scheme have become the most widely used method.

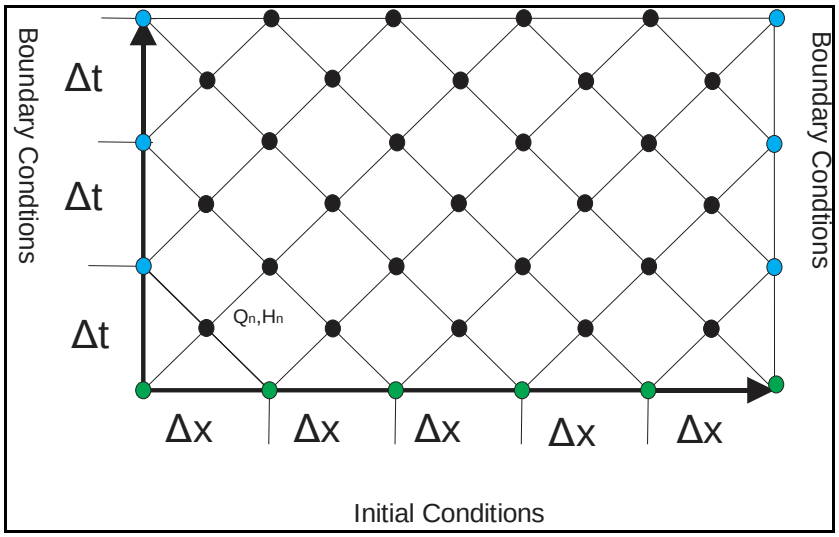

Figure 2. 2 - Fixed-grid characteristic for the method of characteristic (MOC)

Perkins et al. (1964) showed that $\Delta t/\Delta x \leq 1/a_c$ for the fixed-grid characteristic scheme to be numerically stable. The condition is called the Courant's stability condition. Streeter & Wylie (1967) suggested that the first-order finite difference was sufficiently accurate since the time interval for most of the practical problems were usually small. Evangelisti (1969) proposed to equal the time interval Δt to $1/16$ to $1/24$ of the transit time.

In his thesis, Lai (1961) included a nonlinear hydraulic losses term in the MOC and implemented it in a code. Streeter (1962) developed laws for the closing and opening of valves. He implemented these laws as boundary conditions in the MOC and solved the problem with and without the friction term. Streeter & Lai (1963) tested the MOC for different closure time and various pipe connections. They compared results with experimental work and earlier methods of resolution.

As the wave velocity a_c is considered constant for a pipe section, the number of reaches Δx for that section can be computed with the Courant's stability condition. This method, called the method of specified time interval, well suited for simple pipe systems, generates numerical errors for complex pipe systems. Considering the wave velocity a_c constant in systems with multiple hydraulic equipment and branches does not reflect the reality and induces numerical errors. Numerical interpolation and/or adjustment of wave speeds or pipe lengths have been introduced to overcome the problem. Vardy (1976) used a space-line interpolation to overcome the problem. Golberg & Wylie (1983) raised the limitations of the space-line interpolation for nonlinear cases and presented the time-line interpolation. Ghidahoui et al. (1998) developed an integrated energy approach to understand how discretization errors associated with time and space-line interpolation arose and how they could be controlled. Shimada et al. (2006) and Shimada et al. (2007) introduced an exact method of assessing the numerical error in analysis of unsteady flow. Shimada et al. (2008) used his exact method to predict the numerical errors of both space-line and time-line interpolations for fixed-grids. The analysis of the exact method took place in a long-term program to automate the selection of grid size. Tijsseling & Bergant (2007) removed the need to select the grid size while introducing a one-dimensional meshless method. The new algorithm was validated with conventional frictionless water hammer calculations for instantaneous and slow valve closure.

Other numerical methods were also used to approximate the pressure and flow in a one-dimensional conduit. The Lagrangian method also called wave plan method was introduced by Wood et al. (1966). Wood (2005) compared the wave plan method with the MOC and found that for large pipe network problems, the wave plan method took less CPU time than the MOC. Chaudhry (1985) proved that the second order Finite Difference (FD) method produced better results than the first order MOC. However the method was considered to increase the execution time and storage requirement. The first-order Finite Volume (FV) Gudonov type method was first used for water hammer problems by Guinot (2002). Zhao (2004) developed a second-order explicit of the method and compared its results with the MOC with space-line interpolation. He found that the

second-order explicit Finite Volume Gudonov type method achieved a given level of accuracy with much less CPU time than the MOC with space-line interpolation.

Ghidaoui et al. (2005) gave a brief review of each technique.

2.2.4 Branches of study within the water hammer field

According to Keramat (2012), there are four important items that may affect the classical water hammer results computed from the general Allievi theory. Those are the unsteady friction (UF), column separation (CS), viscoelasticity (VE) and fluid-structure interaction (FSI). Their isolated influence on classical results has been verified in laboratories and numerical models that simulate their impact on water hammer have been developed. Combinations of two or more items have also been investigated and were listed in Keramat et al (2012). The present literature review will not go into details for each subject, but will direct the interested reader towards important papers.

A thorough review of the FSI item is covered in a section on its own since it is the present thesis subject.

2.2.4.1 Unsteady friction models in transient flows

The friction modelisation for transient flow is essential for pipe systems that require simulations well beyond the first wave cycle, really long pipes and pipes with high friction.

Streeter & Wylie (1985) considered the Darcy-Weisbach equation at every timestep to evaluate the friction term $\tau_w(t) = \left[\rho_w f(t) |V(t)| V(t)\right] / 8$ also called the quasi-steady friction term. Daily et al (1956) showed high discrepancies between numerical and experimental data when a steady-state based friction equation is used to model rapid transient flows. He decomposed the friction term $\tau_w(t)$ into two terms $\tau_w(t) = \tau_{ws}(t) + \tau_{wu}(t)$ where $\tau_{ws}(t)$ is the quasi-steady friction term and $\tau_{wu}(t)$ is the discrepancies between numerical and experimental results. Various models had been developed to estimate the transient friction term $\tau_{wu}(t)$, but two of them have particularly been studied. Zielke (1969) modeled the transient friction term by using weighted time

histories of past flow conditions and Brunone et al (1991) introduced a model that relies on instantaneous accelerations and required the definition of an empirical factor k_B.

Vardy & Hwang (1991) validated Zielke (1969) work for transient friction in laminar flow and showed its applicability for turbulent flows at low Reynolds number. Bergant & Simpson (1994) compared experimental results with Zielke and Brunone's models for a rapid valve closure in a reservoir-pipe-valve system. Vardy & Brown (1995) deduced the weighted function model (W_a) of transient friction for flows in smooth pipe assuming the turbulent viscosity to vary linearly within a thick shear layer surrounding a core of uniform velocity.

$$W_a = \frac{A^* \exp(-B^* \psi)}{\sqrt{\psi}} \tag{2.4}$$

where A^* and B^* are two non dimensional constants that depend on the geometry of the pipe, the viscosity of the fluid and the Reynolds number. The non dimensional variable ψ reflects the time aspect of the formula. The expression is simple to evaluate and applies for a large range of Reynolds number. Vardy & Brown (1996) made a generalization form of their model that used the non-dimensional historical time ψ and shear decay coefficient C^*.

$$W_a = \frac{A^* \exp(-\psi / C^*)}{\sqrt{\psi}} \tag{2.5}$$

Bergant & Simpson (1999) analytically predicted the empirical Brunone's friction constant k_B using the Vardy shear decay coefficient C^*. He then incorporated the two unsteady friction models into the method of characteristic and compared the numerical results with experimental data for different rapid valve closure. Vitkowsky et al (2000) showed that the constant k_B value varies with local flow conditions. He showed that a variable k_B gave a better representation of the damping and improved fit to experimental data. Silva-Araya & Chaudhry (2001) introduced an energy dissipation model to represent the unsteady friction losses for smooth-to-rough transition and fully rough pipes. The model was implemented into the characteristic method and numerical results

were compared with the experimental data. Bergant et al. (2002a) compared the quasi-steady and Brunone's model for downstream rapid and slow valve closure with laboratory and hydropower plant data. He found good agreement between results and data for rapid and slow valve closure using Brunone model and for slow valve closure using quasi-steady model. Bergant et al. (2002b) showed that, as opposed to the Zielke model, the Brunone model failed to represent a valve opening event. Ghidahoui (2002) & Mansour derived an approximation of the Vardy-Brown model that is more computationally efficient than the exact one and showed good agreement with experimental data over a large range of Reynolds number. Vitkowsky et al. (2004) developed an accurate and efficient algorithm to represent the unsteady friction with the exact Vardy-Brown model for turbulent flows. The algorithm was shown to be less computationally efficient, but more accurate than the algorithm using the approximation of the Vardy-Brown model (Ghidahoui et al. (2002)). Vitkowsky et al. (2006) compared the Zielke and the Brunone model for rapid valve opening and closure with experimental data. Comparisons were made for both valves located downstream and upstream to the pipeline. As opposed to the Zielke model, the Brunone model failed to correctly represent the rapid valve opening event. Vardy & Brown (2007) presented theoretical prediction of the unsteady friction for all flow conditions, from smooth to fully rough and for Reynolds varying from 10^3 to 10^8. Duan et al. (2012) investigated the importance of pipe system scale. They showed that the effect of unsteady friction becomes less important as the ratio length/diameter $\left(L_p / D_p\right)$ increases. The use of small scale system had led the researchers to overestimate the importance of unsteady friction.

2.2.4.2 Column separation models in transient flows

The recognition of the water hammer with column separation dates back to Joukowski (1900) who was the first to observe and understand it. However, even if its danger was recognized in the thirties, a comprehensive investigation was not possible before the numerical era in the sixties. Wallis (1969) introduced the symbol $\alpha_v = \forall_v / \forall_m$ that defined the void fraction vapor within the fluid where $\forall_v$ is the volume of vapor and $\forall_m$ is the total volume of the liquid/vapor mixture. The symbol distinguished the two types of

vaporous cavitation in pipelines. A large value of α_v indicates a local column separation and a small value indicates a distributed vaporous cavitation. Bergant et al. (2006) reviewed the different mathematical models used to numerically simulate the column separation in water hammer. Wylie & Streeter (1978, 1993) described the most commonly used model for column separation called the discrete vapor cavity model (DVCM). The model allows the cavities to form at grid points if the pressure computed is below the vapor pressure. Vapor cavities are thus confined to form at computational sections. Bergant & Simpson (1999) showed that the model contains numerical instabilities and unrealistic spikes of pressure. These deficiencies can be suppressed by assuming a small amount of initial free gas. The model is thus described as discrete gas cavity model (DGCM), a generalization form of the DVCM. Fanelli (2000) summarized the experimental work carried out between 1971-1991 by IAHR to develop and validate the model implemented in computer codes.

2.2.4.3 Viscoelasticity

Due to its low price and high resistance properties, plastic used in water supply systems have increased considerably in the last decades. Its viscoelastic behaviour greatly influences the water hammer by attenuating the pressure wave and increasing the dispersion of the travelling wave [Bergant et al. (2008)]. The linear viscoelastic model described by Gally et al. (1979) divides the strains in an elastic part, included in the wave speed, and a viscoelastic part, added to the continuity equation (Chapter 2.3). An excellent paper that reviewed the advancement on the subject was given in Covas et al. (2004) and Covas et al. (2005).

2.2.5 Review and history of the influence of the FSI on the water hammer

Conventional water hammer analyses described by Allievi (1925) did not take the pipe inertia and axial pipe motion into account. Neglecting the importance of the fluid-structure interaction can lead to false pressure and stress predictions. Tijsseling & Vardy (2008) determined its importance using a method based on time scales. Three fluid-structure interaction mechanisms can be distinguished: Friction Coupling that represents the mutual friction between liquid and structure, Poisson Coupling that links the pressures in the fluid to the longitudinal stresses in the pipe and Junction Coupling that

acts at specific points in a pipe system such as valves, pumps and bends. The Friction Coupling is usually neglected due to its relatively small contribution and will not be covered in the present work. Poisson and Junction Coupling models evolution are presented in sections 2.2.5.1 and 2.2.5.2. Numerical and experimental works are presented in subsequent sub sections.

Section 2.2.5.1 Analytical poisson-coupling model

The coupled equations model that simulates the Poisson Coupling effect has been slowly evolved during the twentieth century. Table 2.1 shows the evolution of the model throughout the time and its method of resolution. The equations of motions were summarized in Wiggert & Tijsseling (2001).

	Number of Equations	Domain	Notes	Motions					Method of Computation
				Axial	Radial	In-Plane Bending	Out-of-Plane Bending	Torsional	
Skalak, 1956	4	Time	1,2,3	X					
Lin & Morgan, 1956	4	Time	1,2,3,4	X					MOC *
Bürmann et al, 1979,1980	4	Time	1	X					MOC
Walker & Phillips, 1977	6	Time	1	X	X				MOC
Valentin, Phillips & Walker, 1979	8	Time	1	X		X			MOC **
Joung & Shin, 1985	9	Time	1,2,3,4	X		X			MOC
Wilkinson, 1978	14	Frequency	2	X		X	X	X	
Wilkinson, 1980	14	Time	1,2	X		X	X	X	
Wiggert et al. 1987	14	Frequency	1,2,3,4	X		X	X	X	Compenent-Synthesis Method
Wiggert et al, 1985,1986,1987	14	Time	1,2,3,4	X		X	X	X	MOC
Lavoj & Tijsseling, 1990	14	Time	1,2,3,4	X		X	X	X	MOC & MOC-FEM

Table 2. 1 - Evolution of the coupled equations model and its method of computation

Notes for Table 2.1

1. Includes the Poisson Effect
2. Includes the Bending Stiffness
3. Includes the Rotatory Inertia

4. Includes the Tranverse Shear

* Solved by King & Frederick (1968)

** Solved by Hu & Phillips (1981)

Bürman et al. (1979b) presented a simplified model of Skalak that represents most of the practical problems.

2.2.5.2 Analytical junction-coupling model

Philips & Valentin (1978) built a model that represent the junction coupling and quantified the transmitted and reflected waves for different bending angles. The model considers the bending, shear and axial forces and the in-plane, rotation and axial displacements. Otwell (1984) modeled the effect of the bend motion on the transient pressure. He found that the transient pressure significantly increases for unrestrained bends and stays the same for restrained bends. Wiggert et al. (1985a) analytically decomposed the effect of the anchors axial and bending stiffness on the transient pressure. He validated his results with experimental data. Heinsbroek & Tijsseling (1994) found that the junction coupling is small when the anchor rigidity is larger than the axial stiffness of one meter of pipe. For less stiff anchor, a static (steady-state) and dynamic (fluid-structure interaction) stress analyses are required. Tijsseling & Vaugrante (2001) represented the junction coupling effect in the frequency domain and validated its results with experimental data.

2.2.5.3 Numerical work

The complex degree of the analytical Poisson and Junction Coupling equations makes closed-loop solutions impossible. Table 2.1 showed which numerical methods have been used to resolve each Poisson Coupling model. This present section shows complex numerical work that includes all FSI effects.

Tijsseling & Heinsbroek (1999) numerically simulated a rapid valve closure in a system (Fig.3) with two restrained and four unrestrained bends. He solved the main frequencies, extreme pressures, stresses and anchor forces using the MOC for the fluid fields and the Finite Element Method (FEM) for the structural fields. The simulation considered all FSI mechanisms and pipe flexure was modelled through the Euler-Beam theory.

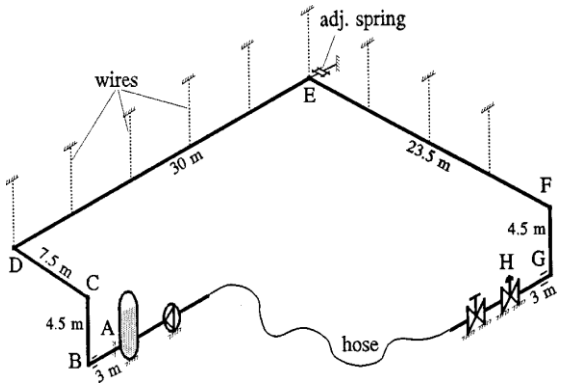

Figure 2. 3 - System numerically solved by Tijsseling (1999)

Shalaby & Younan (1999) simulated rapid valve closure and opening events in a bend model using ABAQUS nonlinear finite element code. The simulation took the geometric and material nonlinearities into account. Altstadt et al. (2003) investigated the local effect of the transient pressure in anchored bends for a rapid valve closure on ANSYS. Both fluid and structural domains were meshed with finite elements. Kanyanta et al. (2009) simulated flow transient within arteries using a 3D Finite Volume Method (Open Foam). The model considered only the Poisson Coupling thus neglecting the Friction and Junction Coupling.

2.2.5.4 Experimental work

In parallel to the development of analytical models and numerical methods of resolution, experimental work in laboratories had been done to validate the developed models.

Thorley (1969) was the first to observe the effect of the fluid-structure interaction in a reservoir-pipe-valve arrangement. Its experiment and results are presented in Figs.2.4 a-b. The small rise of pressure at mid-span (A), called precursor wave, between 2 and 4 ms is caused by the Poisson coupling effect and travels faster than the primary wave.

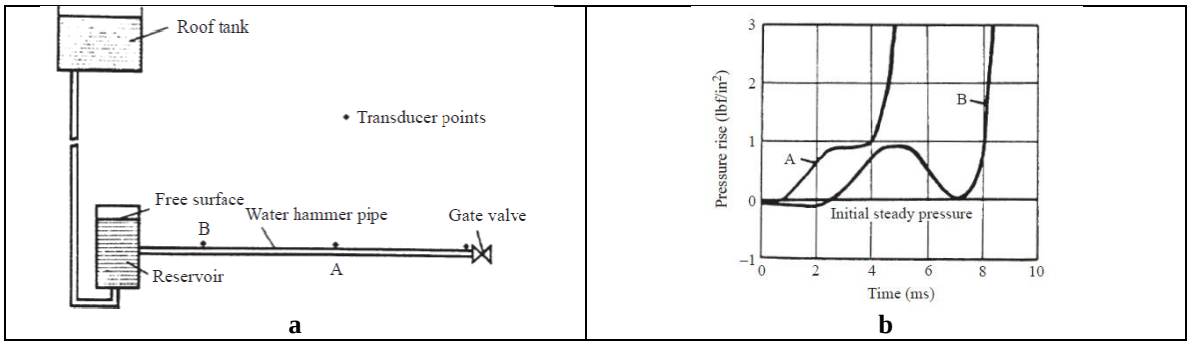

Figure 2. 4 - Experiment of Thorley (1969), (a) Model, (b) Results

Subsequent experimental work done on the fluid-structure interaction subject required a large collaboration of researchers, universities, governments and companies in which each party benefits.

The 10 years research program at Michigan State University, USA conducted by Wiggert and Hatfield resulted in many valuable publications: Wiggert et al. (1985a), Wiggert et al. (1985b), Wiggert (1986), Wiggert et al. (1987). Figure 2.5 a presents the model used by the researchers. Figure 2.5 b compares its recorded data with those computed with the computer code. Both results show the combined impact of the Poisson and Junction coupling effect on the recorded pressure at the valve end.

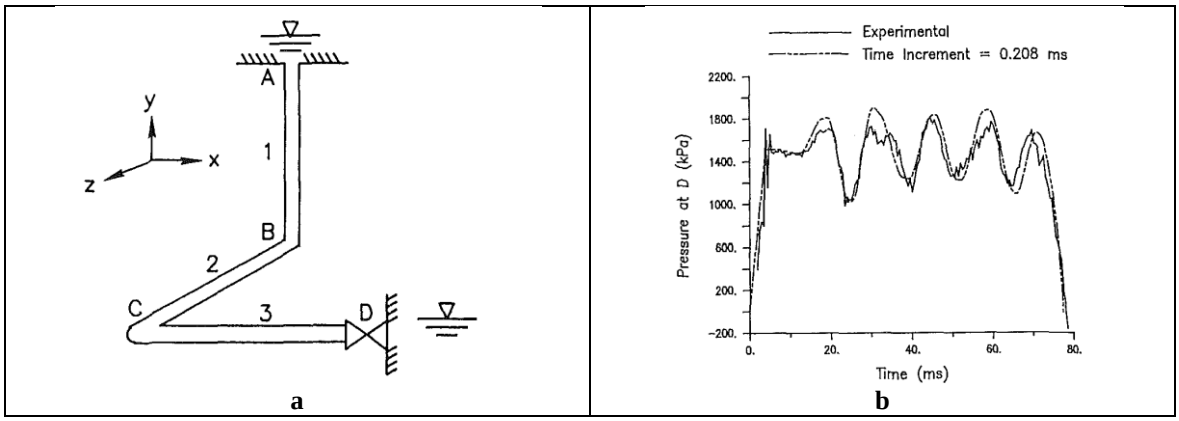

Figure 2. 5 - Experiment of Wiggert et al. (1985b), (a) Model, (b) Results

At the University of Dundee, United Kingdom, Vardy & Fan (1986) proposed a model that have been widely used due to its simplicity and accuracy. The model shown in Fig. 2.6 a accurately measures the axial and flexural waves propagations in a freely suspended pipe system. Compared to previous models, the latter has no steady-state pressure gradient, does not required the valve charateristic and has a negligible pipe support.

Figure 2.6 b shows the impact of the Poisson coupling without being influenced by the Junction coupling.

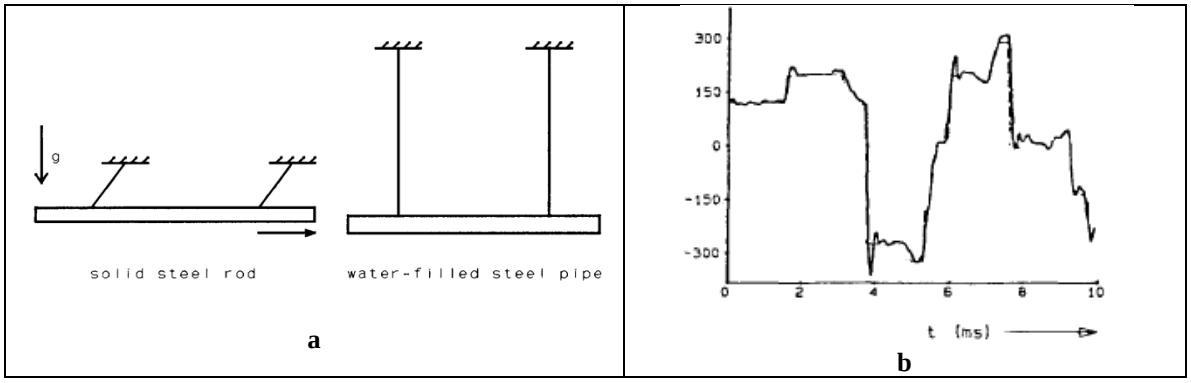

Figure 2. 6 - Experiment of Vardy & Fan (1986), (a) Model, (b) Results

Based upon the work done at Michigan State University by Wiggert and Hatfield, a large project (FLUSTRIN) had been developed at Delft University, Netherlands. The project intended to model the water hammer phenomenon, developed a computer code that simulates it and validates the code with laboratory tests. The model from Kruisbrink & Heinbroek (1993) studied the Poisson and Junction coupling effect for a multiple bends system. Figure 7.a shows the model used for the experimental tests. Figure 7.b compares its recorded data with those computed with the computer code. Junction coupling effect has been shown to be more significant when the pipe bends are free to move.

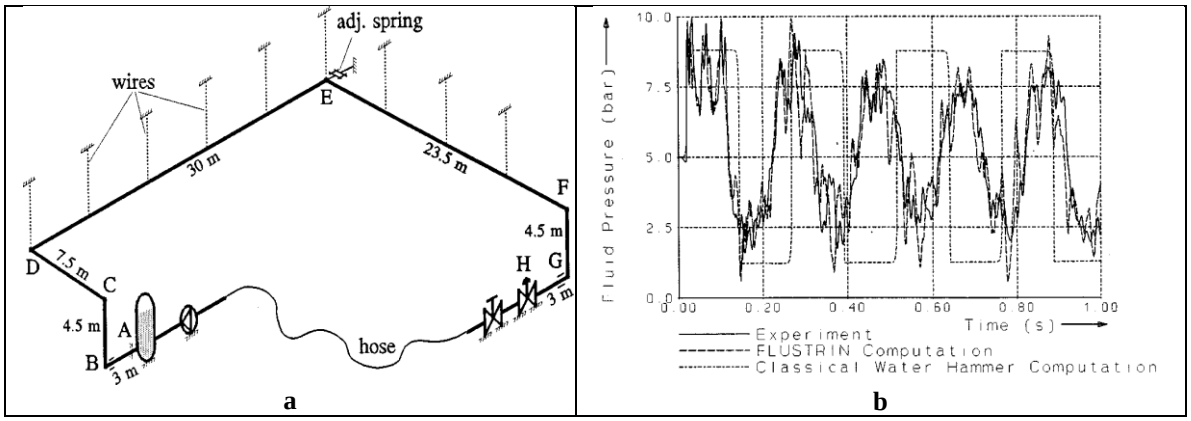

Figure 2. 7 - Experiment of Kruisbrink & Heinbroek (1993), (a) Model, (b) Results

2.3 Water Hammer: Governing Equations

The complex water hammer phenomenon is an extremely costly and often dangerous phenomenon, especially for large penstocks used to convey water to hydropower units.

Under certain conditions such as sudden closure of a valve, the fluid no longer follows the Bernouilli's law and both the pressure and velocity distributions must be calculated using other methods. The rigid water column and elastic water column are two different models used to derive the equations used to solve the two time-dependant pressure distributions for a highly transient fluid motion, also known as water hammer (Parmakian (1963)). A set of equations is presented below and solved in different ways.

2.3.1 Rigid Water Column Theory

2.3.1.1 Theoretical assumptions

1. The water in the pipe is incompressible
2. The pipe walls are non-deformable regardless of the pressure inside the pipe
3. The pipe remains full of water at all times and the minimum pressure inside the pipe is in excess of the vapour pressure of water
4. The hydraulic losses and the velocity head are negligible when compared to the pressure changes
5. The velocity of water in the direction of the axis of the pipe is uniform throughout the cross section of the pipe
6. The pressure is uniform throughout the cross section of the pipe and is equal to the pressure at the center line of the pipe
7. The reservoir level remains constant during gate closure
8. There are no gas bubbles in the liquid (no cavitation occurs)

2.3.1.2 Free-Body Diagram

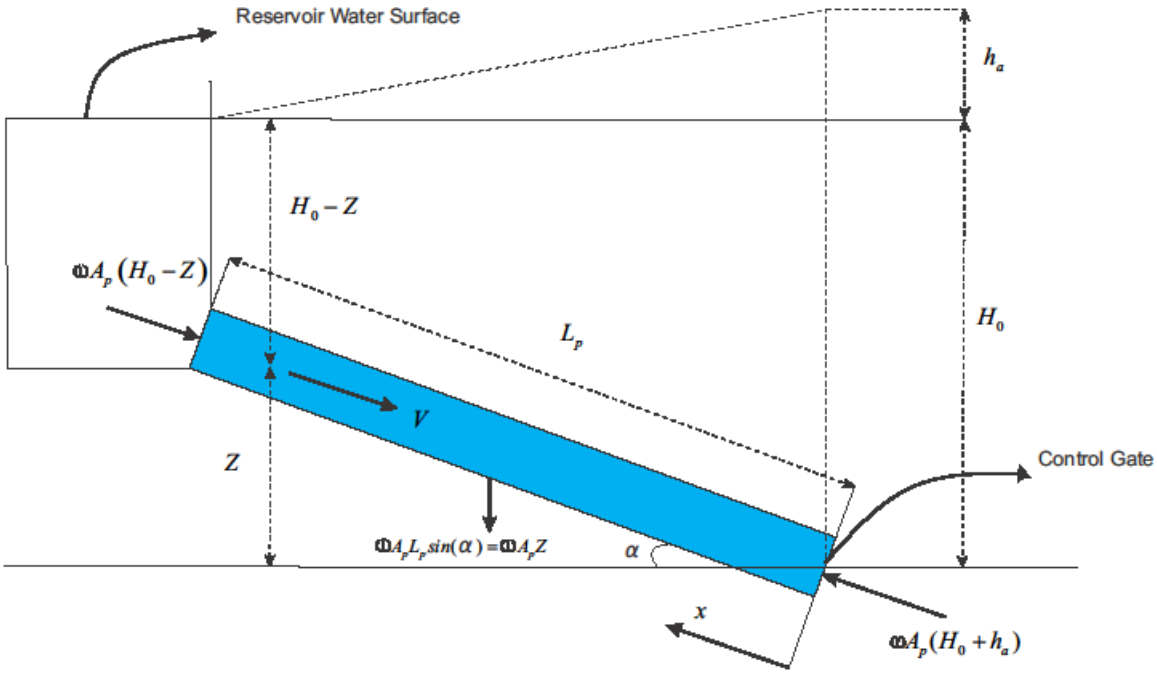

Figure 2. 8 - Rigid Water Column diagram

ω	Specific weight of water, N/m^3
A_p	Area of the pipe, m^2
H_0	Static pressure head at the pipe's outlet, m
h_a	Transient Pressure caused by the water hammer, m
Z	Elevation point, m
L_p	Length of the pipe, m
V	Velocity of water, m/s
α	Inclination angle, $^{\circ}$
t	Time, s
g	Gravity, m/s^2
x	Longitudinal direction of the pipe, m

2.3.1.3 Dynamic Equilibrium

The dynamic equation of equilibrium can be expressed as follows. Summing the pressure and water gravity forces, the transient pressure h_a at the gate can be found.

$$\sum F_x = \omega A_p (H_0 + h_a) - \omega A_p L_p \sin(\alpha) - \omega A_p (H_0 - Z) \tag{2.6}$$

Since:

$$L_p \sin(\alpha) = Z \tag{2.7}$$

then:

$$\begin{aligned} &\sum F_x = \omega A_p (H_0 + h_a) - \omega A_p Z - \omega A_p (H_0 - Z) \\ &= \omega A_p (H_0 + h_a - Z - H_0 + Z) \end{aligned} \tag{2.8}$$

$$\sum F_x = \omega A_p (h_a) \tag{2.9}$$

$$\sum F_x = -m_w a_x = \frac{\omega A_p L_p}{g} (-\frac{dV}{dt}) \tag{2.10}$$

where:

a_x	Acceleration of the water, m/s^2
m_w	Mass of the water, kg

(2.9) in (2.10)

$$\omega A_p (h_a) = \frac{\omega A_p L_p}{g} (-\frac{dV}{dt}) \tag{2.11}$$

$$h_a = -\frac{L_p}{g} (\frac{dV}{dt}) \tag{2.12}$$

2.3.1.4 Discharge through a Gate

The relation computing the discharge through a gate is used to express the water velocity as a function of h_a, the transient pressure calculated in the previous section.

$$Q_0 = A_p V_0 = (C_d A_g)_0 \sqrt{2gH_0} \tag{2.13}$$

Q_0 Initial flow rate, m^3/s

V_0 Initial velocity of water at the gate, m/s

C_d Coefficient of discharge through the gate

A_g Cross-sectional area of the gate opening, m^2

Eq. (2.13) allows the initial velocity to be expressed in terms of the static pressure

$$V_0 = B_0\sqrt{H_0} \tag{2.14}$$

where

$$B_0 = \left(\frac{C_d A_g}{A_p}\sqrt{2g}\right)_0$$ Effective gate opening at time $t = 0$ (2.15)

For any other time, the water velocity at the gate is equal to:

$$V = B\sqrt{H_0 + h_a} \tag{2.16}$$

where

$$B = \frac{C_d A_g}{A_p}\sqrt{2g}$$ Effective gate opening (2.17)

The ratio $\frac{V}{V_0}$ gives:

$$\frac{V}{V_0} = \frac{B}{B_0}\sqrt{1+\frac{h_a}{H_0}} = \tau\sqrt{1+\frac{h_a}{H_0}} \tag{2.18}$$

τ Ratio of the full gate effective closure

For a partial or complete uniform gate closure the above ratio is equal to:

$$\tau = 1 - \frac{V' t}{V_0 T} \tag{2.19}$$

where

V' Difference between initial and final velocities, m/s

T Time for gate closure, s

Eq. (2.19) in (2.18) gives:

$$V = (V_0 - \frac{V' t}{T})\sqrt{1 + \frac{h_a}{H_0}} \tag{2.20}$$

2.3.1.5 Maximum Transient Pressure

Combining Eqs. (2.12) and (2.20), the maximum transient pressure caused by the gate closure can be found by setting $d(h_a)/dt = 0$. Essentially, this would correspond to an instantaneous gate closure. This equation has originally been found by Allievi (1925).

$$\frac{(h_a)_{max}}{H_0} = \frac{\vartheta}{2} + \sqrt{\vartheta + \frac{\vartheta^2}{4}} \tag{2.21}$$

where

$$\vartheta = \left(\frac{L_p V'}{g H_0 T} \right)^2 \tag{2.22}$$

2.3.1.6 Limitations

Due to assumptions 1 and 2, the pressure change is felt immediately throughout the pipe. Those assumptions limit then the theory's applicability for relatively slow gate movements. Reliable results are obtained only if the time for closure "T "is greater than $L_p/1000$.

2.3.2 Elastic Water Column Theory

2.3.2.1 Theoretical Assumptions

1. The pipe line remains filled with water at all times and the minimum pressure inside the pipe is in excess of the vapour pressure of water.
2. Hydraulic losses and velocity heads are negligible when compared to pressure changes.
3. The velocity of the water in the longitudinal direction of the pipe is uniform throughout its cross section.

4. The pressure is uniform throughout the cross section of the pipe and is equal to the pressure at the center line of the pipe.
5. The reservoir level remains constant during gate opening and its closure
6. There are no gas bubbles in the liquid (no cavitation occurs)

2.3.2.2 Free-Body Diagram

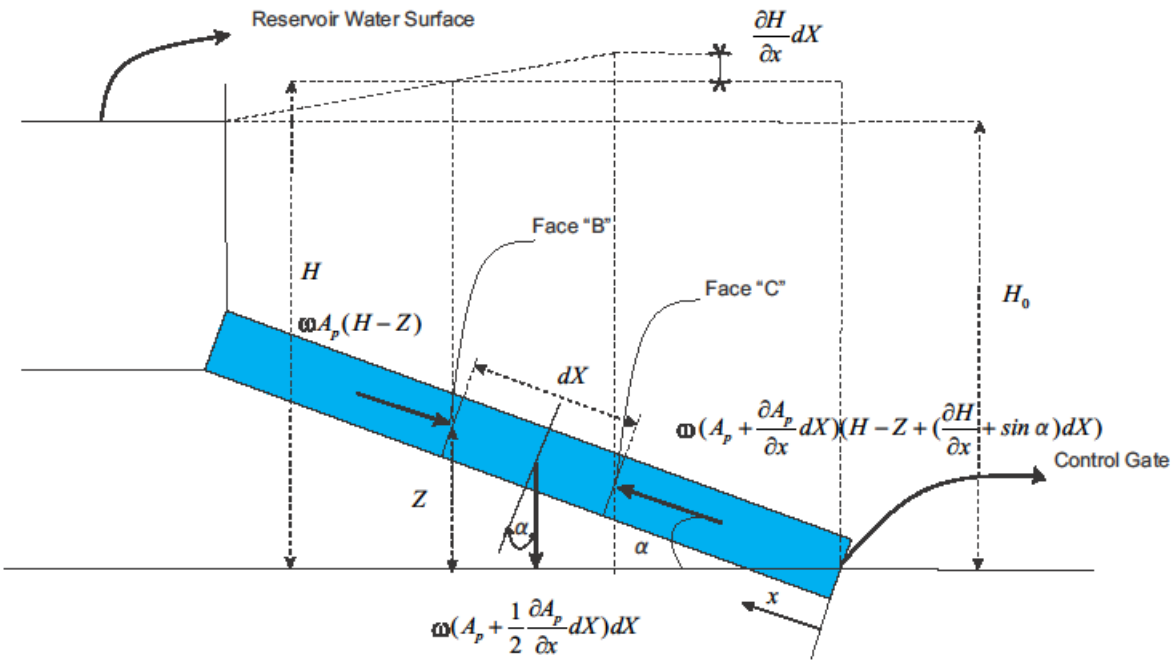

Figure 2. 9 - Elastic Water Column diagram

dX	Element length, *m*
H	Pressure head, *m*

2.3.2.3 Momentum Equation

$$\sum F_x = \omega(A_p + \frac{\partial A_p}{\partial x}dX)(H - Z + (\frac{\partial H}{\partial x} + \sin\alpha)dX) - \omega A_p(H - Z) - \omega(A_p + \frac{1}{2}\frac{\partial A_p}{\partial x}dX)dX \quad (2.23)$$

Eliminating the second order derivative and simplifying, the above equation is reduced to:

$$\sum F_x = \omega\left[A_p\frac{\partial H}{\partial x} + \frac{\partial A_p}{\partial x}(H - Z)\right]dX \quad (2.24)$$

The second term in the parenthesis is very small compared to the first one, so that it can be neglected. Hence, one obtains:

$$\sum F_x = \omega A_p \frac{\partial H}{\partial x} dX \tag{2.25}$$

According to the second law of motion

$$\omega A_p \frac{\partial H}{\partial x} dX = \frac{\omega}{g} A_p dX \left(-\frac{dV}{dt}\right) \tag{2.26}$$

$$\frac{dV}{dt} = \frac{\partial V}{\partial t} + \frac{\partial V}{\partial x}\frac{\partial x}{\partial t} = \frac{\partial V}{\partial t} + V\frac{\partial V}{\partial x} \quad \text{since } V \text{ is a function of } t \text{ and } x \tag{2.27}$$

Combining Eqs. (2.26) and (2.27), the momentum equation becomes:

$$\frac{\partial H}{\partial x} = -\frac{1}{g}\left(\frac{\partial V}{\partial t} + V\frac{\partial V}{\partial x}\right) \tag{2.28}$$

2.3.2.4 The Continuity Theorem

The continuity theorem is necessary to find the second partial differential equation relating the pressure and the velocity. The transient pressure, h_a created by the water hammer has lead to an expansion of the pipe shell and a compression of the water volume, thus changing the water element length shown on Figs. 2.3 and 2.4. Equalizing the water element length (Sec. 2.1.2.4.1) to the sum of the effects (Sec. 2.1.2.4.2 and 2.1.2.4.3) allows one to obtain the governing differential equation.

2.3.2.4.1 Water Element Length Change

Fig. 2.10 shows the velocities at sections B and C at time t before the water element has been hit by the transient pressure h_a. Fig. 2.11 shows the velocities at sections D and F at time $t + dt$ after the water segment has been affected by the transient pressure h_a.

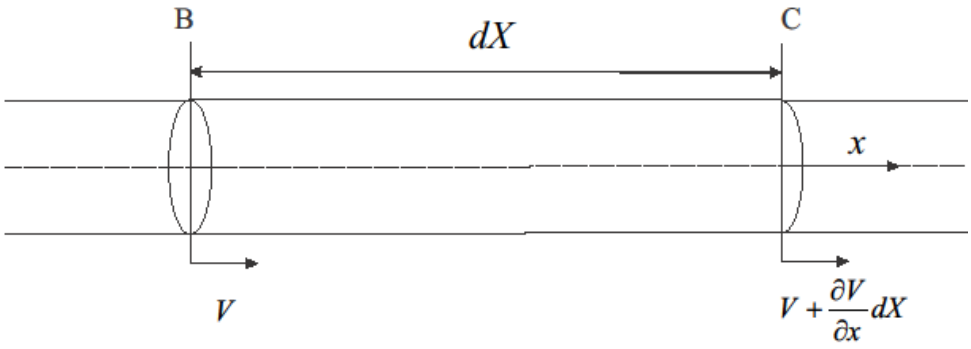

Figure 2. 10 - Water element at time t

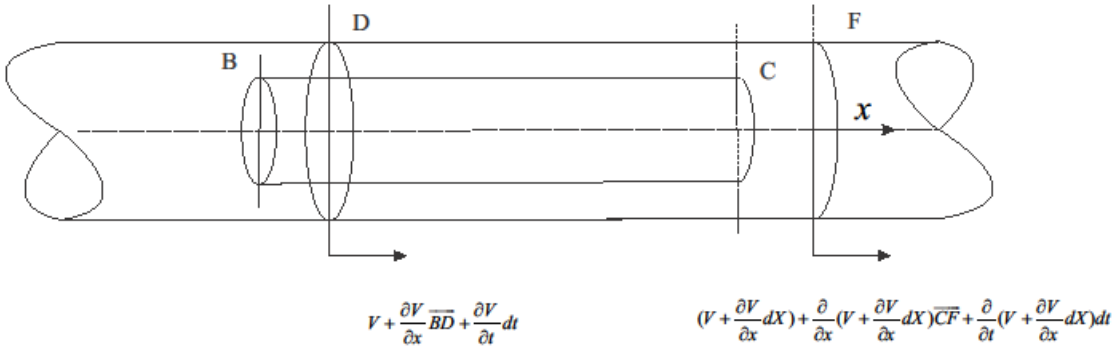

Figure 2. 11 - Water element at time t+dt

The distance $\overrightarrow{BD}$ can be found by taking the average velocity between sections B and D and multiplying it by an increment of time dt.

$$\overrightarrow{BD}=(V+\frac{1}{2}\frac{\partial V}{\partial x}\overrightarrow{BD}+\frac{1}{2}\frac{\partial V}{\partial t}dt)dt \tag{2.29}$$

Same thing can be done to found the distance $\overrightarrow{CF}$

$$\overrightarrow{CF}=((V+\frac{\partial V}{\partial x}dX)+\frac{1}{2}\frac{\partial}{\partial x}(V+\frac{\partial V}{\partial x}dX)\overrightarrow{CF}+\frac{1}{2}\frac{\partial}{\partial t}(V+\frac{\partial V}{\partial x}dX)dt)dt \tag{2.30}$$

Neglecting its higher derivative terms and subtracting the two vectors, one can find the length change of the water element between time t and $t+dt$.

$$\overrightarrow{BD}-\overrightarrow{CF}=(-\frac{\partial V}{\partial x}dX)dt \tag{2.31}$$

2.3.2.4.2Pipe shell expansion

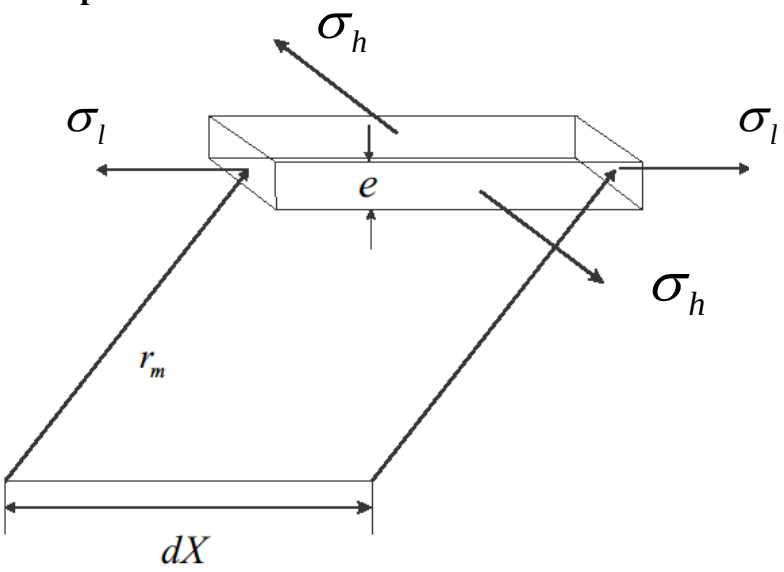

Figure 2. 12 - Pipe element Stresses

σ_l	Longitudinal Stress, *MPa*
σ_h	Hoop Stress, *MPa*
r_m	Pipe's middle radius, *m*
Δr_m	Radius changed in the pipe, *m*
D_p	Diameter, *m*
e	Thickness, *m*
δx	Change in the longitudinal length, *m*
E	Young's Modulus, *Pa*
dH	Pressure changed in the pipe, *m*
μ	Poisson's coefficient

The strains and the stresses have components in the circumferential and longitudinal direction.

i) Strain in the circumferential direction:

$$\frac{\Delta r_m}{(r_m + e/2)} E = (\Delta\sigma_h - \mu\Delta\sigma_l) \tag{2.32}$$

$$\Delta r_m = \frac{(r_m + e/2)}{E}(\Delta\sigma_h - \mu\Delta\sigma_l) \tag{2.33}$$

$$\Delta r_m \approx \frac{r_m}{E}(\Delta\sigma_h - \mu\Delta\sigma_l) \tag{2.34}$$

ii) Strain in longitudinal direction:

$$\delta x = \frac{dX}{E}(\Delta\sigma_l - \mu\Delta\sigma_h) \tag{2.35}$$

iii) The length variation:

$$\frac{\Delta v_p}{A_p} = \frac{\pi(r_m + \Delta r_m)^2(\delta x + dX) - \pi {r_m}^2 dX}{\pi {r_m}^2} = \delta x + 2\frac{\Delta r_m}{r_m} dX \tag{2.36}$$

where:

Δv_p Variation of pipe volume, m^3

Inserting Eqs. (2.34) and (2.35) in (2.36), one obtains:

$$\delta x + 2\frac{\Delta r_m}{r_m} dX = \frac{dX}{E}(\Delta\sigma_l - \mu\Delta\sigma_h) + (\frac{2}{E})(\Delta\sigma_h - \mu\Delta\sigma_l))dX \tag{2.37}$$

iv) Boundary Conditions

Depending on the boundary conditions of the pipe, the stresses values differ. The boundary conditions can be defined as:

1. Anchored at the upper end, free to move in the longitudinal direction
2. Anchored against longitudinal movement throughout its entire length.
3. Pipe with expansion joints between anchors throughout the pipe.

Case 1

$$\Delta\sigma_l = \frac{dH\omega D_p}{4e} \tag{2.38}$$

$$\Delta\sigma_h = \frac{dH\omega D_p}{2e} \tag{2.39}$$

Inserting (2.38) and (2.39) into (2.37), one obtains:

$$\delta x + 2\frac{\Delta r_m}{r_m}dX = \frac{dX}{E}\left(\frac{dH\omega D_p}{4e} - \mu\frac{dH\omega D_p}{2e}\right) + \frac{2dX}{E}\left(\frac{dH\omega D_p}{2e} - \mu\frac{dH\omega D_p}{4e}\right) \tag{2.40}$$

$$\delta x + 2\frac{\Delta r_m}{r_m}dX = \frac{dH\omega D_p}{Ee}\left(\frac{5}{4} - \mu\right)dX \tag{2.41}$$

Case 2

$$\Delta\sigma_l = \frac{dH\mu\omega D_p}{2e} \tag{2.42}$$

$$\Delta\sigma_h = \frac{dH\omega D_p}{2e} \tag{2.43}$$

$$\delta x + 2\frac{\Delta r_m}{r_m}dX = \frac{dH\omega D_p}{Ee}(1-\mu^2)dX \tag{2.44}$$

Case 3

$$\Delta\sigma_l = 0 \tag{2.45}$$

$$\Delta\sigma_h = \frac{dH\omega D_p}{2e} \tag{2.46}$$

$$\delta x + 2\frac{\Delta r_m}{r_m}dX = \frac{dH\omega D_p}{Ee}\left(1 - \frac{\mu}{2}\right)dX \tag{2.47}$$

v) General Equation

From the three cases, a general relation can be stated

$$\Delta L_{pe} = \delta x + 2\frac{\Delta r_m}{r_m}dX = \frac{dH\omega D_p dX}{Ee}c_1 \tag{2.48}$$

where:

c_1 Constant function of the boundary conditions of the pipe

ΔL_{pe} Variation of the pipe's length caused by the elasticity of the wall, *m*

2.3.2.4.3 Compression of water

$$\Delta v_w = \frac{(\omega dH)\cdot(\pi r_m{}^2 dX)}{k} \tag{2.49}$$

$$\Delta L_{pw} = \frac{\Delta v_w}{A_p} = \frac{(\omega dH)\cdot(\pi r_m{}^2 dX)}{k\cdot(\pi r_m{}^2)} = \frac{(\omega dH dX)}{k} \tag{2.50}$$

where:

k Bulk modulus of the water, *Pa*

Δv_w Variation of water volume, m^3

ΔL_{pw} Variation of the pipe's length caused by the compressibility of the water, *m*

ΔL_{pt} Total variation of the pipe's length, *m*

$$\Delta L_{pt} = \Delta L_{pe} + \Delta L_{pw} = \frac{\omega D_p dH dX}{Ee} c_1 + \frac{\omega}{k} dH dX = \omega dH dX\left(\frac{1}{k} + \frac{D_p}{Ee} c_1\right) \tag{2.51}$$

The variation of pressure dH is functioned of the time and the axial direction. One can then write:

$$dH = \frac{\partial H}{\partial t}\partial t + \frac{\partial H}{\partial x}\partial X = \left[\frac{\partial H}{\partial t} + V\frac{\partial H}{\partial x}\right]dt \tag{2.52}$$

Inserting Eqs. (2.52) in (2.51) gives:

$$\omega\left(\frac{1}{k} + \frac{D_p}{Ee} c_1\right)\left[\frac{\partial H}{\partial t} + V\frac{\partial H}{\partial x}\right]dt dX \tag{2.53}$$

2.1.2.4.4 PDE Equation Resulting From The Continuity Theorem

Equalizing Eqs. (2.31) and (2.53), one can obtain:

$$\left(-\frac{\partial V}{\partial x} dX\right)dt = \omega\left(\frac{1}{k} + \frac{D_p}{Ee} c_1\right)\left[\frac{\partial H}{\partial t} + V\frac{\partial H}{\partial x}\right]dt dX \tag{2.54}$$

$$\frac{\partial V}{\partial x} = -\omega\left(\frac{1}{k} + \frac{D_p}{Ee}c_1\right)\left[\frac{\partial H}{\partial t} + V\frac{\partial H}{\partial x}\right] \tag{2.55}$$

$$\left[\frac{\partial H}{\partial t} + V\frac{\partial H}{\partial x}\right] = -\frac{a_c^{\,2}}{g}\cdot\frac{\partial V}{\partial x} \tag{2.56}$$

2.3.2.5 PDE System

To recapitulate, the two partial equations modeling the water hammer phenomenon are:

$$\frac{\partial H}{\partial x} = -\frac{1}{g}\left(\frac{\partial V}{\partial t} + V\frac{\partial V}{\partial x}\right)$$ From the momentum equation (2.28)

$$\left[\frac{\partial H}{\partial t} + V\frac{\partial H}{\partial x}\right] = -\frac{a_c^{\,2}}{g}\cdot\frac{\partial V}{\partial x}$$ From the continuity equation (2.56)

The speed variation according to x is negligible when compared to the speed variation over time.

$$\partial V/\partial x \lll\lll \partial V/\partial t \tag{2.57}$$

The pressure variation according to x is negligible when compared to the pressure variation over time.

$$\partial H/\partial x \lll\lll \partial H/\partial t \tag{2.58}$$

Considering those facts, the Eqs. (2.28) and (2.56) above can be restated

$$\frac{\partial H}{\partial x} = -\frac{1}{g}\left(\frac{\partial V}{\partial t}\right) \tag{2.59}$$

$$\frac{\partial H}{\partial t} = -\frac{a_c^{\,2}}{g}\cdot\frac{\partial V}{\partial x} \tag{2.60}$$

2.4 Water Hammer: Resolving methods

2.4.1 Arithmetic Method

The system of partial differential Eqs. (2.59) and (2.60) has once been resolved in Allievi (1925). Its solution, which applies for the entire length of the penstock, is shown here.

$$H - H_o = F(t - x/a_c) + f(t + x/a_c) \tag{2.61}$$

$$V - V_o = -\frac{g}{a_c}\left[F(t - x/a_c) - f(t + x/a_c)\right] \tag{2.62}$$

Where:

$F\left(t - x/a_c\right)$ Pressure wave travelling from the gate toward the reservoir, m (2.63)

$f(t + x/a_c)$ Reflected wave travelling from the reservoir toward the gate, m (2.64)

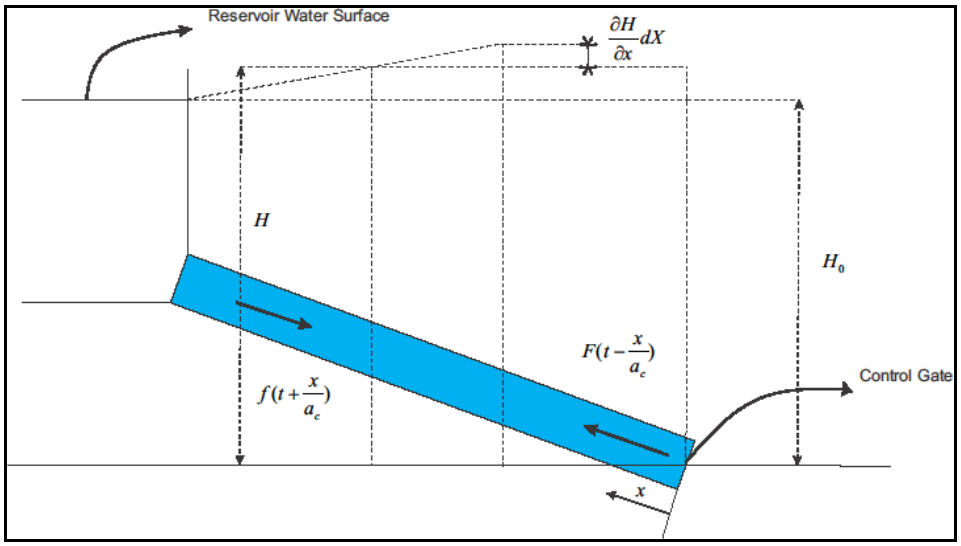

Figure 2. 13 - Arithmetic Method Diagram

2.4.1.1 Concept

In the particular case in which $T < 2L_p/a_c$,the maximum pressure computed at the gate is affected by only the F wave since it takes $2L_p/a_c$ seconds for the reflected wave f to reach the gate. In this particular case, that considers the rapid gate closure, the pressure magnitude can be determined by equaling the second term on the right side of the Eq. (2.61) to 0. The obtained formula matches the early water hammer theory (Joukowski 1900).

$$H - H_0 = \frac{a_c}{g}(V - V_0) \; or \; \Delta H = \frac{a_c}{g}\Delta V \tag{2.65}$$

However, practicality and security reasons from real situations often require $T > 2L_p/a_c$ in which the Joukowski's equation no longer stands. For these cases, the F and f

pressure waves add and their sum can be calculated using the arithmetic method previously developed (Gibson 1920)

The arithmetic method assumes that the gate closes in a N number of timestep (Fig. 2.7). For every ΔV related to the timestep, a water hammer of magnitude ΔH is generated according to Eq. (2.65). The summation of all ΔH at a precise location for each timestep allows one to find the time response of h_a.

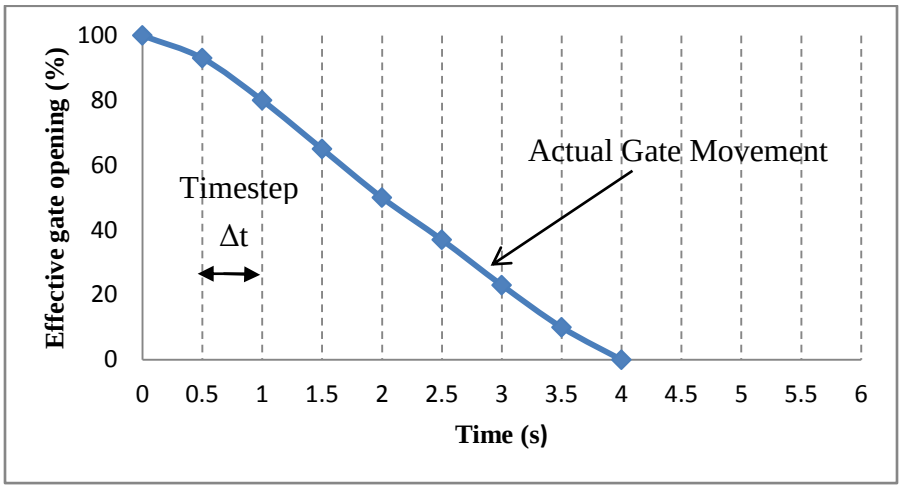

Figure 2. 14 - Timestep in the Arithmetic Method

2.4.1.2 Method of Computation

Unknowns from Eqs. (2.61) and (2.62) can only be solved with two additional equations. The first equation can be derived from the physics of the problem stating that, at position x_1, the value of a reflected wave is equaled in magnitude but opposite in sign of the primary wave $2L_x/a_c$ seconds later (Fig. 2.8).

$$f(t) = -F(t - 2L_x/a_c) \tag{2.66}$$

where:

x_1	Location where the pressure is computed
L_x	Length between the position x_1 and the inlet boundary condition, m

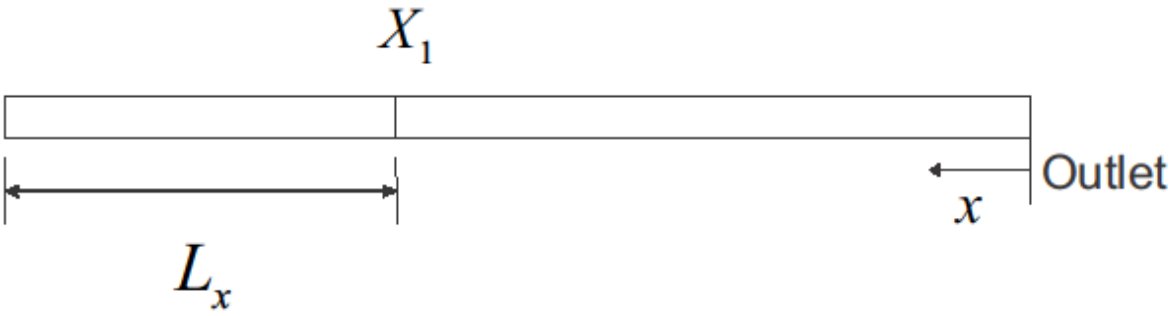

Figure 2. 15 - Pressure Location

The second equation that relates the velocity to the reflected wave at the gate is calculated with the equation of flow discharged through an orifice.

$$Q = (C_d A_g)\sqrt{2gH} \tag{2.67}$$

Q Flow rate, m^3/s

$C_d A_g$ Effective area of the gate, m^2

Using (2.61), (2.62) and (2.67) and isolating V, one can obtain the velocity at the gate:

$$V = -\frac{a_c B^2}{2g} + \frac{B}{2}\sqrt{\left(\frac{a_c B}{g}\right)^2 + 4\left(H_0 + \frac{a_c V_0}{g} + 2f\right)} \tag{2.68}$$

Eqs. (2.61), (2.62), (2.66) and along with the gate closure time relation (Fig. 2.8) allows one to plot the pressure time response at any location x_1. Time response for any location x_1 can be plotted as long as the used timestep is smaller than $2L_x/a_c$.

Computation using the arithmetic method is limited to simple cases that involve a constant thickness wall in which valves and reservoirs act as boundary conditions. Furthermore, due to its large amount of calculations, the method requires the need of a computer.

The next method presented has been developed throughout the 50's to overcome the arithmetic method limitations.

2.4.2 Graphical Method

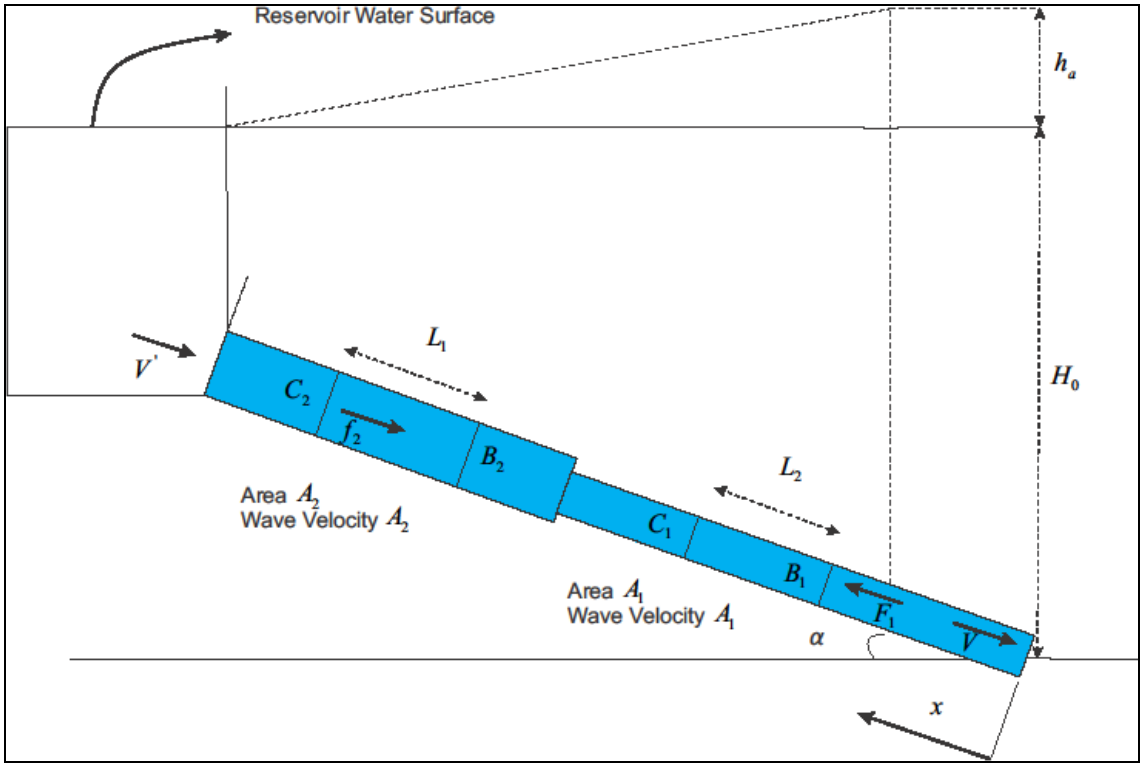

Figure 2. 16 - Graphical Method

2.4.2.1 Concept

In order to express the pressure time response for any locations and any types of penstock, a graphical method has been developed (Bergeron (1950); Parmakian (1963)). In the subsequent paragraph, the theory behind the method will be derived.

2.4.2.2 Method of Computation

Step 1:

Adding and subtracting equation (2.61) and (2.62) one can obtain:

$$H - H_0 = \frac{a_c}{g}(V - V_0) + 2F(t - \frac{x}{a_c}) \tag{2.69}$$

$$H - H_0 = -\frac{a_c}{g}(V - V_0) + 2f(t + \frac{x}{a_c}) \tag{2.70}$$

Step 2:

Refer to Fig. 2.9 to understand annotations. Eqs. (2.69) and (2.70) are applied to the (B1,C1) sections and (B2,C2) sections at time t=0,1,2,.....

$$H_{B1t1} - H_{B1t0} = \frac{a_{c1}}{g}(V_{B1t1} - V_{B1t0}) + 2F_1 \tag{2.71}$$

$$H_{C1t2} - H_{C1t0} = \frac{a_{c1}}{g}(V_{C1t2} - V_{C1t0}) + 2F_1 \tag{2.72}$$

$$H_{C2t3} - H_{C2t0} = -\frac{a_{c2}}{g}(V'_{C2t3} - V'_{C2t0}) + 2f_2 \tag{2.73}$$

$$H_{B2t4} - H_{B2t0} = -\frac{a_{c2}}{g}(V'_{B2t4} - V'_{B2t0}) + 2f_2 \tag{2.74}$$

Assuming at t=0 that:

$$H_{B1t0} = H_{C1t0} \tag{2.75}$$

$$H_{C2t0} = H_{B2t0} \tag{2.76}$$

$$V_{B1t0} = V_{C1t0} \tag{2.77}$$

$$V'_{C2t0} = V'_{B2t0} \tag{2.78}$$

One can find:

$$H_{B1t1} - H_{C1t2} = \frac{a_{c1}}{g}(V_{B1t1} - V_{C1t2}) \tag{2.79}$$

$$H_{C2t3} - H_{B2t4} = -\frac{a_{c2}}{g}(V'_{C2t3} - V'_{B2t4}) \tag{2.80}$$

Step 3:

Considering those ratios:

$$h = H/H_0 \tag{2.81}$$

$$v = V/V_0 \tag{2.82}$$

We can rewrite the equations as:

$$h_{B1t1} - h_{C1t2} = 2\rho_1(v_{B1t1} - v_{C1t2}) \tag{2.83}$$

$$h_{C2t3} - h_{B2t4} = -2\rho_2(v'_{C2t3} - v'_{B2t4}) \tag{2.84}$$

where:

$$\rho_1 = \frac{a_{c1}V_0}{2gH_0} \quad \text{pipe line constant 1} \tag{2.85}$$

$$\rho_2 = \frac{a_{c2}V_0'}{2gH_0} \quad \text{pipe line constant 2} \tag{2.86}$$

a_{c1} Velocity of pressure wave at section 1, m/s (2.87)

a_{c2} Velocity of pressure wave at section 2, m/s (2.88)

Step 4

Boundary conditions are necessary to resolve the problem. A system of a reservoir and a gate is here presented to the reader and illustrated in Paramakian (1963).

Reservoir boundary condition:

For constant reservoir level, $H = H_0$, so

$$h_r = 1 \quad h_r \text{ ratio at the reservoir} \tag{2.89}$$

Gate:

Under steady conditions, from Eq. (2.14) one knows that:

$$V_{A0} = B_0\sqrt{H_{A0}} \tag{2.90}$$

At any gate opening:

$$V_A = B\sqrt{H_A} \tag{2.91}$$

Considering those ratios:

$$v = \frac{V_A}{V_{A0}} \tag{2.92}$$

$$h = \frac{H_A}{H_{A0}} \tag{2.93}$$

$$\tau = \frac{B}{B_0} \tag{2.94}$$

One can obtain:

$$v_A = \tau\sqrt{h_A} \tag{2.95}$$

2.4.3 Characteristic Method

2.4.3.1 Concept

The method of characteristic (MOC) is a one dimensional analysis currently used by many listed industrial software (Ghidaoui et al. (2005)) to represent the water hammer phenomena. It transforms the partial differential equations (PDE) of motion and continuity stated in Eqs. (2.56) and (2.28) into ordinary differential equations. It allows the user to determine the pressure and flow variation for any location on the pipe axis at any instant and for any complicated pipe system.

2.4.3.2 Method of Computation

To facilitate the reader's comprehension, the friction term has been neglected from the following development. In depth details can be read in Wylie & Streeter (1993).

Reformulate Eqs. (2.28) and (2.60)

$$L_D = \frac{\partial H}{\partial x} + \frac{1}{g}\left(\frac{\partial V}{\partial t}\right) = 0 \rightarrow L_D = gA_p\frac{\partial H}{\partial x} + \frac{\partial Q}{\partial t} = 0 \quad \text{Dynamic Equation} \tag{2.96}$$

$$L_C = \frac{\partial H}{\partial t} + \frac{a_c^{\,2}}{g}\left(\frac{\partial V}{\partial x}\right) = 0 \rightarrow L_C = gA_p\frac{\partial H}{\partial t} + a_c^{\,2}\left(\frac{\partial Q}{\partial x}\right) = 0 \quad \text{Continuity Equation} \tag{2.97}$$

Multiply (2.97) by an arbitrary constant λ and add (2.96) to the product:

$$L_D + \lambda L_C = (\frac{\partial Q}{\partial t} + \lambda a_c^{\,2} \frac{\partial Q}{\partial x}) + gA_p \lambda (\frac{\partial H}{\partial t} + \frac{1}{\lambda} \frac{\partial H}{\partial x}) = 0 \tag{2.98}$$

Since the pressure $H(x,t)$ and the flow $Q(x,t)$ are functioned of the longitudinal direction and the time, their total derivative can be written as:

$$\frac{dH}{dt} = \frac{\partial H}{\partial t} + \frac{\partial H}{\partial x} \frac{\partial x}{\partial t} \tag{2.99}$$

$$\frac{dQ}{dt} = \frac{\partial Q}{\partial t} + \frac{\partial Q}{\partial x} \frac{\partial x}{\partial t} \tag{2.100}$$

From Eqs. (2.98), (2.99) and (2.100) it can be seen that $\partial x/\partial t$:

$$\frac{\partial x}{\partial t} = \lambda a_c^{\,2} = \frac{1}{\lambda} \rightarrow \lambda = \pm \frac{1}{a_c} \tag{2.101}$$

Inserting Eq. (2.101) in Eq. (2.98)

$$\frac{dQ}{dt} + \frac{gA_p}{a_c} \frac{dH}{dt} = 0 \qquad \text{for } dx/dt = a_c \tag{2.102}$$

$$\frac{dQ}{dt} - \frac{gA}{a_c} \frac{dH}{dt} = 0 \qquad \text{for } dx/dt = -a_c \tag{2.103}$$

Many solutions have been proposed to solve these equations.

- Streeter & Wylie (1967) proposed a first order finite difference method
- Evangelisti (1966) proposed a predictor-corrector method
- Lister (1960) proposed a first and second order finite difference method

Streeter & Wylie's method is the simplest, but requires small increments of time and low friction losses in the pipe.

- Increments of time will be chosen so the method will be stable.
- Friction losses are low enough due to the large difference between the diameter and the thickness of the pipe.

Eq. (2.101) represents two lines illustrated on a $x-t$ graphic (Fig. 2.10) that have a slope of $\pm 1/a_c$. The lines are called characteristics lines.

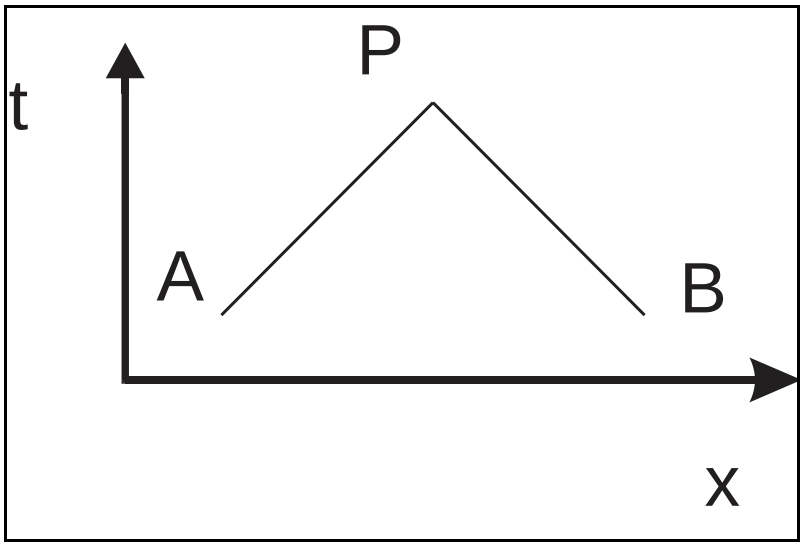

Figure 2. 17 - Characteristic lines in the x-t plane

2.4.3.3 Method's Representation

The goal of the method is to draw, for a chosen length's increment, two characteristic lines and determine, at the junction P (Fig. 2.10), the pressure and flow values.

For its simplest expression, the method can be analysed with a length increment of L, i.e. the complete length of the pipe. Point A is located at the entrance of the pipe and point B at the gate.

According to Fig 2.10 the variation of flow and pressure along the line AP is equal to:

$$dQ = Q_P - Q_A \tag{2.104}$$

$$dH = H_P - H_A \tag{2.105}$$

Similarly, the variation of flow and pressure along the line BP is equal to:

$$dQ = Q_P - Q_B \tag{2.106}$$

$$dH = H_P - H_B \tag{2.106}$$

Putting Eqs. (2.104) and (2.105) in Eq. (2.102) and multiplying by dt , one can obtain:

$$(Q_p - Q_A) + \frac{gA_p}{a_c}\left(H_p - H_A\right) = 0 \tag{2.108}$$

Similarly, putting Eqs. (2.106) and (2.107) in Eq. (2.103) and multiplying by dt, one can obtain:

$$(Q_p - Q_B) + \frac{gA_p}{a_c}\left(H_p - H_B\right) = 0 \tag{2.109}$$

Eqs. (2.108) and (2.109) can be written:

$$Q_{P1} = C_p - C_a H_P \quad \text{Positive Characteristic Equation} \tag{2.110}$$

$$Q_{P2} = C_n + C_a H_P \quad \text{Negative Characteristic Equation} \tag{2.111}$$

in which:

$$C_p = Q_A + \frac{gA_p}{a_c} H_A \quad \text{Constant used in the characteristic method} \tag{2.112}$$

$$C_n = Q_B - \frac{gA_p}{a_c} H_B \quad \text{Constant used in the characteristic method} \tag{2.113}$$

$$C_a = \frac{gA_p}{a_c} \quad \text{Constant used in the characteristic method} \tag{2.114}$$

Note that the Eq. (2.110) is valid along the AP line and Eq. (2.111) is valid along the BP line. In Eqs. (2.110) and (2.111), the two unknowns Q_P, H_P can be found by resolution.

$$Q_P = \frac{C_p + C_n}{2} \tag{2.115}$$

$$H_P = \frac{1}{C_a}\left(\frac{C_p - C_n}{2}\right) \tag{2.116}$$

A time and length increment discretization of a given domain in which Q_P, H_P values can be computed at specific location and time (Fig. 2.11). Previously to the computations,

initial values (green dots) and boundary conditions (blue dots) must be specified by the user.

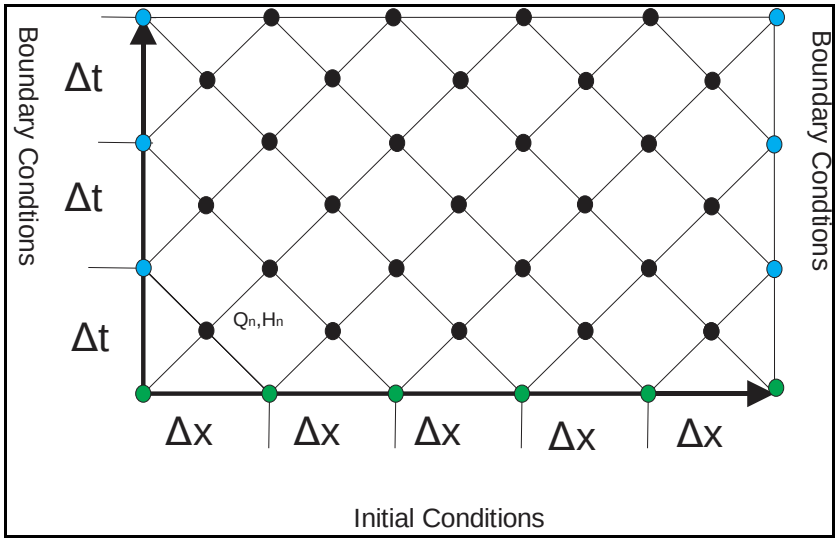

Figure 2. 18 - Characteristic Grid

Initial conditions values can easily be found using the Darcy-Weisbach equation for steady-state conditions.

Boundary conditions vary according to the problem type. Common boundary conditions (Chaudry (1979); Wylie & Streeter (1993); Ellis (2008)) are:

- Reservoirs and tanks
- Branches and changes in pipe properties
- Actuated valves and pipeline fittings
- Pumps
- Turbines

2.5 Conclusion

Chapter 2 covered the historical knowledge of the water hammer.

Section 2.2 reviewed the advancement of the water hammer knowledge throughout the researchers work from the beginning of the twentieth century until today. It then explained the purpose of the present work and what it brings to the scientific community.

Section 2.3 reviewed the water hammer theory, so a newcomer to the topic could follow the thesis. Two theories were developed. The rigid water column theory was based on the assumptions that the pipe wall is rigid and the water incompressible. It leads to a simple equation that could only be applied at under certain restrictions. The elastic water column theory assumed the pipe wall flexible and the water compressible. It lead to a partial differential equation (PDE) system that can be resolved with method explained in Section 2.4

Section 2.4 explains the three methods used to resolve the PDE system. The theories of the arithmetic, graphical and characteristic methods were explained and references were given. Those methods consider the water hammer unidimensional and don't consider the fluid-structure interaction effect.

The following thesis reproduces the water hammer using another method explained in details in Chapter 4. Unlike the three previous methods, this method represents the water hammer in three dimensions and takes the fluid-structure interaction into consideration.

CHAPTER 3 –CLASSICAL DESIGN

3.1 Objectives

This chapter intends to inform the reader on the rational steps used for a classical penstock design and to develop an analytical reference case.

Section 3.2 first explains the process step by step on how penstocks are currently designed in the industry sector.

Section 3.3 develops an analytical case of a simply supported pipe using a real case project. The case will be used as a comparison point with the numerical model built in Chapter 4 and presented in Chapter 5.

3.2 Design Steps

As shown in Fig. 3.1, penstock is a water conveyance pipe system that connects the dam to the powerhouse on a hydropowersite.

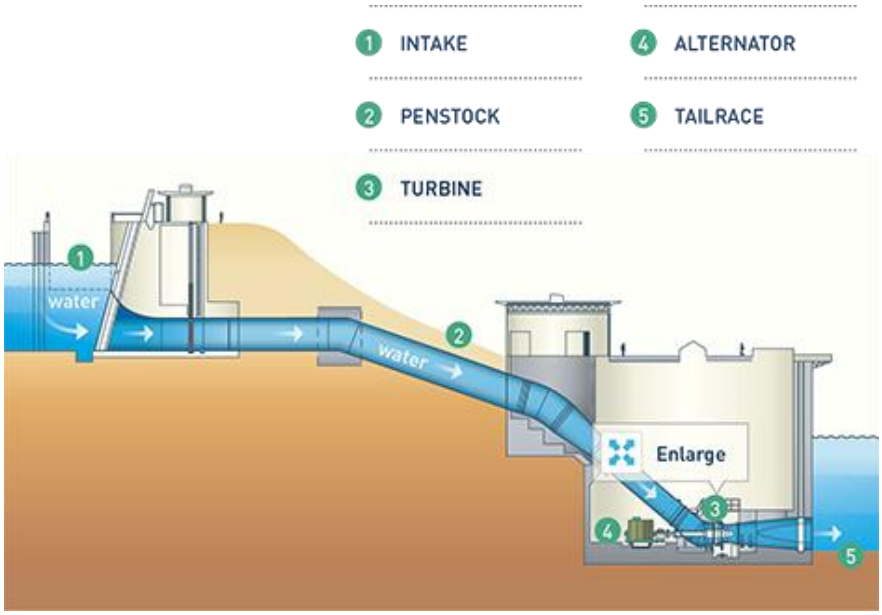

Figure 3. 1 – Hydropower Site

http://www.innergex.com/en/energy-sources

It is designed based on environmental, economical, technical and social considerations. The details are provided in the following

3.2.1 Input Data Validation

In the whole rational process of a hydro site development, the penstock design does not come first. Hydrological and geological data must have been collected prior to its design and will be used as input requirements. A short description of each requirement is described here.

3.2.1.1 Geotechnical Data and Elevations

Geological data are obtained from investigations and written down in a soil report. It includes the specification of core samples and the nature and characteristic of the soil. Elevations are obtained from a survey done in the first stage of the design. Both are input requirements used for the general layout of the penstock.

3.2.1.2 The design flow

The design flow is one of two major input parameters that dictate the total amount of energy produced at the powerhouse over its lifetime. It is determined throughout an iteration process using a flow-duration curve of a river and a turbine efficiency curve. The first of the two, shown in Fig. 3.2, represents the historical flow at a site from maximum to minimum flow. The second one, shown in Fig. 3.3, is a graph that represents the turbine efficiency for different flows. The iteration process is well documented and explained in RETScreen (2004). The design flow is an input requirement used in the penstock diameter optimization.

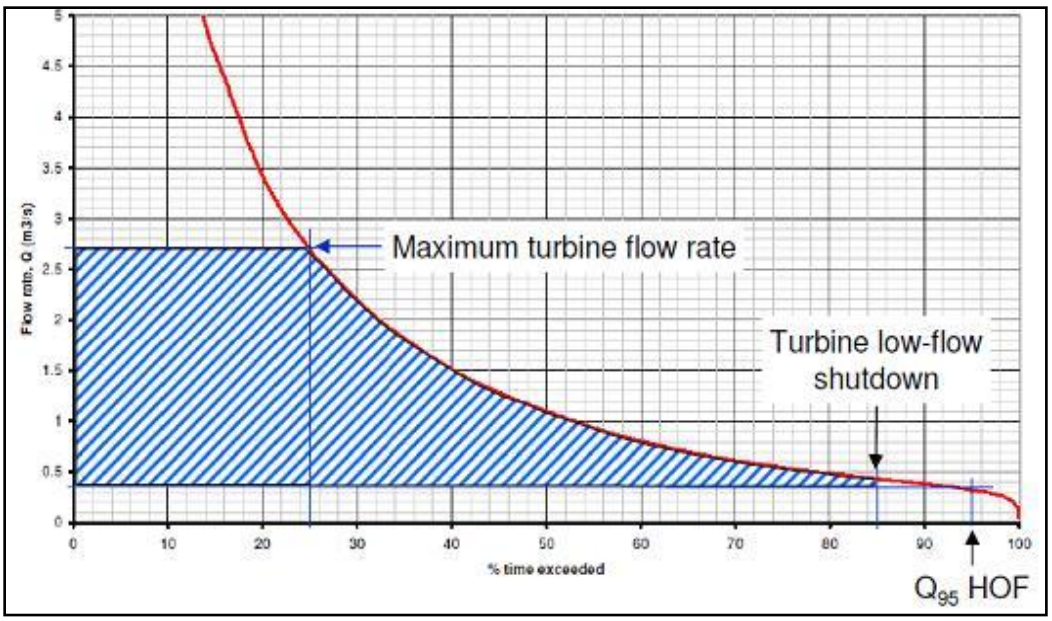

Figure 3. 2 - Flow Duration Curve of a River

http://www.renewablesfirst.co.uk/Hydro-feasibility-study.html

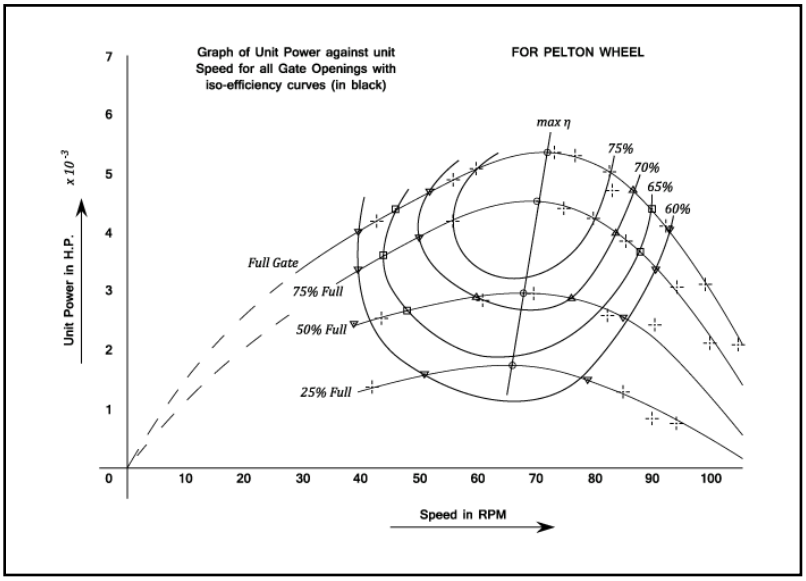

Figure 3. 3 - Turbine Efficiency Curve

http://www.codecogs.com/reference/engineering/fluid_mechanics/machines/turbines/specific_speed_and_unit_conditions.php

3.2.1.3 The gross head

The gross head is the second major input used for the energy production calculation. Its value is the difference between the headwater and the tail water levels under normal operating condition. It is determined throughout a socio-economic process within which

the headwater level is a compromise between profitability of the project and public acceptance. The gross head is an input requirement into the pipe-fluid analysis.

3.2.2 Determination of the General Layout

The general layout aims at economically conveying water from the reservoir to the powerhouse. The type of the soil, steepness of the terrain, existing infrastructure, temperature, environmental and social constraints will greatly affect the penstock layout. A design aims, as much as possible, at minimize the penstock length, to reduce the number of bends, facilitate the installation process and keep the penstock buried so it does not disturb the natural habitat. Unlike buried penstock segments, elevated ones are subjected to thermal effects induced by atmospheric temperature differentials. Also, they require supports that could increase the cost of the project.

3.2.3 Economic Diameter determination

The penstock's diameter (D_p) is determined through an optimization process. For a given design flow, the penstock diameter is inversely proportional to the fluid velocity and thus inversely proportional to the square of the head loss. A parabolic curve relating the cost of the head loss over the powerhouse lifetime for different diameters can then be drawn. Another curve relating the manufacturing and the installation cost of the penstock to its diameter is superimposed on the same graph. The intersection of both curves shown on Fig. 3.4 provides the optimal diameter. One must know that the second curve is a cost approximation based on similar projects done in the past.

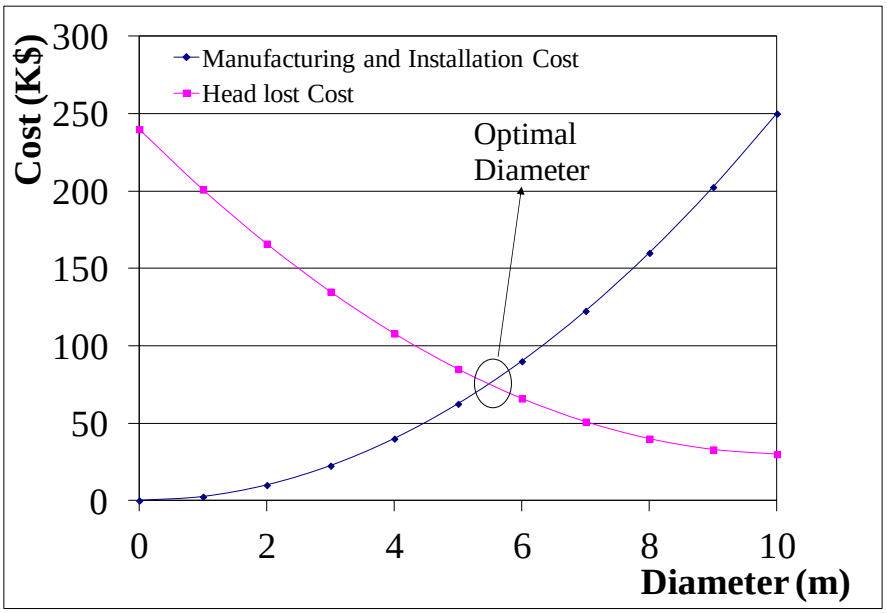

Figure 3. 4 - Economic Diameter Curves

Several economic diameter equations that estimate the value of the intersection point have been published and are available to the designers in Clause 1.4 of AWWA (2004). As a rule of thumb, a diameter corresponding to a head loss of four percent is typical in medium and small powerhouses.

3.2.4 Thickness determination

The thickness of the pipe (e) is the variable that is last adjusted to meet different cases requirement. Its value is determined in a document called Design Report which consists in a comprehensive, detailed calculation that clearly describes the stresses in a penstock. One must ensure that the thickness satisfies the minimum requirements listed in Section. 3.2.4.1. Loadings and allowable stresses required to calculate the third minimum requirement are listed in Section 3.2.4.2 .

3.2.4.1 Minimum thickness requirements

The minimum thickness of the penstock $e_{\min}$ should be the largest of the four following cases:

1. Penstock wall thickness should be large enough to ensure adequate shipment and handling. The largest value of the following formula taken from Clause 4.1.2.1 of ASCE (1993) should be used.

$$e_{min} = \frac{D_p}{288} \tag{3.1}$$

$$e_{min} = \frac{D_p + 20}{400} \tag{3.2}$$

2. Wall thickness should be large enough to ensure a maximum deflection δ_{max} of

$$\delta_{max} < \frac{L_p}{360} \tag{3.3}$$

3. Wall should be thick enough to resist the imposed loads given certain allowable stress conditions

4. An allowance for corrosion must be considered in the calculations.

5. The D_p / e ratio should be larger than 158 to avoid pipe buckling due to full internal vacuum.

3.2.4.2 Loading

i. Circumferential stresses

Circumferential stresses can be induced due to internal and/or external pressure. Internal pressure, as defined in Clause 3.1.5.1 of ASCE (1993) includes the pressure induced by static head, water hammer and hydrostatic tests. External pressure, as defined in Clause 3.1.5.2 of ASCE (1993), is induced by the ground water seepage pressure, the vacuum generated by dewatering, the soil height over the pipe and the loads generated by the concrete pouring during the construction phase.

ii. Longitudinal stresses

Loading causing longitudinal stresses includes dead and live loads which induce bending into the pipe wall, thermal effects and friction loads. Also, internal pressure can induce longitudinal stresses when the pipe ends are restrained due to the Poisson effect.

3.2.4.3 Combined stresses and Allowable Stresses

The von Mises effective stress σ_{vm}, a combined value of the circumferential σ_h and the longitudinal stresses σ_l, must be equal or less than an allowable stress σ_k. Both values are defined below.

$$\sigma_{vm} = (\sigma^2{}_h - \sigma_h \sigma_l + \sigma^2{}_l)^{1/2} \tag{3.4}$$

$$\sigma_k = K\sigma_f \tag{3.5}$$

where:

$$\sigma_f = \min(\frac{2}{3}S_y, \frac{1}{3}S_u) \tag{3.6}$$

S_y	Tensile Strength, *MPa*
S_u	Ultimate Strength, *MPa*
K	Increase factor

K is an increase factor. It depends on the type of conditions for which the stresses are calculated (Normal, Intermittent, Emergency, Exceptional, Construction, Hydrostatic test) and the category of those stresses (General Primary, Local Primary, Secondary). Table 3.5 of ASCE (1993) lists the value of the K factors for all different cases.

3.3 Practical Design Problem

The case is taken at the powerhouse Upper Bear Creek located in the city of Sechelt B.C. Calculations are made for the elevated straight section simply supported located between saddle S15-4 and S15-5.

3.3.1 Statement of the problem

Figure 3.5 shows a 15.384 m steel pipe segment filled with pressurized water $(\rho_w = 1000.02\ kg/m^3)$ and inclined by 25.86° with the horizontal. A hydraulic analysis had previously determined an economic diameter of 1.067 m. Steel ASTM A1018 Grade 60, $\left(\rho_s = 7850 kg/m^3,\ \mu = 0.3,\ E = 200 GPa,\ S_y = 413.7 MPa,\ S_u = 517.1 MPa\right)$ has been

used to manufacture the pipe. The expansion joint allows the pipe to move freely in the longitudinal direction and has a resistance force of $500D_p$ lbs in which D_p is in inches. The static pressure H_o that creates the distributed load is considered constant and equal to 455.267 m. The preliminary transient analysis using the characteristic method has predicted a water hammer amplification factor of 1.1.

It is required to determine the thickness of the pipe under normal operating conditions according to an increase factor of $K = 1$.

3.3.2 Free Body Diagram

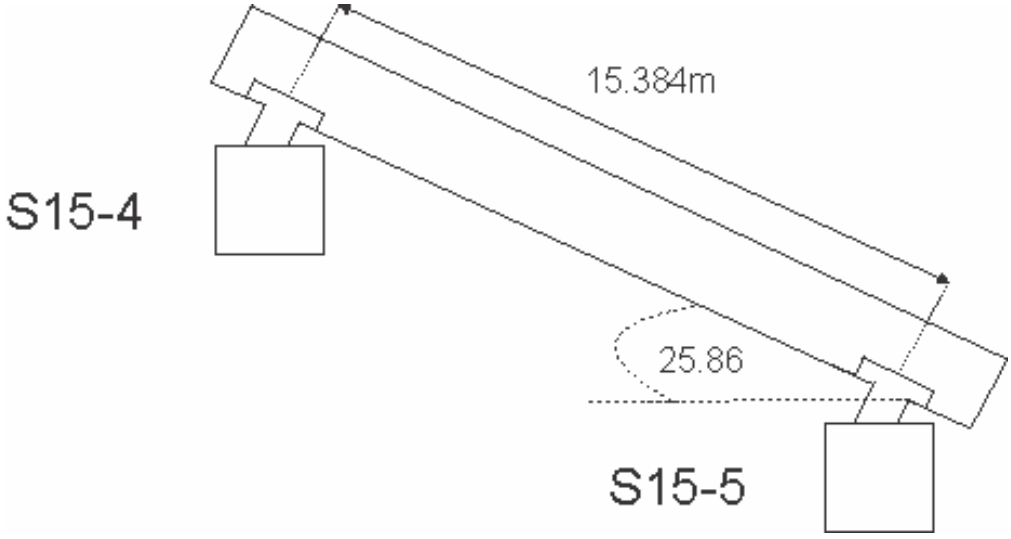

Figure 3. 5 - Free Body Diagram of the elevated straight segment at Upper Bear Creek

3.3.3 Assumptions

Due to the relatively small values of the radial stress, a plane state loading that generates circumferential and longitudinal stresses is considered.

3.3.4 Calculations

3.3.4.1 Stresses

i. Allowable Stresses

Take the smallest value

Allowable stress induced by the yield strength

$$\sigma_y = \frac{2S_y}{3} = \frac{2 \times 413.7MPa}{3} = 275.8MPa \tag{3.7}$$

Allowable stress induced by the ultimate strength

$$\sigma_u = \frac{S_u}{3} = \frac{517.1MPa}{3} = 172.4MPa \tag{3.8}$$

$$\sigma_k = K \times \min(\sigma_y, \sigma_u) = 1 \times 172.4MPa \tag{3.9}$$

ii. Minimum thickness required

$$e_t = \frac{H_o g \rho_w D_p f}{2\sigma_k} = \frac{455.3m \times 9.81m/s^2 \times 1000.02 \times (1.067)kg/m \times 1.1}{2 \times 172.4MPa} = 15.2mm \tag{3.10}$$

where:

f Water hammer amplification factor

According to the "Steel Penstock Specification, Upper and Lower Bear Hydro Project, "an allowance of 1.6mm, for corrosion purpose, is to be added to the thickness computed in Eq. (3.10) resulting in a total required thickness of $e_c = 16.8mm$. The closest available thickness is $e = 19.05mm$. Using the 19.05mm thickness, the hoop stress is recalculated as:

$$\sigma_h = \frac{H_o g \rho_w D_p f}{2e} = \frac{455.3m \times 9.81m/s^2 \times 1000.02kg/m^3 \times (1.067)m \times 1.1}{2 \times 0.0191m} = 137.6MPa \tag{3.11}$$

iii. Longitudinal Stress

A. Bending Stress due to gravity

The distributed force induced by the weight of the steel is

$$w_s = \frac{\pi(r_o^2 - r_i^2)L_p \rho_s}{L_p} = \frac{\pi \times (0.5526^2 - 0.5335^2)m^2 \times 15.384m \times 7850kg/m^3 \times 9.80665 \times 10^{-3}(kN/kg)}{15.384m} = 5.02k\,N/m \tag{3.12}$$

The distributed force induced by the weight of the water is

$$w_w = \frac{\pi(r_i^2)L_p\rho_w}{L_p}$$
$$= \frac{\pi \times (0.5335^2)m^2 \times 15.384m \times 1000.02\,kg/m^3 \times 9.80665 \times 10^{-3}\,(kN/kg)}{15.384m} \quad (3.13)$$
$$= 8.77\,kN/m$$

The total distributed force induced by the weight is

$$w_t = 5.02\,kN/m + 8.77\,kN/m = 13.8\,kN/m \quad (3.14)$$

The component of self weight inducing bending is

$$w_b = 13.8\,kN/m \times \cos(25.86^\circ) = 12.4\,kN/m \quad (3.15)$$

Assuming a simply supported condition, the maximum bending moment is

$$M_b = \frac{w_b L_p{}^2}{8} = \frac{12.4\,kN/m \times 15.384^2 m^2}{8} = 367kNm \quad (3.16)$$

And the corresponding maximum longitudinal stress is

$$\sigma_b = \frac{M_b}{S_p} = \frac{367kNm}{\pi r_i^2 e} = \frac{367kNm}{\pi \times (0.5335^2)m^2 \times 0.01905m} \quad (3.17)$$
$$= 21.5MPa$$

where:

r_i	Pipe inner radius, m
S_p	Pipe section modulus, m^3

B. Longitudinal Stress due to gravity

The component of self weight inducing normal stress is

$$w_l = 13.8\,kN/m \times \sin(25.86^\circ) = 6.02\,kN/m \quad (3.18)$$

and the corresponding maximum longitudinal stress is

$$\sigma_a = \frac{w_l L_p}{A_p} = \frac{6.02kN/m \times 15.384m}{\pi(r_o^2 - r_i^2)} = \frac{6.02kN/m \times 15.384m}{\pi \times (0.5526^2 - 0.5335^2)m^2} = 1.42MPa \quad (3.19)$$

where:

r_o Pipe's outside radius, m

C. Longitudinal Stress due to the expansion joint

Clause 4.1.2.3 of ASCE (1993) requires to consider a compressive force value of $500D_p$ to account for friction forces within the joint, i.e.,

$$T_e = 500D\ lbs = 87.6D\ kN \quad (3.20)$$

$$T_e = 87.6kN \times 1.067m = 93.47kN \quad (3.21)$$

The corresponding maximum longitudinal stress is

$$\sigma_e = \frac{93.47kN}{\pi \times (0.5526^2 - 0.5335^2)m^2} = 1.43MPa \quad (3.22)$$

Given the small value of the stress induced, the corresponding axial stress within the expansion joint will be neglected.

D. Total Longitudinal Stress

$$\sigma_l = -21.5MPa - 1.42MPa = -22.9MPa \quad (3.23)$$

The longitudinal stress due to Poisson effect and the thermal stresses are neglected due to the presence of the expansion joint

iv. Stress Combination (von-Mises Theory)

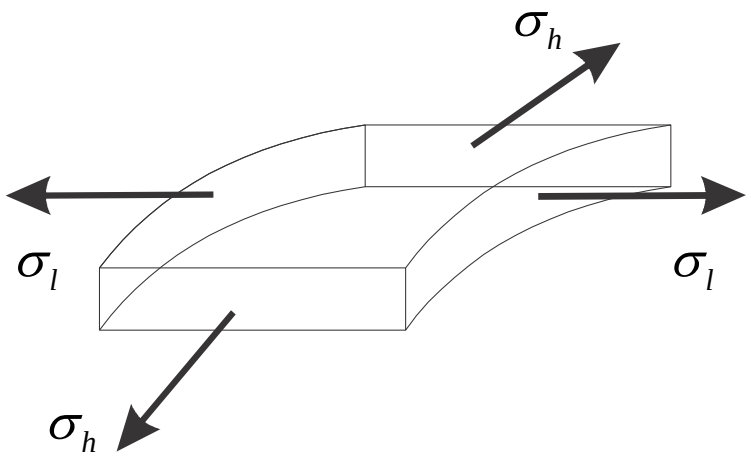

Figure 3. 6 - Stresses on an infinitesimal element of the penstock

$$\sigma_{vm} = (\sigma^2{}_h - \sigma_h\sigma_l + \sigma^2{}_l)^{1/2}$$
$$= \left(138^2\,MPa - 138MPa \times (-22.9MPa) + (-22.9)^2\,MPa\right)^{1/2}$$
$$= 150.8MPa$$

$$FS = \frac{\sigma_k}{\sigma_{vm}} = \frac{172.4MPa}{150.8MPa} = 1.14 \tag{3.25}$$

3.3.4.2 Deflection

$$\delta_{max} = \frac{5w_b L_p{}^4}{384EI_p} = \frac{5 \times 12.4kN/m \times 15.384^4 m^4}{384 \times 200GPa \times (\pi(D_{po}{}^4 - D_p{}^4)/32)} \tag{3.26}$$
$$= 4.72mm$$

D_{po} Pipe outside diameter, m

I_p Inertia of the Pipe, m^4

3.3.4.3 Explanation according to the thickness criteria

1. The thickness meets both requirements to ensure adequate shipment and handling

$$e > \frac{D_p}{288} = \frac{1.067}{288} = 3.7mm \tag{3.27}$$

$$e > \frac{D_p + 20}{400} = \frac{1.067 + 0.02}{400} = 2.71mm \tag{3.28}$$

2. Wall ensures a maximal deflection equaled to $L_p/360$ of the span.

$$\delta_{max} < \frac{L_p}{360} = \frac{15.384m}{360} = 42.73mm \tag{3.29}$$

3. Wall is thick enough to resist the imposed loads given certain allowable stress conditions.

$$FS = \frac{\sigma_k}{\sigma_{vm}} = \frac{172.4MPa}{150.8MPa} = 1.14 \tag{3.30}$$

4. The D_p/e ratio is not larger than 158 to avoid pipe buckling due to full internal vacuum.

$$\frac{D_p}{e} = \frac{1.067m}{0.01905m} = 56 < 158 \tag{3.31}$$

3.4 Conclusion

Chapter 3 has performed an analytical case based on a real case project that responds to industrial standard requirements. It will serve as a comparison point with the numerical model developed in Chapter 4 and presented in Chapter 5.

CHAPTER 4 – DESCRIPTION OF THE FLUID-STRUCTURE INTERACTION MODEL

4.1 Objectives

This chapter describes the details of the fluid-structure interaction (FSI) model used to model the reference case and parametric cases in following chapters. The model is based on the Finite Element Method-Finite Volume Method (FEM-FVM) techniques. Unlike the structural solver which uses the Finite Element Method (FEM) to discretize the equilibrium equations, the fluid solver uses the Finite Volume Method (FVM) to discretize the Navier Stokes Equations. The latter method differs from the FEM in that it calculates the field variable values within control volumes fixed in space on a meshed geometry. Each element of the mesh acts as a control volume for which the partial differential equations (PDE) of conservation (mass, momentum and energy) are discretized. The discretization procedure transforms the PDE into a system of algebraic equations, which are subsequently solved numerically. The general concepts of FSI analysis are first explained in Section 4.2 and their general implementation within the ANSYS-CFX environment is next described in Section 4.3. Sections 4.4 to 4.6 define, more in details, the model geometry, its steady-state and transient input files.

4.2 General Concepts in Fluid-Structure Interaction (FSI) Analysis

General concepts of both steady-state and transient FSI are presented in this section. It shows the input and output type of both analyses and shows how they are inter-related. A steady-state simulation is required to determine the initial condition before a transient analysis can be conducted. It allows the moving mesh of the pipe wall to stabilize under the action of the reference pressure and the gravity forces prior conducting the transient analysis caused by gate closure. Without the steady state analysis, a high acceleration of the mesh would occur in the transient analysis which causes the fluid solver to fail to converge. To achieve steady-state convergence, ANSYS-CFX uses a pseudo-transient algorithm that iterates on the fluid fields through a pseudo-time (i.e., not an elapsed time). The algorithm starts with an initial guess displacement vector to determine the steady state condition.

Since the analysis is steady-state, it does not include the transient effects (Inertia forces). As shown in Fig. 4.1, the steady-state analysis involves two stages of convergence to achieve the expected results.

Structural Loop: For a geometrically non-linear analysis, the stiffness of the structure depends upon the displacement fields, and the resulting equilibrium equations are nonlinear in the displacement fields. Displacements are first obtained by the structural solver through a convergence loop. When equilibrium is established, the displacement fields are sent to the fluid solver as input.

Fluid Loop: Given the displacement fields, pressure and velocity fields are computed by the fluid solver through another convergence loop. Forces are calculated by integrating the pressure field over the pipe tributary area and are sent to the structural solver as input.

Coupling Loop: The whole process of exchanging data between the structural solver and fluid solver is done through a coupling loop. The loop compares the difference of obtained fields at the i and $i-1$ iteration steps against a user-specified convergence criterion to establish whether or not convergence is achieved.

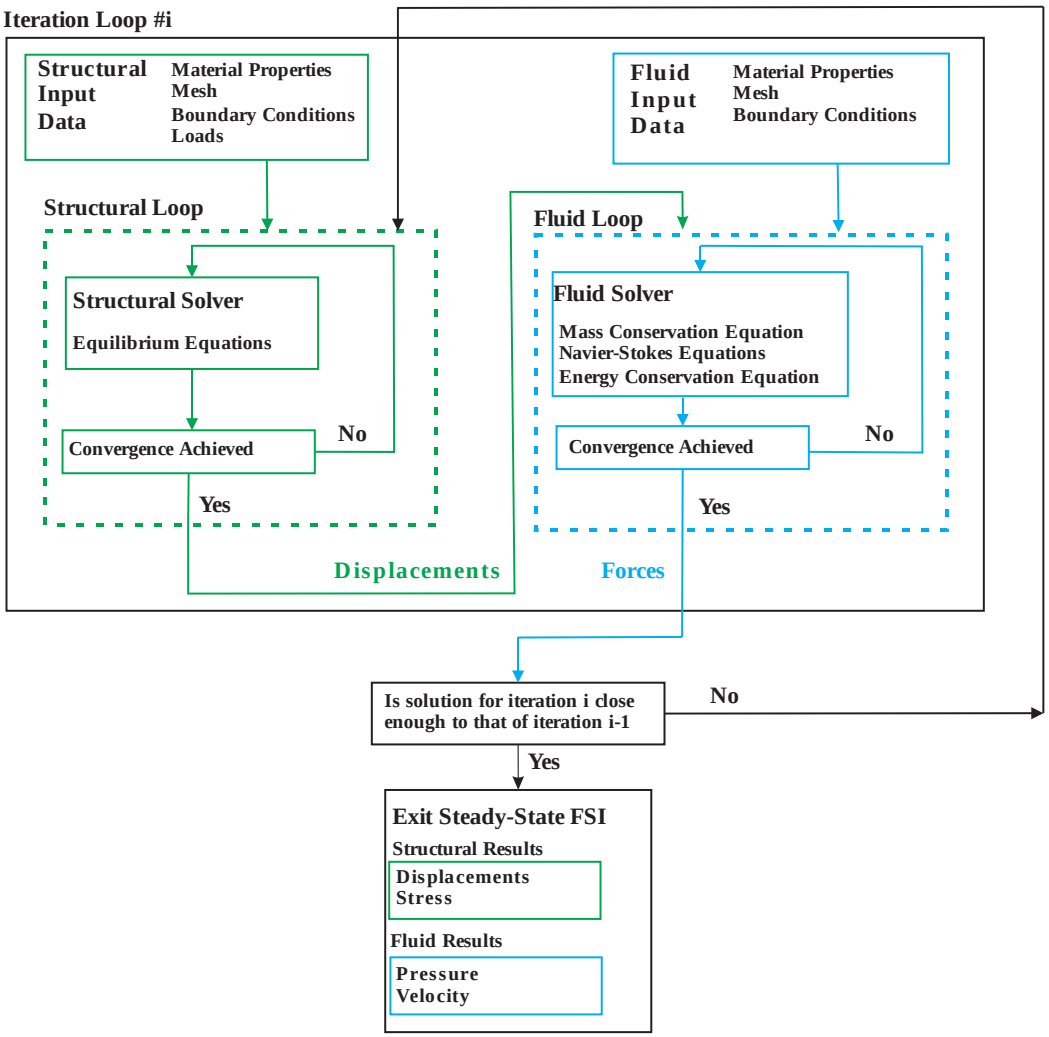

Figure 4. 1 - Flow chart of a Steady-State Fluid-Structure Interaction (FSI)

As shown in Fig.4.2, the transient FSI analysis requires the steady state structural and fluid output results as initial conditions. For a given time increment, three levels of iterations are performed in a transient analysis. These are a structural convergence loop, fluid convergence loop, and interaction convergence loop. Once the interaction convergence loop has attained convergence, the pressure, displacement, velocity, and acceleration fields are stored and passed as input to start the commutations for the next time increment and the process is repeated

Transient Fluid-Structure Interaction (FSI)

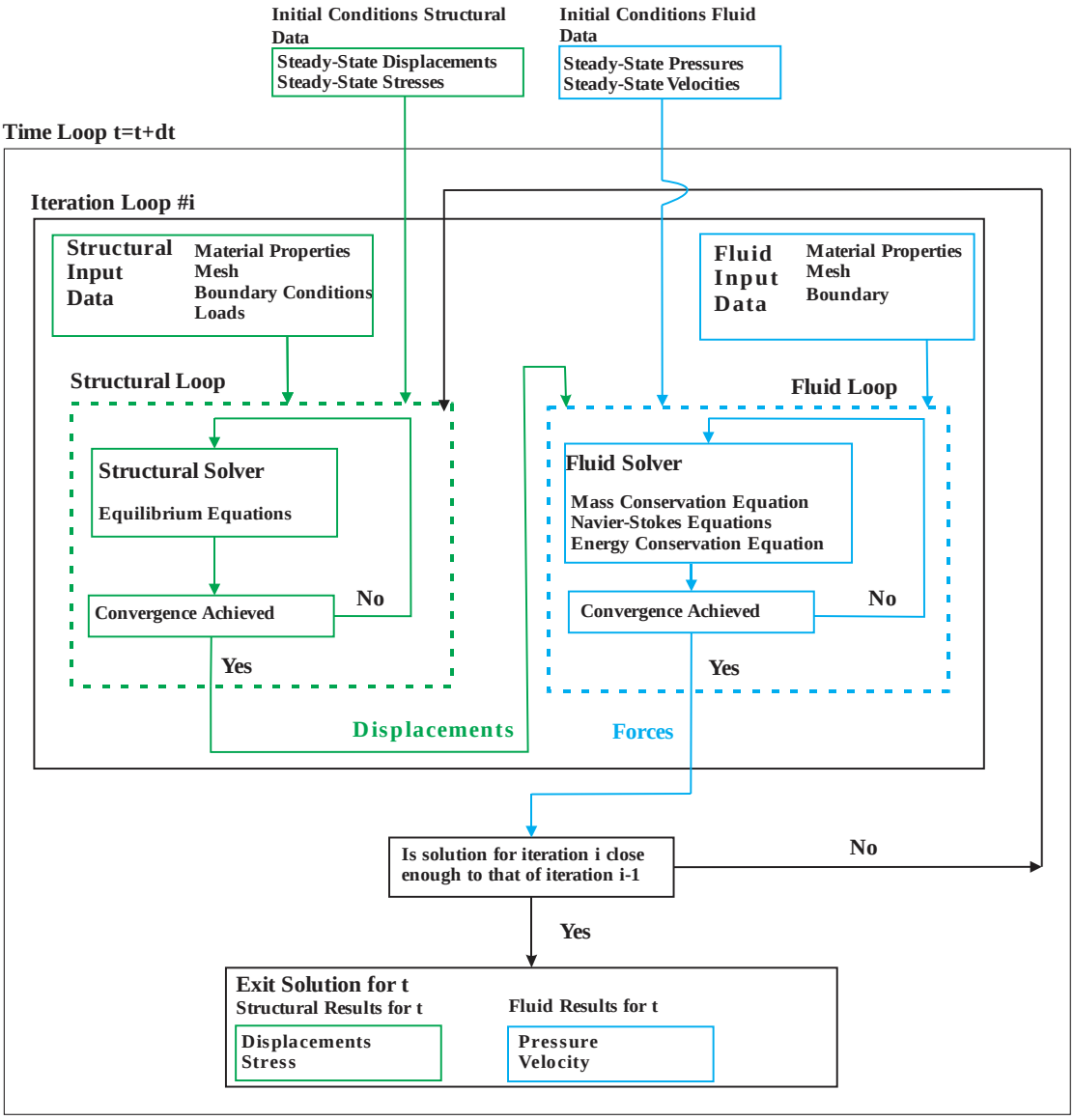

Figure 4. 2 - Flow chart of a Transient Fluid-Structure Interaction (FSI)

4.3 General Implementation of a FSI Model in ANSYS-CFX

The general layout of the model depicted in Fig. 4.3 illustrates how an FSI model is built using the ANSYS-CFX software and how to visualize the results of the steady-state and the transient simulations. The steps identified on the figure are described in Sections 4.4, 4.5, and 4.6. At the bottom of each Box in the diagram, a section number is provided which refers the reader to the relevant section in the chapter which provides more details.

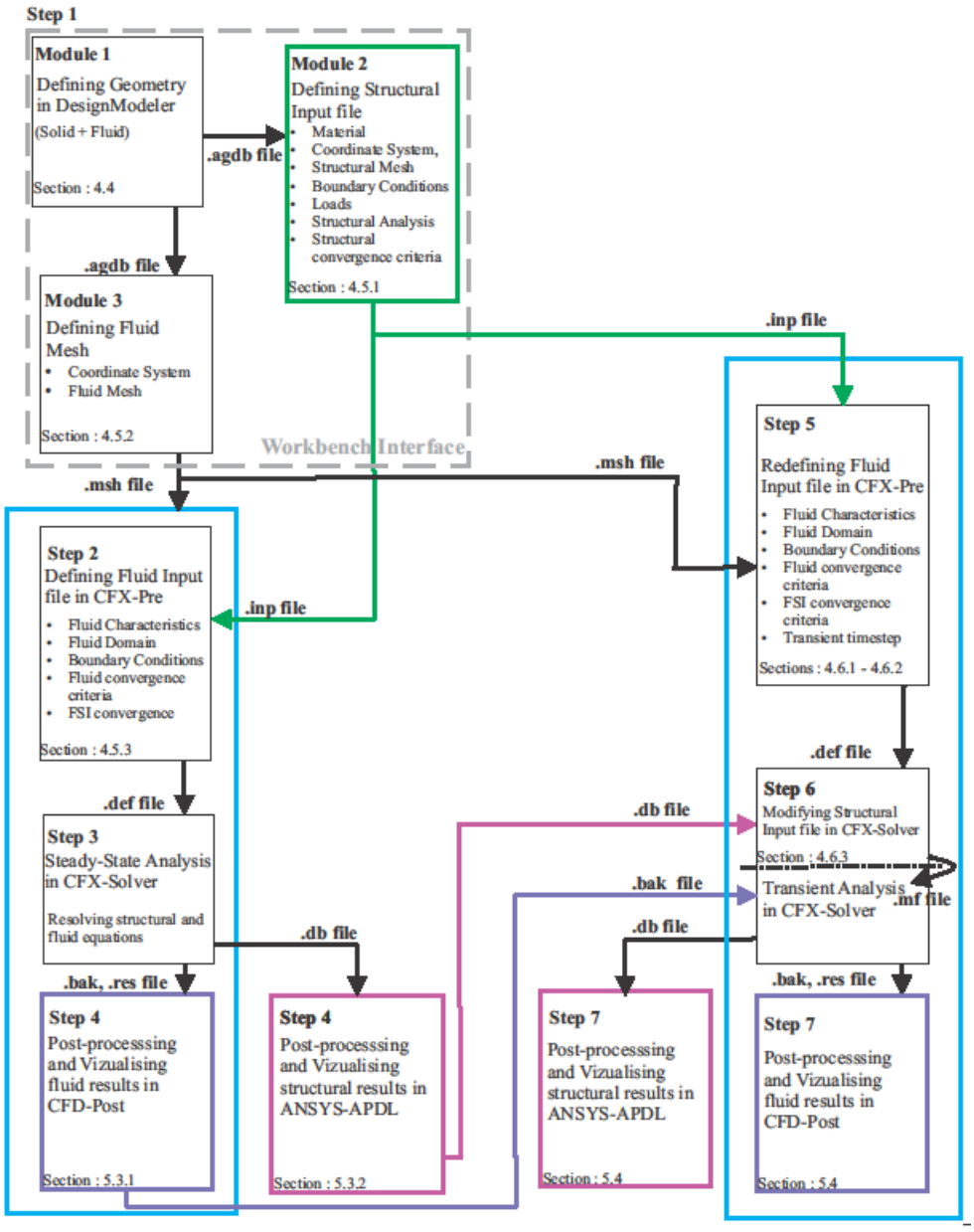

Figure 4. 3 - Flow Chart of a Transient Fluid-Structure Interaction (FSI)

Step 1: The workbench platform shown on Fig. 4.4 is used to create three modules. Module 1 which defines the model geometry within the geometry interface DesignModeler. This module is linked to Modules 2 and 3 and ensures the same geometry will be used for the solid and fluid models. The model geometry is defined in Section 4.4.

Module 2 which defines the structural input file (.inp) which specifies the structural properties, structural coordinate system, structural mesh, structural boundary conditions, structural loads, type of structural analysis and structural convergence criteria. These include a residual force convergence criterion, residual moment convergence criterion. The structural input steps are defined in Section 4.5.1.

Module 3 defines the fluid coordinate system and the fluid mesh file (.msh) in Section 4.5.2.

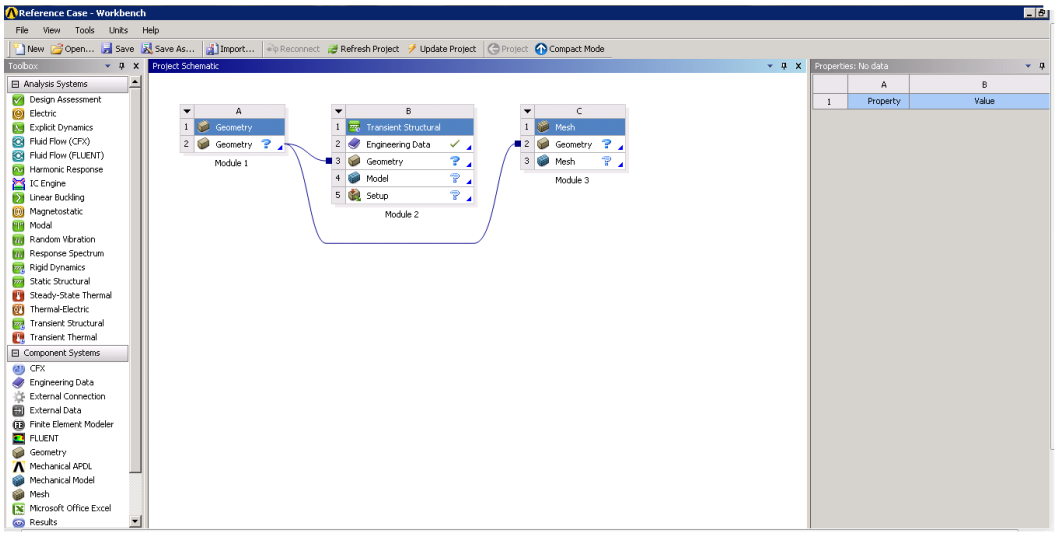

Figure 4. 4 - Defining the Geometry, Structural inputs and Fluid mesh in Workbench

Step 2: On the CFX-Pre interface shown in Fig. 4.5, a Fluid input file for Steady-State analysis is defined using the files created in Step 1. Specified on this interface are:

- Fluid Properties (Density, Dynamic viscosity, Thermal conductivity, Absorption coefficient)
- Fluid domain and boundary conditions (Opening, Out, Wall)
- Type of fluid analysis (Steady State, Transient)

- Fluid and Interaction convergence criteria

Once the model is built, data can be written in a definition file (.def) using the **"Define Run"** Option location in the **"Tool"** bar. The fluid steps definition are presented in Section 4.5.3.

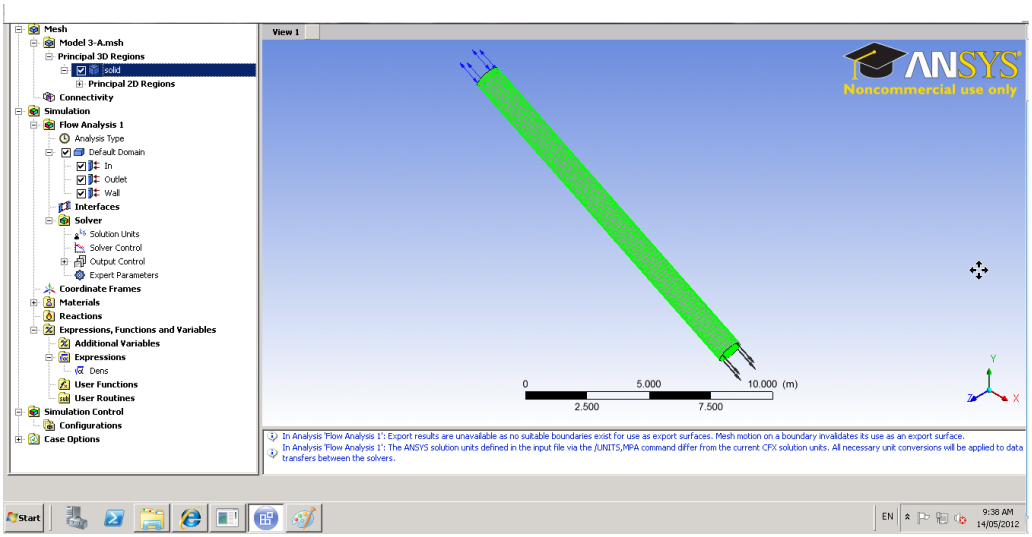

Figure 4. 5 - Defining Fluid input into CFX-Pre for the steady-state analysis

Step 3: The definition file (.def) created in Step 2 is input into the CFX-Solver shown in Fig. 4.6 to execute the iterative process until the steady-state convergence is achieved. The fluid (.bak and .res) and structural (.db) output files, that contain the physics, the mesh, the results of the steady-state analysis, will be input as initial conditions for the transient analysis.

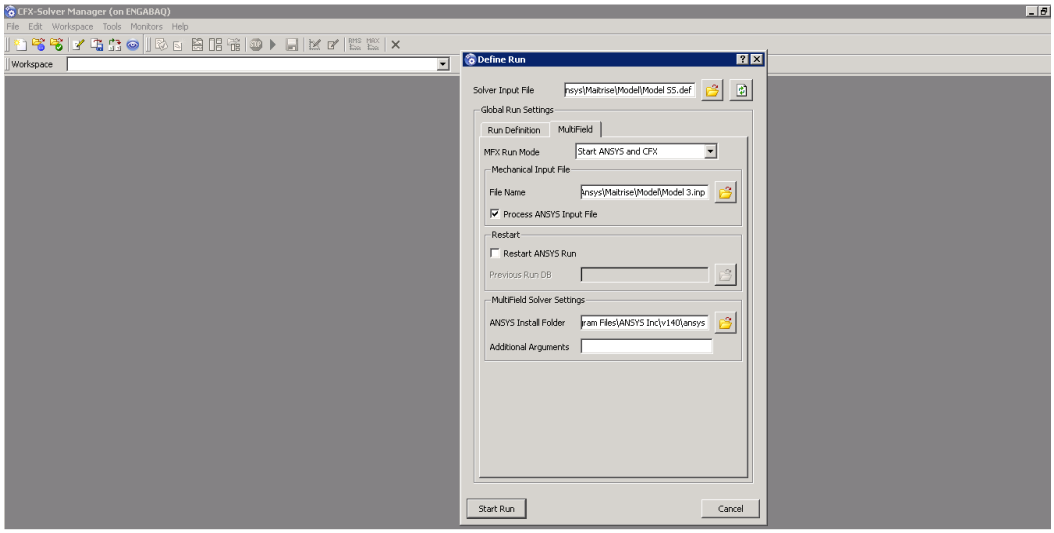

Figure 4. 6 - Executing the iterative process for the Steady State analysis into CFX-Solver

Step 4: Structural results files (.db) built in the steady-state analysis are read and post-processed within the ANSYS-APDL interface using the **Data & File Opts** command. Fluid results files (.bak and .res) are read and post-processed within the interface CFD-Post.

Step 5: On the CFX-Pre interface shown in Fig. 4.7, a Fluid Input File for transient analysis is redefined using the files created in Step 1. Fluid Characteristics, Fluid Domain, Fluid Boundary Conditions, Fluid Convergence Criteria, FSI Convergence Criteria must be redefined within this interface. Timesteps and transient duration time are also input in CFX-Pre. The file (.def) created from this interface is input into the CFX-Solver to execute the transient iterative process as explained in Step 6.

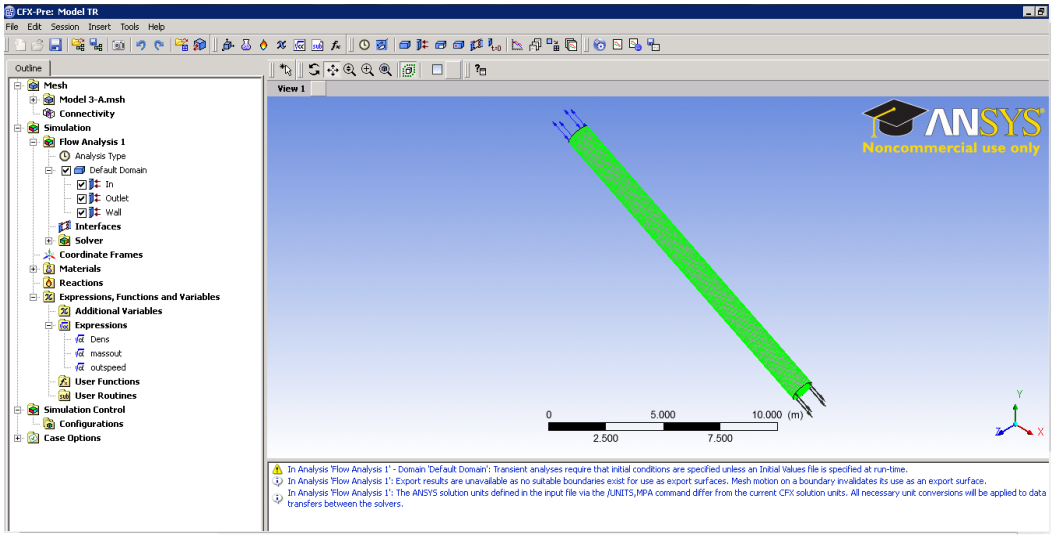

Figure 4. 7 - Redefining the Fluid Input File into CFX-Pre for the transient analysis

Step 6: On the CFX-Solver interface, two sub steps must be executed before a transient simulation can be done.

- The Inertia effect must be added to the structural input file (.inp) for the transient analysis and saved as a (.mf) file throughout a Run Mode called "**Process Input File Only**" (Fig. 4.8). To be executed, the Run Mode requires the structural results file (.db) generated in Step 4. Section 4.6.3 shows the details of the operation.
- The modified file (.mf) is input into the Run Mode "**Start ANSYS and CFX**" shown in Fig. 4.9. Added to the structural results file (.db), this mode requires the fluid results file (i.e., either the .bak or .res) generated in Step 4 as initial conditions.

The analysis generates three files. These are the fluid (.trn and .res) and structural (.db) output files which contain the physics, the mesh and the solution data of the transient solution.

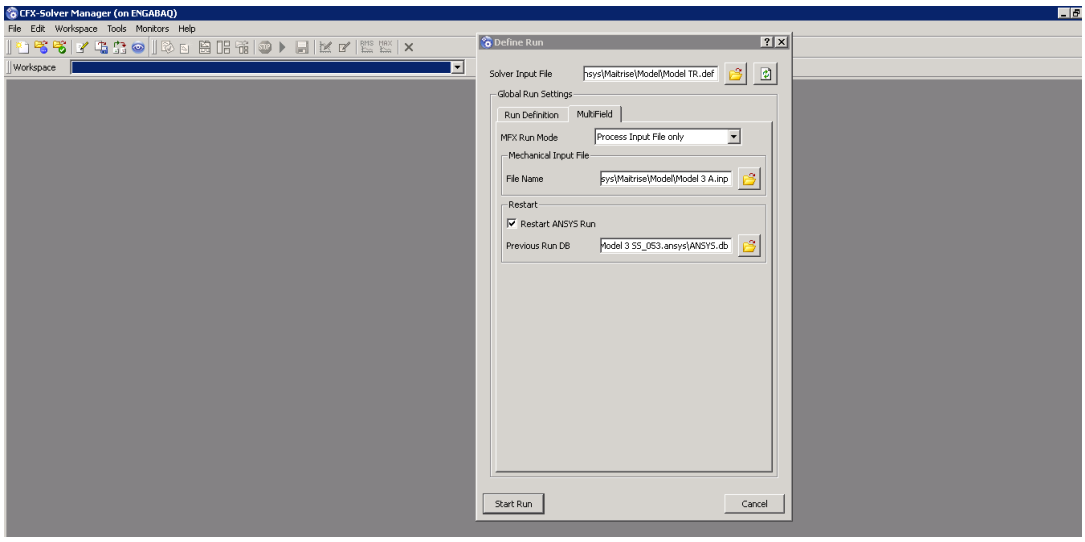

Figure 4. 8 - Adding the Inertia effect to the structural input file for the Transient analysis

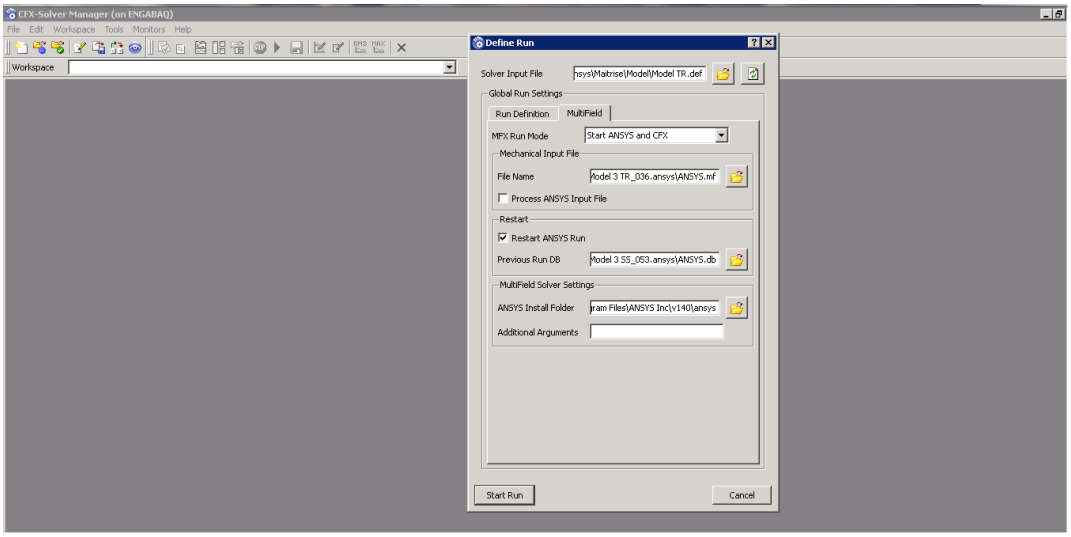

Figure 4. 9 - Executing the iterative process for the Transient analysis into CFX-Solver

Step 7: Structural results files (.db) generated from transient analysis can be read and post-processed within the ANSYS-APDL interface using the **Data & File Opts** command. Fluid results files (.trn and .res) files can be read and post-processed within the CFD-Post interface.

4.4 Defining the Model Geometry

For the reference case, the model geometry has been sketched according to the dimensions of Fig. 3.4. Both structural and fluid models are generated with the same sketches to ensure compatibility between the structural and fluid models. The suppress body option allows one to work on the fluid or the structure models separately.

4.4.1 Defining the Structural Model Geometry

Figure 4.10 illustrates a sweep operation that generates a surface from a defined profile extruded along a path. The surface thickness has to be user defined to zero.

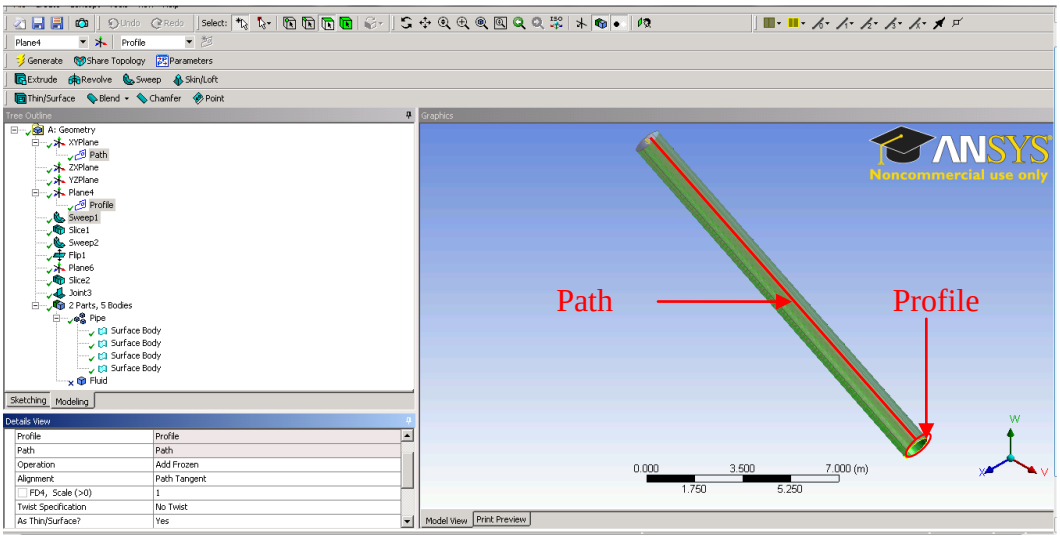

Figure 4. 10 - Defining the Structural Model Geometry on DesignModeler

For meshing purposes explained in Section 4.5.1.3.3, the surface must be cut in four equal bodies throughout two slice operations. Newly created bodies must be grouped in one part to avoid any discontinuities that could occur in the mesh generated. A flip surface operation, that allows the user to reverse the force orientation on the surface, is finally defined. By default, the orientation of the normal is defined on the outer side of the surface of the pipe. The flip surface operation allows the user to have the fluid forces applied on the inner side of the surface to allow it to interact with the fluid pressure.

4.4.2 Defining Fluid Model Geometry

Figure 4.11 illustrates a sweep operation that generates a solid from a defined profile (circular in this case) extruded along a path (linear in this case).

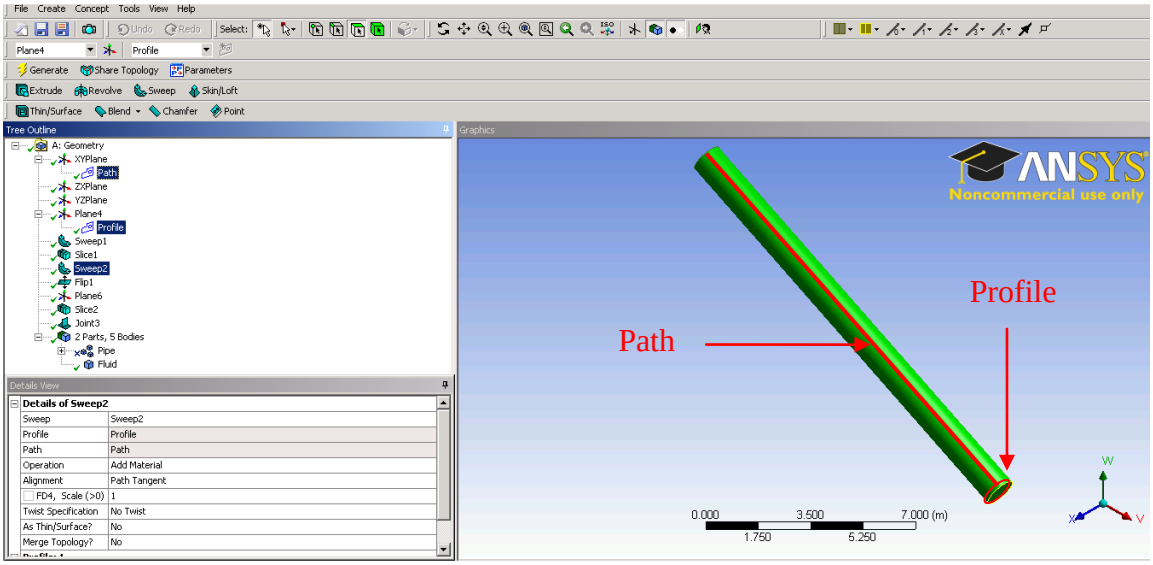

Figure 4. 11 - Defining the Fluid Model Geometry on DesignModeler

4.5 Defining input for Steady-State Model

4.5.1 Defining the Structural Input File

Defining the Structural Input File requires to properly set its properties, coordinate system, mesh, boundary conditions, loads and analysis type. Once everything is set, the input file (.inp) can be generated using the **tools** option.

4.5.1.1 Defining the properties of the pipe

The pipe surface is made out of structural steel with properties already defined in Section 3.3.1.

Other properties explained below can be seen on Fig. 4.12:

- The material non-linearity is not considered since the von-Mises stress is kept well under the allowable von-Mises stress value computed in Section 3.3.4.1.
- The thermal stress effects are not considered since the temperature is assumed to remain constant.
- As already defined in Section 3.3.4.1, the pipe's thickness is defined here as 19.05 mm for the reference case.
- The element nodes are specified to be on the inside surface of the element (Within ANSYS, this is termed as the bottom side).

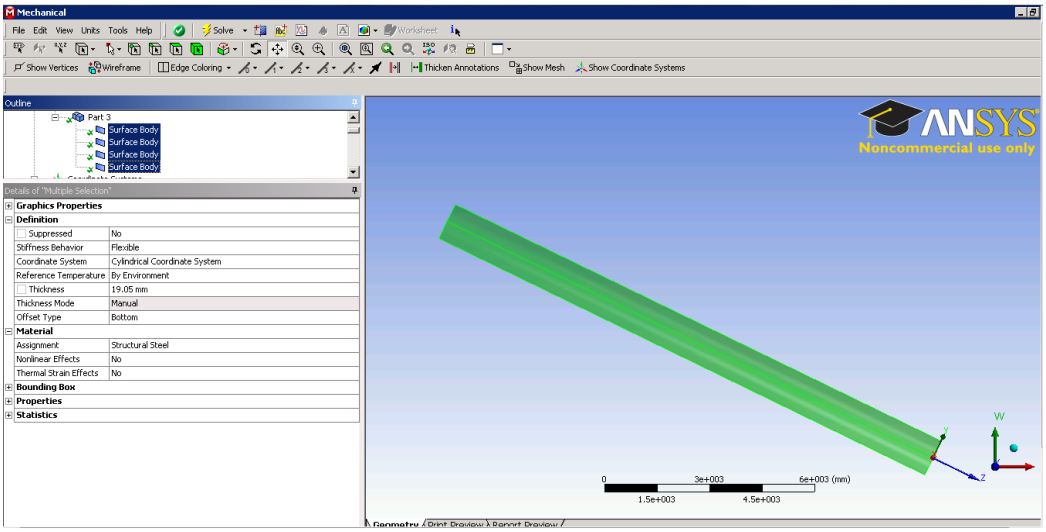

Figure 4. 12 - Defining the properties of the Structural Model

4.5.1.2 Defining the Structural Coordinate System

A cylindrical coordinate system with an origin located at the center of the pipe outlet end (Fig. 4.13) is selected for the structural model. This system allows one to define the boundary conditions described in Section 4.5.1.4 and to visualize and extract the simulation results along the longitudinal, circumferential, and radial directions of the pipe.

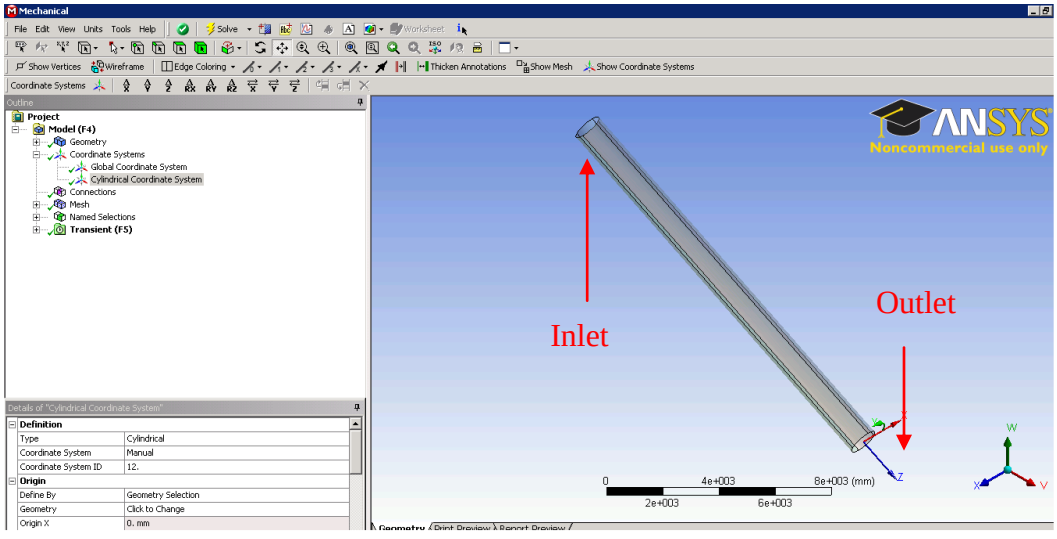

Figure 4. 13 - Defining the Structural Cylindrical Coordinate System

4.5.1.3 Defining the Structural Mesh

Structural element characteristic, meshing parameters and meshing operations are presented in this section.

4.5.1.3.1 Defining the Structural Element Characteristics

The structural element that meshes the pipe is SHELL181 (Fig. 4.14). It is a four noded shell element with six degrees of freedom at each node (three translations and three rotations). It is well-suited for linear, large rotation and large strain nonlinear applications. It is capable of capturing the follower effects of distributed pressures.

Option KEYOPT(3) specifies the mode integration of the shell element.

- Set as (0), it uses a reduced integration with hourglass control
- Set as (2), it uses a full integration with incompatible mode

Full integration (i.e., Option (2)) is most effective with problems involving bending. The reduced integration option would require a refined mesh and would increase the computing time. KEYOPT(3) is set at (2) for the current problem.

Option KEYOPT(8) specifies the layer data storage.

- Set as (0), it stores data for bottom-surface of bottom layer and top-surface of top layer
- Set as (1), it stores top and bottom-surface data for all layers
- Set as (2), it stores top, bottom and mid-surface for all layers

KEYOPT(8) is set at (2) for the current problem.

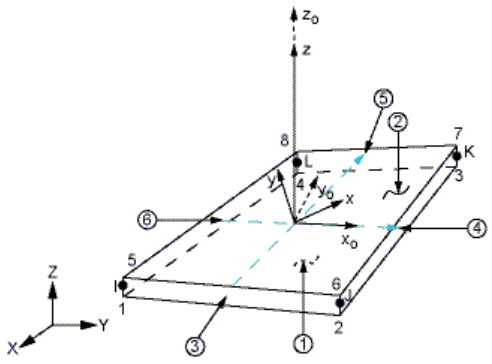

Figure 4. 14 - Shell Element SHELL181

In order to keep the aspect ratio of the element to two, and achieve a reasonable balance between accuracy of results and computational time, element dimensions of 85 mm x 170 mm were chosen.

4.5.1.3.2 Defining the Mesh Parameters

Meshing parameters set for the automatic mesher are shown in Fig. 4.15 and listed in Table 4.1. Parameters are detailed in the following.

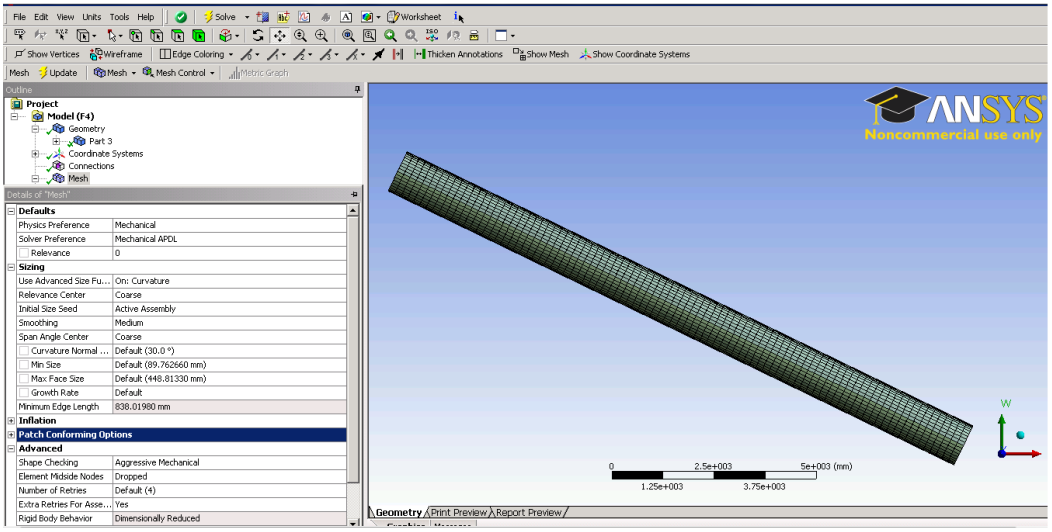

Figure 4. 15 - Defining Structural Meshing Parameter

Table 4. 1 - Structural Meshing Parameters

Physics Preference	Mechanical
Use Advanced Size Function	On:Curvature
Curvature	18°
Shape Checking	Aggressive Mechanical
Element Midside Nodes	Dropped

Physics Preference: This option allows the user to specify the physics of the problem (Mechanical, Electromagnetic, CFD, Explicit). In the present problem, the mechanical option is specified.

Use Advanced Size Function: When the advanced size function is set to **On: Curvature**, the maximum angle that an element edge is allowed to subtend is specified. The default angle curvature value of 18° is used for the model.

Shape Checking: The shape checking can be either set to standard or aggressive for mechanical physics. For linear analysis, standard shape checking provides shell elements with Jacobian ratio computed at integration points lower than 40. For large-deflection or large strains analyses, an aggressive shape checking ensures shell elements with Jacobian ratio computed at nodal points lower than 40.

Element Midside Nodes: The shell element can be either 4 or 8 nodded. When the midside node is specified as dropped, the software specifies a 4 nodes shell element. When specified as kept, the software specifies 8 nodes.

4.5.1.3.3 Defining the Mesh Operations

Based on the element size given in Section 4.5.1.3.1, the structural model has 40 elements in the circumferential direction and 91 elements in the longitudinal direction totalling 3640 elements. Three local mesh controls are used to define the above mesh:

- An Edge Sizing Control defined on an edge specifies the number of elements or the length of the elements along this edge. The Edge Sizing control in Fig. 4.16. specifies an element length of 170 mm in the longitudinal direction.
- An Edge Sizing control in the circumferential direction (Fig. 4.17) defines the number of elements as 40.
- A Mapped Face Meshing Control defines a mapped mesh on a selected surface. The pipe surface in Fig. 4.16 has been mapped with quadrilateral elements. (4 nodded element)

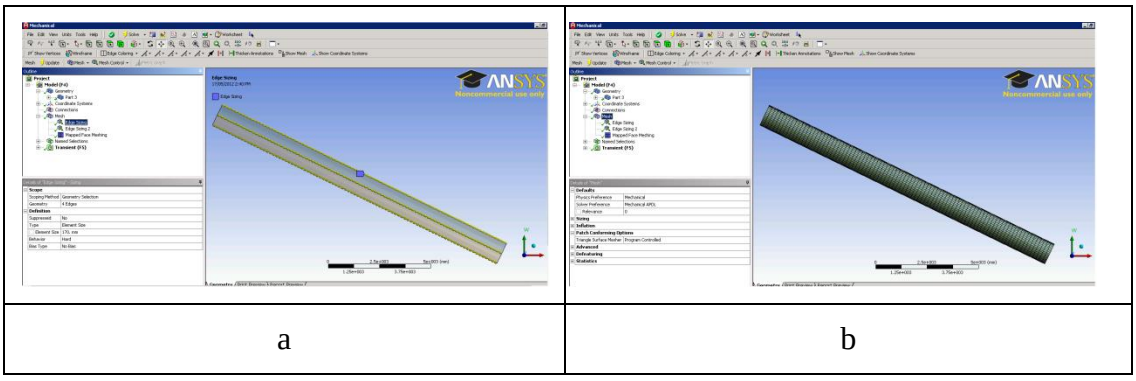

a b

Figure 4. 16 - Defining the Structural Longitudinal Mesh a) Edge Sizing Operation b) Mesh

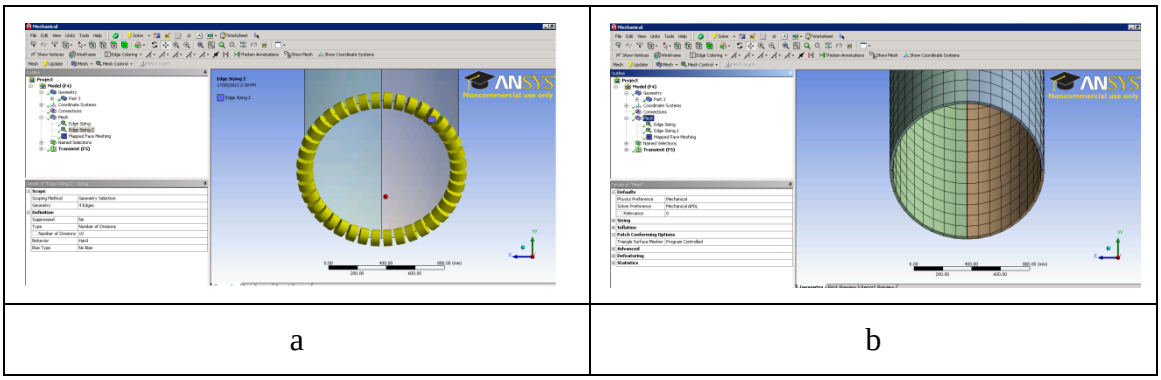

a b

Figure 4. 17 - Defining the Structural Circumferential Mesh a) Edge Sizing Operation b) Mesh

4.5.1.4 Defining the Structural Boundary Conditions

The pipe ends consist of three regions shown in three different colors in Fig.4.18:a) the lower half perimeter which is constrained from moving in the radial and tangential directions by the saddle (Red Nodes), b) the upper half parameter which is free to expand radially (Green Nodes), and c) the two midheight nodes (Orange Nodes). A complete description of the boundary conditions is provided in Table 4.2. In order to define the boundary conditions, three node groups had to be defined at each end. This was done through the name selection feature in Ansys. Also, the nodal coordinate system had to be changed from Cartesian to Cylindrical. This has been done using the nodal orientation feature.

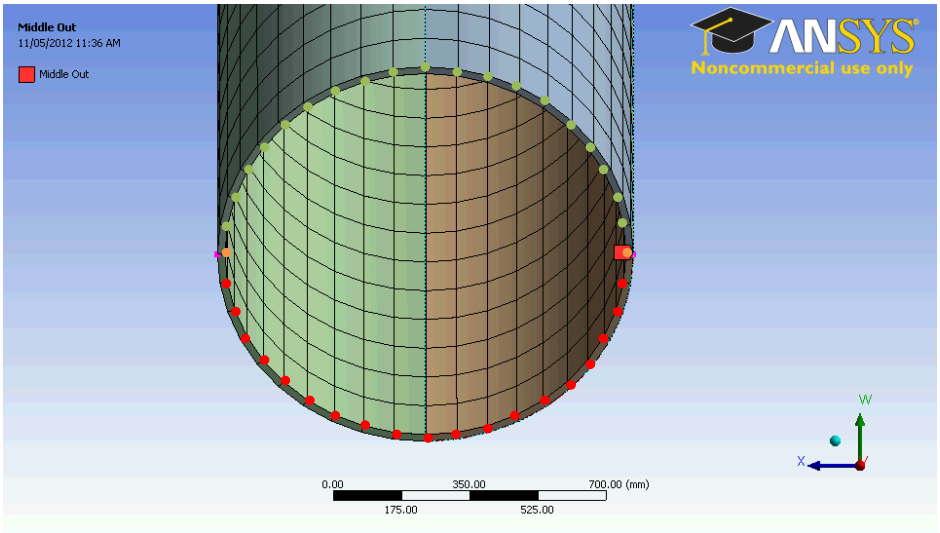

Figure 4. 18 - Defining the Structural Boundary Conditions on the three pipe regions

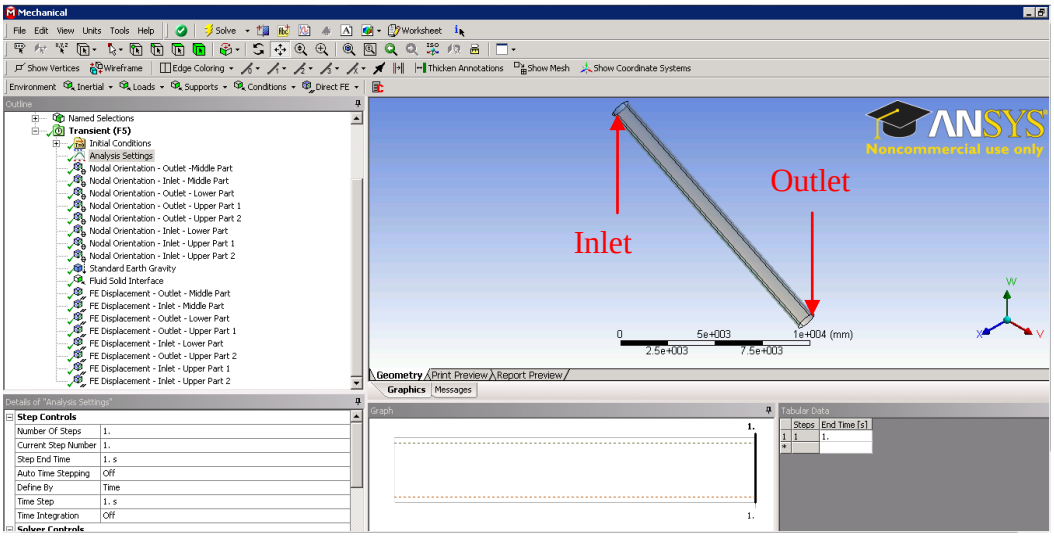

Figure 4. 19 - Changing the nodal coordinate system from Cartesian to Cylindrical

Table 4. 2 - Structural boundary conditions in the cylindrical coordinate system

		Inlet			Outlet		
Cylindrical Coordinate System		Lower Half Perimeter	Two Midheight nodes	Upper Half Perimeter	Lower Half Perimeter	Two Midheight nodes	Upper Half Perimeter
x	Circumferential Direction	X			X		
y	Tangential Direction	X	X	X	X	X	X
z	Axial Direction		X				

4.5.1.5 Defining the Structural Loads

Two types of loading are input into the structural model: gravity and fluid-solid interface.

The gravity load models the force induced by the pipe weight that will further create the pipe bending effect. As illustrated on the Fig. 4.20, the gravity acceleration is set to 9.80665 m/s^2 by default in ANSYS, and is applied along the "y" direction of the Cartesian Coordinate System.

The fluid-solid interface load acts as a link between the fluid and structural solvers. As explained in Section 4.4.1, it is defined on the inner side of the pipe. It allows the displacements computed by the structural solver to be transferred to the fluid solver and the forces computed by the fluid solver to be transferred to the structural solver.

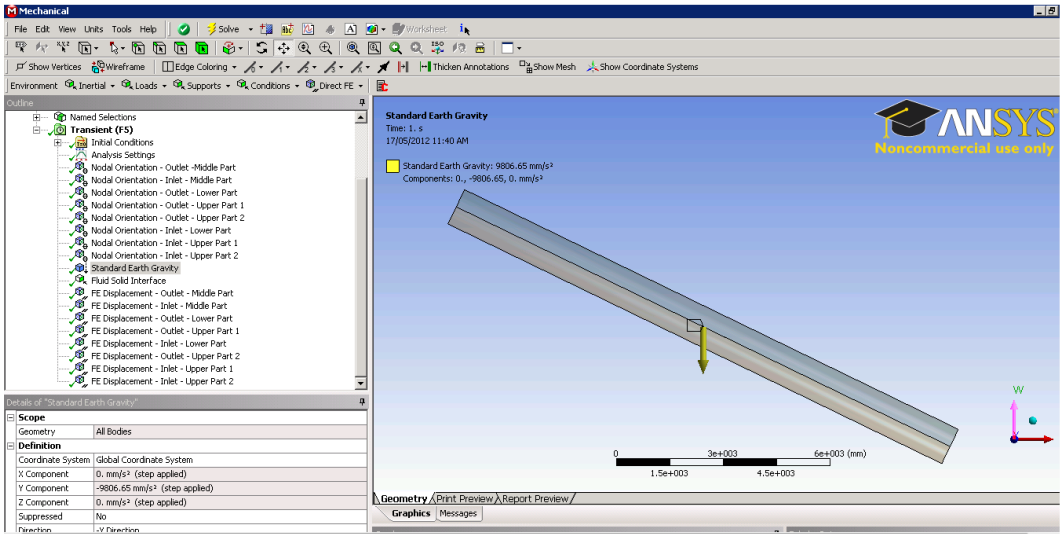

Figure 4. 20 - Defining the Gravity Load

4.5.1.6 Defining the Structural Convergence Criteria

The analysis settings allow one to control the steps, the solver, the non-linearity convergence criteria and the numerical damping. Relevant choices are shown in Fig. 4.21, listed in Table 4.3 and explained below.

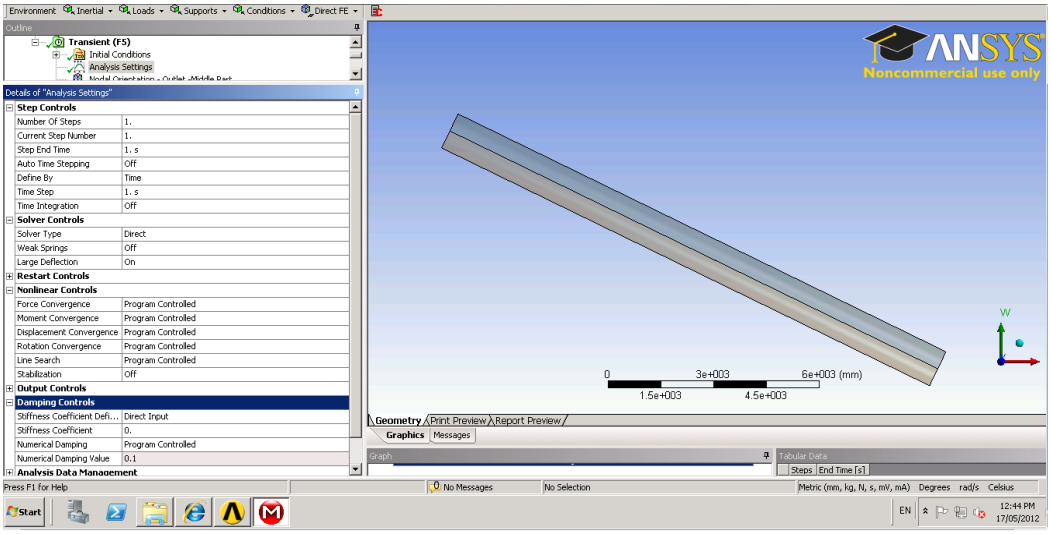

Figure 4. 21 - Defining the Structural Analysis Settings

Table 4. 3 - Analysis Settings

Auto time Stepping	Off
Time Integration	On
Solver Type	Direct
Large Deflection	On
Force Convergence	Program Controlled
Moment Convergence	Program Controlled
Displacement Convergence	Program Controlled
Rotation Convergence	Program Controlled
Numerical Damping	0.1

Auto time Stepping: This option allows one to specify the number of sub steps. Sub steps are points within a time increment at which solutions are calculated. It is usually used for non linear Steady-State analysis in order to apply the loads gradually so that an accurate solution can be obtained. In FSI analysis, the use of sub steps, sub cycling, is not recommended since loads provided by the Fluid Solver are not updated for each sub step and only the final displacement will be transferred to it. Sub cycling within the Structural Solver would unnecessarily increase the computational effort. Setting it to off gives a single sub step per coupling timestep.

Time integration: This option allows the solver to account for inertia effects in the transient analysis. This option is set off during the steady-state simulation, but is turned on during the transient simulation as explained in Section 4.6.3.

Solver Type: The solver type can be either direct (Sparse) or iterative (Preconditioned Conjugate Gradient). The direct solver is more robust and more appropriate for non-linear models with shells elements. This iterative procedure is more efficient and is recommended for models dominated by linear elastic behaviour. Since geometric non-linearity is considered into the FSI simulation, the solver chosen is the direct one

Large Deflection: The large deflection feature allows geometric non-linearity to be accounted for in the analysis and thereby incorporating stress stiffening (or softening) effects into the analysis. In an FSI analysis, this feature should always be on, regardless of magnitude of the structural displacements. Without this feature, the forces output from the Fluid Solver would be applied to the initial structural mesh as opposed to the movable mesh.

Force, Moment, Displacement and Rotation Convergence: Tolerances on convergence are used during the iterative Newton-Raphson process to dictate when a model has converged or balanced. Default convergence criteria work for the FSI model developed. Tighter tolerances were experimented with and were found to result in an increase in computational time while not to significantly affecting the accuracy of the solution.

Numerical Damping: The structural numerical damping is set to 0.1 for the reference case as suggested in ANSYS (AWB130_Dynamics_01) and will be varied in the parametric study presented in Chapter 6.

4.5.2 Defining the Fluid Mesh File

The fluid mesh file (.msh) contains the fluid coordinate system and the fluid mesh. As stated in Section 4.3, it is generated within Workbench and will be input into CFX-Pre. Once completed, the mesh has to be exported into a Fluent mesh file (.msh).

4.5.2.1 Defining the Fluid Coordinate System

To match the Structural Coordinate System defined in Section 4.5.1.2, the Fluid Coordinate System shown in Fig. 4.22 is also cylindrical. Its origin is located at the center of the pipe outlet end.

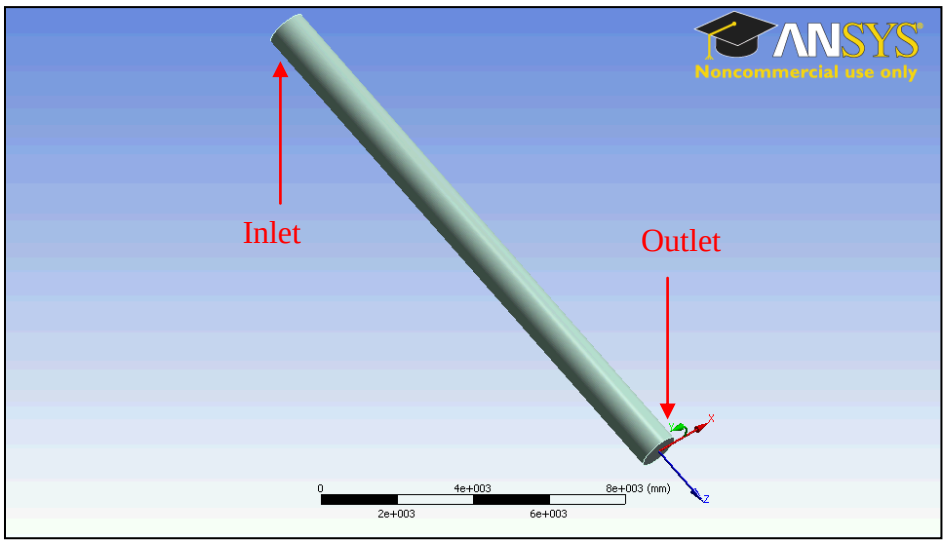

Figure 4. 22 - Defining the Fluid Cylindrical Coordinate System

4.5.2.2 Fluid Mesh Details

Meshing parameters and operations are presented in this section.

Unlike in a single fluid mesh sensitivity, an element refinement in a fluid-structure interaction analysis can create a divergence in the solution. The control volume dimensions have been set following a mesh sensitivity analysis that optimizes the structural and fluid meshes based on the accuracy of results and computational cost. The control volume dimensions do not exceed 85 mm in the circumferential direction and equals 170 mm in the longitudinal direction.

4.5.2.2.1 Meshing Parameters

Meshing parameters are shown in Fig. 4.23, listed on Table 4.4 and explained below.

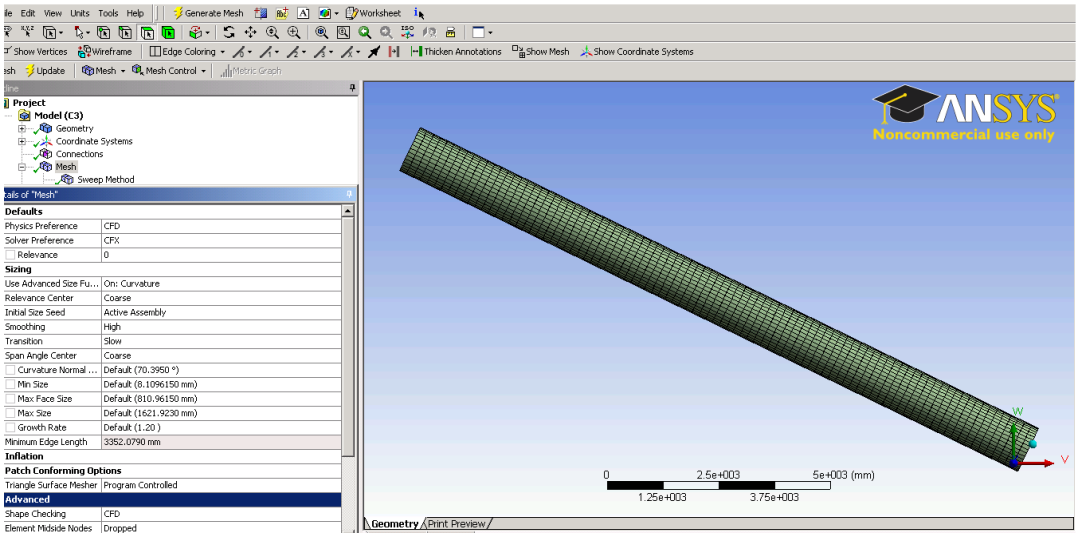

Figure 4. 23 - Defining the Fluid Meshing Parameters

Table 4. 4 - Fluid Meshing Parameters

Physics Preference	CFD
Solver Preference	CFX
Use Advanced Size Function	On:Curvature
Shape Checking	CFD

Physics Preference: This option allows the user to specify the physics of the problem (Mechanical, Electromagnetic, CFD, Explicit). In the present case, the CFD option is specified

Solver Preference: The fluid model can be solved either by the CFX or Fluent solver. Since the current analysis is defined on the CFX interface, the fluid model will be solved by the CFX solver.

Use Advanced Size Function: When the advanced size function is set to **On:Curvature**, a maximum angle that one element edge is allowed to span is specified. The default angle curvature value of 18° is used for the fluid model.

Shape Checking: The shape checking for fluid uses a shape checking criterion based on element volume.

4.5.2.2.2 Meshing Operations

Based on the element size given in Section 4.5.2.2, the fluid model has 94,640 elements. Two meshing methods, that set the general shape and the element type, and one local mesh controls, that organizes the elements locally, allows one to comply the element requirements given in Section 4.5.2.2

- A sweep meshing method is used for a model that revolves around an axis where the source and target faces share topology. It meshes the model for a given element length in the axis direction. The present model specifies an element length of 170 mm as illustrated in Fig. 4.24.
- An Edge Sizing control in the circumferential direction has defined the number of element (40) in Fig. 4.25
- An Inflation method is used to gradually reduce the element thickness from the pipe center toward the wall. It allows the solver to efficiently solve the model in the boundary layer near the pipe wall. Throughout the meshing process, the inflation method will be implemented before the sweeping method. The current inflation method specifies a total thickness of 500 mm and a number of layers of 25.

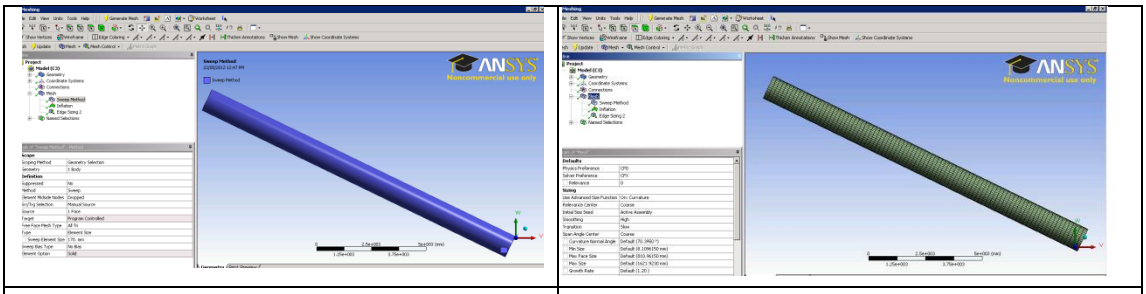

a	b

Figure 4. 24 - Defining the fluid longitudinal mesh through a sweep method a) Sweep Method Mesh

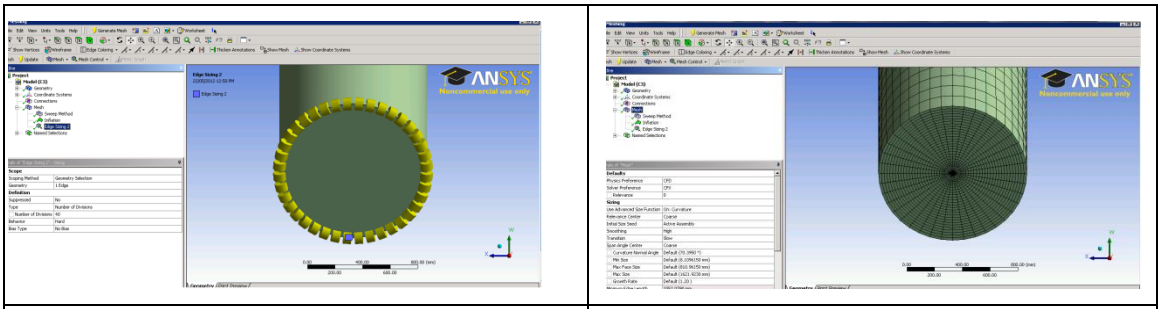

a	b

Figure 4. 25 - Defining the fluid circumferential mesh through an edge sizing control a) Edge Sizing Operation b) Mesh

4.5.3 Defining the Fluid Input File

As mentioned in Step 2 of Section 4.3, CFX-Pre Interface is used to define and generate the fluid definition file (.def) used as input in the iterative process for the Steady-State analysis.

4.5.3.1 Pre-Setting

Before the analysis can be defined, the Structural Input File (.inp) from section 4.5.1 and the Fluid Mesh File (.msh) from section 4.5.2 have to be input.

- The Structural Input File must be inserted into the **Analysis Type** tab
- The Fluid Mesh File must be imported as a fluent file (.msh) by right-clicking on the **mesh** tab.

4.5.3.2 Fluid Characteristics

The fluid used for the simulation is pressurized water at $P_{ref} = 4.467MPa$ and $T_{ref} = 20^{\circ}C$. Fluid characteristics are input under the **material** tab and the fluid itself are specified as water under the **domain** tab.

The density ρ_w is a function of the absolute pressure P_{abs}. It is defined as an expression in the **material** tab.

$$\rho_w = \rho_{w0} \times (1 + \frac{P_{abs}}{k_0}) \tag{4.1}$$

ρ_{w0} Density of the water at an absolute pressure $P_{abs} = 101.3kPa$ and a reference temperature $T_{ref} = 20^{\circ}C$

k_o Bulk Modulus of the water at an absolute pressure $P_{abs} = 101.3kPa$ and a reference temperature $T_{ref} = 20^{\circ}C$

4.5.3.3 Fluid Domain Parameters

Domain parameters are shown in Figs. 4.26 and 4.27, listed in Table 4.5, and explained below.

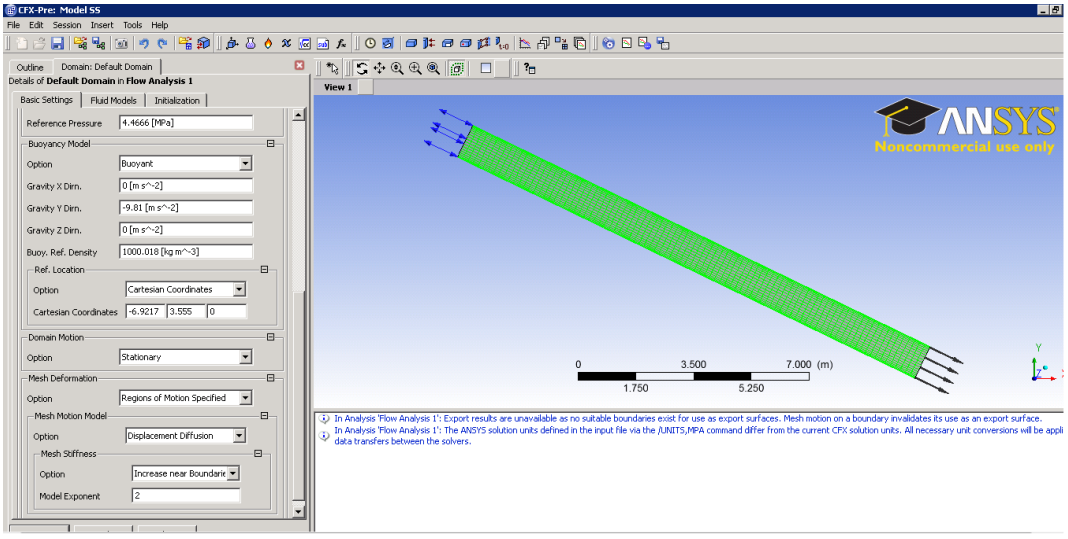

Figure 4. 26 - Defining the Domain Parameters (Basic Settings)

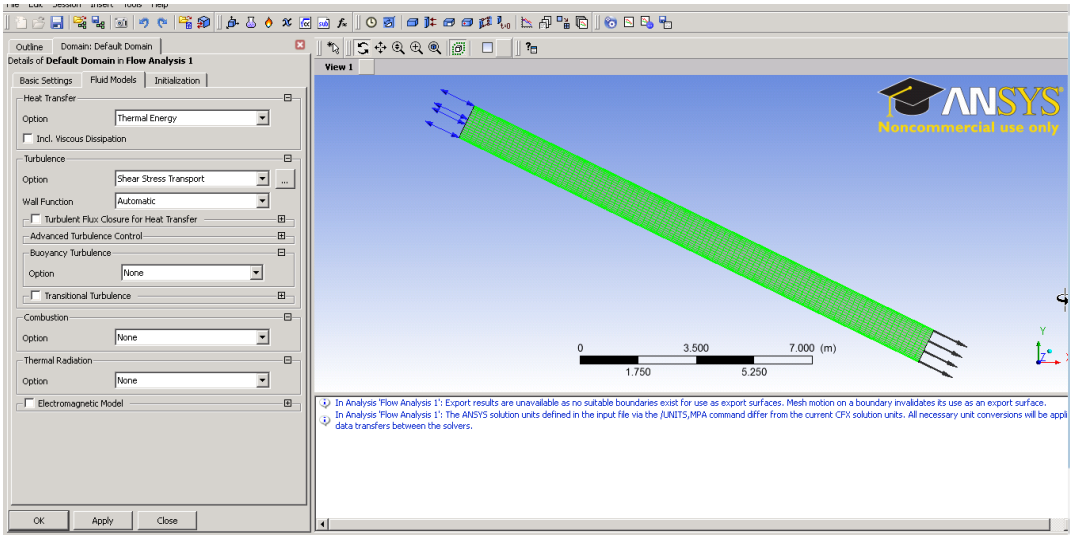

Figure 4. 27 - Defining the Domain Parameters (Fluid Models)

Table 4. 5 – Fluid Domain Parameters

Reference Pressure	4.466		Mpa
Buoyancy Model	Gravity X Direction	0	m/s²
	Gravity Y Direction	-9.80665	m/s²
	Gravity Z Direction	0	m/s²
	Buoyancy Ref. Density	1000.018	kg/m³
	Ref.Location	Center (Circumferential and longitudinal)	
Mesh Deformation	Mesh Stiffness	Increase near boundary	
	Exponant	2	

Reference Pressure: The reference pressure is the absolute pressure datum from which all relative pressures are assumed to vary. Deviations from the reference pressure will be called relative pressure. Due to the high static pressure input to the problem (4.467 MPa), the use of relative pressure eliminates round-off errors that would arise if the analyst adopts absolute pressure (i.e., the sum of the reference pressure and the relative pressure). The reference pressure is defined in the analysis through the function "**include pref in forces"** located in the expert parameter tab. Its value is equal to the static pressure P_s as defined in Section 3.3.1.

Buoyancy Model: The buoyancy model allows the model to simulate the weight of the fluid. It is applied in the "y" direction of the Cartesian Coordinate System and its value is

the standard gravity acceleration of $9.80665\,m/s^2$. The reference density is an approximation of the expected domain density calculated with $P_{ref} = 4.467MPa$.

Mesh Deformation: The mesh deformation option must be activated to allow the interaction between the fluid and the structure to take place. Specifying the option **"Increase near boundary"** increases the mesh stiffness close to the boundary compared to that far from it. The mesh stiffness controls which regions deform to absorb the motion and which ones remain relatively rigid. It can be adjusted with an exponent value and monitored throughout the mesh diffusivity, contained in the (.res) file. Sensivity tests have determined that an exponent value of 2 is most suitable.

Turbulence: Turbulence is included in the model. The pressure waves will gradually be damped by the losses associated with dissipation through internal fluid friction with the pipe wall. Turbulence models, available in CFX are RANS Eddy Viscosity models (Standard, SST) or RANS Reynolds-Stress Models (SSG, BSL). Experiments from Gersten et al. (1987) suggest that the SST must be applied for pressure wave simulations.

4.5.3.4 Boundary Conditions

The boundary conditions have been chosen on the basis of simulating conditions that are representative of reality while having the most robust solution possible.

Representativeness of Reality: The water hammer problem implies an opening inlet end to allow the water to come in and out of the pipe and a flow reduction at the outlet end that initiate the pressure wave.

Solution Robustness: To ensure the solution robustness and comply with the flow outlet requirement, an opening pressure has been specified on the opening end of the pipe.

The corresponding boundary conditions are shown in Fig. 4.28 and are detailed in the following.

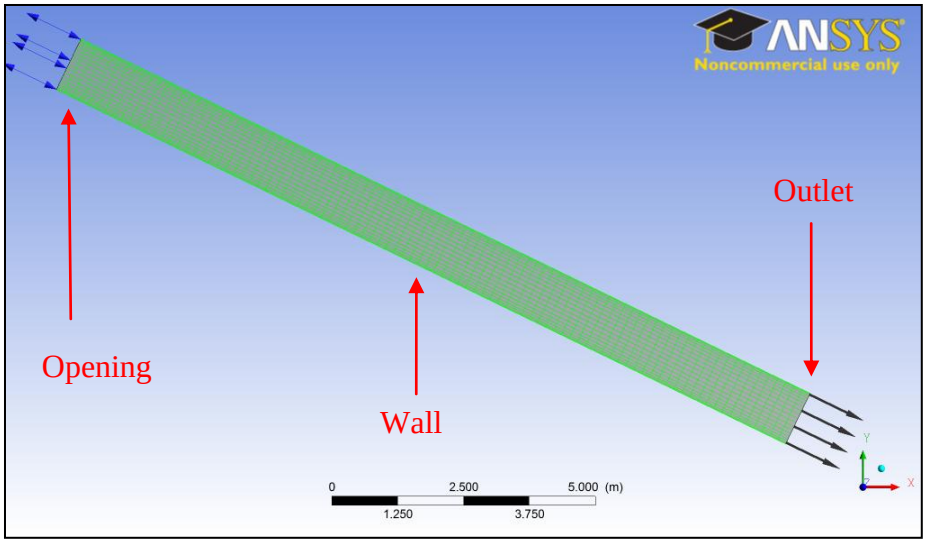

Figure 4. 28 - Fluid boundary conditions. a) Opening, b) Outlet, c) Wall

Pipe Opening: At the pipe inlet, the boundary condition is specified as an opening with a relative pressure of $0\,kPa$ and a temperature of $20^{o}C$. It allows the water to flow in and out of the pipe. To comply with the structural boundary conditions described in Table 4.2, an unspecified mesh motion has been specified for the fluid surface defined at the opening. Opening parameters are summarized in Table 4.6.

Table 4. 6 - Opening Boundary Conditions Parameters

Mesh Motion	Option	Unspecified	
Mass and Momentum	Option	Opening Pressure and Direction	
	Relative Pressure	0	Pa
Flow Direction	Option	Normal to Boundary Condition	
Turbulence	Option	Medium (Intensity=5)	%
Heat Transfer	Option	Static Temperature	
	Static Temperature	20	C°

Pipe Outlet: At the pipe outlet, the boundary condition is specified as having a mass flow rate of $3190\,kg/s$. To also conform with the structural boundary conditions described in Table 4.2, an unspecified mesh motion has been set on this fluid boundary at the outlet. Outlet parameters are provided in Table 4.7.

Table 4. 7 - Outlet Boundary Conditions Parameters

Mesh Motion	Option	Unspecified	
Mass	Option	Mass Flow Rate	
and Momentum	Mass Flow Rate	3190	kg/s

Pipe Wall: The wall boundary conditions are the interface between the fluid and the structure. As indicated in Table 4.8, forces from the fluid solver are transmitted to the structural solver and displacements from the structural solver are transmitted to the fluid solver. It is assumed that the wall is smooth and the heat transfer is adiabatic.

Table 4. 8 - Wall Boundary Conditions Parameters

Mesh Motion	Option	ANSYS Multifield
	Receive from ANSYS	Total Mesh Displacement
	ANSYS Interface	FSIN_1
	Send to ANSYS	Total Force
Mass and Momentum	Option	No Slip Wall
	Wall Vel. Rel. To	Mesh Motion
Wall Roughness	Option	Smooth Wall
Heat Transfer	Option	Adiabatic

4.5.3.5 Solver Controls

Conducted numerical experiments have proved that Fluid-Structure Interaction problems involving gravity and high pressure are particularly sensitive to error accumulation which can be greatly amplified causing the solution to eventually diverge. This is the reason behind the following input selections

- A small residual target was input for the fluid solver and for the coupling data transfer convergence target.
- A high maximum iteration number was specified in order to allow both small convergence criteria to be met.
- An “aggressive” length scale factor was specified in order to optimize the magnitude of the pseudo time-step.
- A rather small residual target for mesh displacements was specified in order to avoid any mesh folding.

- An under-relaxation factor of 0.75 was specified meaning that only 75% of the forces are transmitted to the structural side at each coupling step. The specified values for solver controls are shown in Table 4.9

Table 4. 9 - Steady-State Solver Controls

Fluid Equations Control (Except Mesh Displacement)		
Convergence Control	Min Iteration	1
	Max Iteration	500
Timescale Control	Auto Timescale	
Length Scale Control	Aggressive	
Residual Target		1.00E-06
Mesh Displacement		
Residual Target		1.00E-08
External Coupling		
Coupling Step Control	Min Iteration	1
	Max Iteration	300
Coupling Data Transfer Control	Under Relaxation Factor	0.75
	Convergence Target	1.00E-05

4.6 Defining input for Transient Model

Transient Analysis' settings are similar to the ones specified in the steady-state. The changes that must be applied are explained in the following.

4.6.1 Defining the Transient Analysis

The analysis must be set as Transient under the **"Analysis type"** option as shown in Fig. 4.29. The gate closure time, the simulation duration time and the timestep must then be determined and applied to the model.

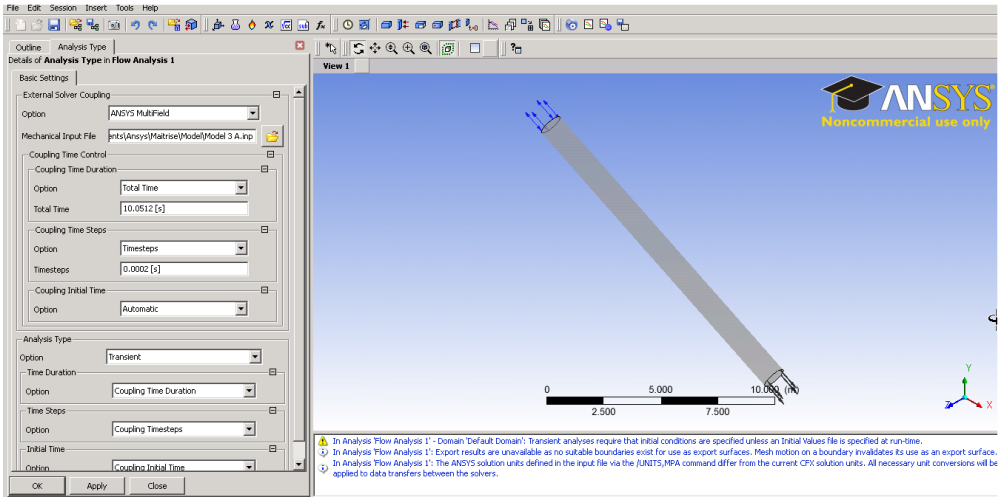

Figure 4. 29 - Transient Analysis Settings

Gate Closure Time: The transient condition of the analysis is caused by the reduction of the flow at the pipe outlet. The flow rate reduction can be found with the Eqs. (4.2), (4.3) and entered as output boundary condition as shown in Fig. 4.30.

$$Q = V \times \pi D_p^{\,2} / 4 \times \rho_w \tag{4.2}$$

$$V = step(T - t/1[s]) \times (V_0 - V_0 t/T) \tag{4.3}$$

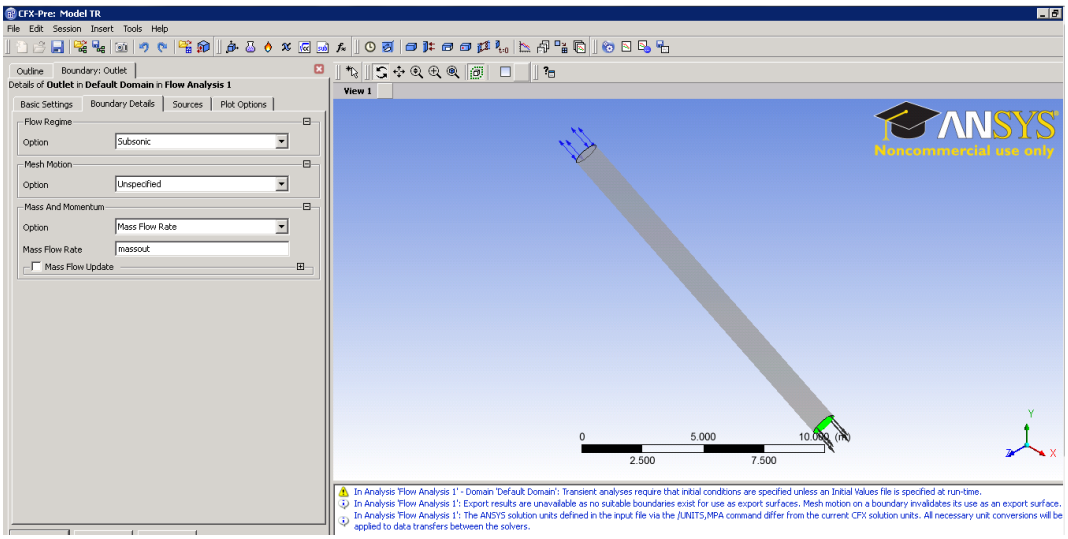

Figure 4. 30 - Defining the Outlet Boundary Conditions Parameters (Transient Analysis)

The gate closure time T determines if the analysis is considered a rapid or a slow gate closure. A rapid gate closure happens if the gate closure time is smaller than $2L_p/a_c$ .A slow gate closure time happens if the gate closure time is larger than $2L_p/a_c$.

Simulation Duration Time: The simulation duration time depends on the type of analysis dictated by the gate closure time. Under a rapid gate closure, a complete water hammer cycle lasts $4L_p/a_c$ seconds. A user determines a rapid gate closure simulation time by multiplying the number of water hammer cycles wanted by the duration time of one cycle.

Under a slow gate closure, the duration time of one cycle must be found by a trial and error process. Section 5.2.2 presents the duration time for the present reference case.

Timestep: For a compressible fluid problem, it is required to determine the timestep Δt as a function of the acoustic Courant Number C_n . The closer the Courant number is to unity, the more accurate the results are.

$$C_n = \frac{(V_o + a_c) \times \Delta t}{l_{el}} \tag{4.4}$$

C_n Courant Number

l_{el} Element dimension in the longitudinal direction, m

4.6.2 Setting the transient solver controls

Solver Control Transient solver controls, presented on Table 4.10, have been determined so the simulation duration time is minimized and results are kept accurate. Figures 4.31 and 4.32 define the controls on the interface CFX-Pre.

Table 4. 10 - Transient Solver Control

	Fluid Convergence Criteria	FSI Convergence Criteria
Min	2	2
Max	5	5

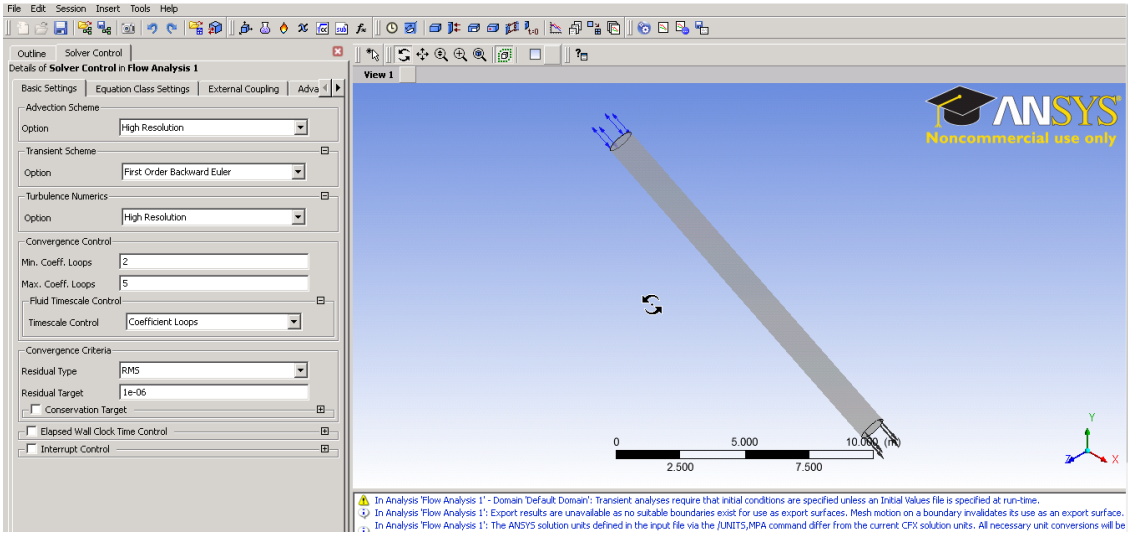

Figure 4. 31 - Defining the Fluid Convergence Criteria (Transient Analysis)

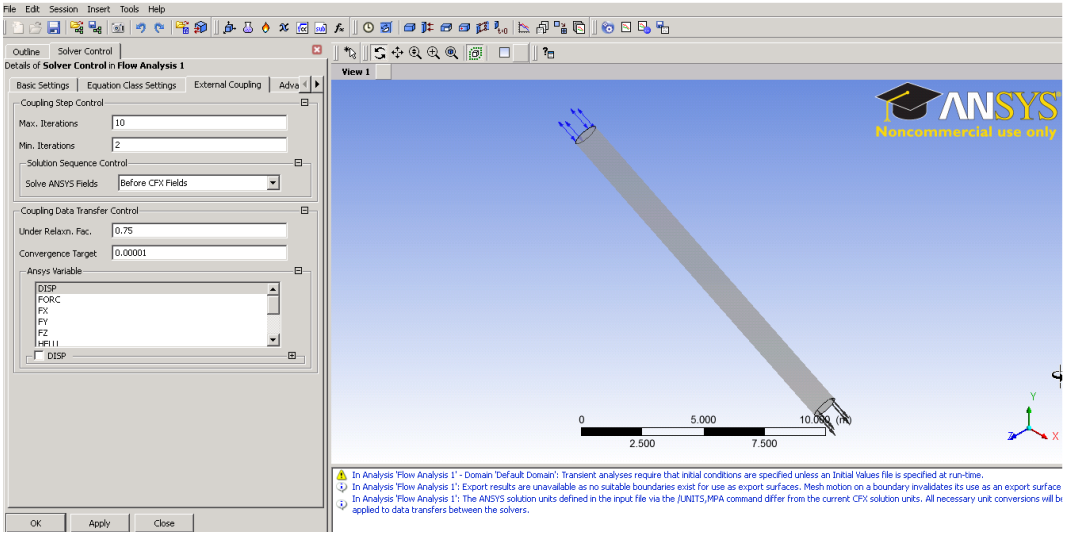

Figure 4. 32 - Defining the FSI Convergence Criteria (Transient Analysis)

4.6.3 Creating the Modified File

Before a transient analysis can be executed, the mechanical input file must be adjusted and saved as a modified file (.mf) in which command have been added.

Command 1: The inertia effect of the pipe structure hasn't been included in the steady-state analysis and must be inserted in the transient one under the command:

TIMINT,ON

Command 2: The timestep specified defined in Section 4.6.1 for the fluid solver must be specified for the structural solver under the command: **DELTIM,** $\Delta t, \Delta t, \Delta t$

4.7 Conclusion

Chapter 4 has presented the general concept of a Fluid-Structure Interaction (FSI) and has described, in details, its implementation into ANSYS-CFX, so one could recreate the water hammer phenomenon into a simply supported straight segment. Structural and Fluid results from the reference case model developed in Sections 4.4 to 4.6 are presented and analyzed in Chapter 5.

CHAPTER 5 –ANALYSIS AND VALIDATION OF AN ELEVATED SIMPLY SUPPORTED PENSTOCK

5.1 Objectives and Scope

This chapter presents the fluid and structural results for the reference case modeled in Chapter 4. Section 5.2 presents timestep comparative analyses for rapid and slow gate closures. It establishes a suitable timestep that strikes a balance between accuracy of results and computational cost. The timestep selected will be used for subsequent simulations. Section 5.3 presents the steady state results. A comparison between the structural results obtained and those based on the beam theory is made to assess the validity of the model. Section 5.4 presents the transient analysis results. A time evolution of the transient pressure, stresses and displacements for both rapid and slow gate closures is presented. A comparison between the transient pressure predicted from the FSI and those based on the arithmetic method introduced in Chapter 2 is made and the validity of the model is assessed. Results from the case of slow gate closure will serve as a reference case for the parametric study in Chapter 6.

5.2 Determining the timestep

Prior to defining the timestep, both gate closure time and simulation time must be determined.

5.2.1 Determining gate closure time

For a rapid gate closure, Section 4.6.1 stated that the gate closure time T must meet the condition $T < 2L_p/a_c$ in which L_p is the length of the pipe and a_c is the velocity of the pressure wave given by

$$a_c = \sqrt{\frac{k}{\rho_w(1+\frac{D_p kc_1}{eE})}} = \sqrt{\frac{2.2GPa}{1000.02kg/m^3\left(1+\frac{1.067m\times 2.2GPa\times 0.85}{0.01905m\times 200GPa}\right)}} \qquad (5.1)$$

$$a_c = 1201.6m/s$$

The threshold value for rapid closure time is computed by

$$\frac{2L_p}{a_c} = \frac{2 \times 15.384m}{1201.6\,m/s} = 0.0256\,\text{sec} \qquad (5.2)$$

This threshold value will be used to define two cases: a) a rapid closure case and b) a slow closure case. A gate closure time of 0.0008sec is less than threshold value determined from Eq. 5.2 and meets the requirement $T < 2L_p/a_c$, and thus characterizes the problem as a rapid gate closure.

For the slow gate closure case, Section 3.3.1 stated that the gate closure time is chosen so that the highest pressure attained at the penstock mid-span section would correspond to 110% of the static pressure P_s. A trial and error procedure has determined that a gate closure time of 0.1135sec would meet this criterion. A gate closure time of 0.1135sec is greater than $2L_p/a_c$ making the problem a slow gate closure case (Section 4.6.1).

5.2.2 Determining the simulation time

Simulation time for rapid gate closure t_{p1} is determined according to Section 4.6.1, which states that one complete transient pressure cycle should last $4L_p/a_c$ seconds. For our problem, one has

$$t_{p1} = \frac{4L_p}{a_c} = \frac{4 \times 15.384m}{1201.6\,m/s} = 0.0512\,\text{sec} \qquad \text{Simulation time for rapid gate closure} \qquad (5.3)$$

The simulation time for slow gate closure has been determined through a trial and error process. To analyze the damping effect of the pressure wave, a simulation time t_{p2} that is long enough to show two consecutive pressure peaks has been chosen.

$$t_{p2} = 0.100\,\text{sec} \qquad \text{Simulation time for slow gate closure} \qquad (5.4)$$

5.2.3 Determining the timestep for rapid gate closure

Based on the model described in Chapter 4 and using the gate closure times determined in Section 5.2.1 and simulation times determined in Section 5.2.2, three analyses for timesteps of 0.0001, 0.0002 and 0.0005 secs. were conducted. Transient pressure results at penstock mid-span were overlaid on Fig. 5.1 for comparison.

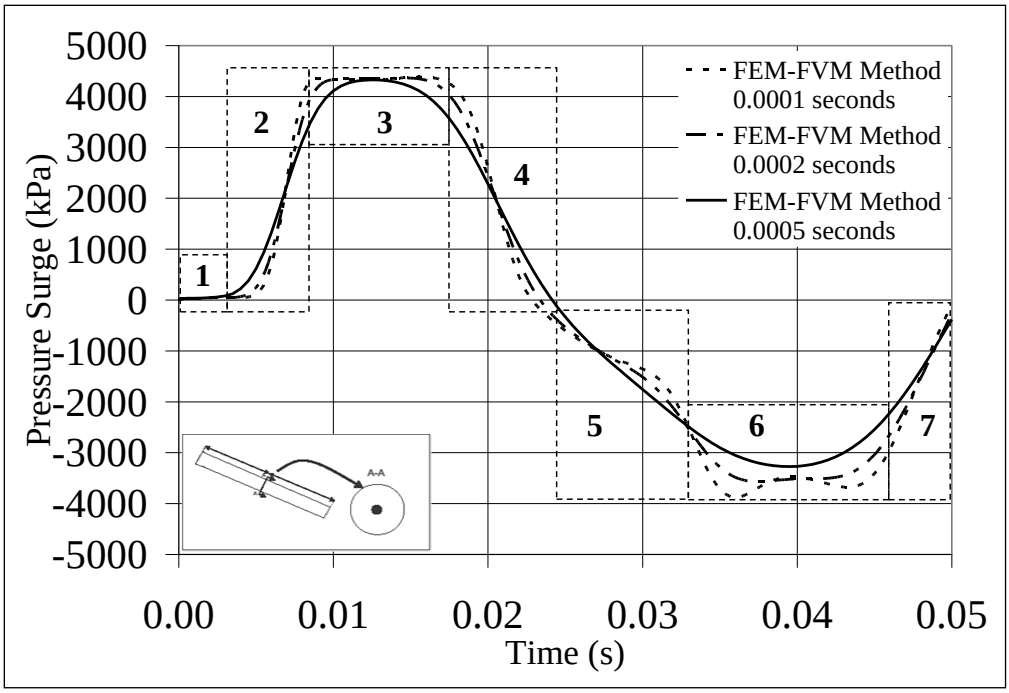

Figure 5. 1 - Sensitivity analysis - Influence of different timesteps for the rapid gate closure on the transient pressure

The positive pressure area between zones 1 and 4 takes place in the time frame during which the pressure wave travels the length of the pipe twice. The negative pressure area between zones 5 and 7 also takes place in the time frame during which the pressure wave travels the length of the pipe twice.

Zone 1 is a time period where the pressure is equal to the static pressure since the pressure wave has not reached the mid-span section yet. A smaller timestep is observed to correspond to a longer predicted Zone 1 period.

Zone 2 is characterized by a rapid increase of pressure from the static pressure value up to a value approximately equal to the positive Joukowski pressure as determined by Eq. 2.65. A smaller timestep is observed to correspond to a steeper slope.

Zone 3 is a period of constant pressure. A smaller timestep is observed to predict to a longer Zone 3 period.

Zone 4 is characterized by a rapid decrease of pressure from the positive Joukowski pressure to the static pressure. A smaller timestep is observed to correspond to a steeper negative slope.

Zone 5 is a rapid decrease of pressure from the static pressure to a value approximately equal to the negative Joukowski pressure (Eq.2.65). A smaller timestep is observed to correspond to a steeper negative slope

Zone 6 is a period of constant pressure. A smaller timestep is observed to correspond to a longer Zone 6 period.

Zone 7 is characterized by a rapid increase of pressure from the negative Joukowski pressure to the static pressure. A smaller timestep is observed to correspond to a steeper decreasing line. Table 5.1 presents the Courant number as determined by (Eq. 4.4), the simulation duration and the maximum transient pressure for each timestep. A comparison between the maximum transient pressure is made to determine the impact of the chosen timestep on the accuracy of the computed pressure. Also shown is the simulation time for the runs. All runs were conducted on a computer with Two Intel Xeon E5520 processors at 2.2 GHZ clock speed and RAM of 12 GB.

It shows that the smaller timestep (0.0001 sec), which corresponds to a computational effort five times larger than that of the largest timestep (0.0005 sec), is only 1.3% more accurate.

Table 5. 1 - Comparison of calculated parameters for different timesteps for a rapid gate closure

Time Step (sec)		Courant Number	Simulation Time	Maximum Pressure Surge (kPa)	Percentage Difference based on Time Step 0.0001 sec	
1°	0.0001	0.705	26h30 min	$P_1 = 4383kPa$	-	-
2°	0.0002	1.41	13h50min	$P_2 = 4362kPa$	$(P_1 - P_2)/P_1$	0.47%
3°	0.0005	3.53	5h37min	$P_3 = 4325kPa$	$(P_1 - P_3)/P_1$	1.30%

5.2.4 Determining the timestep for slow gate closure

Based on the model described in Chapter 4 and using the slow gate closure times determined in Section 5.2.1 and simulation times in Section 5.2.2, three analyses for different timesteps were conducted and compared in Fig. 5.2. As with the rapid gate closure, the transient pressure data have been taken at the mid-span section. Figure 5.2 shows that the smaller the timestep is, the greater the amplitude of the sinusoidal wave.

Reducing the timestep value has a significant impact on the accuracy and magnitude of the pressure peak value.

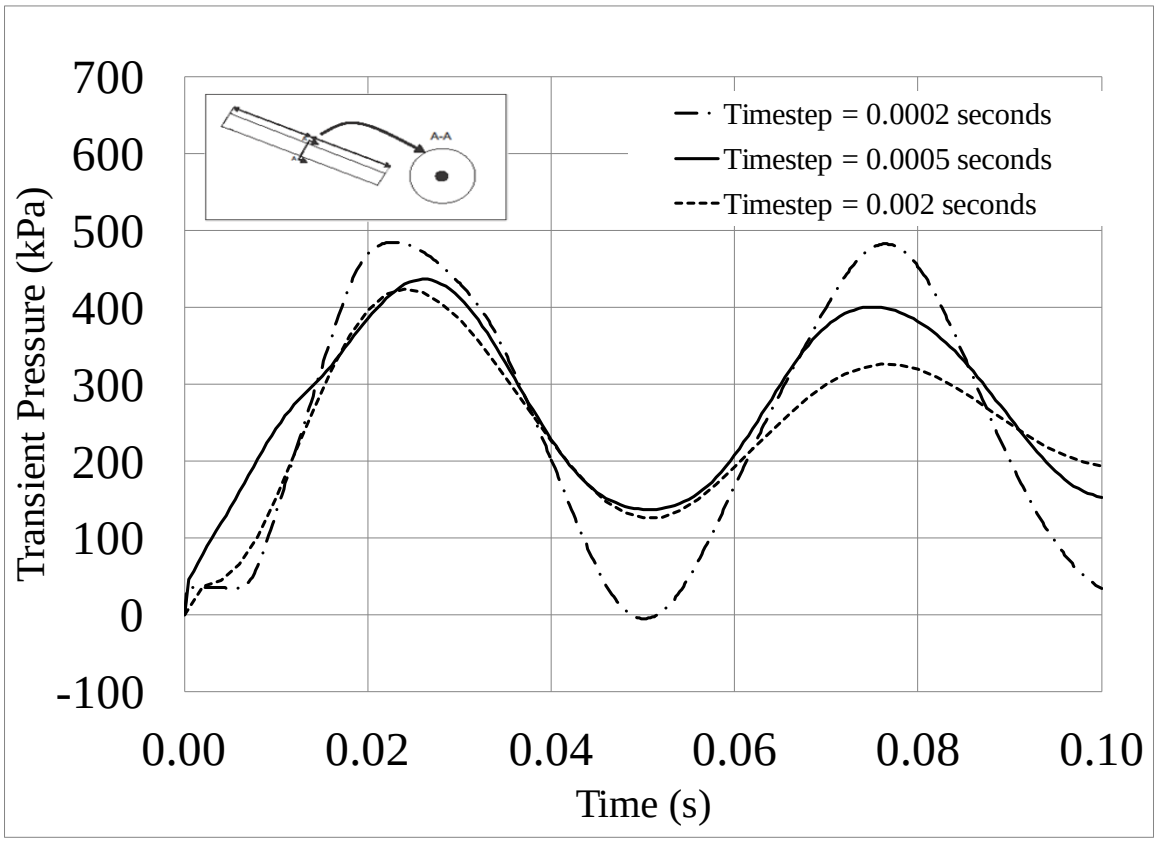

Figure 5. 2 - Sensitivity analysis - Influence of different timesteps on the transient pressure for slow gate closure

Table 5.2 presents the Courant number (Eq. 4.4), the simulation duration and the maximum transient pressure for each timestep. As with the rapid gate closure case, a comparison between the maximum transient pressure is made to determine the impact of the timestep on the accuracy of the computed pressure. It can be noticed that the timestep selection has a moderate effect on the accuracy of maximum transient pressure. A pressure difference of 12.5% is observed between the 0.0002 sec. timestep and the 0.002 sec. timestep. Given the large number of the parametric runs in the present thesis, a timestep of 0.002 sec. has been chosen in subsequent runs. While it is recognized that this introduces an error of the order of 12.6 % in estimating the transient pressure, the associated simulation duration is significantly reduced from 37h 58min to 3h 53min for the present problem.

Table 5. 2 - Effect of the timestep on transient pressure for slow gate closure

Time Step (sec)		Courant Number	Simulation Time	Maximum Pressure Surge (kPa)	Percentage Difference based on Time Step 0.0002 sec	
1°	0.0002	1.41	37h58 min	$P_1 = 484kPa$	-	-
2°	0.0005	3.53	8h00min	$P_2 = 436kPa$	$(P_1 - P_2)/P_1$	9.90%
3°	0.002	14.1	3h53min	$P_3 = 423kPa$	$(P_1 - P_3)/P_1$	12.6%

5.3 Results of Steady State Model

Results from the steady-state model described in Section 4.5 are presented in this section. Section 5.3.1 first presents the fluid fields (velocity and dynamic pressure) while Section 5.3.2 presents the structural contour plots (longitudinal and hoop stresses). Comments and comparisons to closed form solutions are provided.

5.3.1 Fluid Results for Steady-State Model

5.3.1.1 Velocity Profile Results

Figure 5.3 shows the general velocity profile development for a turbulent flow in a pipe. The figure consists of a plan view of the velocity profile at the inlet shown on Fig. 5.3a, at the mid-span on Fig. 5.3b and at the outlet on Fig. 5.3c.

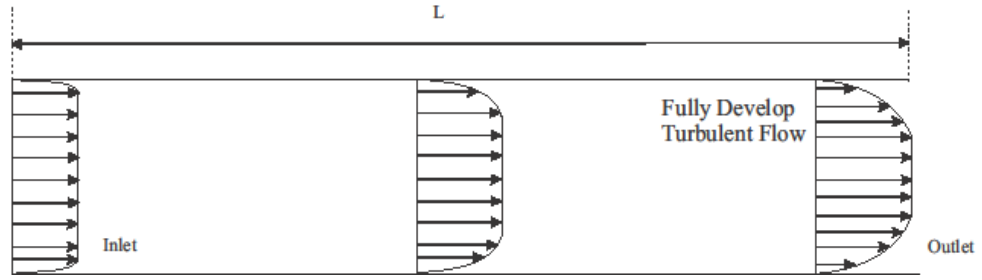

Figure 5. 3 – Conceptual Turbulent Flow Development at (a) Inlet, (b) Mid-Span, and (c) Outlet

For comparison, the velocity profiles as extracted from the FEM-FVM are provided in Figure 5.4. A plan view is shown in Fig. 5.4a, an elevation view in Figure 5.4b, and inlet and outlet views in Figs. 5.4c and 5.4d. For clarity, velocity is kept between $3.0\,m/s$ and $3.8\,m/s$.

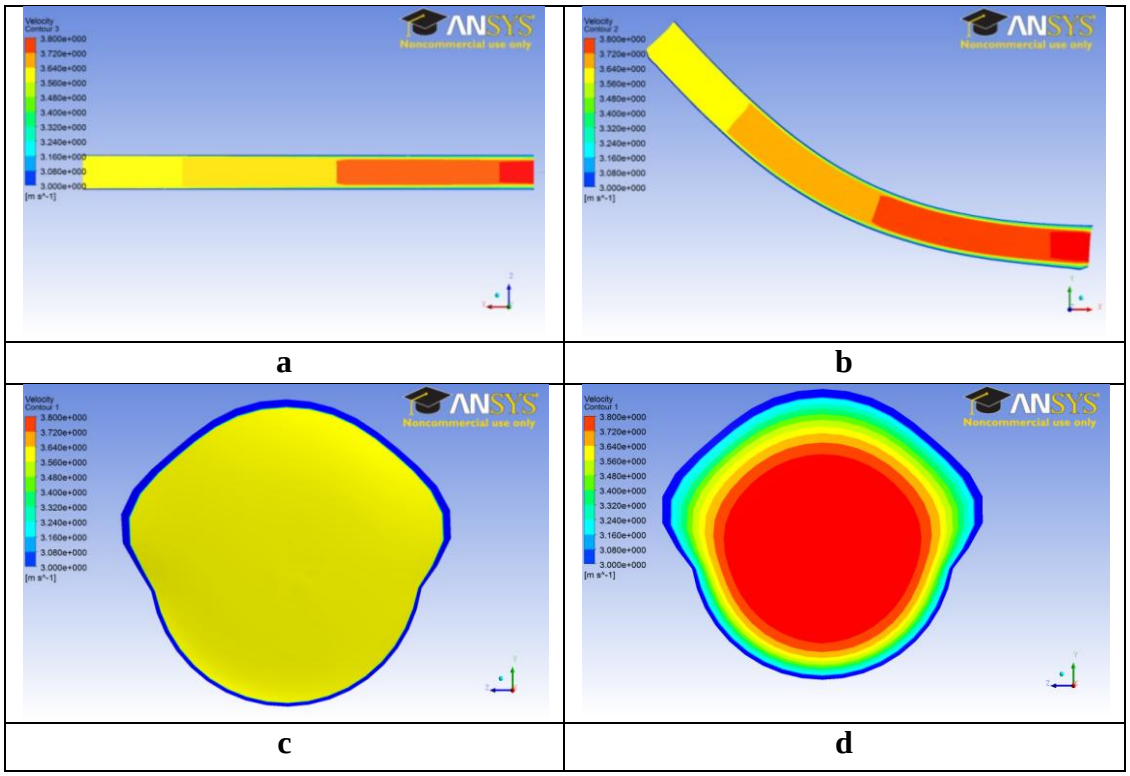

Figure 5. 4 - Longitudinal Velocity Contours a) Plan View of Core Velocity, b) Elevation View of Core Velocity, c) Inlet Velocity, and d) Outlet Velocity

The general velocity profile development along the pipe length is shown in Fig. 5.4a which compares well with the plan view on Fig. 5.3a-c. Both figures display a core velocity that increases in magnitude from the inlet to the outlet. Also, the inlet section contour plot on Fig. 5.4c compares well with the profile presented in Fig. 5.3a. Both figures display an essentially uniform velocity profile which rapidly drops in velocity near the pipe wall, which is indicative of a small boundary layer. The outlet section contour plot shown on Fig. 5.4d also compares well to the velocity profile on Fig. 5.3c. Both figures display a relatively large boundary layer near the pipe wall in which the velocity slowly decreases from the pipe core towards the pipe wall. It is also noteworthy to note that the velocity profiles at the inlet and outlet (Figs. 5.4c and 5.4d) adapt to the deformed configuration of the pipe, a feature that can be captured only in a 3D analysis FSI analysis such as the one adopted in the present study.

5.3.1.2 Pressure Profile Results

Figure 5.5 shows the contour plots of the dynamic pressure profile from the FEM-FVM model. An elevation view is shown in Fig. 5.5a, and inlet and outlet views in Figs. 5.5b, c. For clarity, dynamic pressure is kept between -7.4 kPa and -6.4kPa. Figure 5.5a shows the pressure loss between the inlet and the outlet of the pipe. As with the velocity profile, the pressure profile develops along the pipe length from the inlet (Fig. 5.5b) to the outlet (Fig.5.5c).

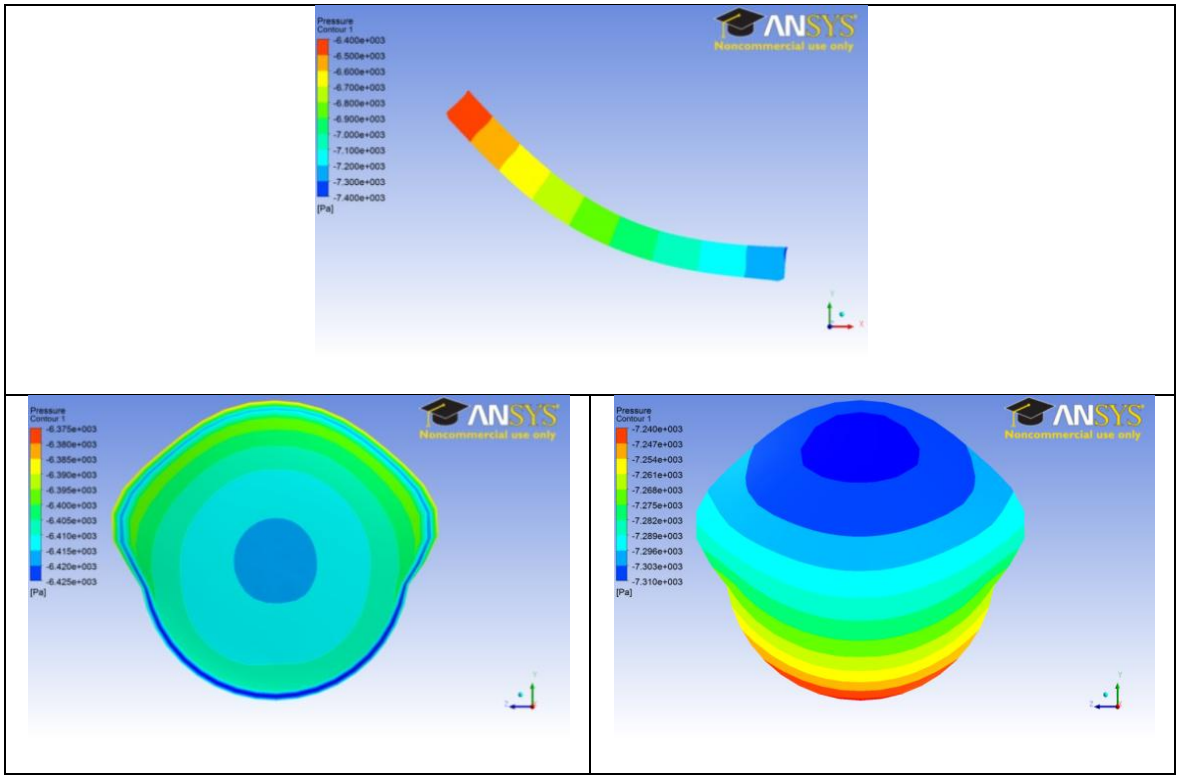

Figure 5. 5 - Dynamic pressure profile from an a) Elevation View, b) Inlet, c) Outlet

5.3.2 Structural Results for Steady-State Model

Figures 5.6 and 5.7 show the location and notation of where structural results were retrieved from the FEM-FVM model. Longitudinal and hoop stresses are extracted at four different locations around the circumference (Fig.5.6) and two through-thickness locations: the outside (O) surface and inside (I) surface (Fig.5.7).

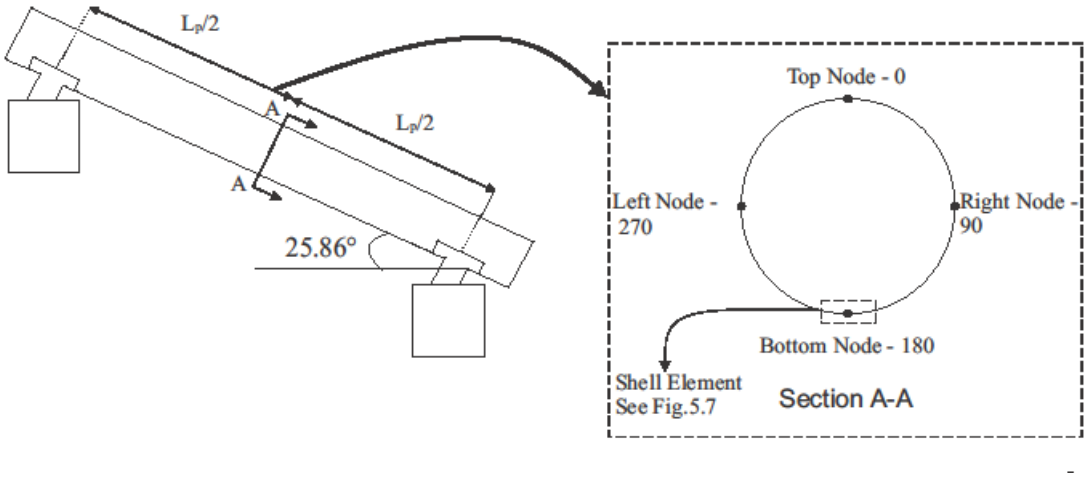

Figure 5. 6 - Nodes location around the pipe mid-length perimeter

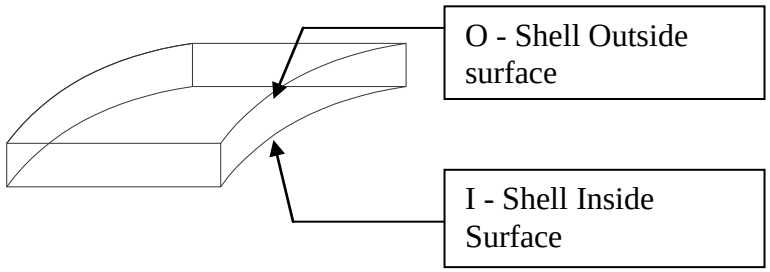

Figure 5. 7 - Nodes location on a typical shell element

5.3.2.1 Longitudinal Stress Results

Figure 5.8 provides the deformed contour plot of the longitudinal stress on the outside surface. A plan view is shown in Fig. 5.8a, an elevation view in Figure 5.8b, and inlet and outlet views are provided in Figs. 5.8c and 5.8d. For clarity purposes, the longitudinal stress limits on the contour are kept between -30 MPa and 30 MPa.

The longitudinal stress distribution in Fig. 5.8 indicates that the results of the FEM-FVM model are consistent with those based on the conventional Euler Bernouilli beam theory for a simply supported beam. In agreement with the beam theory, the longitudinal stress in Fig. 5.8b has a maximal tensile value at the bottom of the pipe and a maximal compressive value at the top. Longitudinal stresses at the top and bottom fibers extend from zero at the pipe ends, where the bending moment and axial force vanish, to a peak value at mid-span where the bending moments have a maximal value. The longitudinal stress located at position 90° and 270° (Fig. 5.6) at mid-span is equal to zero.

Longitudinal stress located at position 0° and 180° (Fig. 5.6) at mid-span is computed in Section 3.3.1 and recalled here in its short form.

$$\sigma_l = \sigma_b + \sigma_a = \frac{M_b}{S_p} + \frac{w_a L_p}{A_p} = \frac{367kNm}{\pi r_i^2 e} + \frac{6.02kN/m \times 15.384m}{\pi(r_o^2 - r_i^2)}$$
$$= 21.5MPa + 1.42MPa = 22.9MPa \qquad (5.5)$$

Table 5.3 shows that FEM-FVM longitudinal stress values at top and bottom fibres are within 8.25% of the beam theory.

The deformed shape of the pipe ends (Figs. 5.8 c-d) confirms the ability of the model to adequately represent a pipe sitting on saddles. While the upper part of the circumference is that free to move in the radial direction, the lower part was restrained from moving in the tangential and radial directions. It is shown on Fig. 5.8b that, except for the inlet end mid height nodes, both pipe ends nodes are free to move in the longitudinal direction.

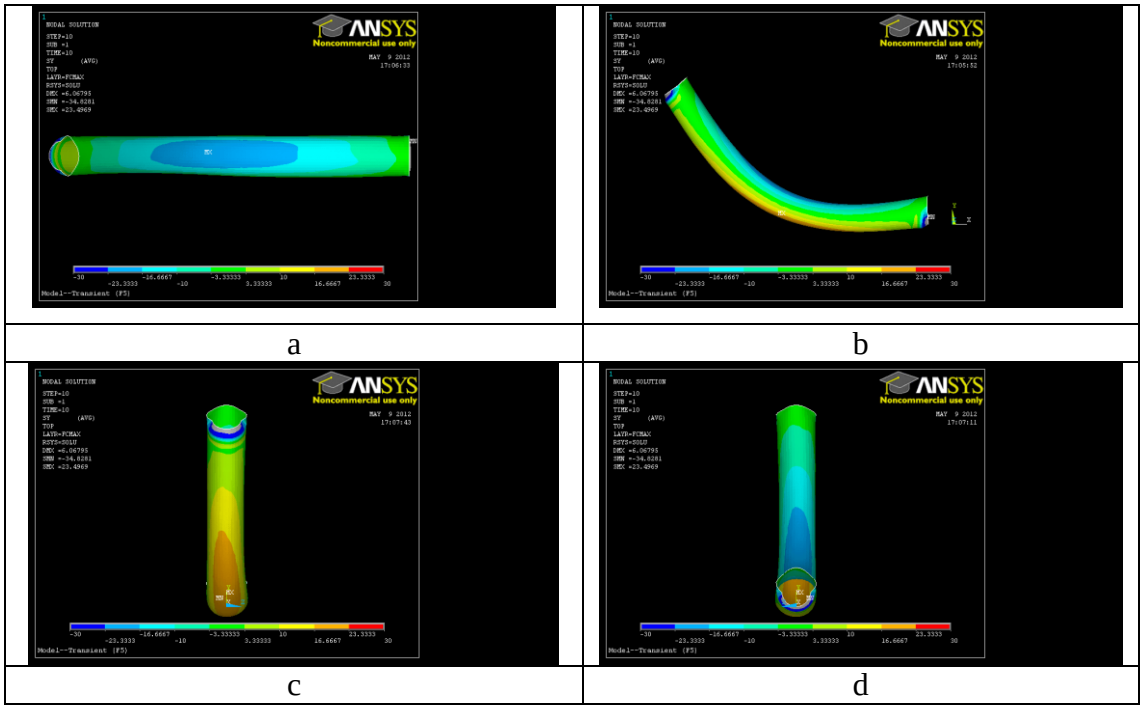

Figure 5. 8 - Longitudinal stress from a) Plan View, b) Elevation View, c) Inlet View, d) Outlet View

Table 5.3 provides a comparison for the longitudinal stress model results from the locations defined in Figs. 5.6 and 5.7 to those based on the beam theory solution.

Table 5. 3 - Comparing the analytical stress with FEM-FVM longitudinal stress

	Longitudinal Stress (MPa)							
Element Position	0-O	0-I	90-O	90-I	180-O	180-I	270-O	270-I
Numerical Solution [1]	-21.18	-23.63	0.04	-0.61	21.70	24.79	1.53	-0.31
Classical Solution [2]	-22.90	-22.90	0.00	0.00	22.90	22.90	0.00	0.00
Percentage Difference ([2]-[1])/[1]	7.51%	3.19%	-	-	5.24%	8.25%	-	-

5.3.2.2 Hoop Stress Results

Figure 5.9 provides the deformed contour plots for the hoop stress on the outside surface. A plan view is shown in Fig. 5.9a, an elevation view in Figure 5.9b, and inlet and outlet views are provided in Figs. 5.9c and d, respectively. For clarity and comparison purposes, hoop stress limits are kept between 120 MPa and 130 MPa in all figures. The hoop stress distribution in Fig. 5.9 indicates that the FEM-FVM model results are similar to those expected under static pressure. One recalls from Section 3.3.4 that the hoop stress values as calculated from the classical solution based on equilibrium of a half ring is

$$\sigma_h = \frac{H_o g \rho_w D_p}{2e} = \frac{455.3m \times 9.81 m/s^2 \times 1000.02 kg/m^3 \times (1.067) kg/m}{2 \times 0.0191 m} = 125.1 MPa$$

in which the pressure H_o was taken at mid-span. The increase in static pressure from the inlet to the outlet causes a slight variation in hoop stress values along its longitudinal direction of the pipe. Also, the ovalization of the pipe cross-section near pipe mid-span (Fig. 5.10) causes another slight variation in the hoop stresses in the angular direction, both effects captured by the present FEM-FVM model but not by the classical solution

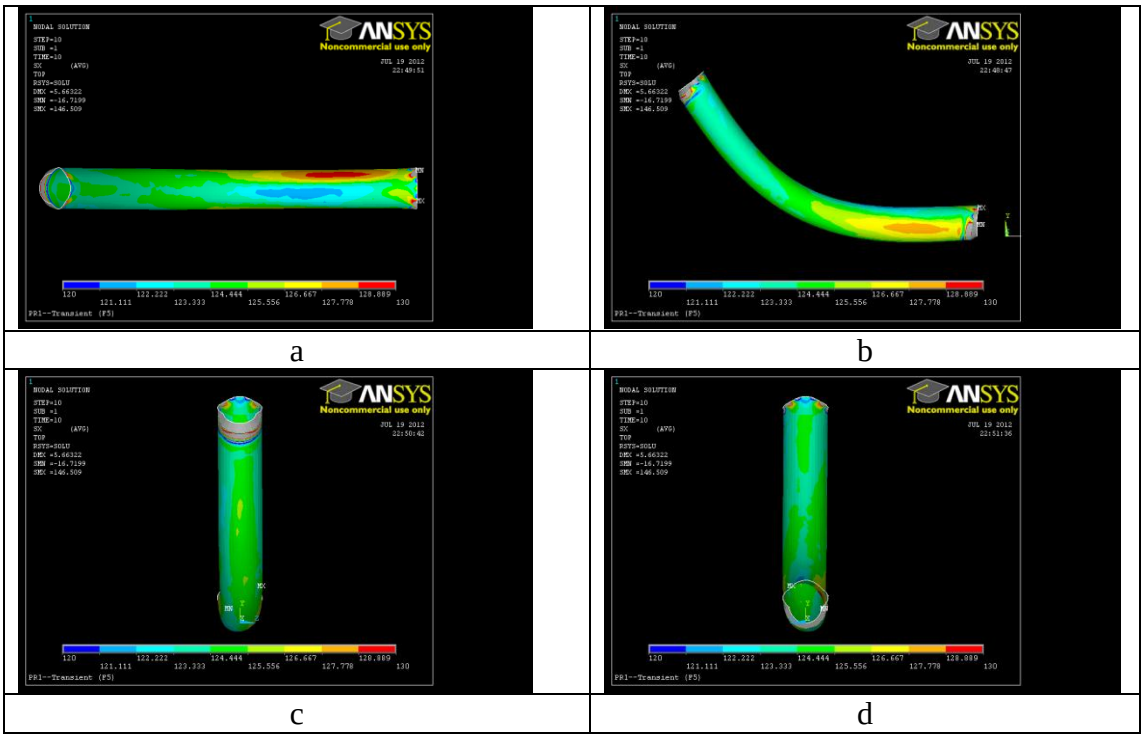

Figure 5. 9 - Hoop stress from a) Plan View, b) Elevation View, c) Inlet View, d) Outlet View

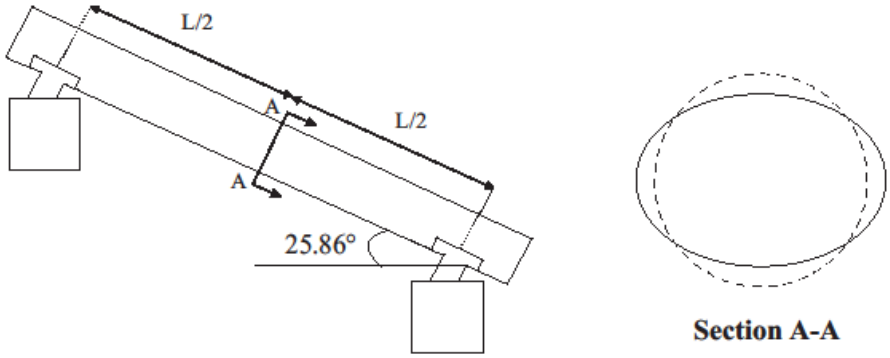

Figure 5. 10 - Angular Variation of the Hoop stress

Table 5.4 provides a comparison of the hoop stress results retrieved from locations defined in Figs. 5.6 and 5.7 to closed form solutions. It shows that FEM-FVM hoop stress values are within 3% of the classical solution.

Table 5. 4 - Comparison for Hoop Stresses

	Hoop Stress (MPa)							
Element Position	0-O	0-I	90-O	90-I	180-O	180-I	270-O	270-I
Numerical Solution [1]	127.8	122.4	126.9	124.0	125.3	126.9	128.7	121.9
Classical Solution [2]	125.1	125.1	125.1	125.1	125.1	125.1	125.1	125.1
Percentage Difference ([2]-[1])/[1]	-2.11%	2.21%	-1.42%	0.89%	-0.16%	-1.42%	-2.80%	2.63%

The comparison between the classical solution and FEM-FVM results for different locations is used to determine the node, within the top and bottom nodes, that will be used as a reference node for subsequent runs. With the lowest percentage difference sum (5.4%), the node 180-O will be the reference node.

5.4 Transient Model Results

Results from the transient model introduced in Section 4.6 are presented in this section. Section 5.4.1 shows the fluid and structural results for the rapid gate closure case and provides a comparison of fluid results to those based on the arithmetic method introduced in Section 2.4.1. Section 5.4.2 presents the fluid and structural results for the slow gate closure case and provides a comparison of fluid results section to those based on the arithmetic method. The slow gate closure case will serve as a reference case in the parametric study to be presented in Chapter 6.

5.4.1 Rapid Gate Closure Model Results

The rapid gate closure case is only of academic interest and its results will not be used for further comparison in the present work. Since results from the rapid gate closure are not used for further comparison in the present work, the present analysis uses the most accurate run previously presented (Section 5.2.3). The analysis uses a timestep of 0.0001 seconds and a simulation time of 0.0512 seconds (Eq. 5.3).

5.4.1.1 Transient pressure induced by rapid gate closure

Figure 5.11 shows eight locations of interest where transient pressure results were extracted within the simulation time. Figure 5.12 shows a 3D plot of the temporal curves for each location. From $3L_p/4$ to the outlet, each curve reaches the Joukowski pressure as determined by Eq. 2.61, i.e.,

$$\Delta H = \rho_w a_c \Delta V = 1000.02\,kg/m^3 \times 1201 m/s \times 3.567\,m/s = 4.28 MPa\,.$$

Figure 5.12 shows that the closer the location is to the outlet, the longer the Joukowski pressure is maintained**.**

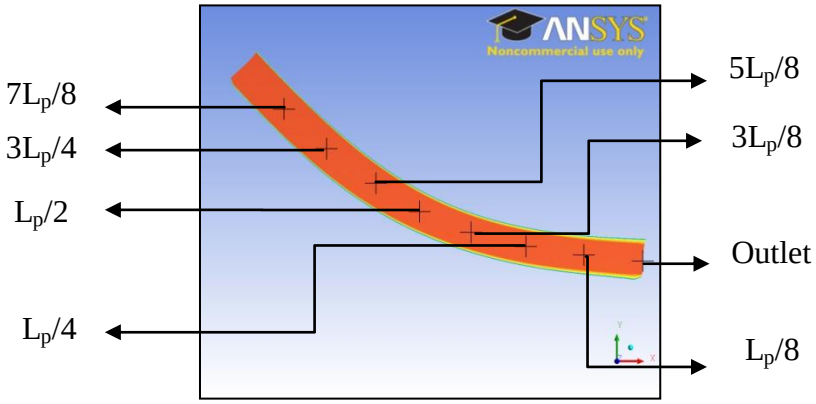

Figure 5. 11 - Locations of the pressure results from the outlet along the pipe axis

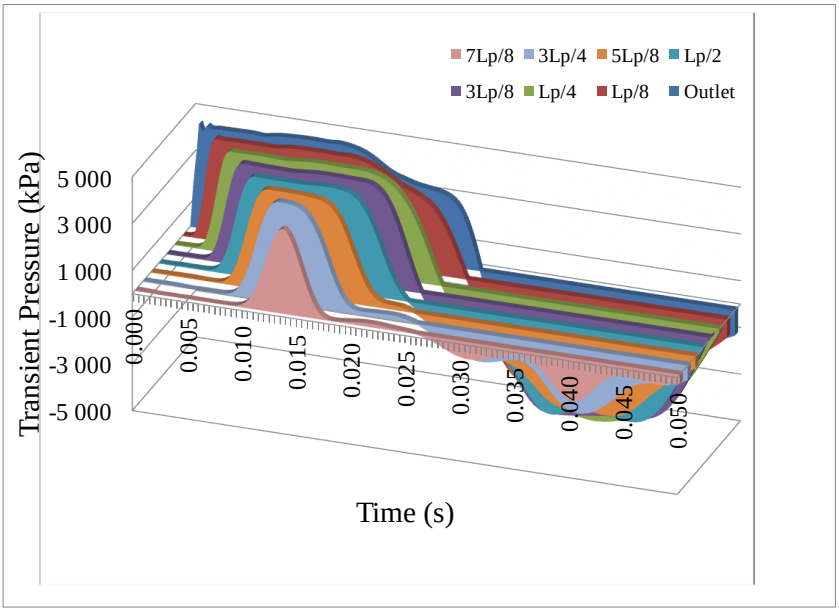

Figure 5. 12 - Evolution in time and space of the transient pressure for rapid gate closure

5.4.1.2 Fluid and structural responses of water hammer

Figures 5.13 show the fluid and structural responses at mid-span section created by a rapid gate closure. In an experimental study, Tissjeling (1990) observed that the first half period of transient pressure is not greatly affected by the fluid-structure interaction effects. In contrast, he also observed a more significant effect in the second half period that is manifested by an additional sinusoidal wave of higher frequency and smaller amplitude to the classical transient pressure wave. In the present study, a similar effect was observed when the timestep value chosen was small. Figure 5.1 shows that a timestep of 0.0001 seconds is required to capture the FSI effect reported by Tissjeling (1990).

Both the longitudinal and hoop stresses are observed to be affected by the transient pressure. The longitudinal stress curves (Figs. 5.13 g-h) show the Poisson ratio coupling effect, a consequence of the fluid-structure interaction. A flow reduction generates a travelling pressure rise and radially expands the pipe wall. This radial expansion is accompanied by an axial contraction due to the Poisson ratio effect, which induces a longitudinal stress wave throughout the pipe (Tissjeling, 1990). The stress wave speed $a_s = \sqrt{E/\rho_s}$ depends on the mechanical properties of the pipe (Young Modulus and density of the pipe material). For a steel pipe, Tissjeling (1990) observed that the stress wave is approximately three times faster than the pressure wave. Figures 5.13a and g show that for every peak of transient pressure, there are approximately three peaks of longitudinal stress. It is also observed that, at pipe mid-span, the first peak of longitudinal stresses takes place before the pressure peak takes place. These results can be explained by the fact that, for a steel pipe, the stress wave travels approximately three times faster than the pressure wave. The first peak of longitudinal stress would then be the result of the first pressure peak created at the outlet.

For the first half period, the shape of the hoop stress curve (Fig. 5.13c) is perfectly synchronized with the transient pressure curve. In the second half period, the small difference between the two curves is caused by the Poisson ratio coupling effect.

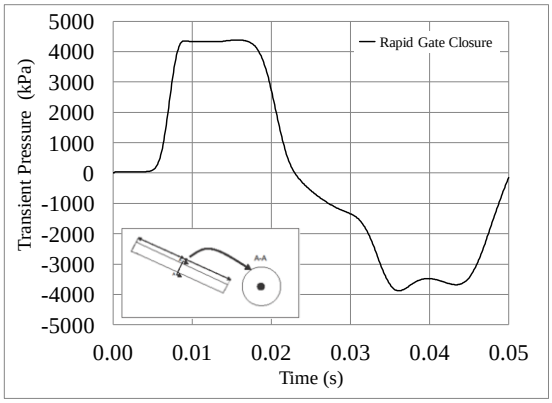
Transient Pressure (kPa)
5000
4000
3000
2000
1000
0
-1000
-2000
-3000
-4000
-5000
Rapid Gate Closure
0.00
0.01
0.02
0.03
0.04
0.05
Time (s)

a

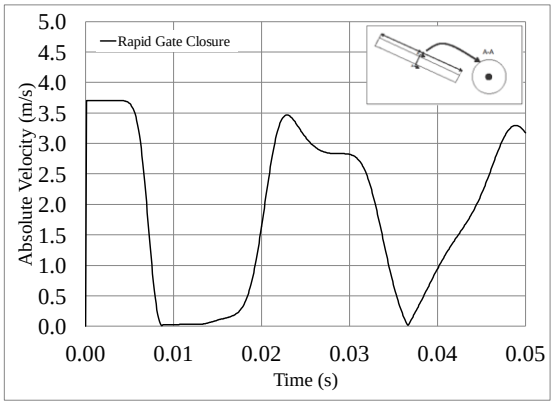
Absolute Velocity (m/s)
5.0
4.5
4.0
3.5
3.0
2.5
2.0
1.5
1.0
0.5
0.0
Rapid Gate Closure
0.00
0.01
0.02
0.03
0.04
0.05
Time (s)

b

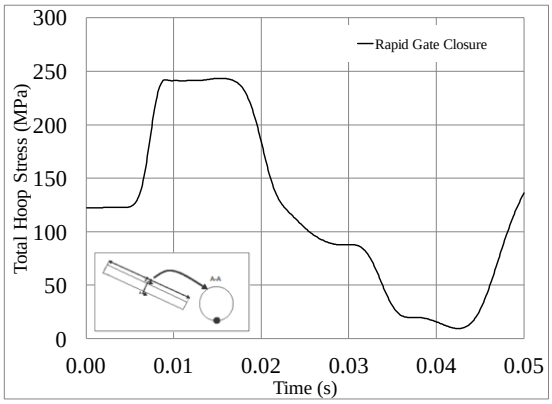
Total Hoop Stress (MPa)
300
250
200
150
100
50
0
Rapid Gate Closure
0.00
0.01
0.02
0.03
0.04
0.05
Time (s)

c

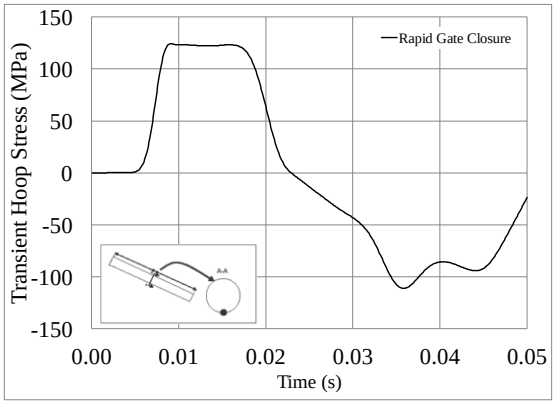
Transient Hoop Stress (MPa)
150
100
50
0
-50
-100
-150
Rapid Gate Closure
0.00
0.01
0.02
0.03
0.04
0.05
Time (s)

d

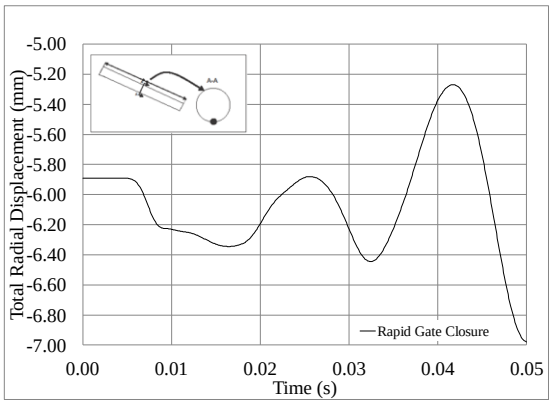
Total Radial Displacement (mm)
-5.00
-5.20
-5.40
-5.60
-5.80
-6.00
-6.20
-6.40
-6.60
-6.80
-7.00
Rapid Gate Closure
0.00
0.01
0.02
0.03
0.04
0.05
Time (s)

e

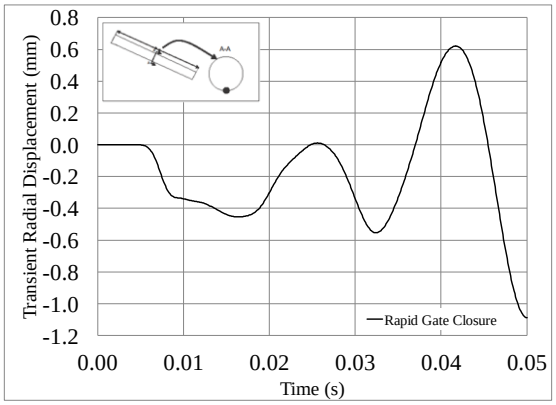
Transient Radial Displacement (mm)
0.8
0.6
0.4
0.2
0.0
-0.2
-0.4
-0.6
-0.8
-1.0
-1.2
Rapid Gate Closure
0.00
0.01
0.02
0.03
0.04
0.05
Time (s)

f

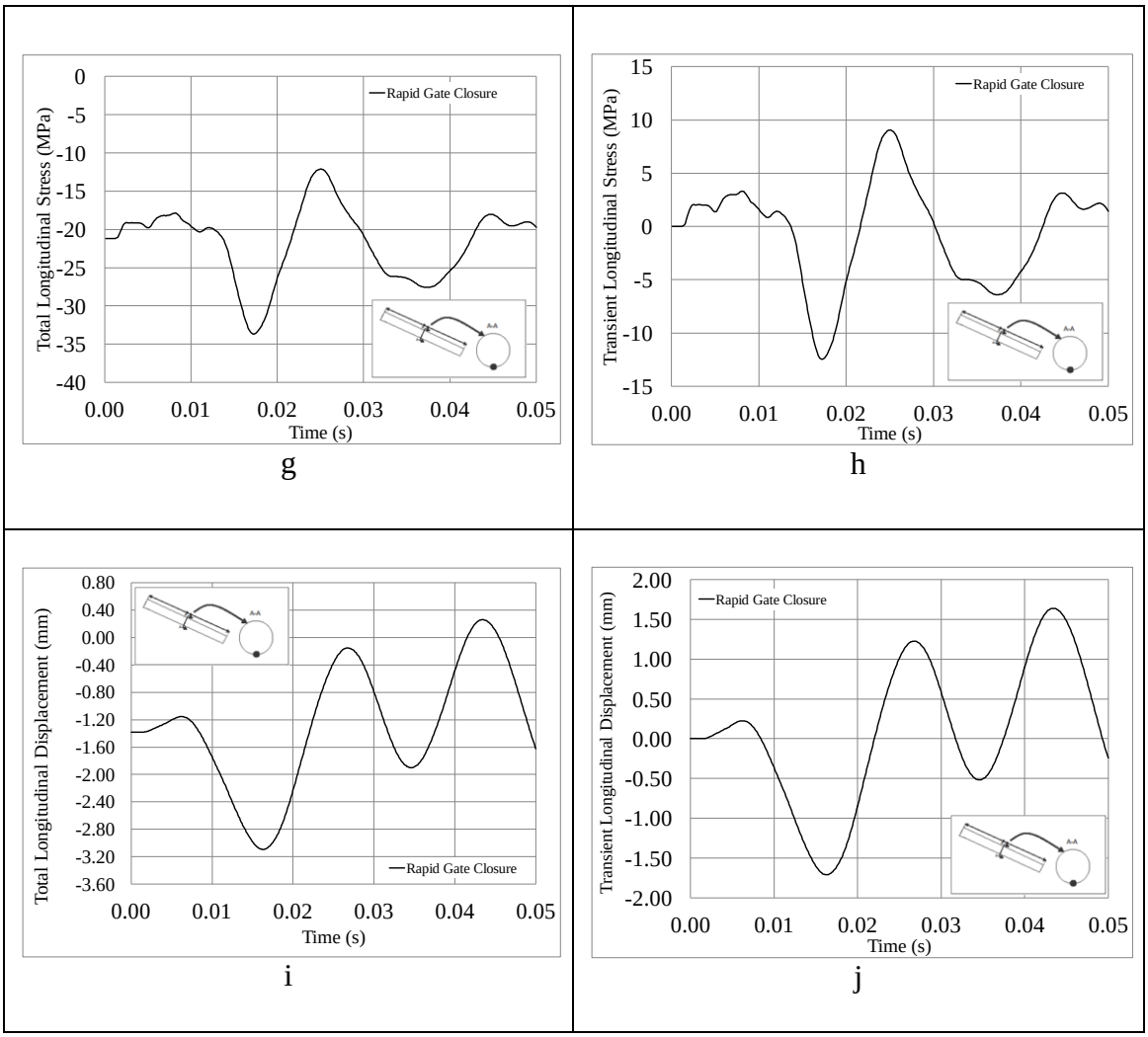

Figure 5. 13 - Temporal curves for a rapid gate closure: (a) Transient Pressure, (b) Absolute Velocity, (c) Absolute Hoop Stress, (d) Relative Hoop Stress, (e) Absolute Hoop Displacement, (f) Relative Hoop Displacement, (g) Absolute Longitudinal Stress, (h) Relative Longitudinal Stress, (i) Absolute Longitudinal Displacement, (j) Relative Longitudinal Displacement

5.4.1.3 Comparing pressure field against the arithmetic method predictions

For comparison purposes, the arithmetic method (Section 2.4.1) is implemented in Excel and applied to the present problem. Figure 5.14 overlays the results of the arithmetic method over the pressure results already presented in Fig. 5.1. For the first half period, the smaller the timestep, the closer the FEM-FVM curves are observed to be to the arithmetic method curve. However, regardless of the timestep selected, the maximum transient pressure value for each FEM-FVM curve remains essentially unchanged. Due to the fluid-structure interaction effect, the FEM-FVM curves start deviating from the arithmetic method curve in the second half period. Transient pressure curves computed

from the FEM-FVM method are observed to exhibit a faster damping effect and a longer period than predicted by the arithmetic method. Compared to the FEM-FVM method, the arithmetic method underestimates the damping effect, thus overestimating the transient pressure from the second half period onwards.

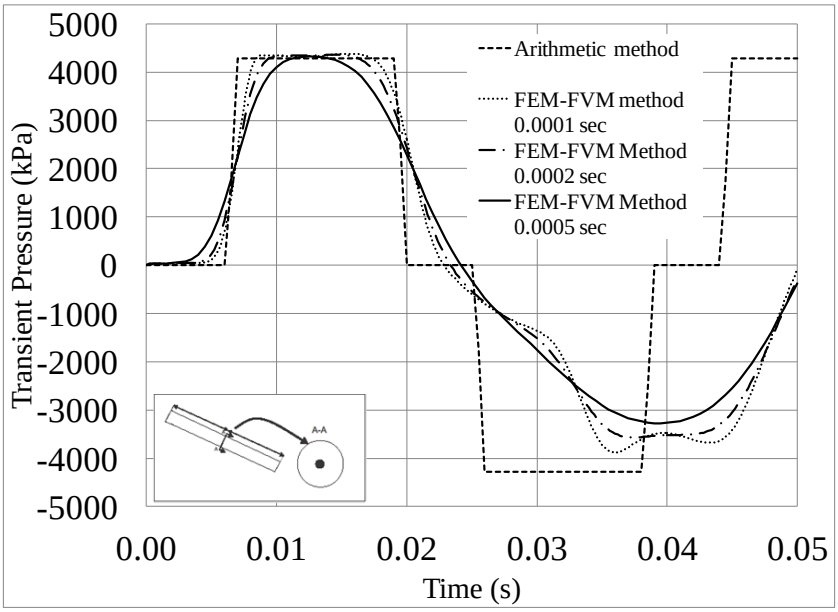

Figure 5. 14 - FEM-FVM method compared with the arithmetic method for the rapid gate closure

A comparison between the various FEM-FVM and arithmetic method predictions or the maximum transient pressure results is provided in Table 5.5. The percentage of difference is based on the transient pressure value of the FEM-FVM method with a timestep of 0.0001 seconds. In the case of rapid gate closure, the arithmetic method and FEM-FVM method predict maximum transient pressure values in close proximity.

Table 5. 5 - Comparing arithmetic method results to FEM-FVM results for rapid gate closure

	Arithmetic Method	FEM-FVM Method Time Step 0.0005 sec	FEM-FVM Method Time Step 0.0002 sec	FEM-FVM Method Time Step 0.0001 sec
Absolute Value (kPa)	4281	4325	4362	4382
Percentage Difference compared to FEM-FVM 0.0001sec	-2.32%	-1.31%	-0.47%	0.00%

5.4.2 Slow Gate Closure Model Results

5.4.2.1 Transient pressure induced by slow gate closure

As discussed in Section 5.2.4, a 0.002 second timestep was chosen for subsequent runs due to the large number of parametric runs in the present thesis. While it is recognized that this introduces an error of the order of 12.6% in estimating the transient pressure, the associated simulation duration is significantly reduced from 37h 58min to 3h 53min for the reference case considered in this chapter. Determining the necessary simulation time for slow gate closure is a trial and error process. A value of 0.100 sec has been selected in order to capture two consecutive pressure peaks.

Figure 5.15 shows a 3D plot of the temporal curves for each location (Fig. 5.11). Unlike the rapid gate closure case, the farther the location from the outlet, the smaller the maximum transient pressure. A linear relationship can be observed between the maximum transient pressure and the distance from the outlet. Figure 5.15 shows that the relationship is valid from the outlet up to a distance of $3L_p/4$.

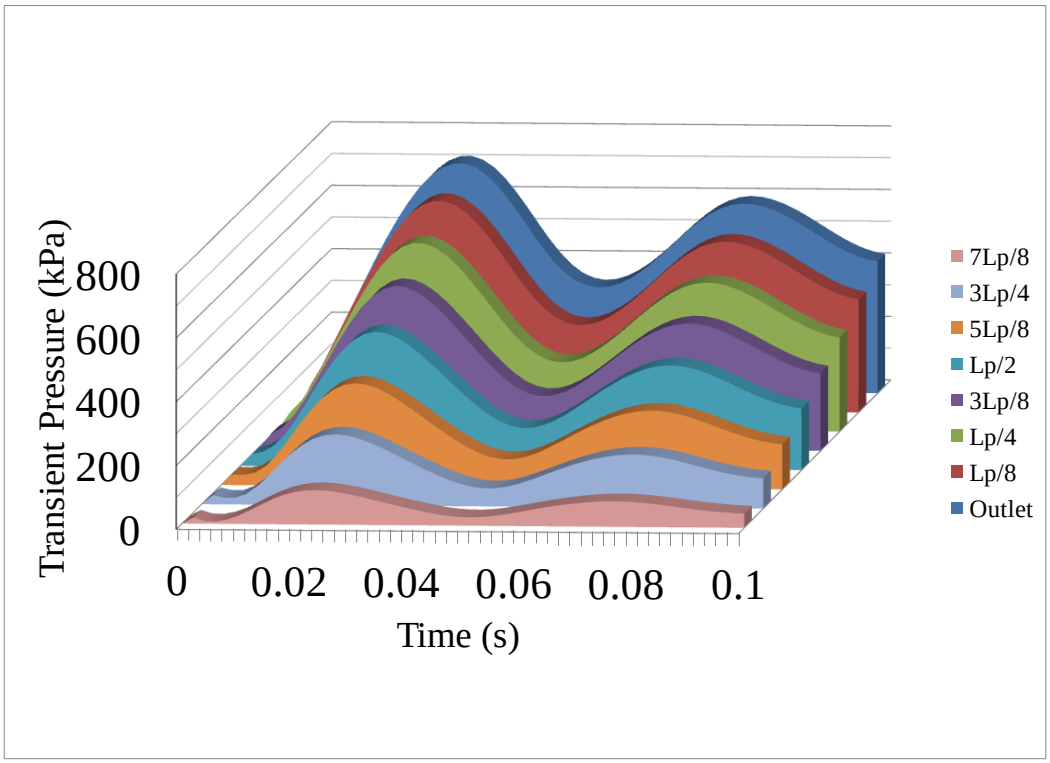

Figure 5. 15 - Evolution in time and space of the Transient Pressure for slow gate closure

5.4.2.2 Fluid and structural responses of water hammer at mid-span

Figure 5.16 shows the fluid and structural responses at mid-span section induced by a slow gate closure. These results will serve as a reference case for the parametric study presented in Chapter 6. Results are presented in absolute and relative forms. Except for relative velocities, each relative field value is computed by subtracting its respective absolute initial steady state value from its respective absolute transient value at the core of the penstock at mid-span. In contrast, the relative velocity is computed for each timestep by subtracting its absolute velocity at mid-span from its absolute velocity at the outlet.

Figure 5.16a shows that the absolute pressure takes the form of a damping oscillatory distribution with time and remains above the initial static pressure value since the gate remains in closing mode at the end of the duration. Due to the coarse timestep chosen in Section 5.2.4, one must recall that results used for the reference case underestimate the maximum transient pressure and overestimate the damping effect.

Similar to the rapid gate closure case, both hoop and longitudinal stresses are observed to be affected by the transient pressure. Figures 5.16e and 5.16f show that the hoop stress is synchronized with the transient pressure. Figures 5.16i and 5.16j shows that the longitudinal stress is affected by the Poisson's ratio coupling effect, as described in Section 5.4.1.2. Similar to the rapid gate closure, the longitudinal stress wave is approximately three times faster than the pressure wave.

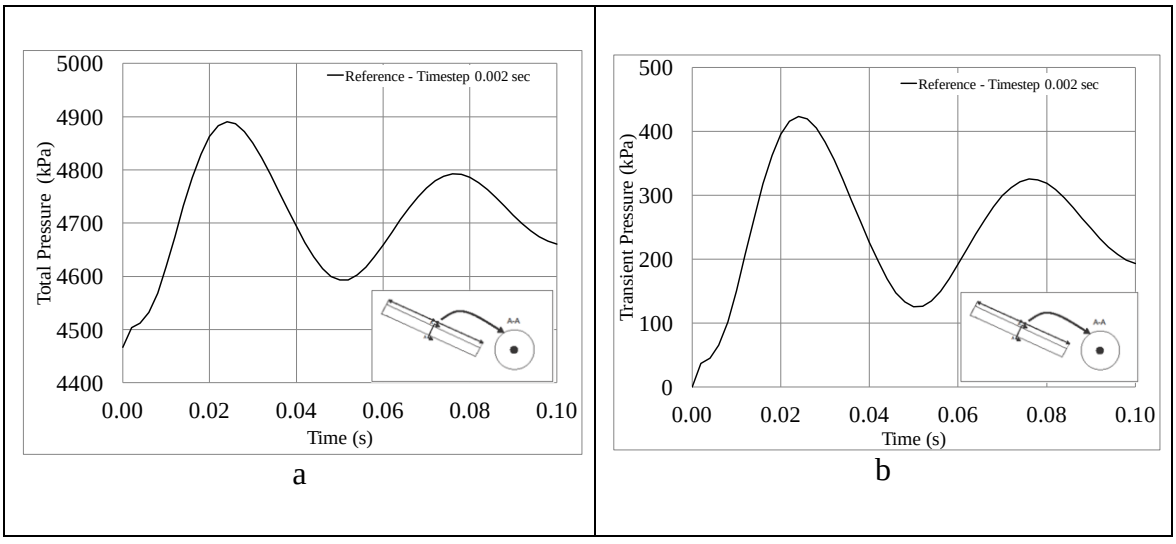

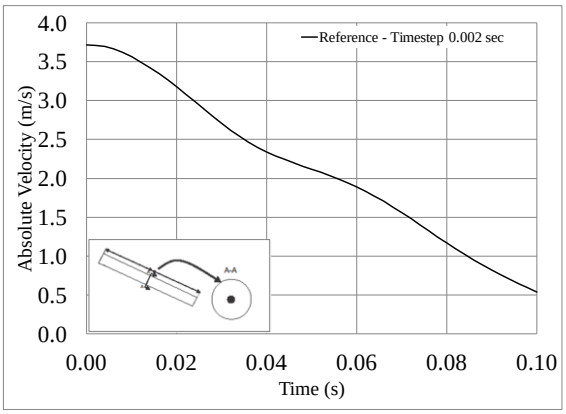
Reference - Timestep 0.002 sec
Absolute Velocity (m/s)
4.0
3.5
3.0
2.5
2.0
1.5
1.0
0.5
0.0
0.00
0.02
0.04
0.06
0.08
0.10
Time (s)

c

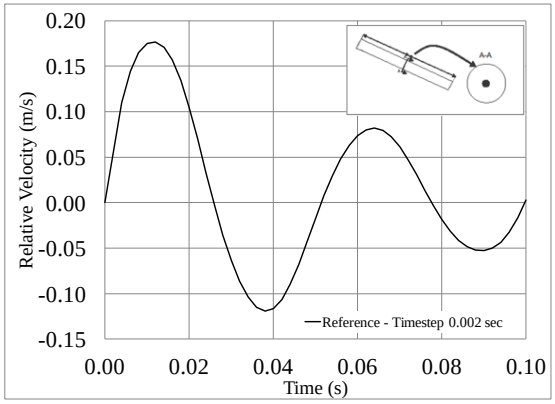
Reference - Timestep 0.002 sec
Relative Velocity (m/s)
0.20
0.15
0.10
0.05
0.00
-0.05
-0.10
-0.15
0.00
0.02
0.04
0.06
0.08
0.10
Time (s)

d

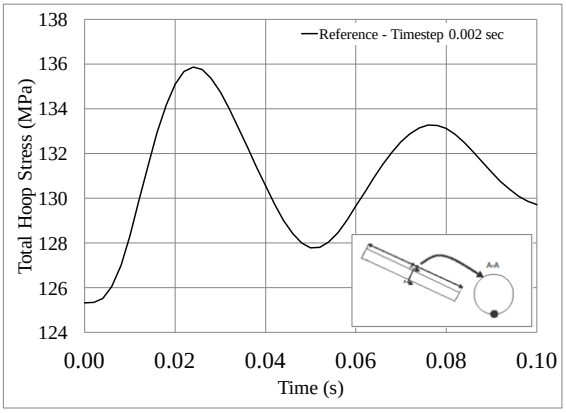
Reference - Timestep 0.002 sec
Total Hoop Stress (MPa)
138
136
134
132
130
128
126
124
0.00
0.02
0.04
0.06
0.08
0.10
Time (s)

e

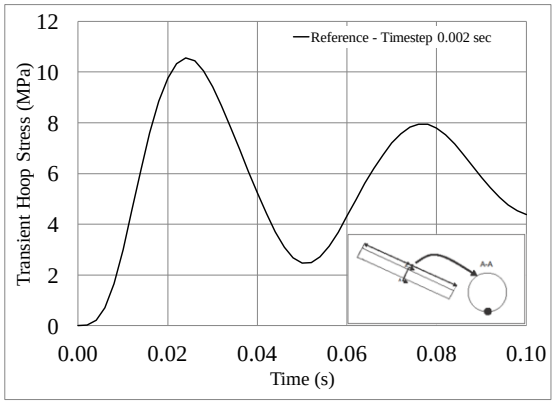
Reference - Timestep 0.002 sec
Transient Hoop Stress (MPa)
12
10
8
6
4
2
0
0.00
0.02
0.04
0.06
0.08
0.10
Time (s)

f

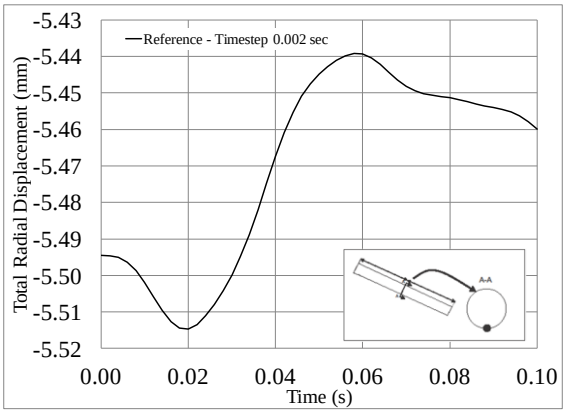
Reference - Timestep 0.002 sec
Total Radial Displacement (mm)
-5.43
-5.44
-5.45
-5.46
-5.47
-5.48
-5.49
-5.50
-5.51
-5.52
0.00
0.02
0.04
0.06
0.08
0.10
Time (s)

g

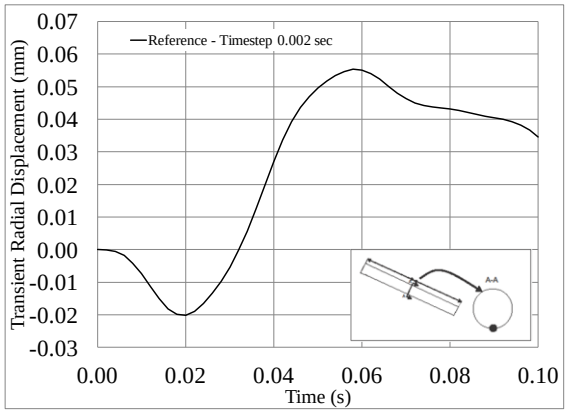
Reference - Timestep 0.002 sec
Transient Radial Displacement (mm)
0.07
0.06
0.05
0.04
0.03
0.02
0.01
0.00
-0.01
-0.02
-0.03
0.00
0.02
0.04
0.06
0.08
0.10
Time (s)

h

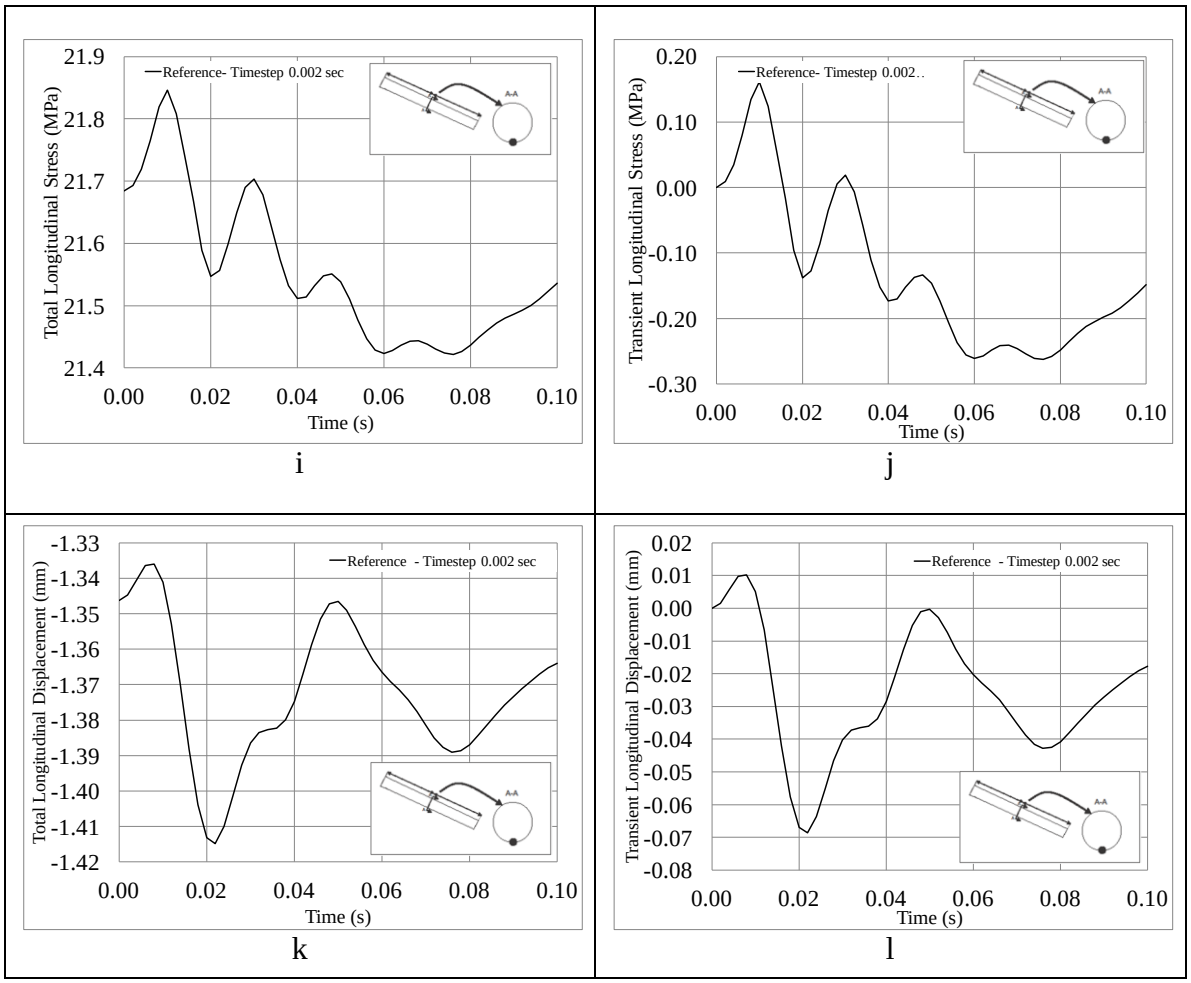

Figure 5. 16 - Temporal curves for a slow gate closure : (a) Total Pressure, (b) Transient Pressure (c) Absolute Velocity, (d) Relative Velocity (e) Absolute Hoop Stress, (f) Relative Hoop Stress, (g)Absolute Hoop Displacement, (h) Relative Hoop Displacement, (i) Absolute Longitudinal Stress, (j) Relative Longitudinal Stress, (k) Absolute Longitudinal Displacement, (l) Relative Longitudinal Displacement

5.4.2.3 Comparing pressure field results against arithmetic method predictions

In the same manner as Fig. 5.14, Fig. 5.17 shows the predictions of the arithmetic method overlaid on the FEM-FVM results already given in Fig. 5.2. The arithmetic method results were generated based on a 0.0005 sec. timestep. Figure 5.17 clearly shows that for the slow gate closure, the arithmetic method underestimates the transient pressure as predicted by the FEM-FVM method.

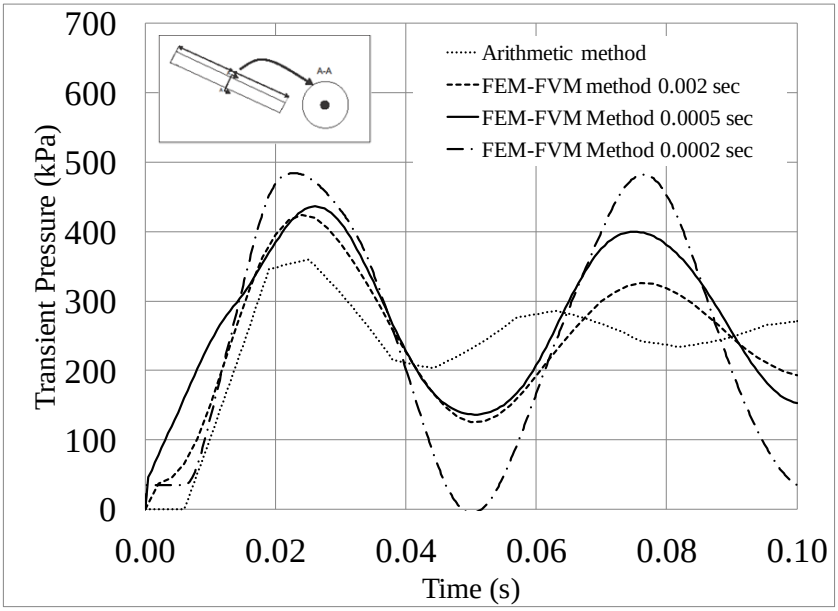

Figure 5. 17 - FEM-FVM method compared with the arithmetic method for the slow gate closure

A numeric comparison between the maximum transient pressure results based on both methods is provided in Table 5.6. All percentage of differences is based on the transient pressure value of the FEM-FVM method with a timestep of 0.0002 seconds. In the case of slow gate closure case, the arithmetic method is observed to underestimates the maximum transient pressure found with the FEM-FVM method by 25.6%.

Table 5. 6 - Comparing arithmetic method results to FEM-FVM results for slow gate closure

	Arithmetic Method	FEM-FVM Method Time Step 0.002 sec	FEM-FVM Method Time Step 0.005 sec	FEM-FVM Method Time Step 0.0002 sec
Absolute Value (kPa)	360	424	436	484
Percentage Difference (%)	-25.6%	-12.5%	-9.9%	0.00%

5.5 Conclusion

This chapter presented the fluid and structural results for slow and rapid gate closure models introduced in Chapter 4. Section 5.2 quantified proper input parameter values to run both models. This includes the gate closure and the simulation duration time. A sensitivity analysis was performed for different timesteps to determine a suitable time interval that strikes a balance between result accuracy and computation efficiency. Section 5.3 presented the fluid and structural results extracted from the steady-state FEM-FVM model. Structural results were found to be consistent with simple calculations based on the beam theory. Section 5.4 presented the transient fluid and structural results for both slow and rapid gate closure FEM-FVM models. A comparison was made between these results and the arithmetic method results. In the case of slow gate closure, the arithmetic method was observed to underestimate the maximum transient pressure predicted by the FEM-FVM method.

CHAPTER 6 – PARAMETRIC STUDY OF SIMPLY SUPPORTED ELEVATED PENSTOCK

6.1 Objectives

This chapter presents a parametric study based on the model developed in Chapter 4 for six different design parameters (pipe thickness, span, initial flow velocity, damping ratio, closure time, and vertical inclination angle). The reference case discussed in Chapter 5 is used as a basis from which parametric variations are made. For each design parameter, a high and a low parametric value were considered based on practical considerations. The high and low value for each design parameter are provided in Table 6.1. In a given parametric run, a single design parameter is varied from its value in the reference case while keeping the magnitude of all other variables identical to those of the reference case.

Table 6. 1 - Design parameter value changes in the parametric study

Design Parameters [y]	Thickness	Span	Initial Velocity	Damping Ratio	Closure Time	Angle
Unit	mm	m	m/s	%	s	°
Reference Value	19.05	15.384	3.570	10	0.1135	25.86
High Parametric Value	17.00	25.000	7.140	5	0.5540	15
Low Parametric Value	15.00	20.000	1.785	2	0.2270	0

Table 6.2 presents the input parameters for each parametric run conducted in the study. These include the pipe internal diameter D_p, thickness e, span L_p, initial velocity V_0, and closure time T .The corresponding dimensionless ratios are also provided. These are the inclination angle α, damping ratio ξ, diameter to thickness ratio D_p / e, span/diameter ratio L_p / D_p and $V_0 T / L_p$.

Table 6. 2 - Input parameters and dimensionless ratios for the parametric runs

	Ref. Case	Thickness		Span		Initial Flow		Damping		Closure Time		Angle	
		Run 1	Run 2	Run 3	Run 4	Run 5	Run 6	Run 7	Run 8	Run 9	Run 10	Run 11	Run 12
Diameter (m)	1.067	1.067	1.067	1.067	1.067	1.067	1.067	1.067	1.067	1.067	1.067	1.067	1.067
Thickness (mm)	19.05	17.00	15.00	19.05	19.05	19.05	19.05	19.05	19.05	19.05	19.05	19.05	19.05
Length (m)	15.38	15.38	15.384	20.000	25.000	15.38	15.38	15.38	15.384	15.38	15.38	15.38	15.38
Initial Velocity (m/s)	3.570	3.570	3.570	3.570	3.570	1.785	7.140	3.570	3.570	3.570	3.570	3.570	3.570
Closure Time (s)	0.114	0.1135	0.1135	0.1135	0.1135	0.1135	0.1135	0.1135	0.1135	0.2270	0.5540	0.1135	0.1135
Angle (°)	25.86	25.86	25.86	25.86	25.86	25.86	25.86	25.86	25.86	25.86	25.86	15.00	0.00
Damping Ratio (%)	10	10	10	10	10	10	10	5	2	10	10	10	10
D_p/e	56.01	62.76	71.13	56.01	56.01	56.01	56.01	56.01	56.01	56.01	56.01	56.01	56.01
L_p/D_p	14.42	14.42	14.42	18.74	23.43	14.42	14.42	14.42	14.42	14.42	14.42	14.42	14.42
$(V_0xT)/L_p$	0.0263	0.0263	0.0263	0.0203	0.0162	0.0132	0.0527	0.0263	0.0263	0.0527	0.1286	0.0263	0.0263

When comparing results, the magnitude of a fluid and structural output field O corresponding to a variation input design parameter I (listed in Table 6.1) compared to its value in the reference case R is quantified using a variation criterion $\Psi_R(I,O)$ of the output parameter O induced by a parametric variation of input parameter I :

$$\Psi_R(I,O) = \frac{\Psi(I,O) - \Psi(R,O)}{\Psi(R,O)} \tag{6.1}$$

In Eq. 6.1, the output variables O are the pressure (p), the hoop stress (σ_h), the radial displacement (u), the longitudinal stress (σ_l) and the longitudinal displacement (v). Also, $\Psi(I,O)$ denotes the value of output field O based on an input parameter I value different from the reference case (based on a parametric run) and $\Psi_R(I,O)$ denotes the value of output field O based on the reference case. Recalling that for a given field, two variations were considered for each input parameter, Eq. 6.1 can be applied for both values. A large magnitude of the variation denotes a stronger impact of the design parameter on the output.

6.2 Effect of Thickness

Section 6.2 presents the effect of the thickness on the fluid and structural fields between 0.0 and 0.1 seconds. The thickness of the reference model (19.05 mm) is compared with two thickness variations (15 and 17 mm) to simulate various corrosion scenarios throughout the lifetime of the pipe.

6.2.1 Results and Discussion

The initial field values in Figs 6.1a-d indicate that the pipe thickness has no effect on the fluid steady-state results. The total pressure, transient pressure, absolute and relative velocity values have the same value for all thickness variations. In contrast, in the transient regime, pipe thickness is observed to have a rather minor effect on the pressure and velocity. As the pipe wall decreases, the amplitude and period of transient pressure and relative velocity are observed to increase.

The pipe thickness is observed to have a greater effect on the structural response than on the fluid fields. In the steady-state regime, pipe thickness is observed to impact the stress and displacement fields within the pipe wall. Figure 6.1e shows that the hoop stress decreases as the pipe thickness increases. Comparisons in Table 6.2 show that the numerical solution for each thickness, is within 0.32% of the classical solution calculated from $\sigma_h = P_s g \rho_w D_p / 2e$. As with the hoop stress, Fig. 6.1i shows that the longitudinal stress increases as the pipe thickness decreases. For comparison, the longitudinal stress is calculated from the beam theory as presented in Section 3.3.4.1. Table 6.3 shows that the percentage difference between the classical and numerical solution for the longitudinal stress increases as the thickness decreases. The steady-state radial displacements obtained from the FEM-FVM results are shown in Fig. 6.1g. They are compared in Table 6.3 to the classical solution calculated from the sum of the deflection $\delta_{max} = 5 w_b L_p{}^4 / 384 E I_p$ and the hoop displacement $\hbar = r_i (\sigma_h - \mu \sigma_b) / E$. Very good agreement is observed between the classical and numerical results where the maximum percentage difference is less than 6.07%.

Table 6. 3 - Comparison between Steady-State Classical and Numerical Solutions for different thicknesses

	Thickness (mm)	Classical Solution [1]	Numerical Solution [2]	Percentage Difference ([1]-[2])/[2]
Hoop Stress (MPa)	19.05 (Ref.)	125.1	125.3	-0.16%
	17.00	140.2	140.2	0.00%
	15.00	158.8	158.3	0.32%
Longitudinal Stress (MPa)	19.05 (Ref.)	22.97	21.68	5.95%
	17.00	25.74	23.45	9.77%
	15.00	29.18	25.68	13.6%
Radial Displacement (mm)	19.05 (Ref.)	-5.161	-5.494	-6.07%
	17.00	-5.744	-5.931	-3.15%
	15.00	-6.461	-6.483	-0.33%

In the transient regime, pipe thickness is observed to affect the structural fields as well. Figure 6.1f shows that as the pipe thickness decreases, the magnitude of the transient hoop stress increases. For the lowest thickness (15mm), the hoop stress due to transient pressure reaches a maximum value of 14.00 MPa (Table 6.4) that is to be added to the steady-state hoop stress of 158.3 MPa (Table 6.3). Table 6.4 shows that the classical solution systematically overestimates the transient hoop stress compared to the numerical solution. Figure 6.1j shows that the thickness change has a rather negligible effect on the magnitude of the transient longitudinal stress. Transient radial displacement in Fig. 6.1h is taken positive when the pipe expands. It shows that as the pipe thickness decreases, the amplitude of the transient radial displacement increases. However, as seen in Chapter 5 and as shown on Fig. 6.1g, the transient radial displacement is relatively small compared to the steady-state radial displacement.

Table 6. 4 - Classical versus Numerical predictions of Maximum Transient Hoop Stress for different thicknesses

	Thickness (mm)	Classical Solution [1]	Numerical Solution [2]	Percentage Difference ([1]-[2])/[2]
Transient Hoop Stress (MPa)	19.05 (Ref.)	11.87	10.55	12.5%
	17.00	13.49	12.30	9.67%
	15.00	15.35	14.00	9.64%

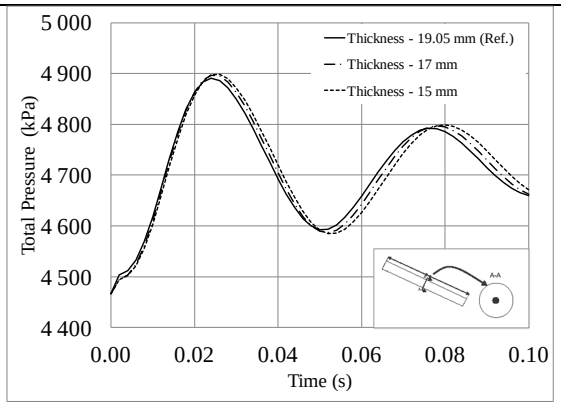
Thickness - 19.05 mm (Ref.)
Thickness - 17 mm
Thickness - 15 mm
Total Pressure (kPa)
5 000
4 900
4 800
4 700
4 600
4 500
4 400
0.00
0.02
0.04
0.06
0.08
0.10
Time (s)

a

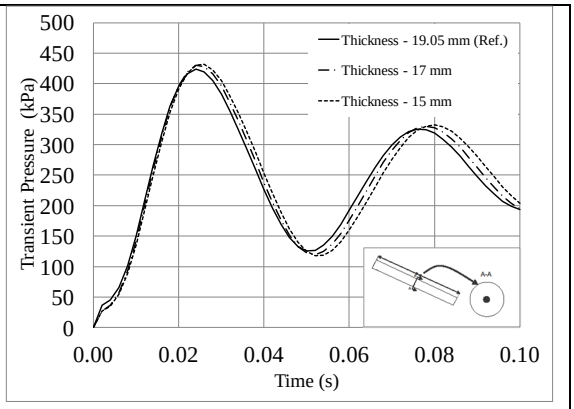
Thickness - 19.05 mm (Ref.)
Thickness - 17 mm
Thickness - 15 mm
Transient Pressure (kPa)
500
450
400
350
300
250
200
150
100
50
0
0.00
0.02
0.04
0.06
0.08
0.10
Time (s)

b

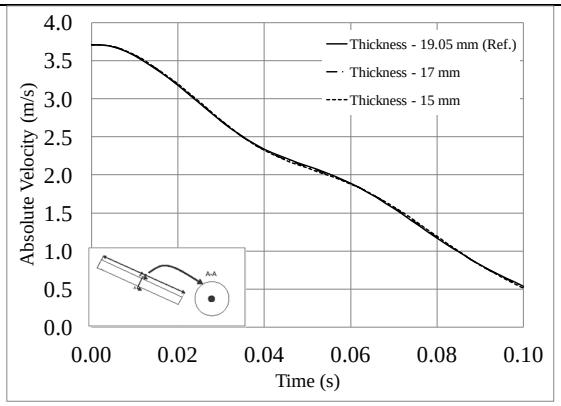
Thickness - 19.05 mm (Ref.)
Thickness - 17 mm
Thickness - 15 mm
Absolute Velocity (m/s)
4.0
3.5
3.0
2.5
2.0
1.5
1.0
0.5
0.0
0.00
0.02
0.04
0.06
0.08
0.10
Time (s)

c

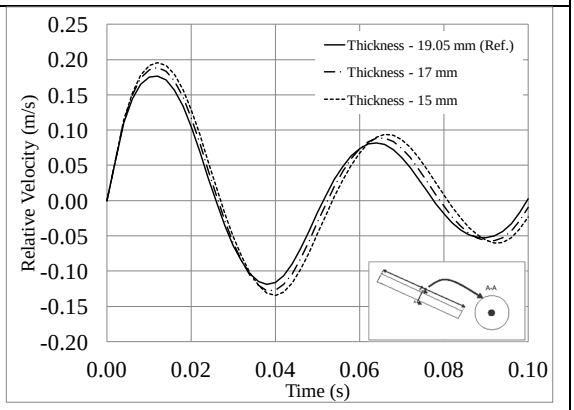
Thickness - 19.05 mm (Ref.)
Thickness - 17 mm
Thickness - 15 mm
Relative Velocity (m/s)
0.25
0.20
0.15
0.10
0.05
0.00
-0.05
-0.10
-0.15
-0.20
0.00
0.02
0.04
0.06
0.08
0.10
Time (s)

d

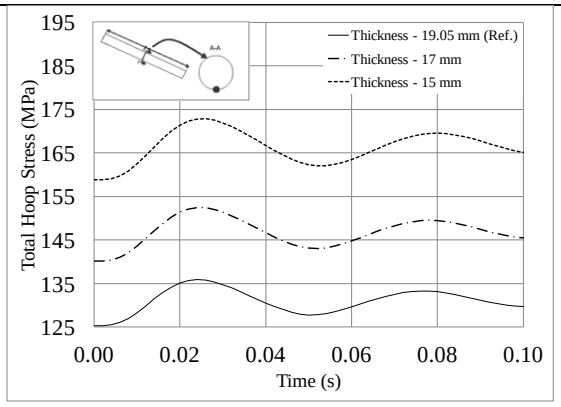
Thickness - 19.05 mm (Ref.)
Thickness - 17 mm
Thickness - 15 mm
Total Hoop Stress (MPa)
195
185
175
165
155
145
135
125
0.00
0.02
0.04
0.06
0.08
0.10
Time (s)

e

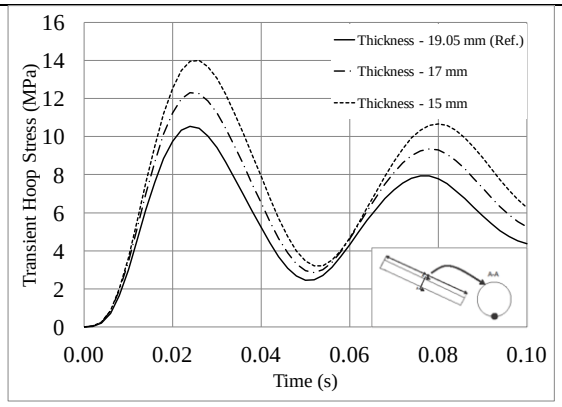
Thickness - 19.05 mm (Ref.)
Thickness - 17 mm
Thickness - 15 mm
Transient Hoop Stress (MPa)
16
14
12
10
8
6
4
2
0
0.00
0.02
0.04
0.06
0.08
0.10
Time (s)

f

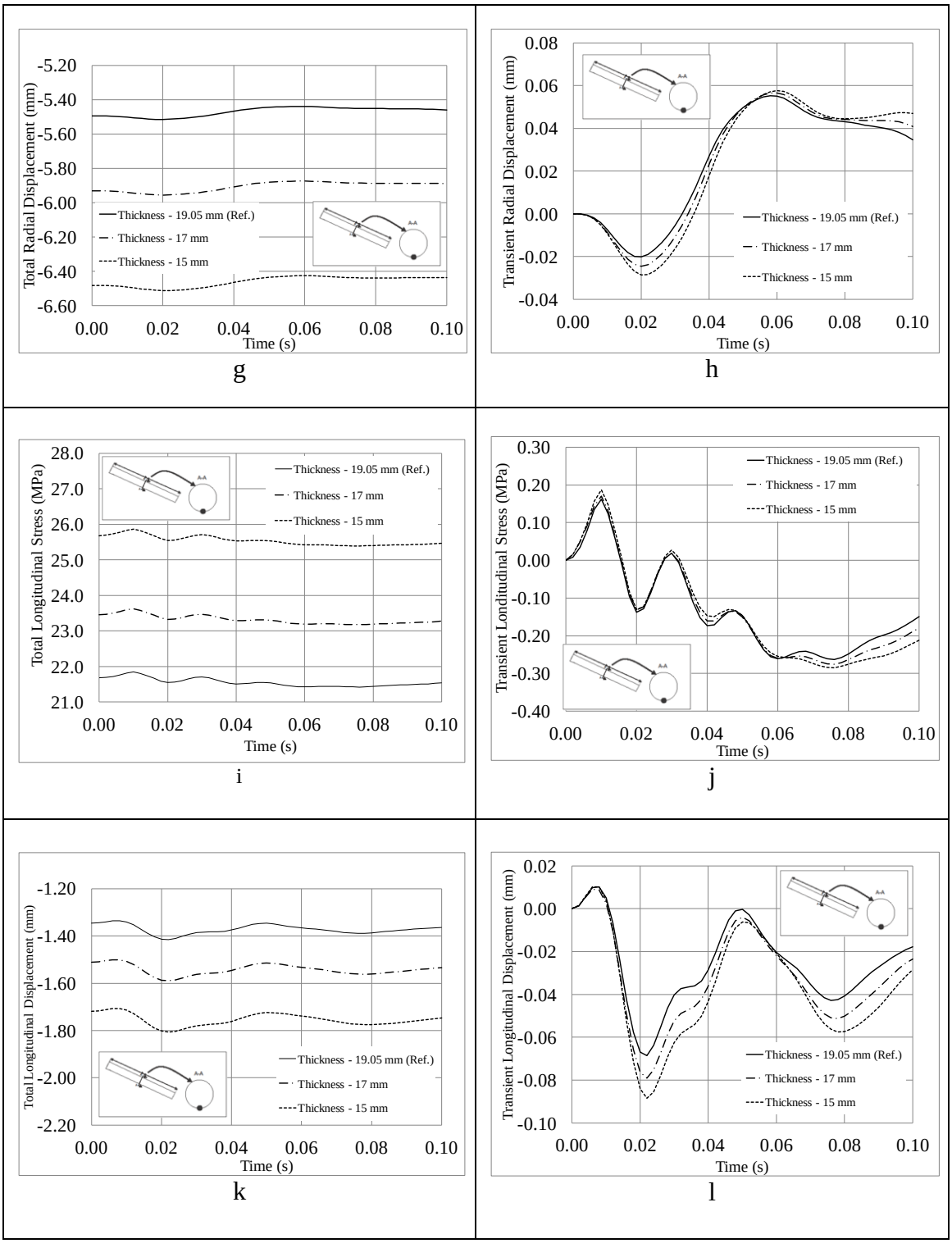

Figure 6. 1 - Thickness comparison for : (a) Total Pressure, (b) Transient Pressure, (c) Absolute Velocity, (d) Relative Velocity, (e) Total Hoop Stress, (f) Transient Hoop Stress, (g) Total Hoop Displacement, (h) Transient Hoop Displacement, (i) Total Longitudinal Stress, (j) Transient Longitudinal Stress, (k) Total Longitudinal Displacement, (l) Transient Longitudinal Displacement

6.2.2 Sensitivity of Results to the Thickness

Table 6.5 ranks the fields from the most sensitive (Longitudinal Displacement) to the least sensitive (Pressure) for steady state and Table 6.6 ranks the fields from the most sensitive (Radial Displacement) to the least sensitive (Pressure). A rank based on the total response (Steady state + Transient) is also provided in Table 6.7 where the longitudinal displacement is observed to be the most sensitive field and the pressure is the least. The sensitivity of each field is assessed based on the variation parameter introduced in Eq. 6.1 from their value in the reference case.

The longitudinal displacement is observed to be impacted the most by the thickness in the steady state with maximum variation of 27.6%. Hoop stress comes in second with 26.3% followed by the longitudinal stress and radial displacement in third.

In the transient state, the radial displacement is observed to be impacted the most with maximum variation of 41.38%. Hoop stress comes in second with 32.1% followed by both longitudinal displacement and stress. It is observed that the change in the magnitude of the longitudinal stress and displacement in the transient state is caused by the Poisson effect as explained in Section 5.4.1.2.

Close variations results of total response to that of steady-state response show that the transient state response has a minor impact on the steady-state response. The field rank for the total response is the same as the steady state response. The longitudinal displacement is impacted the most by the thickness with maximum variation of 27.7%. Hoop stress comes in second with 26.8 % followed by the longitudinal stress and radial displacement in third.

The pressure remains essentially unchanged for the three thicknesses considered. The pressure is barely affected by the thickness change. A small change in the transient pressure is caused by fluid-structure interaction. A thinner pipe wall is observed to cause a slightly higher transient pressure.

Table 6. 5 - Sensitivity of Numerical Results to the Thickness on Steady-State Fields

		Longitudinal Displacement		Hoop Stress		Longitudinal Stress		Radial Displacement		Pressure	
		Magnitude v (mm)	$\Psi_R(e,v)$	Magnitude σ_h (MPa)	$\Psi_R(e,\sigma_h)$	Magnitude σ_l (MPa)	$\Psi_R(e,\sigma_l)$	Magnitude u (mm)	$\Psi_R(e,u)$	Magnitude p (kPa)	$\Psi_R(e,p)$
Steady-State Results	19.05 mm (Ref.)	-1.346	-	125.3	-	21.68	-	-5.494	-	4467	-
	17.00 mm	-1.511	12.2%	140.2	11.9%	23.45	8.16%	-5.931	7.94%	4467	0.00%
	15.00 mm	-1.718	27.6%	158.3	26.3%	25.68	18.5%	-6.483	18.0%	4467	0.00%

Table 6. 6 - Sensitivity of Numerical Results to the Thickness on Transient Fields

		Radial Displacement		Hoop Stress		Longitudinal Displacement		Longitudinal Stress		Pressure	
		Magnitude u (mm)	$\Psi_R(e,u)$	Magnitude σ_h (MPa)	$\Psi_R(e,\sigma_h)$	Magnitude v (mm)	$\Psi_R(e,v)$	Magnitude σ_l (MPa)	$\Psi_R(e,\sigma_l)$	Magnitude p (kPa)	$\Psi_R(e,p)$
Maximum Transient Results	19.05 mm (Ref.)	-0.020	-	10.60	-	-0.069	-	0.161	-	423.7	-
	17.00 mm	-0.025	21.55%	12.30	16.0%	-0.079	15.5%	0.170	5.59%	429.9	1.46%
	15.00 mm	-0.029	41.38%	14.00	32.1%	-0.088	28.9%	0.187	16.1%	431.5	1.84%

Table 6. 7 - Sensitivity of Numerical Results to the Thickness on Total Fields

		Longitudinal Displacement		Hoop Stress		Longitudinal Stress		Radial Displacement		Pressure	
		Magnitude v (mm)	$\Psi_R(e,v)$	Magnitude σ_h (MPa)	$\Psi_R(e,\sigma_h)$	Magnitude σ_l (MPa)	$\Psi_R(e,\sigma_l)$	Magnitude u (mm)	$\Psi_R(e,u)$	Magnitude p (kPa)	$\Psi_R(e,p)$
Total Results	19.05 mm (Ref.)	-1.415	-	135.9	-	21.84	-	-5.515	-	4891	-
	17.00 mm	-1.590	12.4%	152.5	12.2%	23.62	8.15%	-5.955	7.99%	4897	0.13%
	15.00 mm	-1.806	27.7%	172.3	26.8%	25.87	18.4%	-6.511	18.1%	4899	0.16%

6.3 Effect of the Span

Section 6.3 presents the effect of the span on the fluid and structural transient results between 0.0 and 0.1 seconds. The results based on the span of the reference case (15.384 m) are compared with two span variations (20 m and 25 m).

6.3.1 Results and Discussion

The initial field values in Figs 6.2 a-d indicate that the pipe span has no effect on the fluid steady-state results. The total pressure, transient pressure, absolute and relative velocity values have the same initial values for all spans considered. In the transient regime, the transient pressure increases with the span. According to the rigid water column theory (Eqs. 2.21, 2.22), the transient pressure is proportional to the pipe span. In Table 6.8, transient pressure results as calculated by the rigid water column theory based on the reference transient pressure (423.7 kPa) are provided in Column [1] and compared to numerical results in Column [2]. Column [3] provides the percentage differences. The comparison suggests that the transient pressure as numerically predicted is nearly linearly proportional to the span. In contrast to the rigid water column method, the FEM-FVM method considers water compressible, pipe elasticity and the fluid-structure interaction. These differences explain the fact that the rigid water column theory slightly underestimates the transient pressure compared to that predicted by the numerical solution.

Table 6. 8 - Rigid Water Column Theory versus Numerical predictions of Maximum Transient Pressure for different spans

	Span (m)	Rigid Water Column Theory [1]	Numerical Solution [2]	Percentage Difference ([1]-[2])/[2]
Transient Pressure (kPa)	15.384 (Ref.)	-	423.7	-
	20.000	550.8	570.7	-3.48%
	25.000	688.5	724.6	-4.98%

In the steady-state regime, pipe span is observed to impact the stress and displacement fields within the pipe wall. Figure 6.2e shows that the initial hoop stress is essentially insensitive to the pipe span with variations less than 2% in all three cases considered.

Figure 6.2i shows that the longitudinal stress increases as the pipe span increases. For comparison, the longitudinal stress is calculated from the beam theory as presented in Section 3.3.4.1. Table 6.9 shows that the absolute percentage difference between the classical and numerical solution increases as the span increases, a direct result for the increased bending moment with the penstock span. It also shows that as the span increases, the classical solution tends to underestimate the longitudinal stress as predicted by the numerical solution. This underestimation could be attributed to the ovalization effect. In a long pipe, the pipe is subjected to higher longitudinal stresses, which cause more ovalization than in shorter span pipes. The ovalized cross-section has a lower moment of inertia than that of a perfect circular cross-section as assumed in the classical solution. Figure 6.2 g and Table 6.9 show that the steady-state radial displacements largely increase as the span increases.

Table 6. 9 - Comparison between Steady-State Classical and Numerical Solutions for different spans

	Span (m)	Classical Solution [1]	Numerical Solution [2]	Percentage Difference ([1]-[2])/[2]
Hoop Stress (MPa)	15.384 (Ref.)	125.1	125.3	-0.16%
	20.000	125.1	126.1	-0.79%
	25.000	125.1	127.5	-1.88%
Longitudinal Stress (MPa)	15.384 (Ref.)	22.97	21.68	5.95%
	20.000	38.82	41.60	-6.68%
	25.000	60.66	70.71	-14.2%
Radial Displacement (mm)	15.384 (Ref.)	-4.720	-5.178	-8.84%
	20.000	-13.48	-16.87	-20.1%
	25.000	-32.92	-44.60	-26.2%

In the transient regime, pipe span is observed to affect the structural fields as well. Figure 6.2f shows that as the pipe span increases, the magnitude of the transient hoop stress increases. For the longest span considered (25 m), the hoop stress reaches a maximum value of 21.96 MPa (Table 6.10) which is to be added to the steady-state hoop stress of 127.5 MPa (Table 6.9). Table 6.10 compares the transient hoop stress classical solution calculated from $\sigma_h = H_o g \rho_w D_p / 2e$ with the transient hoop stress numerical solution. The percentage difference between the values starts from 12.5% for a pipe span of 15.384 m, decreases to 9.38% for a pipe span of 20 m and increases to -7.60% for a pipe span of

25m. The classical solution slightly overestimates the results based on the numerical solution for the reference pipe span of 15.384 m. As the span increases, ovalization reduces the percentage difference until the classical solution underestimates the results based on the numerical solution for a pipe span of 25 m. Figure 6.2j shows that the span has a small influence on the magnitude of the longitudinal stresses. Figure 6.2h and 6.2l show that as the pipe span increases, the amplitude of the radial and longitudinal displacement increases.

Table 6. 10 - Classical versus Numerical predictions of Maximum Transient Hoop Stress for different spans

	Span (m)	Classical Solution [1]	Numerical Solution [2]	Percentage Difference ([1]-[2])/[2]
Transient Hoop Stress (MPa)	15.384 (Ref.)	11.87	10.55	12.5%
	20.000	15.98	14.61	9.38%
	25.000	20.29	21.96	-7.60%

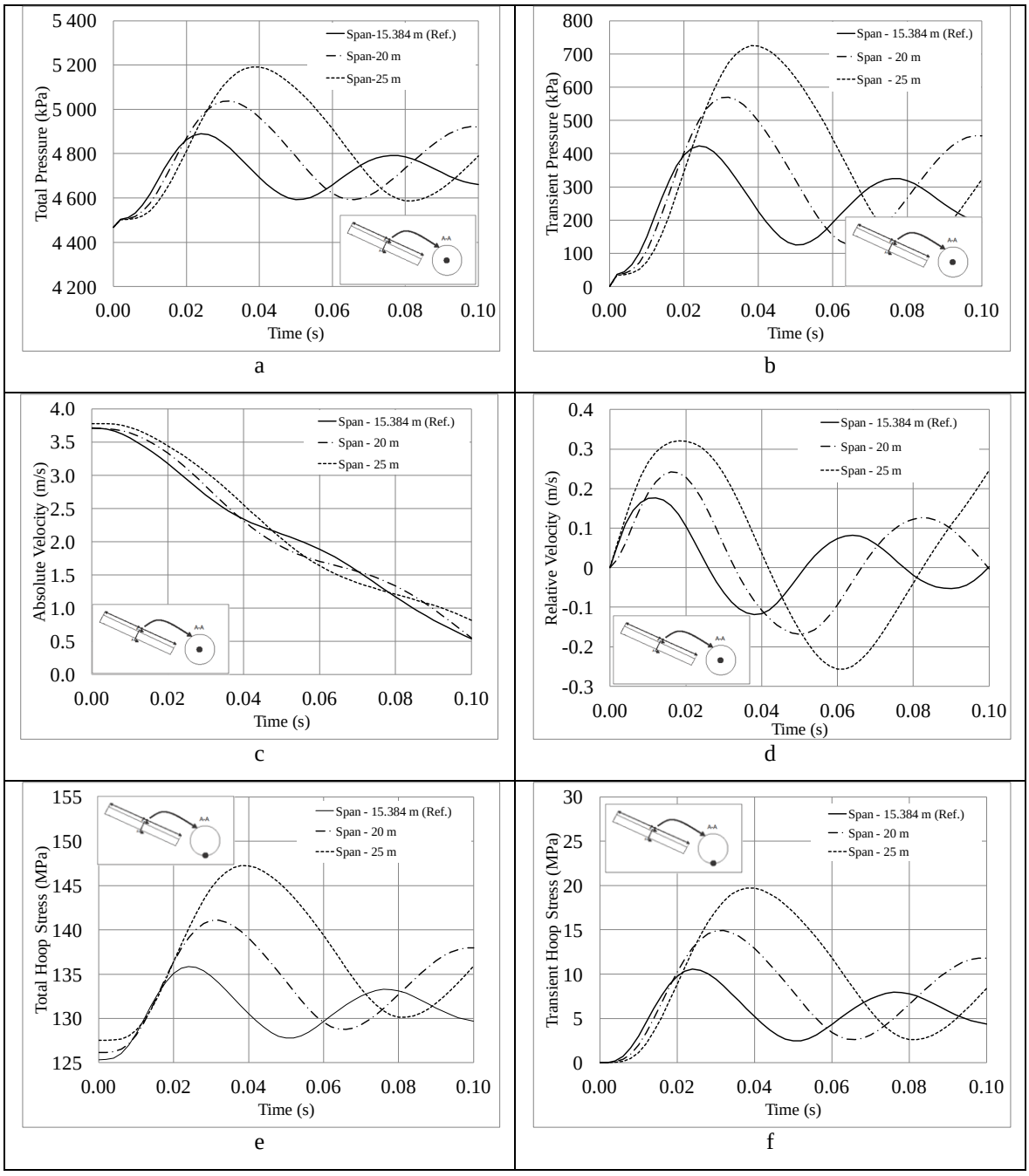
Total Pressure (kPa)
Span-15.384 m (Ref.)
Span-20 m
Span-25 m
Time (s)
a
Transient Pressure (kPa)
Span - 15.384 m (Ref.)
Span - 20 m
Span - 25 m
Time (s)
b
Absolute Velocity (m/s)
Span - 15.384 m (Ref.)
Span - 20 m
Span - 25 m
Time (s)
c
Relative Velocity (m/s)
Span - 15.384 m (Ref.)
Span - 20 m
Span - 25 m
Time (s)
d
Total Hoop Stress (MPa)
Span - 15.384 m (Ref.)
Span - 20 m
Span - 25 m
Time (s)
e
Transient Hoop Stress (MPa)
Span - 15.384 m (Ref.)
Span - 20 m
Span - 25 m
Time (s)
f

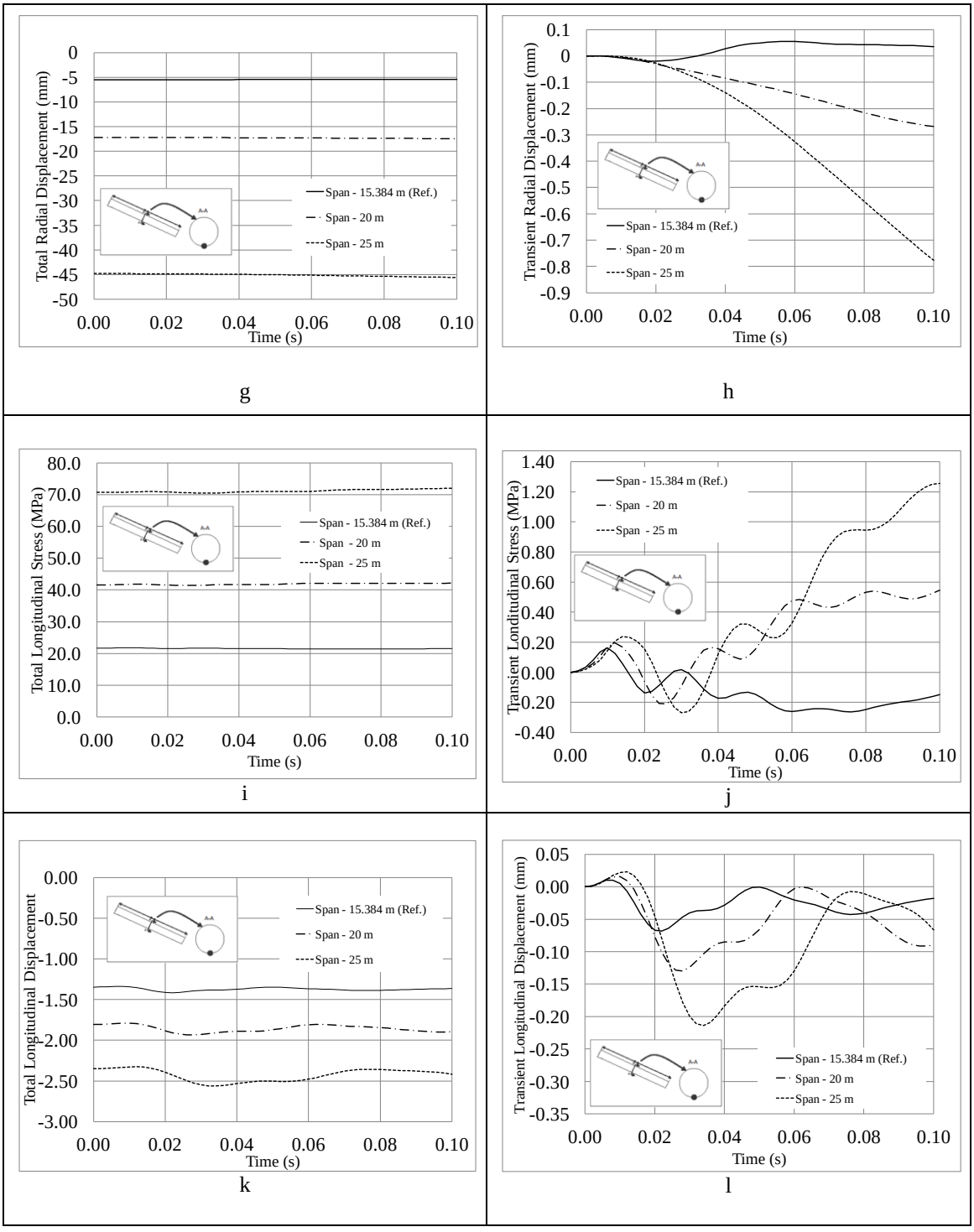

Figure 6. 2 - Span comparison for : (a) Total Pressure, (b) Transient Pressure, (c) Absolute Velocity, (d) Relative Velocity, (e) Total Hoop Stress, (f) Transient Hoop Stress, (g) Total Hoop Displacement, (h) Transient Hoop Displacement, (i) Total Longitudinal Stress, (j) Transient Longitudinal Stress, (k) Total Longitudinal Displacement, (l) Transient Longitudinal Displacement

6.3.2 Analyzing the Effect of the Span

Table 6.11 ranks the fields from the most sensitive (radial displacement) to the least sensitive (pressure) for steady state, transient state and total numerical solution. The sensitivity of each field is assessed based on the variation parameter introduced in Eq. 6.1 from their value in the reference case.

The radial displacement is the field that is impacted the most by the span, with a maximum variation value of 716% for steady state analysis and 3754% for the maximum transient analysis. These correspond to a total variation (based on steady state + maximum transient effects) of 727%. Longitudinal stresses come second with a total variation of 229% and longitudinal displacement come third with a total variation of 81.1%. The total hoop stresses and pressure are 7.32% and 6.15% respectively. They are observed to be slightly affected by the span in spite of being greatly impact within the transient state.

Although the variation in total hoop stresses is not as high as that of the longitudinal stresses, its magnitude remains higher and remains more significant from an engineering point of view.

Table 6. 11 - Sensitivity of Numerical Results to the span

		Radial Displacement		Longitudinal Stress		Longitudinal Displacement		Hoop Stress		Pressure	
		Magnitude u (mm)	$\Psi_R(L_p,u)$	Magnitude σ_l (MPa)	$\Psi_R(L_p,\sigma_l)$	Magnitude v (mm)	$\Psi_R(L_p,v)$	Magnitude σ_h (MPa)	$\Psi_R(L_p,\sigma_h)$	Magnitude p (kPa)	$\Psi_R(L_p,p)$
Steady-State Results	15.384 m (Ref.)	-5.494	-	21.68	-	-1.346	-	125.3	-	4467	-
	20.000 m	-17.17	213%	41.60	91.8%	-1.806	34.1%	124.8	-0.40%	4467	0.00%
	25.000 m	-44.81	716%	70.71	226%	-2.349	74.5%	123.8	-1.17%	4467	0.00%
Maximum Transient Results	15.384 m (Ref.)	-0.020	-	0.162	-	-0.069	-	10.55	-	423.7	-
	20.000 m	-0.268	1231%	0.546	237%	-0.130	89.8%	14.61	38.5%	570.7	34.7%
	25.000 m	-0.777	3754%	1.256	675%	-0.214	212%	21.96	108%	724.6	71.0%
Total Results	15.384 m (Ref.)	-5.515	-	21.85	-	-1.415	-	135.9	-	4891	-
	20.000 m	-17.44	216%	42.15	92.9%	-1.936	36.8%	139.4	2.62%	5038	3.01%
	25.000 m	-45.59	727%	71.97	229%	-2.563	81.1%	145.8	7.32%	5192	6.15%

6.4 Effect of the Initial Flow Velocity

Section 6.4 presents the effect of the initial flow velocity on the fluid and structural transient results between 0.0 and 0.1 seconds. The results based on the initial flow velocity of the reference case (3.57 m/s) are compared with two initial flow velocity variations (1.785 m/s and 7.14 m/s).

6.4.1 Results and Discussion

The initial field values in Figs 6.3 a-b indicate that the initial flow velocity has essentially no effect on the steady-state pressure results. In the transient state, however, variations in transient pressure and relative velocity are observed to vary with the initial flow velocity. It is observed that the period of pressure and velocity do not depend on the initial flow velocity. According to the rigid water column theory (Eqs. 2.21, 2.22), the transient pressure is proportional to the initial flow velocity. In Table 6.12, transient pressure results, as calculated by the rigid water column theory based on the reference transient pressure (423.7 kPa), are provided in Column [1] and compared to numerical results in Column [2]. Column [3] provides the percentage differences. The comparison suggests that the numerically predicted transient pressure is nearly linearly proportional to the initial flow velocity. The aforementioned table shows that the rigid water column theory slightly over predicts the maximum transient pressure compared to the numerical solution.

Table 6. 12 - Rigid Water Column Theory versus Numerical predictions of Maximum Transient Pressure for different initial velocity

	Initial Velocity (m/s)	Rigid Water Column Theory [1]	Numerical Solution [2]	Percentage Difference ([1]-[2])/[2]
Transient Pressure (kPa)	3.570 (Ref.)	-	423.7	-
	1.785	211.9	201.8	4.98%
	7.140	847.3	870.6	-2.67%

In the steady-state regime, the initial flow velocity is observed to slightly impact the stress and displacement fields within the pipe wall. Figure 6.3e shows that the hoop stresses are essentially insensitive to the initial flow velocity, with variations less than 0.30% in all three cases considered. Unlike hoop stresses, Figure 6.3i and Table 6.13

show that the longitudinal stresses decrease as the initial flow velocity decreases. As with the hoop stresses, Figure 6.3g and Table 6.13 show that the radial displacement increases as the initial flow velocity decreases.

Table 6. 13 - Comparison between Steady-State Classical and Numerical Solutions for different initial velocities

	Initial Velocity (m/s)	Classical Solution [1]	Numerical Solution [2]	Percentage Difference ([1]-[2])/[2]
Hoop Stress (MPa)	3.570 (Ref.)	125.1	125.3	-0.18%
	1.785	125.1	125.5	-0.29%
	7.140	125.1	124.7	0.28%
Longitudinal Stress (MPa)	3.570 (Ref.)	22.97	21.68	5.95%
	1.785	22.97	21.67	6.00%
	7.140	22.97	21.71	5.80%
Radial Displacement (mm)	3.570 (Ref.)	-5.161	-5.177	-0.32%
	1.785	-5.161	-5.177	-0.31%
	7.140	-5.161	-5.179	-0.35%

In the transient regime, the initial flow velocity is observed to affect the structural fields as well**.** The magnitude of every structural field (Figs 6.3f-l) increases as the initial flow velocity increases. Figure 6.3f shows that for the highest initial flow velocity (7.140 m/s), the hoop stress due to transient pressure reaches a maximum value of 22.84 MPa (Table 6.14) which is to be added to the steady-state hoop stress of 124.7 MPa (Table 6.13). Table 6.14 shows that the classical solution systematically overestimates the transient hoop stress over the numerical solution.

Table 6. 14 - Classical versus Numerical predictions of Maximum Transient Hoop Stress for different initial velocities

	Initial Velocity (m/s)	Classical Solution [1]	Numerical Solution [2]	Percentage Difference ([1]-[2])/[2]
Transient Hoop Stress (MPa)	3.570 (Ref.)	12.51	10.55	18.6%
	1.785	5.650	4.500	25.6%
	7.140	24.38	22.84	6.76%

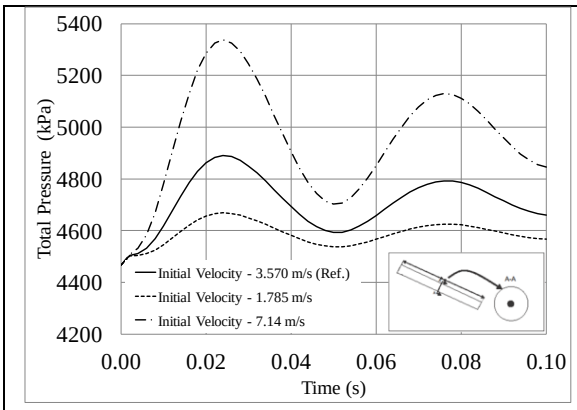
Total Pressure (kPa)
5400
5200
5000
4800
4600
4400
4200
0.00
0.02
0.04
0.06
0.08
0.10
Time (s)
Initial Velocity - 3.570 m/s (Ref.)
Initial Velocity - 1.785 m/s
Initial Velocity - 7.14 m/s

a

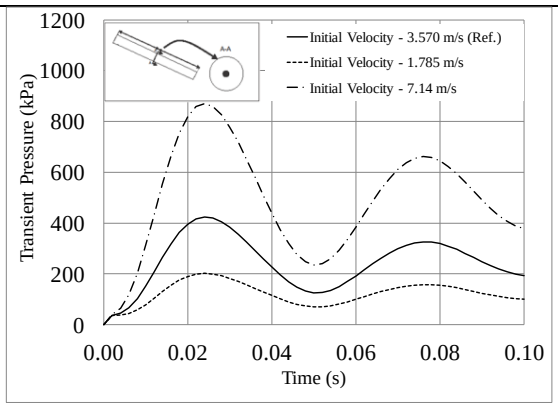
Transient Pressure (kPa)
1200
1000
800
600
400
200
0
0.00
0.02
0.04
0.06
0.08
0.10
Time (s)
Initial Velocity - 3.570 m/s (Ref.)
Initial Velocity - 1.785 m/s
Initial Velocity - 7.14 m/s

b

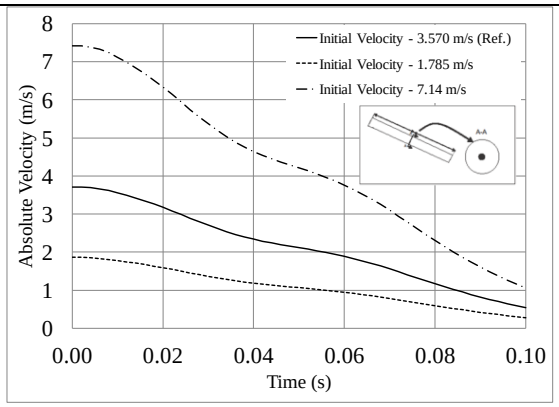
Absolute Velocity (m/s)
8
7
6
5
4
3
2
1
0
0.00
0.02
0.04
0.06
0.08
0.10
Time (s)
Initial Velocity - 3.570 m/s (Ref.)
Initial Velocity - 1.785 m/s
Initial Velocity - 7.14 m/s

c

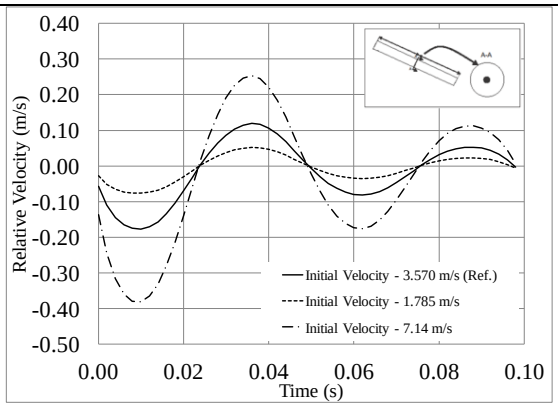
Relative Velocity (m/s)
0.40
0.30
0.20
0.10
0.00
-0.10
-0.20
-0.30
-0.40
-0.50
0.00
0.02
0.04
0.06
0.08
0.10
Time (s)
Initial Velocity - 3.570 m/s (Ref.)
Initial Velocity - 1.785 m/s
Initial Velocity - 7.14 m/s

d

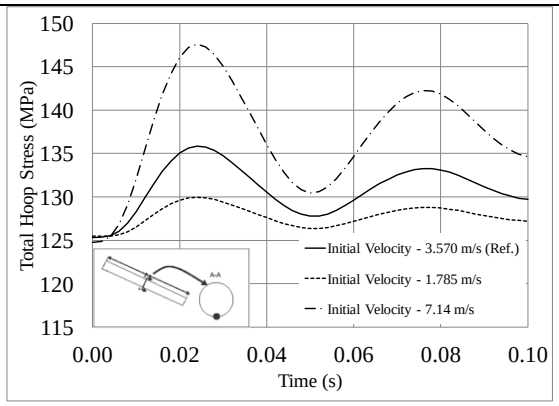
Total Hoop Stress (MPa)
150
145
140
135
130
125
120
115
0.00
0.02
0.04
0.06
0.08
0.10
Time (s)
Initial Velocity - 3.570 m/s (Ref.)
Initial Velocity - 1.785 m/s
Initial Velocity - 7.14 m/s

e

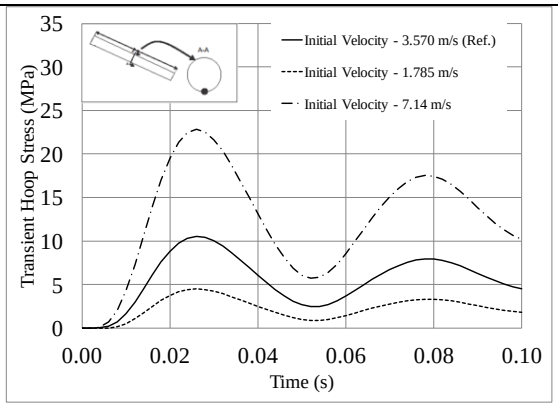
Transient Hoop Stress (MPa)
35
30
25
20
15
10
5
0
0.00
0.02
0.04
0.06
0.08
0.10
Time (s)
Initial Velocity - 3.570 m/s (Ref.)
Initial Velocity - 1.785 m/s
Initial Velocity - 7.14 m/s

f

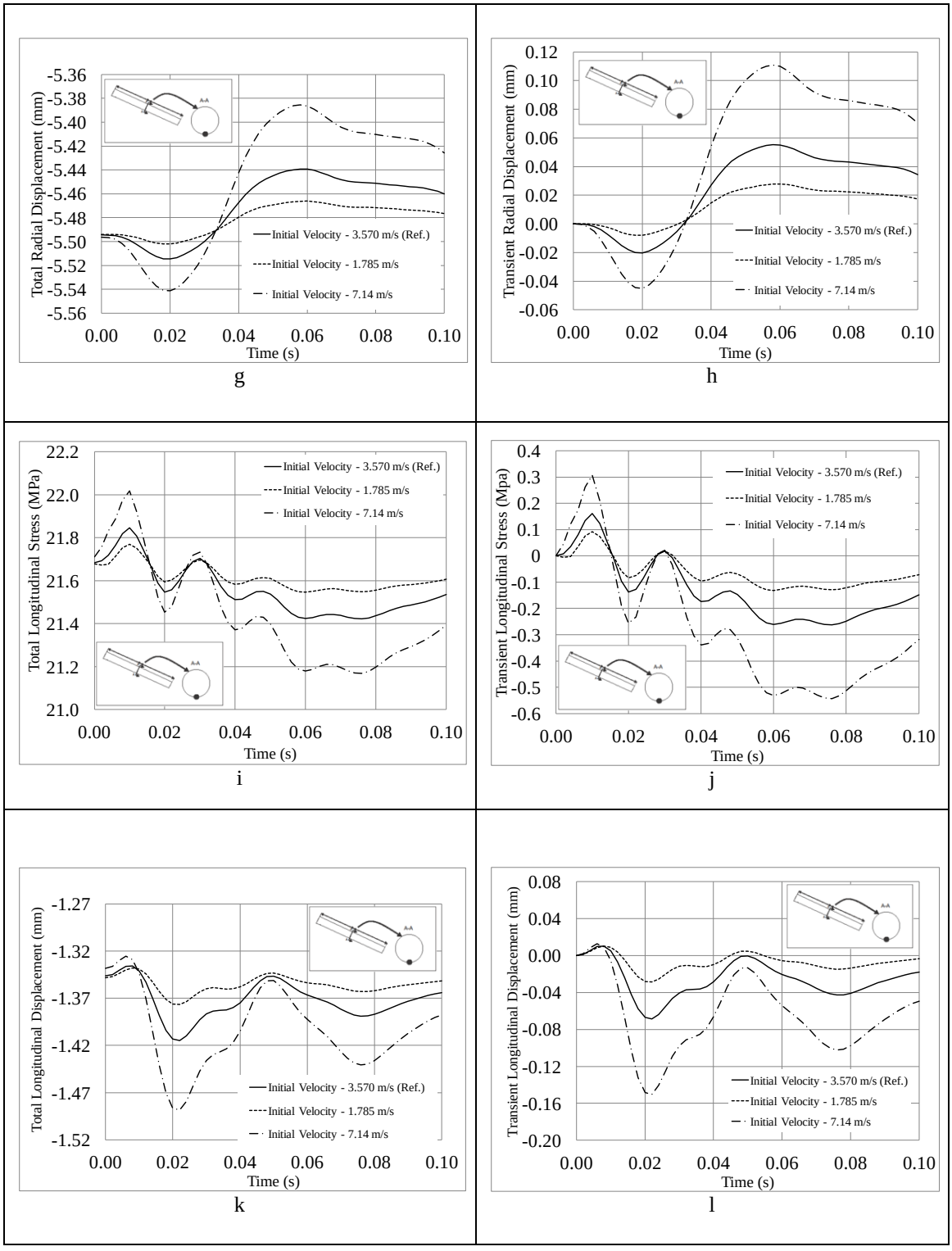

Figure 6. 3 - Initial Flow Velocity comparison for : (a) Total Pressure, (b) Transient Pressure, (c) Absolute Velocity, (d) Relative Velocity, (e) Total Hoop Stress, (f) Transient Hoop Stress, (g) Total Hoop Displacement, (h) Transient Hoop Displacement, (i) Total Longitudinal Stress, (j) Transient Longitudinal Stress, (k) Total Longitudinal Displacement, (l) Transient Longitudinal Displacement

6.4.2 Analyzing the Effect of the Initial Flow Velocity

Table 6.15 ranks the fields from the most sensitive (longitudinal displacement) to the least sensitive (pressure) for steady state and Table 6.16 ranks the fields from the most sensitive (longitudinal displacement) to the least sensitive (radial displacement) for transient state. A rank based on the total response (steady state + transient) is also provided in Table 6.17 where pressure is observed to be the most sensitive parameter and the radial displacement is the least. The sensitivity of each field is assessed based on the variation parameter introduced in Eq. 6.1 from their value in the reference case.

The weak variation parameter values in Table 6.15 indicate that the initial flow velocity has a negligible impact on all steady state of the fields.

The longitudinal displacement is the field that is impacted the most by the initial flow velocity with a variation of 120% in transient state. However, every field is more or less equally impacted by the initial velocity in the transient state.

Table 6.17 shows that only the total pressure and total hoop stresses are mildly impacted by the initial velocity while other total fields show little sensitivity.

Table 6. 15 - Sensitivity of Numerical Results to the Initial Flow Velocity on Steady-State Fields

	Longitudinal Displacement		Hoop Stress		Longitudinal Stress		Radial Displacement		Pressure	
	Magnitude v (mm)	$\Psi_R(V_o,v)$	Magnitude σ_h (MPa)	$\Psi_R(V_o,\sigma_h)$	Magnitude σ_l (MPa)	$\Psi_R(V_o,\sigma_l)$	Magnitude u (mm)	$\Psi_R(V_o,u)$	Magnitude p (kPa)	$\Psi_R(V_o,p)$
3.570 m/s (ref.)	-1.346	-	125.3	-	21.68	-	-5.494	-	4467	-
1.785 m/s	-1.348	0.15%	125.5	0.12%	21.67	-0.07%	-5.494	-0.01%	4467	0.00%
7.140 m/s	-1.338	-0.58%	124.7	-0.46%	21.71	0.12%	-5.496	0.03%	4467	0.00%

Table 6. 16 - Sensitivity of Numerical Results to the Initial Flow Velocity on Transient Fields

	Longitudinal Displacement		Longitudinal Stress		Hoop Stress		Pressure		Radial Displacement	
	Magnitude v (mm)	$\Psi_R(V_o,v)$	Magnitude σ_l (MPa)	$\Psi_R(V_o,\sigma_l)$	Magnitude σ_h (MPa)	$\Psi_R(V_o,\sigma_h)$	Magnitude p (kPa)	$\Psi_R(V_o,p)$	Magnitude u (mm)	$\Psi_R(V_o,u)$
3.570 m/s (ref.)	-0.071	-	-0.069	-	10.55	-	423.7	-	0.055	-
1.785 m/s	-0.029	-58.5%	-0.029	-58.3%	4.500	-57.3%	201.8	-52.4%	0.028	-49.6%
7.140 m/s	-0.156	120%	-0.150	119%	22.84	116%	870.6	105.5%	0.111	100%

Table 6. 17 - Sensitivity of Numerical Results to the Initial Flow Velocity on Total Fields

	Pressure		Hoop Stress		Longitudinal Displacement		Radial Displacement		Longitudinal Stress	
	Magnitude p (kPa)	$\Psi_R(V_o,p)$	Magnitude σ_h (MPa)	$\Psi_R(V_o,\sigma_h)$	Magnitude v (mm)	$\Psi_R(V_o,v)$	Magnitude u (mm)	$\Psi_R(V_o,u)$	Magnitude σ_l (MPa)	$\Psi_R(V_o,\sigma_l)$
3.570 m/s (ref.)	4891	-	135.9	-	-1.417	-	-5.439	-	21.62	-
1.785 m/s	4669	-4.5%	130.0	-4.3%	-1.378	-2.8%	-5.466	0.5%	21.64	0.1%
7.140 m/s	5338	9.1%	147.6	9%	-1.494	5%	-5.385	-1%	21.56	0%

6.5 Effect of the Damping Ratio

Section 6.5 presents the damping effect on the fluid and structural steady state and transient results within 0.0 and 0.1 seconds. The results based on the damping ratio of the reference case (10 %) are compared with variations in the damping ratio (2% and 5%).

6.5.1 Results and Discussion

Figures 6.4 a-d show that, within the steady state and transient regimes, damping has a negligible effect on fluid fields. In the steady-state regime, damping is observed not to impact the stress and displacement fields within the pipe wall.

Transient structural results are observed to slightly be affected by the change in damping ratio. Figures 6.4 e-l indicates that the transient values slightly increase as the damping ratio diminishes. Figure 6.4f shows that for the lowest damping ratio considered (2%), the hoop stress due to the transient pressure reaches a maximum value of 10.56 MPa compared to 10.55 MPa for the reference value of 10% (Table 6.18). Table 6.18 shows that the classical solution systematically overestimates the transient hoop stress compared to the predictions of the numerical solution.

Table 6. 18 - Classical versus Numerical predictions of Maximum Transient Hoop Stress for different Damping Ratio

	Damping Ratio (%)	Classical Solution [1]	Numerical Solution [2]	Percentage Difference ([1]-[2])/[2]
Transient Hoop Stress (MPa)	10 (Ref.)	11.87	10.55	12.5%
	5	11.87	10.56	12.4%
	2	11.87	10.56	12.4%

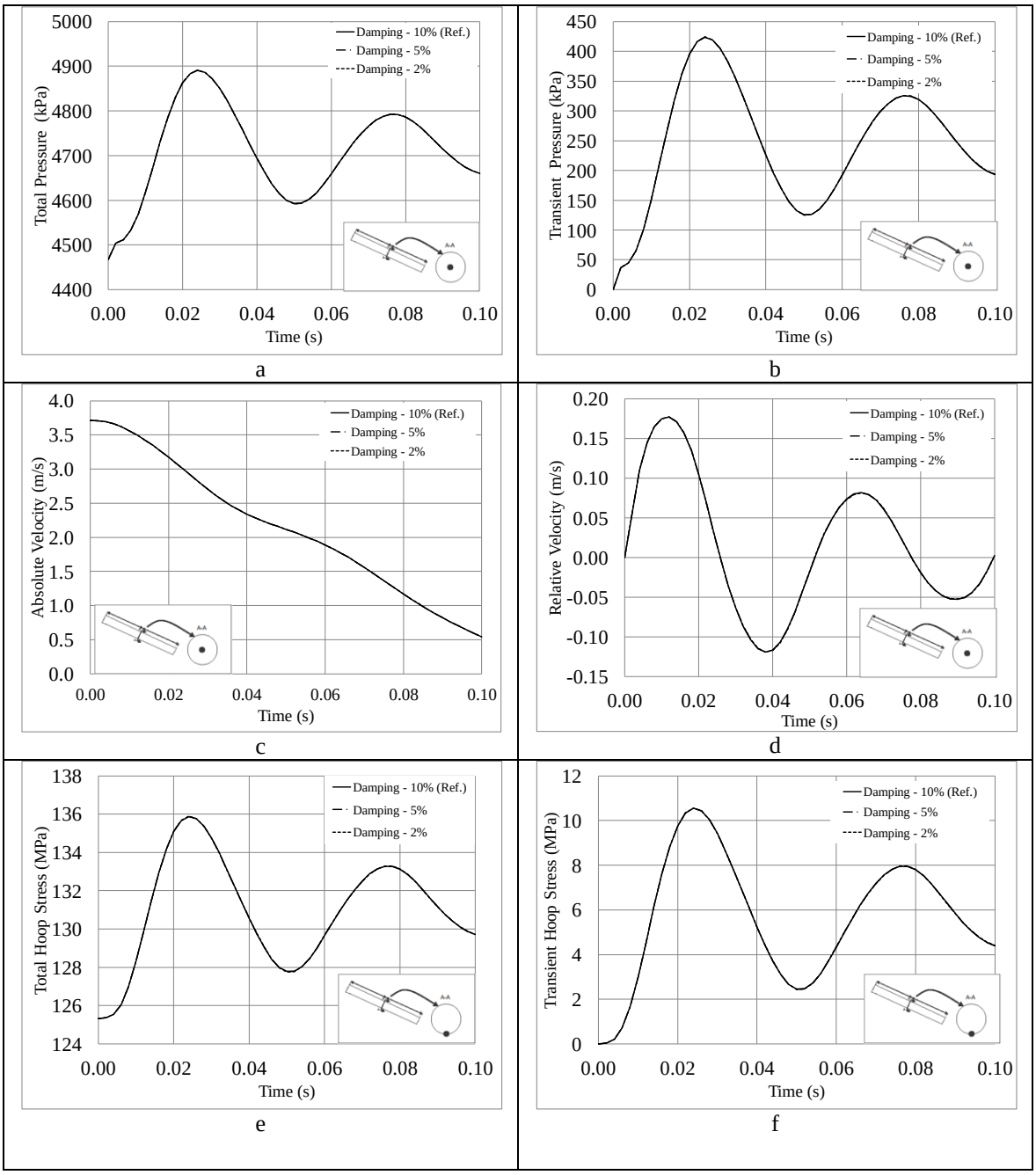
Damping - 10% (Ref.)
Damping - 5%
Damping - 2%
Total Pressure (kPa)
Transient Pressure (kPa)
Absolute Velocity (m/s)
Relative Velocity (m/s)
Total Hoop Stress (MPa)
Transient Hoop Stress (MPa)
Time (s)
a
b
c
d
e
f

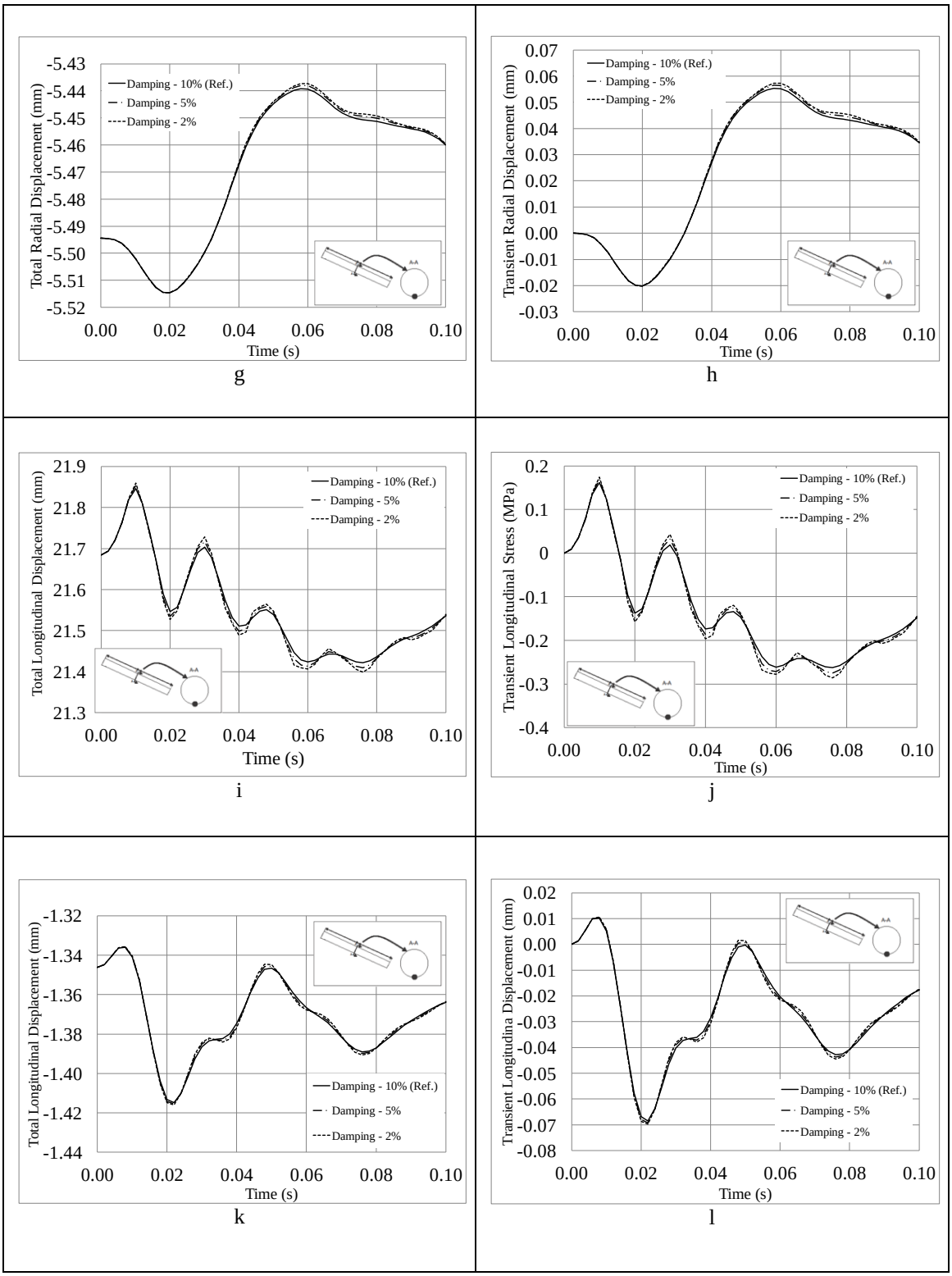

Figure 6. 4 - Damping Ratio comparison for : (a) Total Pressure, (b) Transient Pressure, (c) Absolute Velocity, (d) Relative Velocity, (e) Total Hoop Stress, (f) Transient Hoop Stress, (g) Total Hoop Displacement, (h) Transient Hoop Displacement, (i) Total Longitudinal Stress, (j) Transient Longitudinal Stress, (k) Total Longitudinal Displacement, (l) Transient Longitudinal Displacement

6.5.2 Analyzing the Effect of the Damping Ratio

Table 6.19 ranks the fields from the most sensitive (longitudinal stress) to the least sensitive (pressure) both for the steady state and transient responses. The sensitivity of each field is assessed based on the variation parameter introduced in Eq. 6.1 from their value in the reference case.

The essentially zero variations for all field variables in the steady state and total response suggest that damping has no influence on fields in the steady-state and the total response.

In the transient regime, the longitudinal stress is the field that is impacted the most by the damping ratio with a variation of 7.97% from the reference case. The longitudinal displacement comes second with 1.67% variation while the influence of damping on the other fields is observed to be negligible (<1%). Given that the transient response represents a small part of the total response, the overall influence of damping is considered negligible.

Table 6. 19 - Sensitivity of Numerical Results to the damping ratio

		Longitudinal Stress		Radial Displacement		Longitudinal Displacement		Hoop Stress		Pressure	
		Magnitude σ_l (MPa)	$\Psi_R(\xi,\sigma_l)$	Magnitude u (mm)	$\Psi_R(\xi,u)$	Magnitude v (mm)	$\Psi_R(\xi,v)$	Magnitude σ_h (MPa)	$\Psi_R(\xi,\sigma_h)$	Magnitude p (kPa)	$\Psi_R(\xi,p)$
Steady-State Results	10 % (Ref.)	21.68	-	-5.494	-	-1.346	-	125.3	-	4467	-
	5	21.68	0.00%	-5.494	0.00%	-1.346	0.00%	125.3	0.00%	4467	0.00%
	2	21.68	0.00%	-5.494	0.00%	-1.346	0.00%	125.3	0.00%	4467	0.00%
Maximum Transient Results	10 % (Ref.)	0.162	-	0.055	-	-0.069	-	10.55	-	423.7	-
	5	0.169	4.59%	0.056	2.10%	-0.069	1.02%	10.557	0.08%	423.9	0.04%
	2	0.174	7.97%	0.057	3.44%	-0.070	1.67%	10.56	0.13%	424.0	0.07%
Total Results	10 % (Ref.)	21.85	-	-5.439	-	-1.415	-	135.9	-	4891	-
	5	21.85	0.03%	-5.438	-0.02%	-1.415	0.05%	135.9	0.01%	4891	0.00%
	2	21.86	0.06%	-5.437	-0.04%	-1.416	0.08%	135.9	0.01%	4891	0.01%

6.6 Effect of Closure Time

Section 6.6 presents the effect of the closure time on the fluid and structural transient results within 0.0 and 0.1 seconds. The results based on the closure time of the reference case (0.1135 seconds) are compared with those based on two closure time variations (0.227 seconds and 0.554 seconds).

6.6.1 Results and Discussion

The initial field values in Figs 6.5 a-d indicate that closure time has no effect on the fluid fields in the steady-state. Closure time effect is however observed in the transient regime where transient pressure and velocity variations were observed to decrease with closure time. From Figs. 6.5a and 6.5d, it is observed that the pressure frequency and velocity frequency are insensitive to the closure time. According to the rigid water column theory (Eqs 2.21, 2.22), transient pressure is inversely proportional to the closure time. In Table 6.20, transient pressure results, as calculated by the rigid water column theory based on the reference transient pressure (423.7 kPa), are provided in Column [1] and compared to the numerical results in Column [2]. Column [3] provides the percentage differences. The comparison suggests that the transient pressure as numerically predicted is nearly inversely proportional to the closure time

Table 6. 20 - Rigid Water Column Theory versus Numerical predictions of Maximum Transient Hoop Stress for different closure times

	Closure Time (s)	Rigid Water Column Theory [1]	Numerical Solution [2]	Percentage Difference ([1]-[2])/[2]
Transient Pressure (kPa)	0.1135 (Ref.)	-	423.7	-
	0.227	211.9	201.8	4.98%
	0.554	86.80	90.80	-4.41%

In the steady-state regime, closure time is observed not to impact the stress and displacement fields within the pipe wall. Table 6.21 shows that the hoop stresses, longitudinal stresses and radial displacement do not influence the percentage difference between the numerical and classical solutions. In all cases, excellent agreement is obtained with a maximum percentage difference of less than 5.93% in the longitudinal stress predictions

Table 6. 21 - Comparison between Steady-State Classical and Numerical Solutions for different closure times

	Closure Time (s)	Classical Solution [1]	Numerical Solution [2]	Percentage Difference ([1]-[2])/[2]
Hoop Stress (MPa)	0.1135 (Ref.)	125.1	125.3	-0.18%
	0.227	125.1	125.3	-0.18%
	0.554	125.1	125.3	-0.18%
Longitudinal Stress (MPa)	0.1135 (Ref.)	22.97	21.68	5.93%
	0.227	22.97	21.68	5.93%
	0.554	22.97	21.68	5.93%
Radial Displacement (mm)	0.1135 (Ref.)	-5.161	-5.177	-0.32%
	0.227	-5.161	-5.177	-0.32%
	0.554	-5.161	-5.177	-0.32%

Unlike the steady-state results, closure time is observed to affect the magnitudes of the structural fields in the transient regime**.** The magnitude of all structural fields (Figs 6.5f-l) increases as the closure time decreases. Figure 6.5f shows that for the lowest closure time (0.1135 s), the transient hoop stress due to transient pressure reaches a maximum value of 10.55 MPa (Table 6.22) which is to be added to the steady-state hoop stress of 125.3 MPa (Table 6.21). Table 6.22 shows that the classical solution systematically overestimates the transient hoop stress when compared to numerical solution predictions. The classical solution provides reasonable agreement (within 12.5%) with numerical predictions for fast gate closure (low closure time). For slower gate closures (larger closure time), the classical solution is observed to significantly depart from numeric predictions.

Table 6. 22 - Classical versus Numerical predictions of Maximum Transient Pressure for different closure times

	Closure Time (s)	Classical Solution [1]	Numerical Solution [2]	Percentage Difference ([1]-[2])/[2]	Absolute Difference [1]-[2]
Transient Hoop Stress (MPa)	0.1135 (Ref.)	11.87	10.55	12.5%	1.32
	0.227	5.650	4.519	25.0%	1.13
	0.554	2.540	1.503	69.0%	1.04

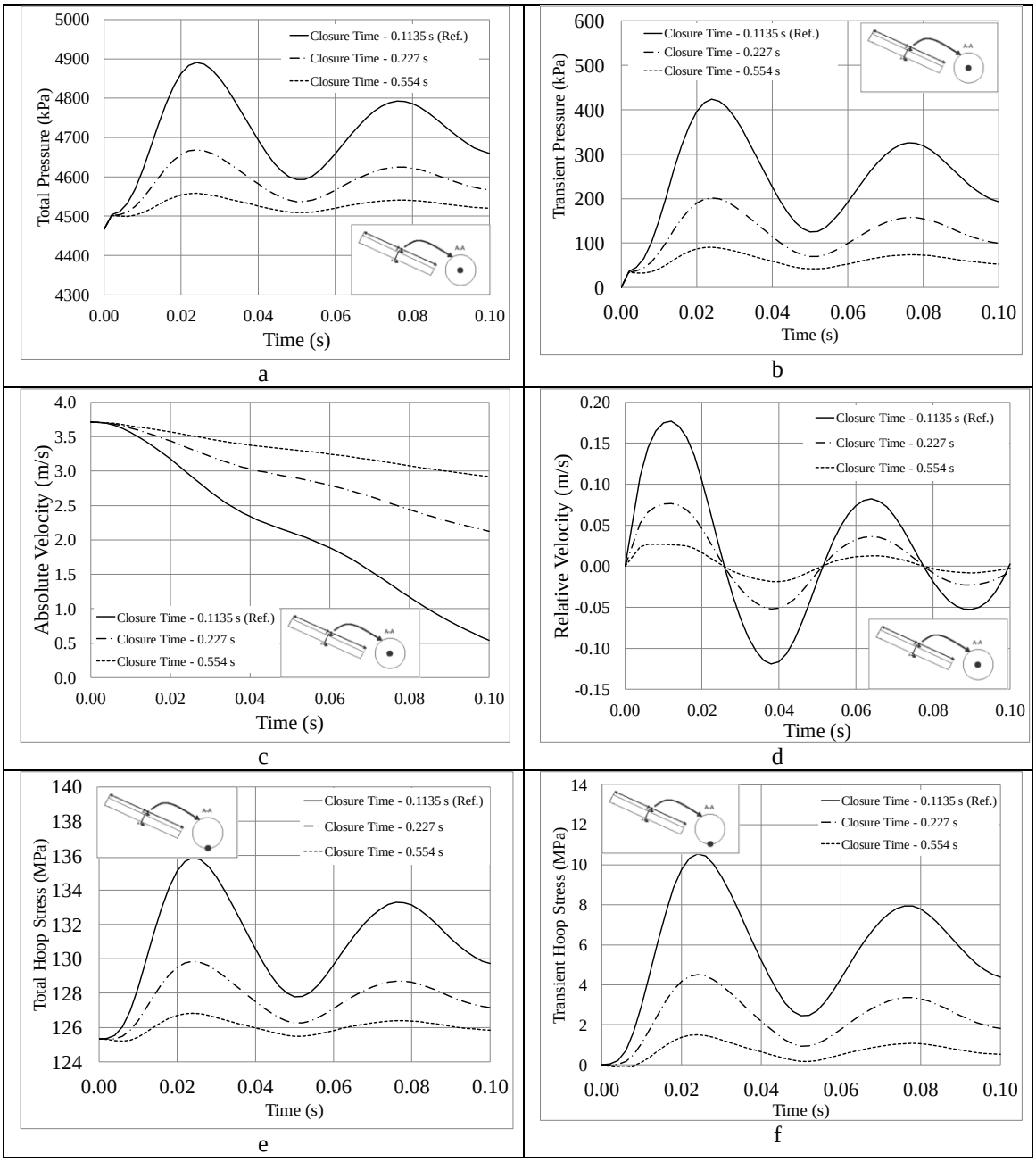
Total Pressure (kPa)
Time (s)
Closure Time - 0.1135 s (Ref.)
Closure Time - 0.227 s
Closure Time - 0.554 s
a
Transient Pressure (kPa)
Time (s)
b
Absolute Velocity (m/s)
Time (s)
c
Relative Velocity (m/s)
Time (s)
d
Total Hoop Stress (MPa)
Time (s)
e
Transient Hoop Stress (MPa)
Time (s)
f

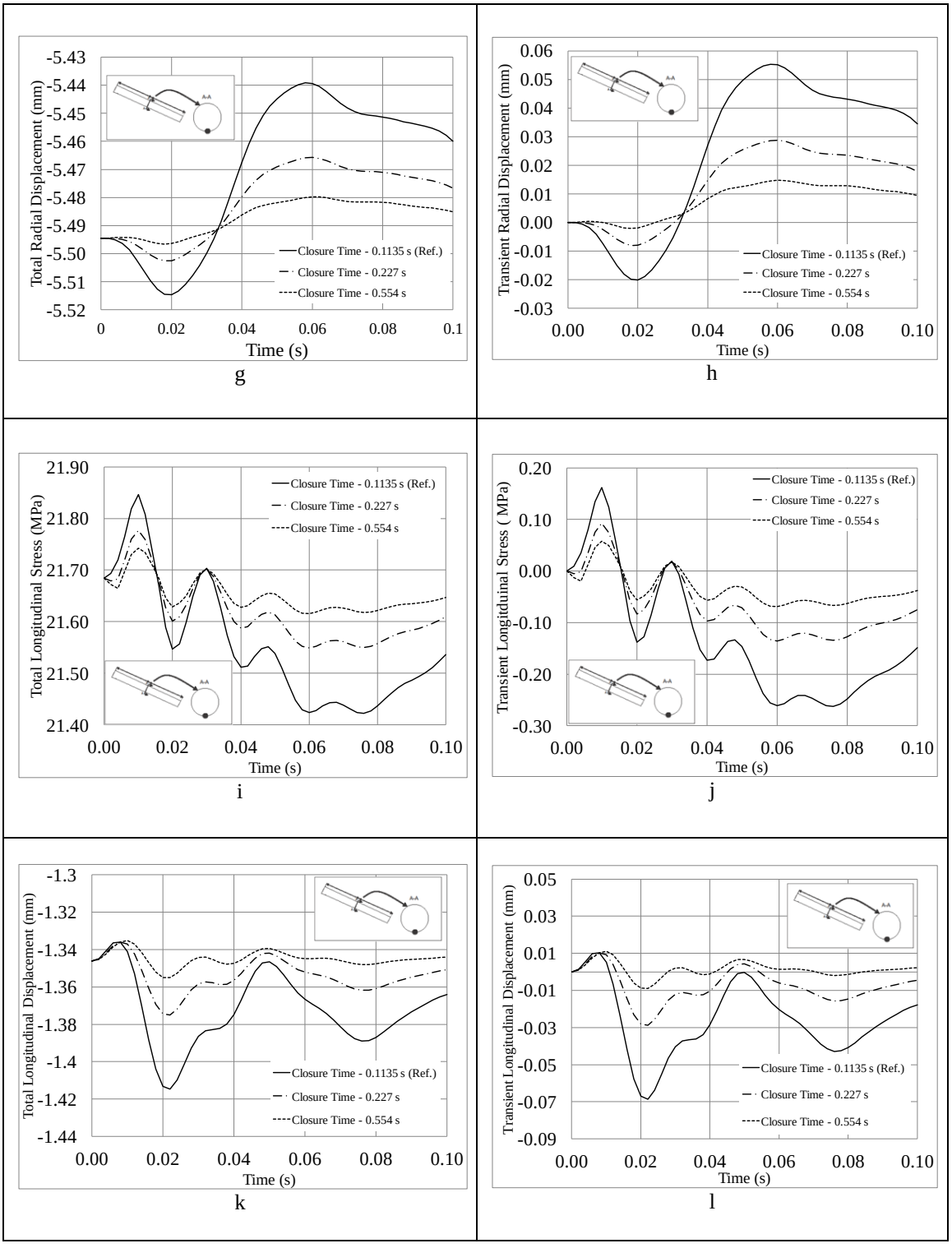

Figure 6. 5 - Closure time comparison for : (a) Total Pressure, (b) Transient Pressure, (c) Absolute Velocity, (d) Relative Velocity, (e) Total Hoop Stress, (f) Transient Hoop Stress, (g) Total Hoop Displacement, (h) Transient Hoop Displacement, (i) Total Longitudinal Stress, (j) Transient Longitudinal Stress, (k) Total Longitudinal Displacement, (l) Transient Longitudinal Displacement

6.6.2 Analyzing the Effect of Closure Time

Since by definition, the steady state solution takes place right before gate closure, zero sensitivity values are inserted into the steady state fields in Table 6.23. Table 6.24 ranks the fields from the most sensitive (radial displacement) to the least sensitive (longitudinal stress) for transient state. A rank based on the total response (steady state + transient) is also provided in Table 6.25 where pressure is observed to be the most sensitive parameter and the radial displacement is the least. The sensitivity of each field is assessed based on the variation parameter introduced in Eq. 6.1 from their value in the reference case, in steady state and transient analyses, as well as the total results.

The radial displacement is the field that is impacted the most by closure time with a variation of 89.4% in transient state. Other fields is nearly equally impacted by closure time in the transient state. The corresponding variations in the total response are minor with the pressure impacted the most, with a 6.81% variation.

Table 6. 23 - Sensitivity of Numerical Results to the closure time on Steady Fields

	Radial Displacement		Longitudinal Displacement		Hoop Stress		Pressure		Longitudinal Stress	
	Magnitude u (mm)	$\Psi_R(T,u)$	Magnitude v (mm)	$\Psi_R(T,v)$	Magnitude σ_h (MPa)	$\Psi_R(T,\sigma_h)$	Magnitude p (kPa)	$\Psi_R(T,p)$	Magnitude σ_l (MPa)	$\Psi_R(T,\sigma_l)$
0.1135 s (Ref.)	-5.494	-	-1.346	-	125.3	-	4467	-	21.68	-
0.227s	-5.494	0.00%	-1.346	0.00%	125.3	0.00%	4467	0.00%	21.68	0.00%
0.454 s	-5.494	0.00%	-1.346	0.00%	125.3	0.00%	4467	0.00%	21.68	0.00%

Table 6. 24 - Sensitivity of Numerical Results to the closure time on Transient Fields

	Radial Displacement		Longitudinal Displacement		Hoop Stress		Pressure		Longitudinal Stress	
	Magnitude u (mm)	$\Psi_R(T,u)$	Magnitude v (mm)	$\Psi_R(T,v)$	Magnitude σ_h (MPa)	$\Psi_R(T,\sigma_h)$	Magnitude p (kPa)	$\Psi_R(T,p)$	Magnitude σ_l (MPa)	$\Psi_R(T,\sigma_l)$
0.1135 s (Ref.)	-0.020	-	-0.069	-	10.55	-	423.7	-	0.162	-
0.227s	-0.008	-60.1%	-0.029	-58.0%	4.519	-57.2%	201.8	-52.4%	0.092	-42.9%
0.454 s	-0.002	-89.4%	-0.009	-87.1%	1.503	-85.8%	90.80	-78.6%	0.058	-64.3%

Table 6. 25 - Sensitivity of Numerical Results to the closure time on Total Fields

	Pressure		Hoop Stress		Longitudinal Displacement		Longitudinal Stress		Radial Displacement	
	Magnitude p (kPa)	$\Psi_R(T,p)$	Magnitude σ_h (MPa)	$\Psi_R(T,\sigma_h)$	Magnitude v (mm)	$\Psi_R(T,v)$	Magnitude σ_l (MPa)	$\Psi_R(T,\sigma_l)$	Magnitude u (mm)	$\Psi_R(T,u)$
0.1135 s (Ref.)	4891	-	135.9	-	-1.415	-	21.85	-	-5.515	-
0.227s	4669	-4.54%	129.8	-4.44%	-1.375	-2.81%	21.78	-0.32%	-5.503	-0.22%
0.454 s	4558	-6.81%	126.8	-6.66%	-1.355	-4.22%	21.74	-0.48%	-5.497	-0.33%

6.7 Effect of Angle of Vertical Inclination

Section 6.7 presents the effect of the angle of vertical inclination on the fluid and structural transient results between 0.0 and 0.1 seconds. The results based on the vertical inclination angle of the reference case (25.86°) are compared with two vertical inclination angle variations (0° and 15°).

6.7.1 Results and Discussion

Figures 6.6 a-d show that, for steady and transient states, the angle of vertical inclination does not significantly influence the pressure and velocity fields. In contrast, the stresses and displacement fields within the pipe wall are observed to be impacted by the angle of inclination.

Figure 6.6e shows that the hoop stresses slightly increases as the angle of vertical inclination decreases. This increase can be attributed to pipe ovalization. A smaller inclination angle corresponds to greater bending moment within the pipe and correspondingly higher longitudinal stresses at the extreme fibers. The higher stresses cause the section to ovalize further.

Table 6.26 shows very good agreement between the classical and numerical solutions with a maximum difference of 1.11%. Figure 6.6i shows that the longitudinal stresses change with the vertical inclination angle, although no specific trend can be noticed. For comparison, longitudinal stresses are calculated from the beam theory as presented in Section 3.3.4.1. As the angle of vertical inclination decreases, the bending action intensifies and the axial action weakens. Table 6.26 shows an excellent agreement between classical and numerical solutions with a maximum difference of 5.95%. The steady-state values of the radial displacements obtained from the FEM-FVM results are

shown in Fig. 6.6g. They are compared in Table 6.26 to those based on the classical solution prediction. Good agreement is observed between the classical and numerical results with a maximum percentage difference of 15.7%.

Table 6. 26 - Comparison between Steady-State Classical and Numerical Solutions for different inclination angles

	Inclination Angle (°)	Classical Solution [1]	Numerical Solution [2]	Percentage Difference ([1]-[2])/[2]
Hoop Stress (MPa)	25.86 (Ref.)	125.1	125.3	-0.16%
	15	125.1	125.8	-0.56%
	0	125.1	126.5	-1.11%
Longitudinal Stress (MPa)	25.86 (Ref.)	22.97	21.68	5.95%
	15	23.99	24.21	-0.89%
	0	23.97	24.38	-1.69%
Radial Displacement (mm)	25.86 (Ref.)	-5.161	-5.494	-6.07%
	15	-5.161	-6.121	-15.7%
	0	-5.161	-5.539	-6.82%

In the transient regime, the inclination angle affects all structural fields except the transient hoop stress**.** Figure 6.6h shows that the transient radial displacement changes as the inclination angle changes. Again, no specific trend can be inferred as a zero inclination angle does not follow the trend of the based on the two other two inclinations (15°, 25.86°). Figure 6.6j shows that as the inclination angle decreases, the amplitude of the transient longitudinal stress curve amplifies. Figure 6.6l shows that the inclination angle slightly affects the longitudinal displacement.

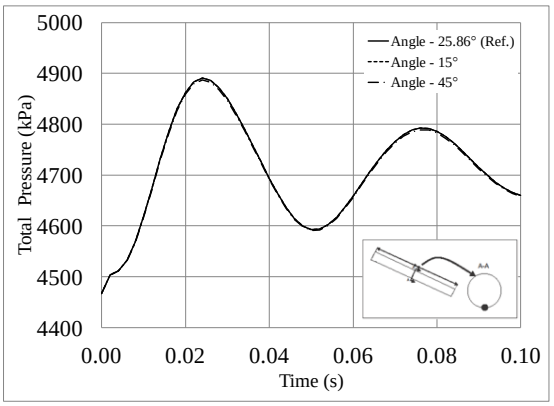
Total Pressure (kPa)
5000
4900
4800
4700
4600
4500
4400
0.00
0.02
0.04
0.06
0.08
0.10
Time (s)
Angle - 25.86° (Ref.)
Angle - 15°
Angle - 45°

a

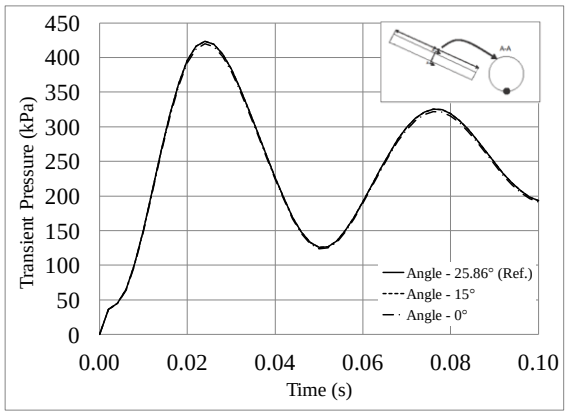
Transient Pressure (kPa)
450
400
350
300
250
200
150
100
50
0
0.00
0.02
0.04
0.06
0.08
0.10
Time (s)
Angle - 25.86° (Ref.)
Angle - 15°
Angle - 0°

b

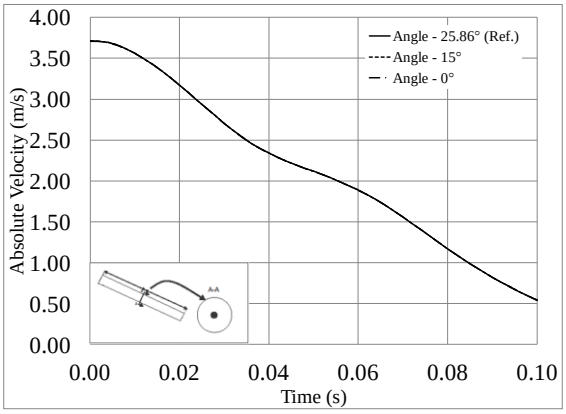
Absolute Velocity (m/s)
4.00
3.50
3.00
2.50
2.00
1.50
1.00
0.50
0.00
0.00
0.02
0.04
0.06
0.08
0.10
Time (s)
Angle - 25.86° (Ref.)
Angle - 15°
Angle - 0°

c

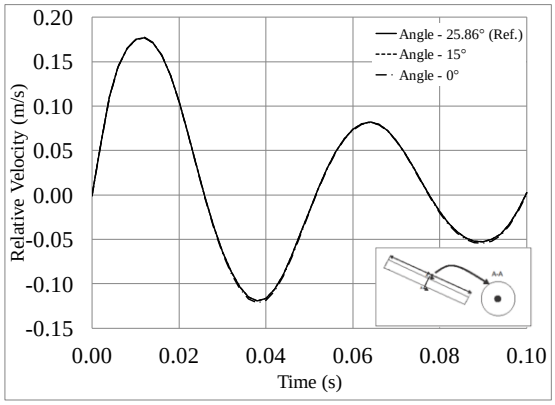
Relative Velocity (m/s)
0.20
0.15
0.10
0.05
0.00
-0.05
-0.10
-0.15
0.00
0.02
0.04
0.06
0.08
0.10
Time (s)
Angle - 25.86° (Ref.)
Angle - 15°
Angle - 0°

d

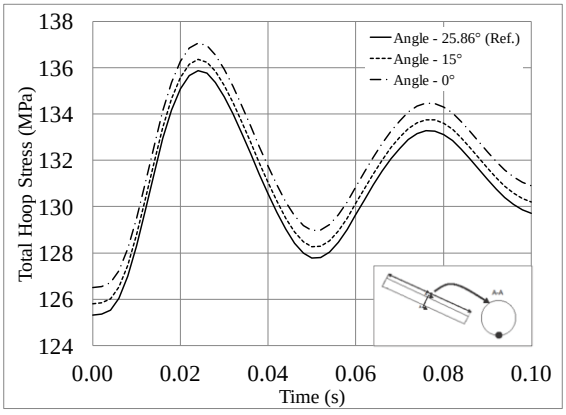
Total Hoop Stress (MPa)
138
136
134
132
130
128
126
124
0.00
0.02
0.04
0.06
0.08
0.10
Time (s)
Angle - 25.86° (Ref.)
Angle - 15°
Angle - 0°

e

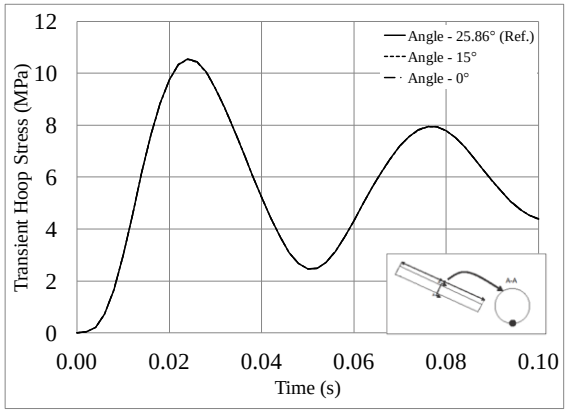
Transient Hoop Stress (MPa)
12
10
8
6
4
2
0
0.00
0.02
0.04
0.06
0.08
0.10
Time (s)
Angle - 25.86° (Ref.)
Angle - 15°
Angle - 0°

f

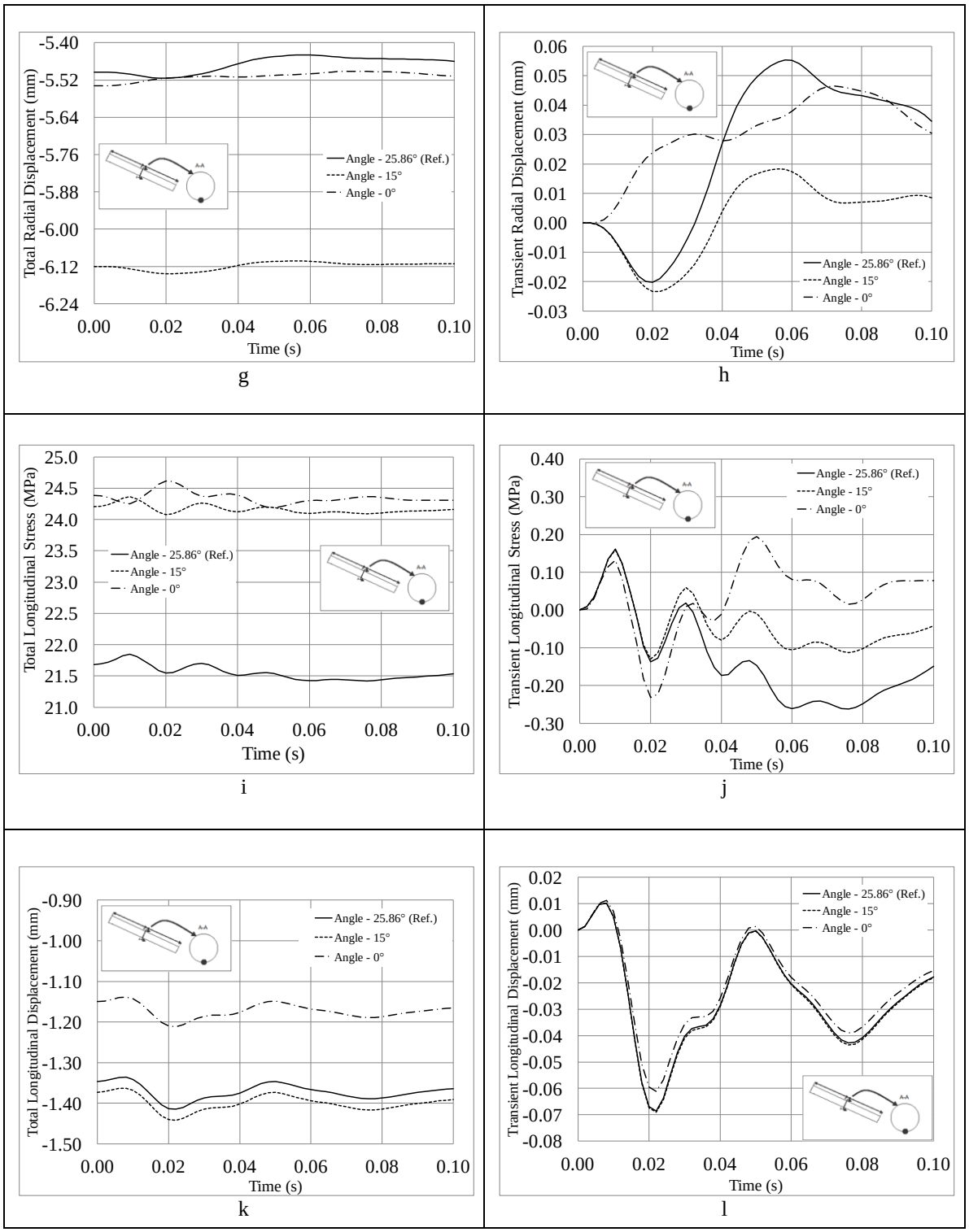

Figure 6. 6 - Angle comparison for : (a) Total Pressure, b) Transient Pressure, (c) Absolute Velocity, (d) Relative Velocity, (e) Total Hoop Stress, (f) Transient Hoop Stress, (g) Total Hoop Displacement, (h) Transient Hoop Displacement, (i) Total Longitudinal Stress, (j) Transient Longitudinal Stress, (k) Total Longitudinal Displacement, (l) Transient Longitudinal Displacement

6.7.2 Analyzing the Effect of the Angle of Vertical Inclination

Table 6.27 ranks the fields from the most sensitive (longitudinal stress) to the least sensitive (pressure) for the steady state and Table 6.28 ranks the fields from the most sensitive (radial displacement) to the least sensitive (pressure) for the transient state. Table 6.29 ranks the fields from the most sensitive (longitudinal stress) to the less (pressure) for the total response. The sensitivity of each field is assessed based on the variation parameter introduced in Eq. 6.1 from their value in the reference case.

In the steady-state, the longitudinal displacement is the field that is impacted the most by the inclination angle with a maximum variation criterion of 12.5%. Longitudinal displacement comes second and the radial displacement comes third. Table 6.27 shows that the inclination angle does not affect the hoop stresses and the pressure in the steady-state. In the transient state, the radial displacement is the field that is impacted the most by the inclination angle with a maximum variation of 16.0%. The longitudinal stresses are observed to come second and longitudinal displacement third. Table 6.25 suggest that the inclination angle is essentially not affecting hoop stresses and the pressure in the transient state. For the total response, Table 6.27 shows that the total longitudinal stresses are influenced the most by the angle of inclinations. No specific trend was observed for the other fields.

Table 6. 27 - Sensitivity of Numerical Results to the Inclination Angle on Steady-State Fields

	Longitudinal Stress		Longitudinal Displacement		Radial Displacement		Hoop Stress		Pressure	
	Magnitude σ_l (MPa)	$\Psi_R(\alpha,\sigma_l)$	Magnitude v (mm)	$\Psi_R(\alpha,v)$	Magnitude u (mm)	$\Psi_R(\alpha,u)$	Magnitude σ_h (MPa)	$\Psi_R(\alpha,\sigma_h)$	Magnitude p (kPa)	$\Psi_R(\alpha,p)$
25.86° (Ref.)	21.68	-	-1.346	-	-5.494	-	125.3	-	4467	-
15°	24.21	11.6%	-1.373	1.98%	-6.121	11.4%	125.8	0.40%	4467	0.00%
0°	24.38	12.5%	-1.150	-14.6%	-5.539	0.80%	126.5	0.96%	4467	0.00%

Table 6. 28 - Sensitivity of Numerical Results to the Inclination Angle on Transient Fields

	Radial Displacement		Longitudinal Stress		Longitudinal Displacement		Hoop Stress		Pressure	
	Magnitude u (mm)	$\Psi_R(\alpha,u)$	Magnitude σ_l (MPa)	$\Psi_R(\alpha,\sigma_l)$	Magnitude v (mm)	$\Psi_R(\alpha,v)$	Magnitude σ_h (MPa)	$\Psi_R(\alpha,\sigma_h)$	Magnitude p (kPa)	$\Psi_R(\alpha,p)$
25.86° (Ref.)	-0.020	-	0.162	-	-0.069	-	10.55	-	423.7	-
15°	-0.023	16.0%	0.160	-1.1%	-0.069	0.79%	10.54	-0.09%	423.6	-0.02%
0°	0.000	-100.0%	0.194	20.1%	-0.061	-10.7%	10.55	0.00%	419.7	-0.95%

Table 6. 29 - Sensitivity of Numerical Results to the Vertical Inclination Angle on Total Fields

	Longitudinal Stress		Radial Displacement		Longitudinal Displacement		Hoop Stress		Pressure	
	Magnitude σ_l (MPa)	$\Psi_R(\alpha,\sigma_l)$	Magnitude u (mm)	$\Psi_R(\alpha,u)$	Magnitude v (mm)	$\Psi_R(\alpha,v)$	Magnitude σ_h (MPa)	$\Psi_R(\alpha,\sigma_h)$	Magnitude p (kPa)	$\Psi_R(\alpha,p)$
25.86° (Ref.)	21.84	-	-5.515	-	-1.415	-	135.9	-	4891	-
15°	24.36	11.6%	-6.144	11.4%	-1.442	1.92%	136.3	0.36%	4891	0.00%
0°	24.58	12.5%	-5.539	0.43%	-1.211	-14.4%	137.1	0.88%	4887	-0.08%

6.8 Sensitivity Analysis

In order to compare the effect of each design parameter I on the fluid and structural output fields O, a sensitivity analysis index, is defined as

$$SI(I,O) = \frac{\Psi(I,O)}{\left(\frac{I-R}{R}\right)} = \left[\frac{\Psi(I,O)-\Psi(R,O)}{\Psi(R,O)}\right] \Big/ \left(\frac{I-R}{R}\right) \tag{6.2}$$

Table 6. 30 - Input Parameter changes in the sensitivity analysis

Design Parameters [y]	Thickness	Span	Initial Velocity	Damping Ratio	Closure Time	Angle
Unit	mm	m	m/s	%	s	°
Reference Value	19.05	15.384	3.570	10	0.1135	25.86
High Parametric Value	17.00	25.000	7.140	5	0.5540	15
Low Parametric Value	15.00	20.000	1.785	2	0.2270	0

This dimensionless index provides an indication of output field sensitivity to the variations in the input design parameter. A greater absolute value indicates a high sensitivity. The sensitivity indices for the parameters are provided in Tables 6.31 to 6.35. Within each table, variables are sorted in a descending order of importance.

Table 6.31 shows that the pipe span is the input parameter that has the most impact on the transient pressure. Next to the span, the initial velocity and closure time come in second place. The thickness has a mildly noticeable impact on the transient pressure, since it plays a modest role in the fluid-structure interaction. Other parameters (inclination angle and damping ratio) have a negligible impact on the transient pressure.

Table 6. 31 - Sensitivity Index of Transient Pressure on Input Parameters

Transient Pressure	Span	Initial Velocity	Closure Time	Thickness	Inclination Angle	Damping Ratio
High Parametric Value	1.1362	1.0548	0.2024	0.1360	0.0006	0.0009
Low Parametric Value	1.1563	1.0474	0.5237	0.0866	0.0095	0.0009

Table 6.32 shows that the pipe thickness is the input parameter to most significantly affect the total hoop stresses. The span, initial velocity and closure time have all an equally small impact on the total hoop stresses. The remaining parameters (inclination angle and damping ratio) have negligible impact on total hoop stresses.

Table 6. 32 - Sensitivity Index of Total Hoop Stresses on Input Parameters

Hoop Stress	Thickness	Span	Initial Velocity	Closure Time	Inclination Angle	Damping Ratio
High Parametric Value	1.135	0.117	0.086	0.017	0.009	0.000
Low Parametric Value	1.277	0.086	0.088	0.045	0.013	0.000

Table 6.33 shows that the span is the parameter that has most impact on the total radial displacement. This is followed by the thickness which has a moderate impact on the total radial displacement. Other parameters (initial velocity, closure time, inclination angle, and damping ratio) have negligible impact on the total radial displacement.

Table 6. 33 - Sensitivity Index of Total Radial Displacements on Input Parameters

Radial Displacement	Span	Thickness	Inclination Angle	Initial Velocity	Closure Time	Damping Ratio
High Parametric Value	11.62	0.743	0.272	0.005	0.001	0.000
Low Parametric Value	7.206	0.850	0.004	0.005	0.002	0.000

Table 6.34 shows that the span is the most influential on the total longitudinal stresses, followed by the thickness which has a moderate effect. The inclination angle, initial velocity, and closure time are observed to have a negligible impact on total longitudinal stresses.

Table 6. 34 - Sensitivity Index (%) of Total Longitudinal Stresses on Input Parameters

Longitudinal Stress	Span	Thickness	Inclination Angle	Initial Velocity	Closure Time	Damping Ratio
High Parametric Value	3.670	0.753	0.274	0.008	0.001	0.001
Low Parametric Value	3.097	0.865	0.125	0.008	0.003	0.001

Table 6.35 shows that the span and thickness have an impact on the total longitudinal displacement. Other parameters (inclination angle, initial velocity, closure time and damping ratio) have a negligible impact on the total longitudinal displacement.

Table 6. 35 - Sensitivity Index (%) of Total Longitudinal Displacements on Input Parameters

Longitudinal Displacement	Span	Thickness	Inclination Angle	Initial Velocity	Closure Time	Damping Ratio
High Parametric Value	1.298	1.149	0.046	0.052	0.011	0.001
Low Parametric Value	1.227	1.302	0.144	0.054	0.028	0.001

The above results are summarized in Table 6.36 which compiles the effect of each of the input parameters on the output fields investigated.

Table 6. 36 - Summary of Influences of input design parameters on magnitude of output fields

	Transient Pressure	Total Hoop Stress	Total Radial Displacement	Total Longitudinal Stress	Total Longitudinal Displacement
Thickness	Small	**Significant**	**Moderate**	**Moderate**	**Significant**
Span	**Significant**	Small	**Important**	**Significant**	**Significant**
Initial Velocity	**Significant**	Small	Negligible	Negligible	Small
Damping Ratio	Negligible	Negligible	Negligible	Negligible	Negligible
Closure Time	**Moderate**	Small	Negligible	Negligible	Negligible
Angle of Inclination	Negligible	Negligible	Negligible	**Moderate**	Small

6.9 Conclusion

Chapter 6 presented a parametric study on six design parameters (pipe thickness, span, initial flow velocity, damping ratio, closure time, and vertical inclination angle) and provided a systematic analysis on their influence on the fluid and structural output fields. Section 6.7 provided a sensitivity analysis that provided a classification of each input parameter investigated on the output parameter of the study.

1. The analysis indicates that the span and initial velocity are the most influential parameters on the transient pressure. The closure time has a moderate impact. The thickness has a small influence on the transient pressure. Its influence is one order of magnitude less than that of the first three parameters, and provides an indication of influence of fluid-structure interaction on the pressure.
2. It is also observed that pipe thickness is the most influential parameter on the total hoop stresses, and thus on the structural design of a penstock. Pipe span, initial velocity and closure time are observed to have a small impact on the total hoop stress. Their impact is found to be approximately one order of magnitude less than that of the thickness.

3. Total radial displacements are primarily impacted by the span while the thickness is observed to have a moderate influence.
4. Total longitudinal stresses are primarily impacted by the pipe span. Pipe thickness and the inclination angle have moderate impact on the longitudinal stresses
5. Total longitudinal displacement was found to be insensitive to many parameters. Only the thickness and the span are observed to have an impact on it.
6. The damping ratio was observed to have little influence on all parameters considered.

Tables 6.4 and 6.14 show that the transient hoop stress calculated by classical structural solutions is consistently higher than that computed by numerical solution. A numerical analysis including the fluid structure interaction effect gives more accurate prediction.

CHAPTER 7 –COMPARATVE STUDY OF ELEVATED HORIZONTALLY AND VERTICALLY BENT PENSTOCKS

7.1 Objective

This chapter presents a comparative study based on the model developed in Chapter 4 for two additional design parameters; the horizontal bend angle, and the vertical bend angle. Towards this goal, a straight pipe is considered as a reference case and various scenarios of horizontal bend and vertical bend angles are investigated and comparisons are made with results based on the reference case.

7.2 Description of Parametric Runs

A reference case similar to that described in Chapter 5 for a straight pipe with no bend is taken as a basis from which parametric variations are made. However, unlike the reference case in chapter 5 in which the pipe was assumed to be inclined by 25.86 degrees with the horizontal, the reference case in this chapter is taken to lie in a horizontal plane. The diameter is 1.067 m, thickness is 19.05 mm, and the total span of the pipe including the bent segment is 15.384 m. Boundary conditions at pipe ends are identical to those defined in Section 4.5. Three additional scenarios are considered for a horizontal bend angle β of 15, 30 and 45 degrees and an additional three cases are considered for vertical bend angles χ of 15, 30, and 45 degrees. In all runs, the straight span L_1 at the inlet is taken equal to the straight span L_3 at the outlet, while the middle span of the curved segment L_2 is taken to vary according to the bend angle while keeping the centerline radius of the bend constant $R = 3.5\,m$, i.e., $L_2 = R\beta \times (\pi/180)$. In all runs, the sum of all spans $L = L_1 + L_2 + L_3$ is taken as 15.384 m. Table 7.1 summarizes the value of angles (β, χ) and spans L_1, L_2 and L_3 for all seven parametric runs conducted in this chapter.

Table 7. 1 - Design parameter value changes in the comparative study

Parametric Run	Horizontal Bend Angle β (Degrees)	Vertical Bend Angle χ (Degrees)	Span L1 (m)	Span L2 (m)	Span L3 (m)
1 (Reference Case)	0	0	15.384	0	0
2	15	0	7.234	0.916	7.234
3	30	0	6.776	1.833	6.776
4	45	0	6.318	2.749	6.318
5	0	15	7.234	0.916	7.234
6	0	30	6.776	1.833	6.776
7	0	45	6.318	2.749	6.318

7.3 Modelling Considerations

Horizontal and vertical bend models in Figs. 7.1 and 7.2 include gravity forces. Boundary conditions at pipe ends are identical to those described at Section 4.5. The structural mesh is as defined in Section 4.5.1.3. The fluid mesh for angle variations $(0^{\circ},15^{\circ},30^{\circ},45^{\circ})$ is modified to achieve convergence by reducing the longitudinal dimension of the fluid element from 170 mm to 85 mm. The fluid mesh in the radial and circumferential directions is kept as defined in Section 4.5.2.2.

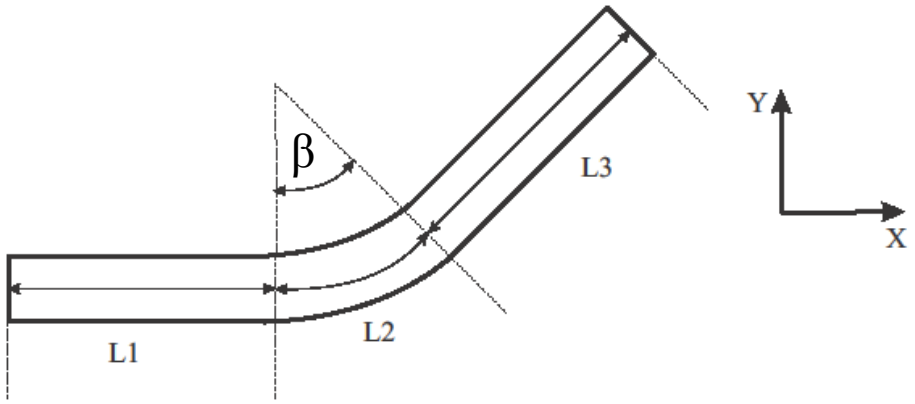

Figure 7. 1 - Geometry of the elevated horizontal bend

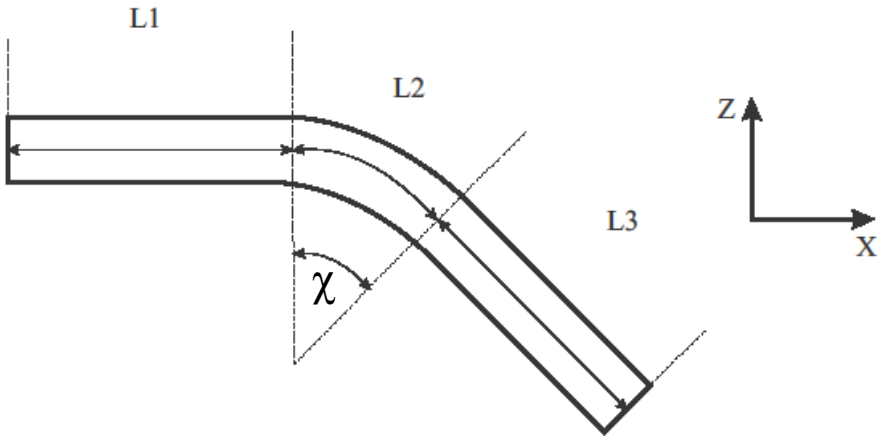

Figure 7. 2 - Geometry of the elevated vertical bend

7.4 Interpretation of Results

When comparing results, the magnitude of a fluid and structural output field O corresponding to variation input design parameter I (angle of horizontal bend or angle of vertical bend) compared to its value in the reference case R is quantified using the same variation criterion $\Psi_R(I,O)$ defined Chapter 6. The output variables O of interest in this chapter are the pressure (p) and the von-Mises stress (σ_{vm}).

7.5 Results for Parametric Runs related to Horizontal Bend Angle

Section 7.5 presents the effect of a horizontal bend on the fluid and structural fields between 0.00 and 0.07 seconds. Results based on the reference model (with zero horizontal bend 0°) are compared with those based on the three horizontal bend angles of (15°, 30°, and 45°).

7.5.1 Results and discussion

Figures. 7.3 and 7.4 indicate that the bend angle has an effect on the fluid steady-state results. For comparison, the dynamic pressure scale on the contour plots is kept constant within -10 kPa and -5.0 kPa. Also, the velocity scale is kept constant within 2.9 m/s and 4.4 m/s. Figure 7.3 shows that dynamic pressure decreases on the inside of the bend from -7.0 kPa for β=0°, -8.5 kPa for β=15°, -9.5 kPa for β=30° to -10 kPa for β=45°. It also shows that dynamic pressure increases on the outside of the bend from -7.0 kPa for β=0°, -6.0 kPa for β=15°, -5.5 kPa for β=30° to -5.0 kPa for β=45°.

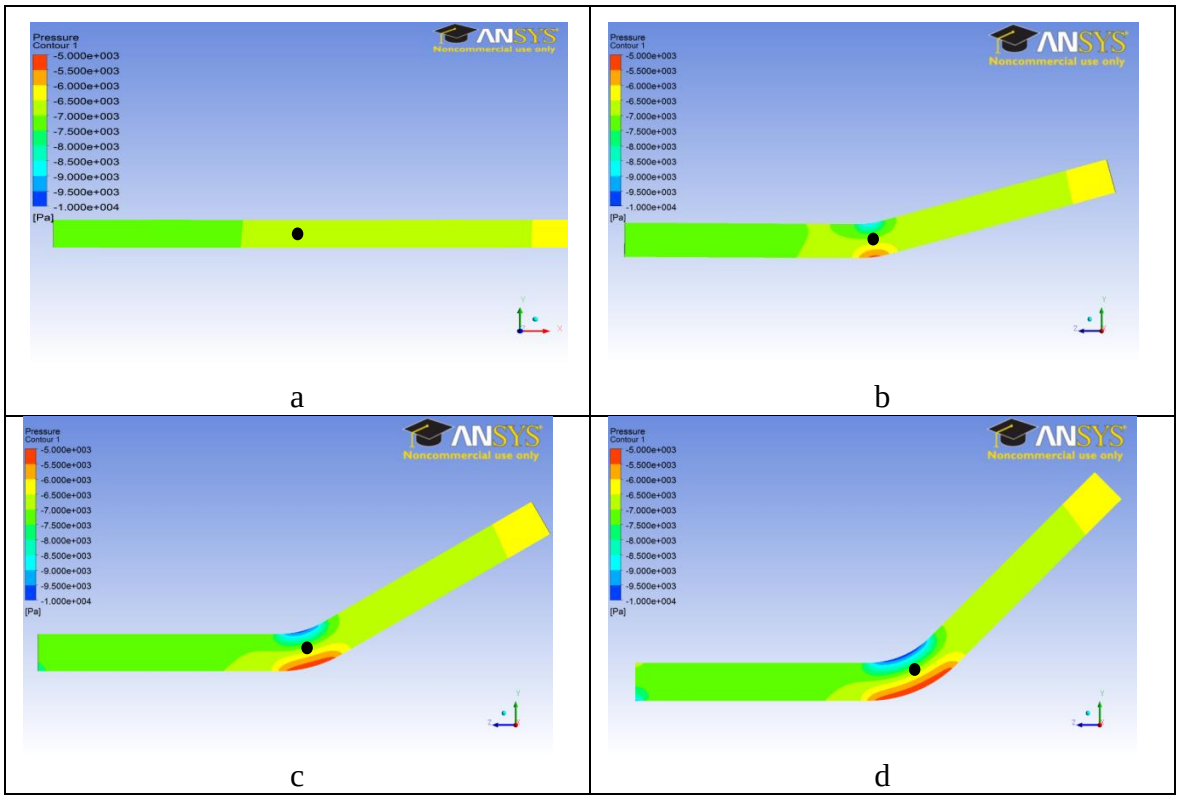

Figure 7. 3 - Pressure Contours for various Horizontal Bend angles β (a) $\beta = 0$ (b) $\beta = 15°$ (c) $\beta = 30°$ (d) $\beta = 45°$

Figure 7.4 shows that velocity increases on the inside of the bend from 3.65 m/s for β=0°, 3.95 m/s for β=15°, 4.25 m/s for β=30° to 4.40 m/s for β=45°. It also shows that velocity decreases on the outside of the bend from 3.95 m/s for β=0°, 3.5 m/s for β=15°, 3.35 m/s for β=30° to 3.2 m/s for β=45°.

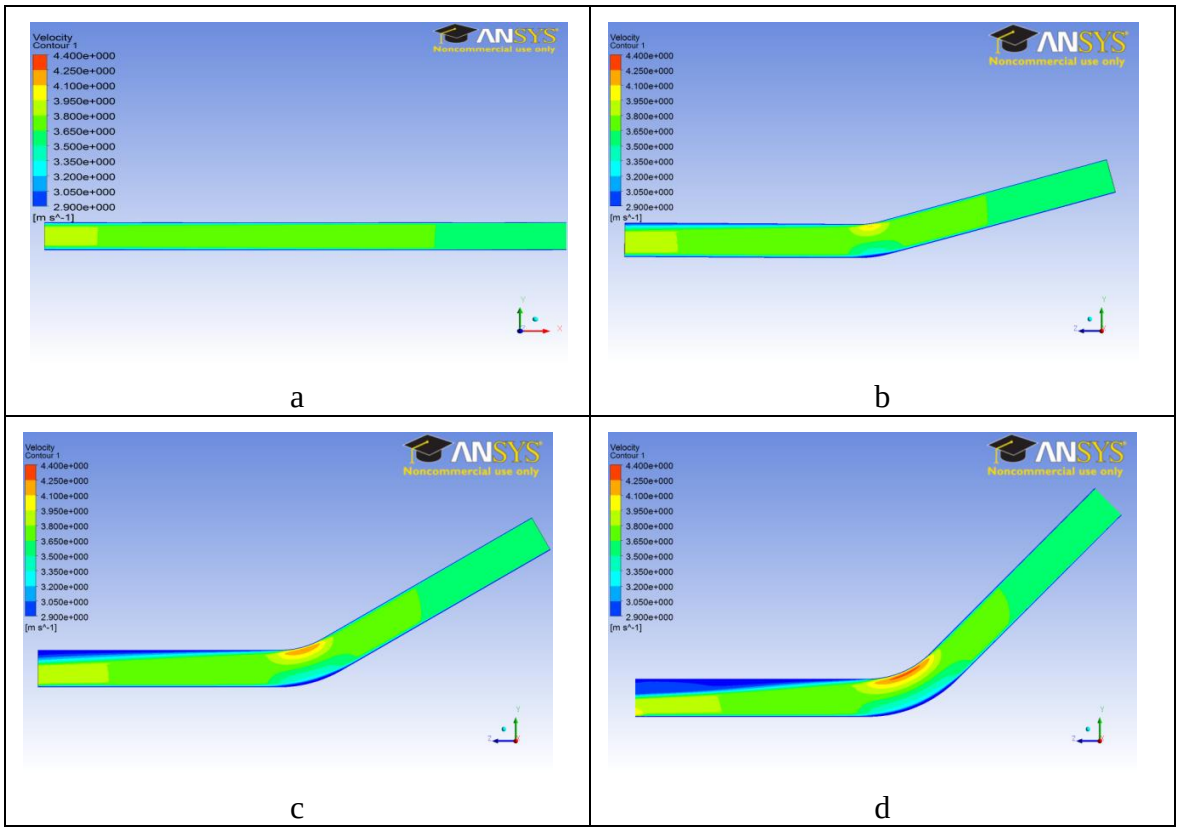

Figure 7. 4 - Velocity Contours for Various Horizontal Bend Angles β (a) $\beta =$ 0° (b) $\beta =$ 15° (c) $\beta =$ 30° (d) $\beta =$ 45°

Figures. 7.5-7.7 show that the horizontal bend angle is observed to have an effect on the structural steady-state results. Figure 7.5 shows the deformed configuration of the bend using a magnification factor of 10.

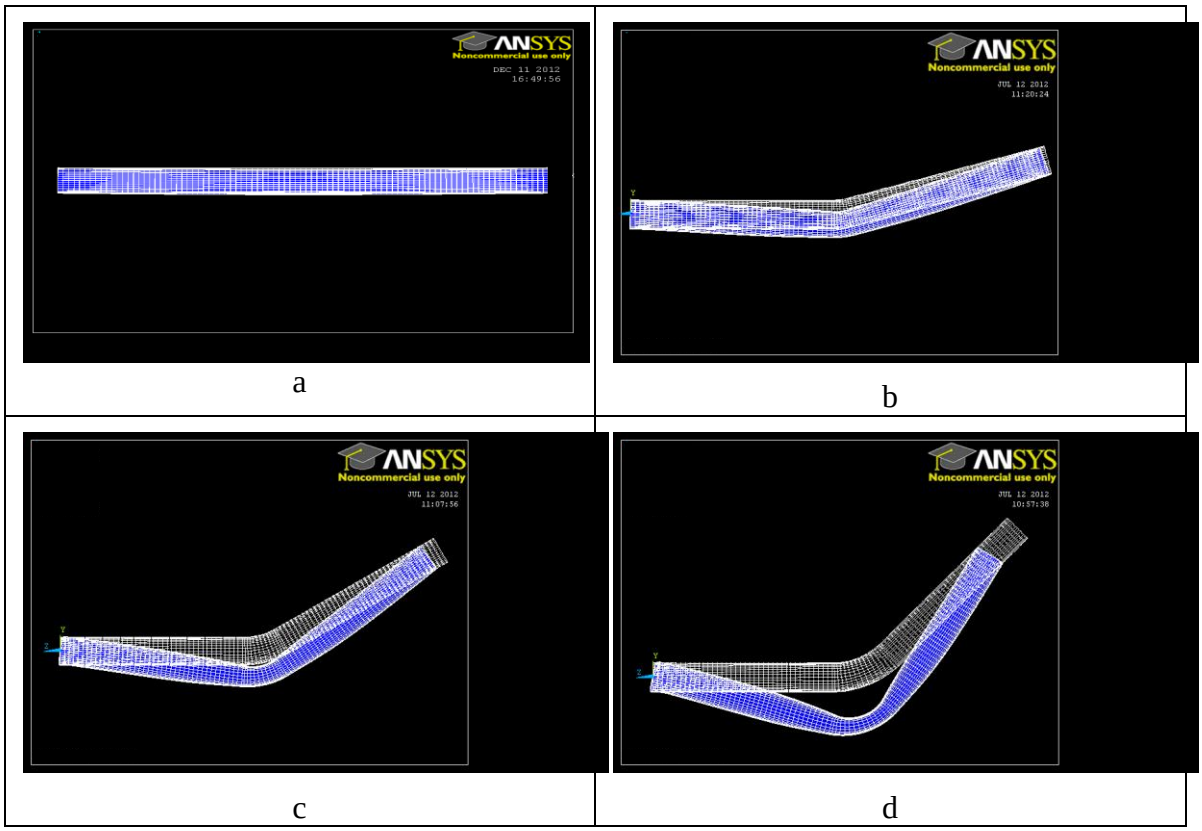

Figure 7. 5 - Deformed Configuration for Various Horizontal Bend Angles β (a) $\beta = 0°$ (b) $\beta = 15°$ (c) $\beta = 30°$ (d) $\beta = 45°$

Figures 7.6 and 7.7 show the von-Mises stress values for each horizontal bend angle. For comparison, von-Mises stresses contour scale is kept constant within 0 MPa and 1000 MPa. Table 7.2 gives the maximum von-Mises stress values for each bend angle shown in Figs. 7.6 and 7.7. The maximum value increases from 139.6 MPa for β=0° until 937.4 MPa for β=45°. Figure 7.7 shows that as the angle of the bend increases, the maximum von-Mises stress moves from the inside of the bend towards the outside. This is caused by the narrowing effect within the bent section.

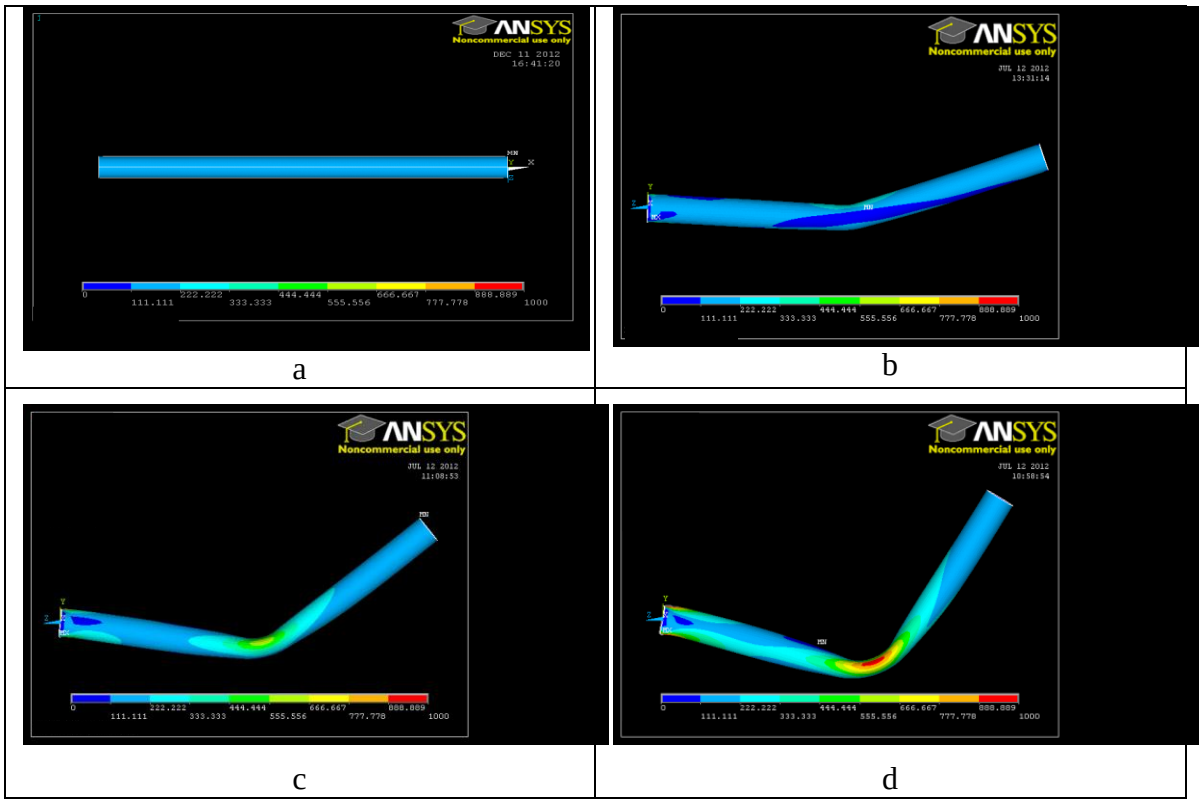

Figure 7. 6 - Plan View of von-Mises Stress contour plots for Various Horizontal Bend Angles β (a) $\beta =$ 0° (b) $\beta =$ 15° (c) $\beta =$ 30° (d) $\beta =$ 45°

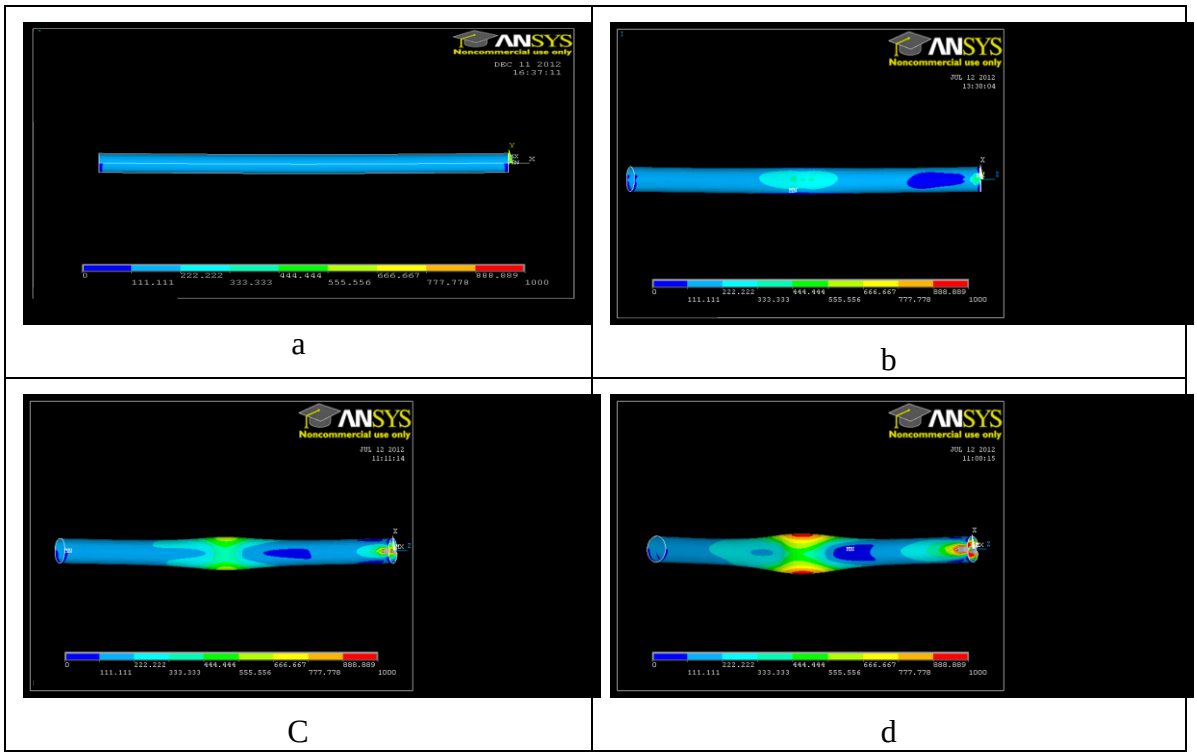

Figure 7. 7 - Elevated View of von-Mises Stress contour plots for Various Horizontal Bend Angles β

(a) $\beta =$ 0° (b) $\beta =$ 15° (c) $\beta =$ 30° (d) $\beta =$ 45°

Table 7. 2 - Maximum von-Mises steady state stress for the horizontal bend

Horizontal Bend Angle β (Degrees)	Maximum von Mises Stress σ_{vm} (MPa)
0°	139.6
15°	345.8
30°	628.3
45°	937.4

Fluid results from transient regime in Figs 7.8 a-d are extracted at the black dot location marked in Figs. 7.3 a-d. In the longitudinal direction, this point is located at pipe mid-span. In the radial direction, it is located at the centre of the pipe. Figure 7.8 b shows that the peak transient pressure starts at a maximum value of about 423.7 kPa for the reference case, attains a maximum value of about 458.5 kPa at a bend angle of 15 degrees and from this peak value, the magnitude of the peak transient pressure is observed to decrease to about 363.9 kPa at a bend angle of 45 degrees. These peak transient pressures correspond to a highest peak total pressure value of 4926 kPa occurring at a bend angle of 15 degrees (Fig. 7.8a) and a lowest peak pressure of 4831 kPa at a bend angle of 45 degrees.

Also, Fig. 7.8 d shows that as the angle of bend increases, the magnitude of the relative velocity increases. When superimposed on the steady state velocity, the difference between the resulting absolute velocities is observed to be negligible as depicted in Fig. 7.8c.

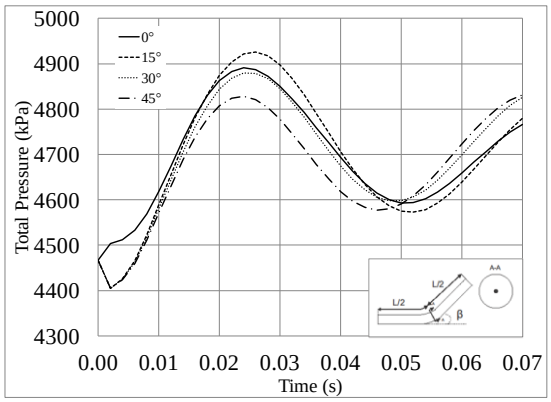

a

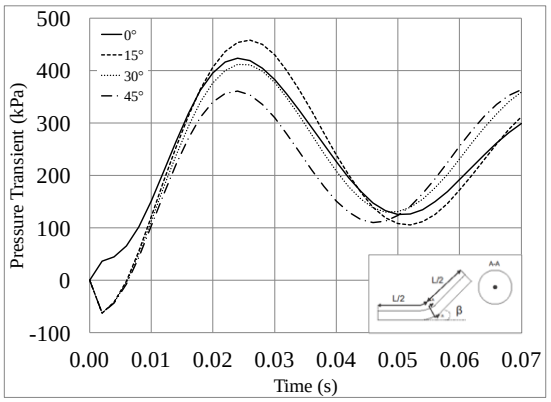

b

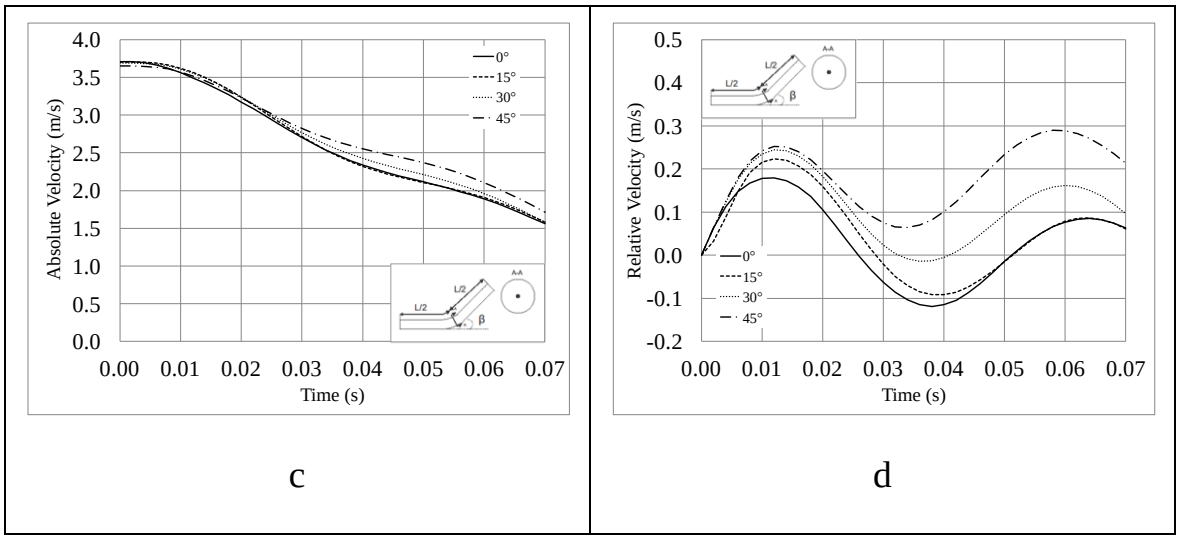

Figure 7. 8 - Effect of Horizontal Bend Angle on (a) Total Pressure, (b) Transient Pressure, (c) Absolute Velocity, (d) Relative Velocity

For each horizontal bend angle considered, the maximum von-Mises stresses within the pipe wall are extracted from transient regime, and the von-Mises history plotted in Figs. 7.9 a-b. It is observed that the maximum transient von-Mises stress increases with the bend angle. It is clear that the total von-Mises for $15^{\circ}, 30^{\circ}, 45^{\circ}$ angles exceed the allowable stress for the steady and transient states as given by Eq. 3.9 for steel grade ASTM A1018. Such situations can be remedied by adopting higher steel grades such ASTM A517 with a tensile strength S_y of 689.47 MPa for the 15° bend angle if the pipe thickeness is to be kept at 19.05mm. For the 30° and 45° bends, additional supports at the bend would be needed.

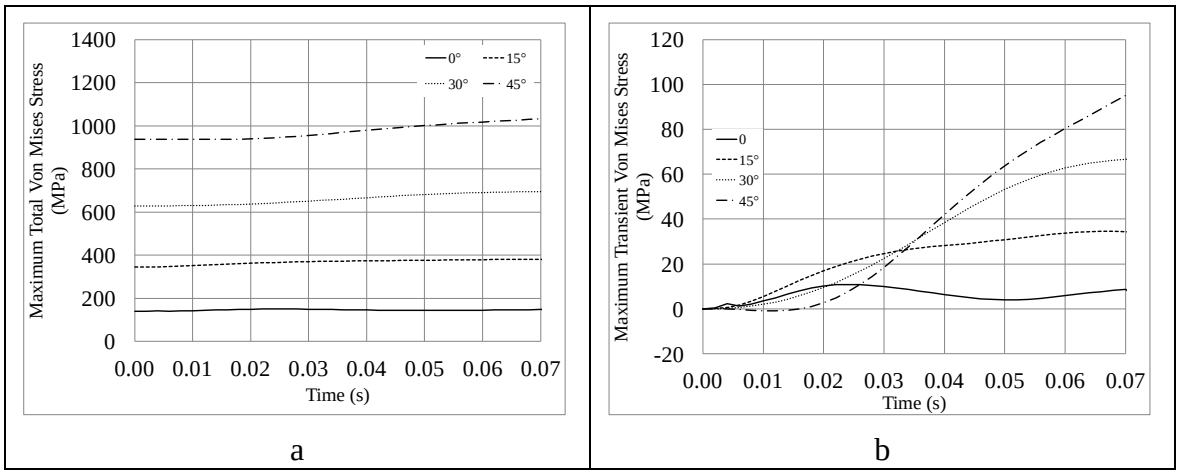

Figure 7. 9 - Effect of Horizontal Bend Angle on (a) Maximum Total von-Mises Stress, and (b) Maximum Transient von-Mises Stress

7.5.2 Sensitivity of Results to Horizontal Bend Angle

Tables 7.3 and 7.4 present the sensitivity of the pressure and von-Mises stress values respectively to the horizontal bend angle. The sensitivity is assessed based on the variation parameter Ψ_R introduced in Eq. 6.1 from their value in the reference case.

The steady state pressure is observed not to be impacted by the horizontal bend angle. In the transient state, the static pressure is observed to be slightly influenced by the horizontal bend angle. However, as observed in Fig. 7.8b, the variation parameter value shows a non-monotonic relationship with the horizontal bend angle. A more refined study based on smaller bend angle increments would be required to more accurately determine the horizontal angle corresponding the higher transient pressure. Given the high magnitude of the high steady state pressure, it is observed that the total pressure is barely influenced by the horizontal angle. In contrast, the von-Mises stress is observed to be greatly impacted by the horizontal bend angle, both in the steady state and transient regime. Figs 7.10 a-b show the total and transient von-Mises stress in function of horizontal bend angles.

Table 7. 3 - Sensitivity of Pressure on Horizontal Bend Angle

	Steady-State		Transient State		Total	
	Pressure p (kPa)	$\Psi_R(\beta,p)$	Pressure p (kPa)	$\Psi_R(\beta,p)$	Pressure p (kPa)	$\Psi_R(\beta,p)$
0 ° (Ref.)	4467	-	423.7	-	4891	-
15°	4467	0.00%	458.5	8.2%	4926	0.71%
30°	4467	0.00%	412.3	-2.69%	4879	-0.23%
45°	4467	0.00%	363.9	-14.1%	4831	-1.22%

Table 7. 4 - Sensitivity of von-Mises Stress on Horizontal Bend Angle

	Steady-State		Transient State		Total	
	von Mises Stress σ_{vm} (MPa)	$\Psi_R(\beta,\sigma_{vm})$	von Mises Stress σ_{vm} (MPa)	$\Psi_R(\beta,\sigma_{vm})$	von Mises Stress σ_{vm} (MPa)	$\Psi_R(\beta,\sigma_{vm})$
0 ° (Ref.)	139.6	-	10.85	-	150.5	-
15°	345.8	148%	34.58	219%	380.4	153%
30°	628.3	350%	66.83	516%	695.1	362%
45°	937.4	571%	104.4	862%	1042	592%

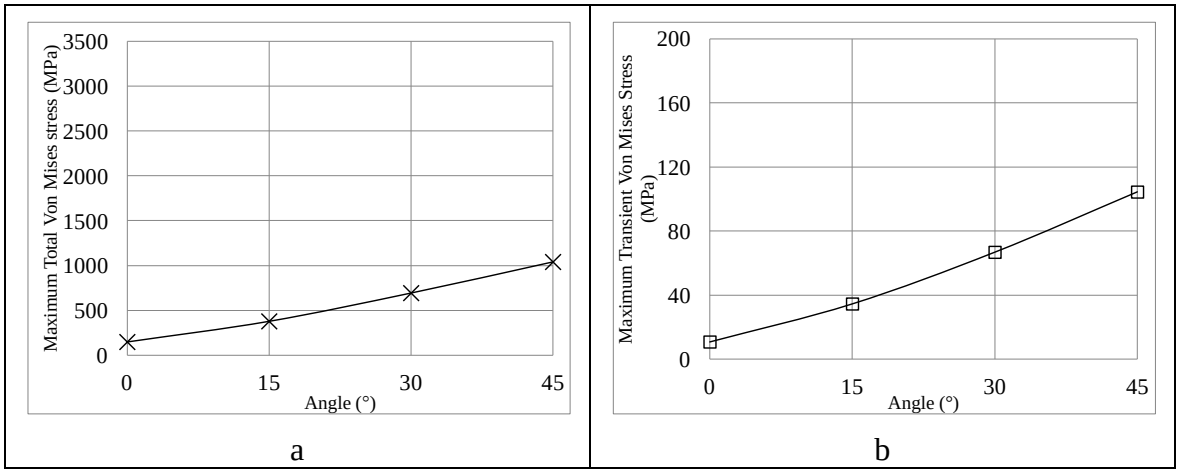

Figure 7. 10 - Effect of horizontal bend angle on von-Mises a) Total Stress, b) Transient Component of the Stress

7.6 Results based on Parametric Runs related to Vertical Bend Angle

Section 7.6 presents the effect of a vertical bend on the fluid and structural fields between 0.00 and 0.07 seconds. Results based on the reference model (with zero horizontal bend 0°) are compared with those based on the three vertical bend angles of (15°, 30°, and 45°).

7.6.1 Results and discussion

Figures 7.11 and 7.12 indicate that the bend angle has an effect on the fluid steady-state results. For comparison, the dynamic pressure scale on the contour plots is kept constant within -10 kPa and -5.0 kPa. Also, the velocity scale is kept constant within 2.9 m/s and 4.4 m/s. Figure 7.11 shows that dynamic pressure decreases on the inside of the bend from -7 kPa for β=0°, -8.5 kPa for β=15°, -9.5 kPa for β=30° to -10 kPa for β=45°. It also shows that dynamic pressure increases on the outside of the bend from -7.0 kPa for β=0°, -6.0 kPa for β=15°, -5.5 kPa for β=30° to -5.0 kPa for β=45°.

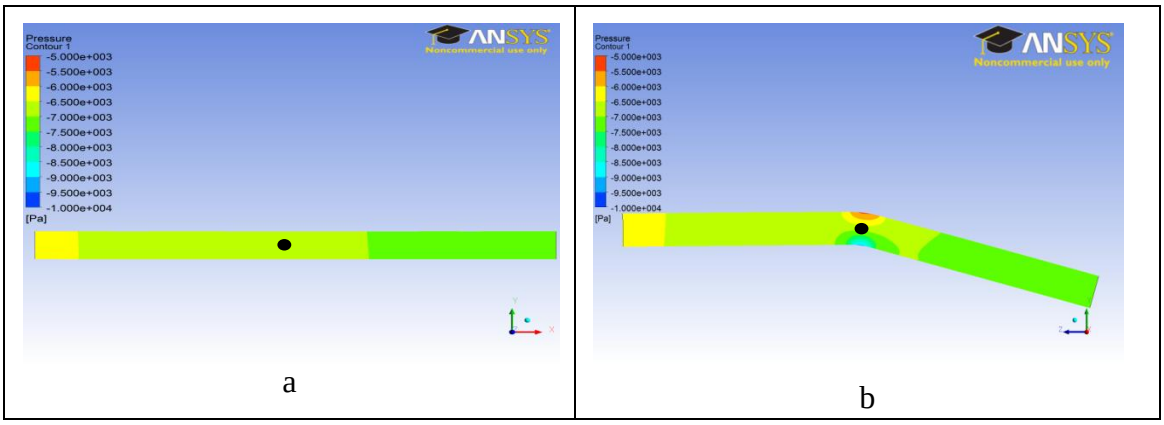

a b

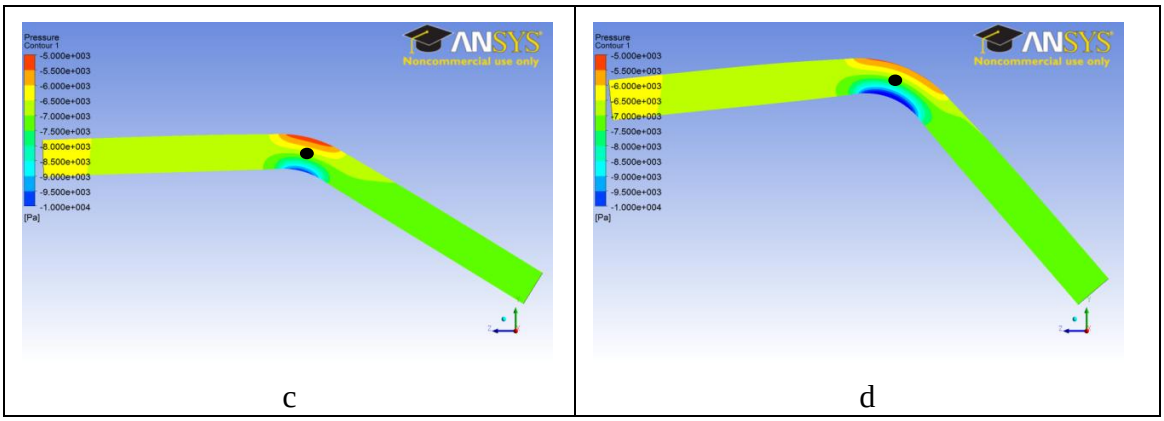

Figure 7. 11 - Pressure Contours for various Vertical Bend angles χ (a) $\chi = 0$ (b) $\beta = 15°$ (c) $\beta = 30°$ (d) $\beta = 45°$

Figures 7.12 a-d show that the velocity increases on the inside of the bend from 3.65 m/s for β=0°, 3.95 m/s for β=15°, 4.25 m/s for β=30° to 4.40 m/s for β=45°. It also shows that dynamic pressure decreases on the outside of the bend from -7.0 kPa for β=0°, -6.0 kPa for β=15°, -5.5 kPa for β=30° to -5.0 kPa for β=45°.

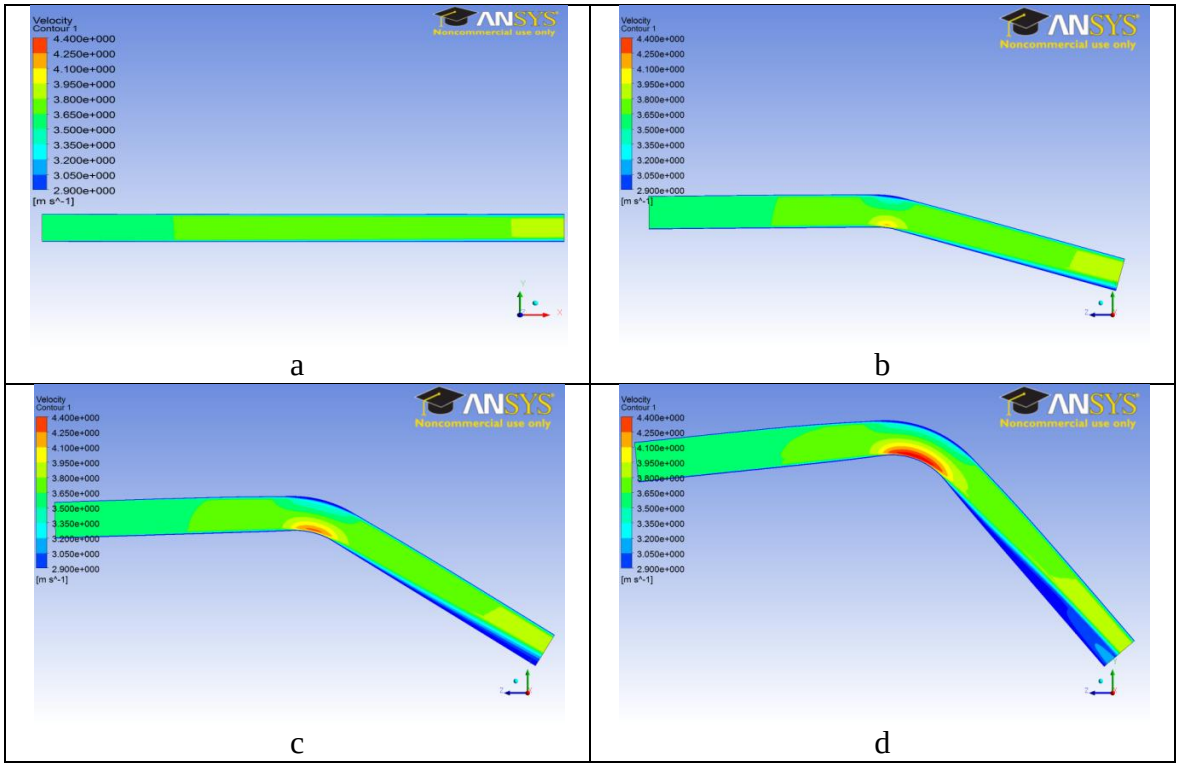

Figure 7. 12 - Velocity Contours for Various Vertical Bend Angles χ (a) $\chi = 0°$, (b) $\chi = 15°$, (c) $\chi = 30°$, and (d) $\chi = 45°$

Figs. 7.13-7.15 show that the vertical bend angle has an effect on the steady-state von-Mises stresses. Figure 7.13 shows the deformed configuration of the various pipe configurations considered using a magnification factor of 5.

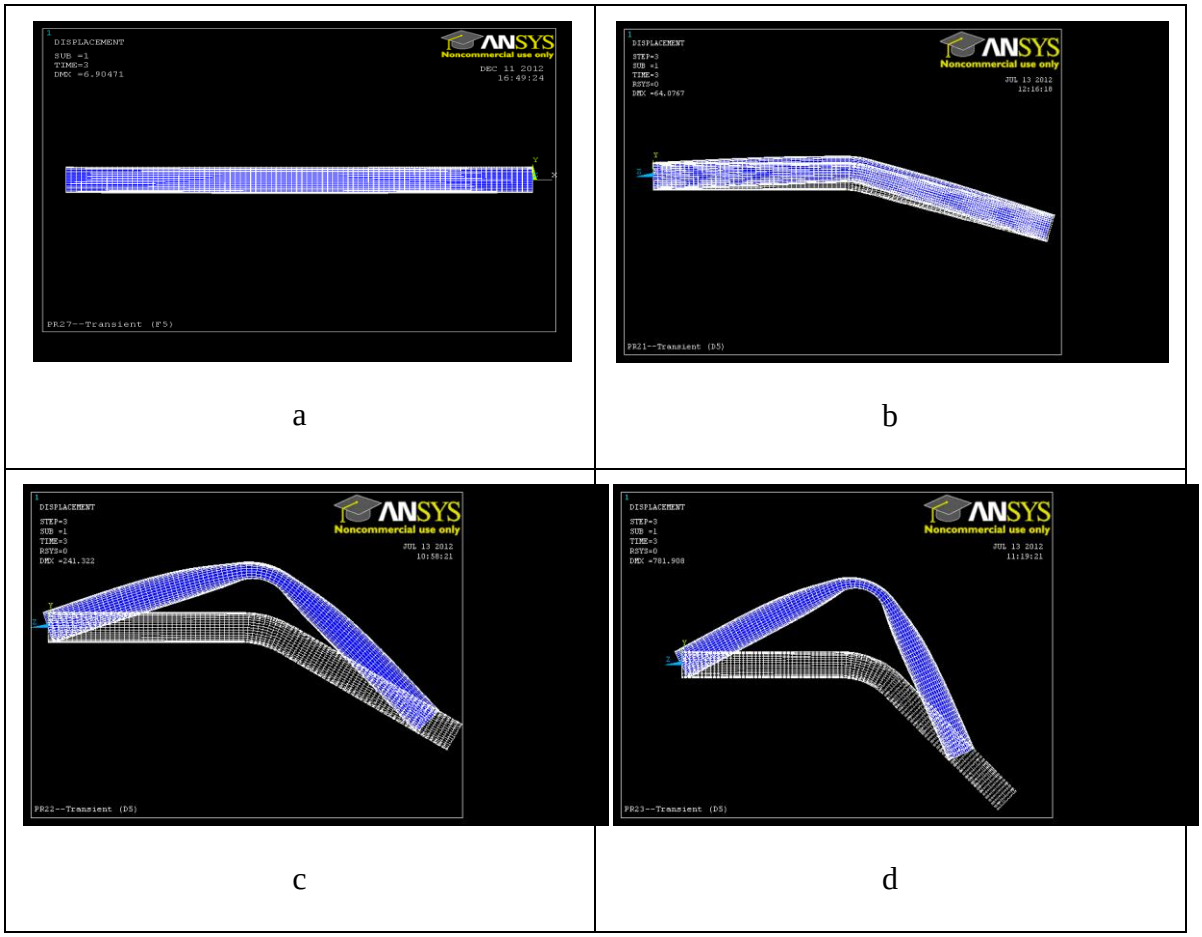

Figure 7. 13 - Deformed Configuration for Various Vertical Bend Angles χ (a) $\chi = 0°$ (b) $\chi = 15°$ (c) $\chi = 30°$ (d) $\chi = 45°$

Figures 7.14 and 7.15 show the von-Mises stress values for each vertical bend angle. For comparison, von-Mises stresses contour scales are kept constant within 0 MPa and 3200 MPa. Table 7.5 gives the maximum von-Mises stress value as a function of the vertical bend angle shown in Figs. 7.14 and 7.15. The maximum value increases from 139.6 MPa for β=0° up to 3,278 MPa for β=45°, clearly showing the need for anchoring details at the bent pipes. Figure 7.15 shows that as the angle of the bend increases, the maximum von-Mises stress moves from the inside of the bend towards the outside. This is caused by the narrowing effect of the bent section.

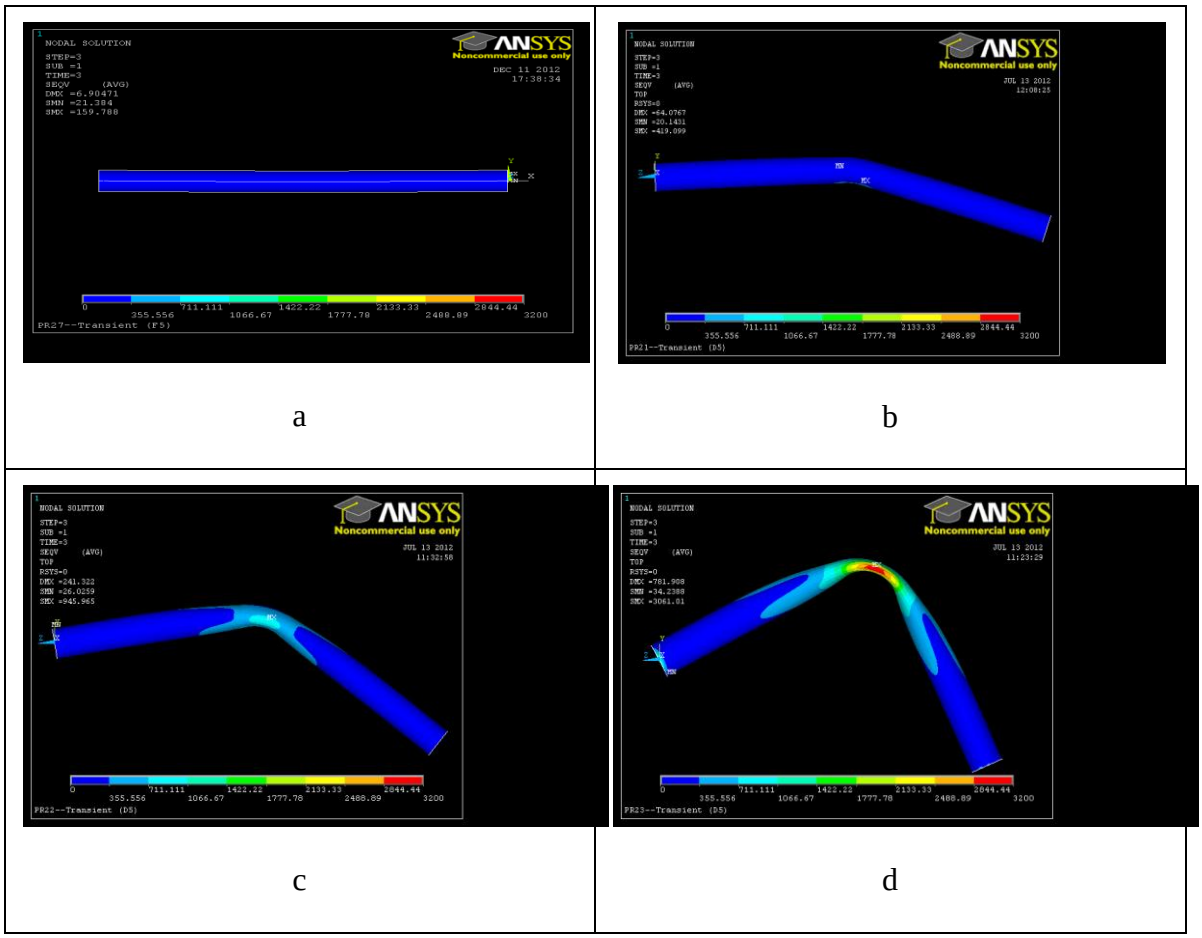

Figure 7. 14 - Elevation Views of von-Mises Stress Contour Plots for Various Vertical Bend Angles χ (a) $\chi = 0°$, (b) $\chi = 15°$, (c) $\chi = 30°$, and (d) $\chi = 45°$

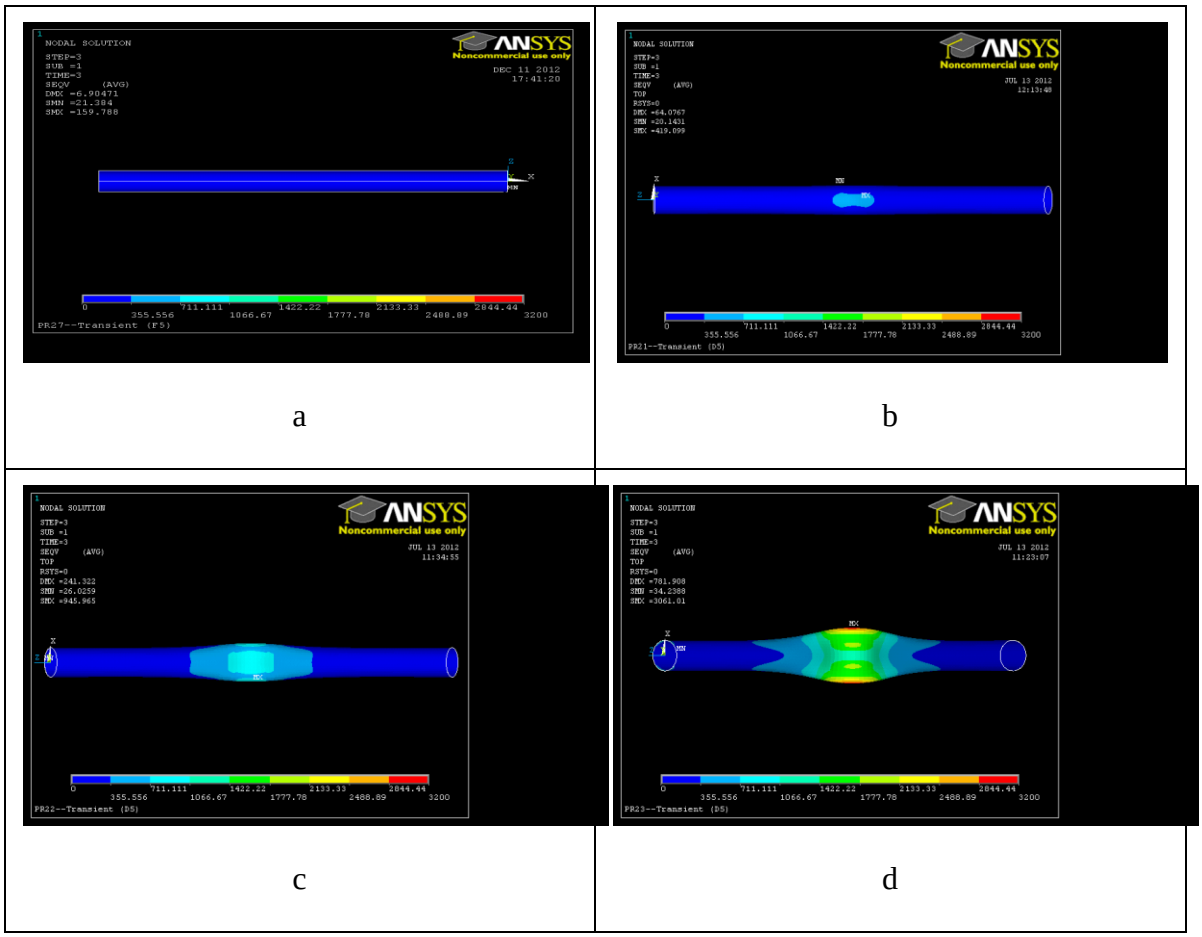

Figure 7. 15 – Plan Views for von-Mises contour plots for Various Vertical Bend Angles χ (a) $\chi =$ 0°, (b) $\chi = 15°$, (c) $\chi = 30°$, and (d) $\chi = 45°$

Table 7. 5 - Maximum steady state von-Mises stress for various vertical bend angles

Vertical Bend Angle χ (Degrees)	Maximum von Mises Stress σ_{vm} (MPa)
0°	139.6
15°	420.6
30°	1025
45°	3278

Fluid results from transient regime in Figs 7.16 a-d are extracted at black dot location shown in Figs. 7.11 a-d. In the longitudinal direction, the black dot is located at pipe mid-span. In the radial direction, it is located at the centre of the pipe. Figures 7.16 show that for the straight pipe, the peak transient pressure is 423.7 MPa. For the other vertically bent penstock, the peak transient pressure is observed essentially to be independent of the vertical bend angle. Figure 7.16 c shows the total velocity history to be insensitive of the bend angle while Fig. 7.16d shows the relative velocity history. No clear trend can be inferred from the figure.

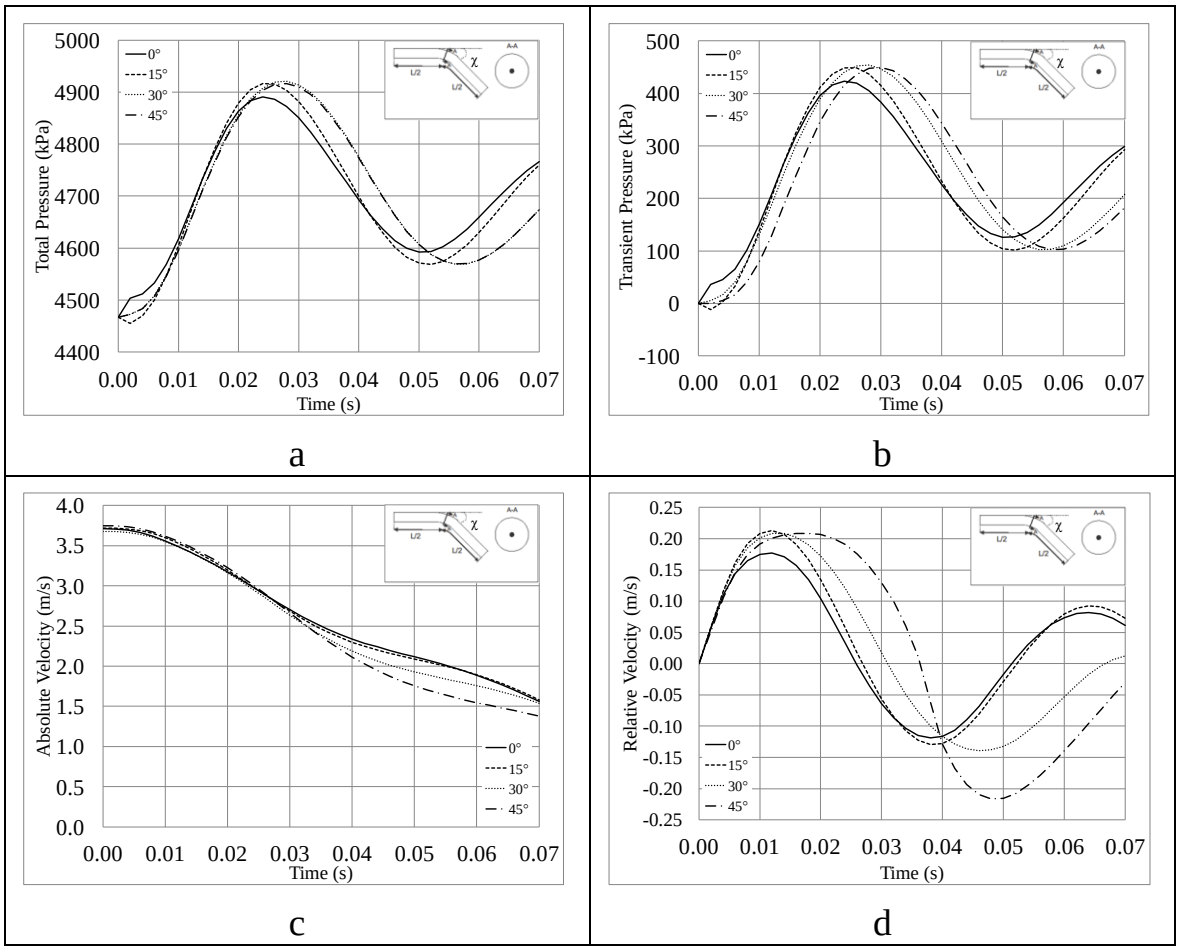

Figure 7. 16 - Effect of Vertical Bend Angle on (a) Total Pressure, (b) Transient Pressure, (c) Absolute Velocity, (d) Relative Velocity

The von-Mises stresses for transient regime are extracted and plotted against time in Figs. 7.17 a-b at the peak location. As the bend angle increases, the maximum transient von-Mises stress increases. It is clear that the maximum total von-Mises stress predicted for

$15^{\circ}, 30^{\circ}, 45^{\circ}$ vertical bend angles do not satisfy the allowable stress limit as given (Eq. 3.9) for the steady and transient states for ASTM A1018 steel grade. A higher grade (ASTM A517) with a tensile strength S_y of 689.47 MPa should be used for the 15° angle. Proper anchoring details which control the movement of the bend are needed at the location of the bend for $\chi = 30^{\circ}, 45^{\circ}$.

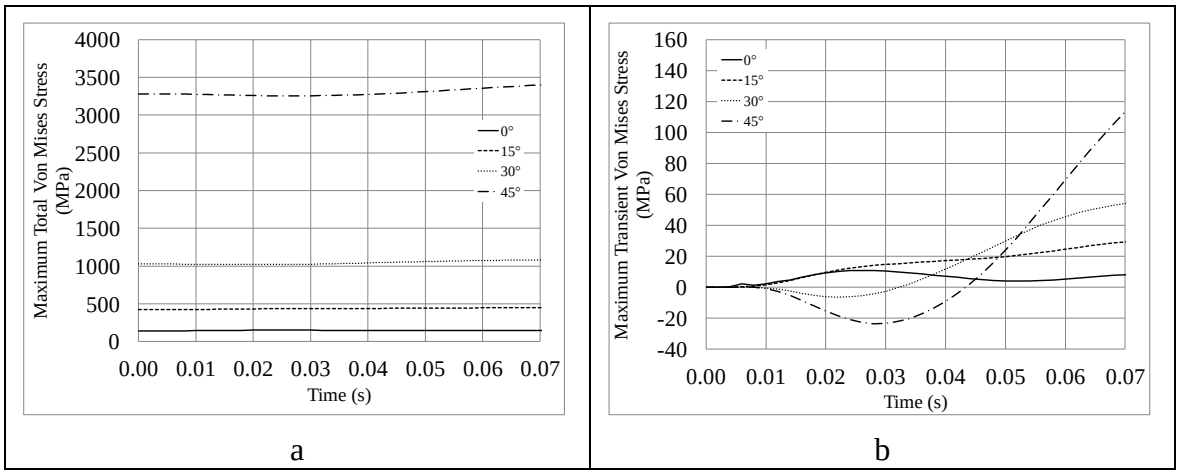

Figure 7. 17 - Effect of vertical bend angle on (a) Maximum Total von-Mises Stress, (b) Maximum Transient von-Mises Stress

7.6.2 Sensitivity of Results to the Vertical Bend Angle

Tables 7.6 and 7.7 present the sensitivity of the pressure and von-Mises stress values respectively. The sensitivity of each field is assessed based on the variation parameter introduced in Eq. 6.1 from their value in the reference case.

The steady state pressure is observed to be independent of the vertical bend angle while the transient pressure is observed to be very slightly influenced by the vertical bend angle. The corresponding total pressure is found insensitive to the vertical bend angle, given the high steady state component of the pressure compared to the transient pressure magnitude. In contrast, the von-Mises stress is observed to be greatly impacted by the vertical bend angle both in the steady state and the transient state. Fig 7.18 shows the total and transient von-Mises stress in function of different bending angle in the vertical plan.

Table 7. 6 - Sensitivity of Pressure on Vertical Angle

	Steady-State		Transient State		Total	
	Pressure p (kPa)	$\Psi_R(\chi,p)$	Pressure p (kPa)	$\Psi_R(\chi,p)$	Pressure p (kPa)	$\Psi_R(\chi,p)$
0 ° (Ref.)	4467	-	423.7	-	4891	-
15°	4467	0.00%	450.0	6.21%	4917	0.54%
30°	4467	0.00%	453.8	7.10%	4921	0.62%
45°	4467	0.00%	449.4	6.07%	4916	0.53%

Table 7. 7 - Sensitivity of von-Mises stress on Vertical Angle

	Steady-State		Transient State		Total	
	Pressure p (kPa)	$\Psi_R(\chi,p)$	Pressure p (kPa)	$\Psi_R(\chi,p)$	Pressure p (kPa)	$\Psi_R(\chi,p)$
0 ° (Ref.)	4467	-	423.7	-	4891	-
15°	4467	0.00%	449.0	5.97%	4916	0.52%
30°	4467	0.00%	453.8	7.10%	4921	0.62%
45°	4467	0.00%	449.4	6.07%	4916	0.53%

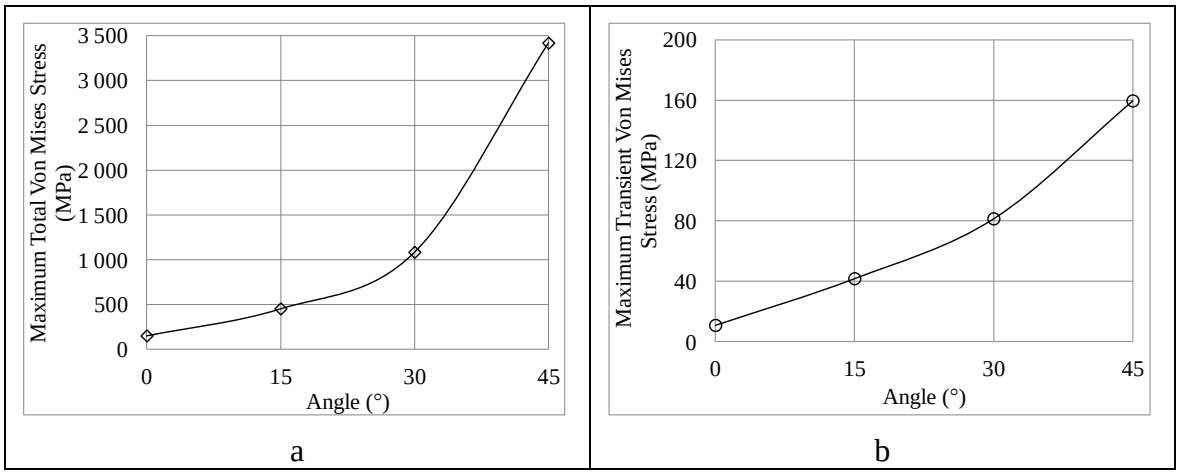

Figure 7. 18 - Effect vertical bend angle on von Mises a) Total Stresses, b) Transient Component of the Stress

7.7 Horizontal Bends versus Vertical Bends

A comparative study on the von-Mises stress between the horizontal bend angle (β) and vertical bend angle (χ) angles for four angle values (0°,15°,30°,45°) is provided in Figs. 7.19-7.20

Figure 7.19 compares the relationships for the transient von-Mises stress for the horizontal and vertical bends. For a given bend angle, the vertical bend is associated with a higher transient von-Mises stress than the horizontal bend. As the bend angle increases, the increase in transient von-Mises stress is observed to be more significant than the increase in transient von-Mises stress for an equal horizontal bend angle. A similar trend is observed in Fig. 7.20 which provides a comparison for the total von-Mises stresses.

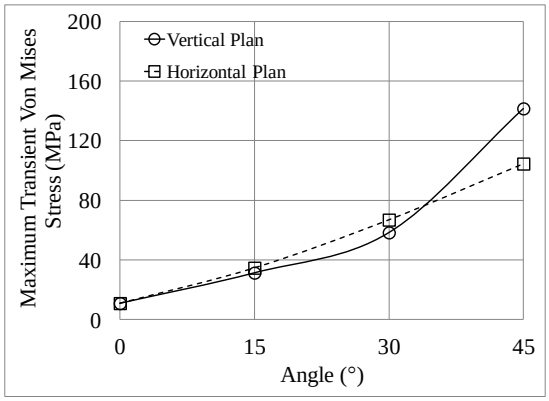

Figure 7. 19 - Effect of horizontal and vertical bend angles for Transient von-Mises Stresses

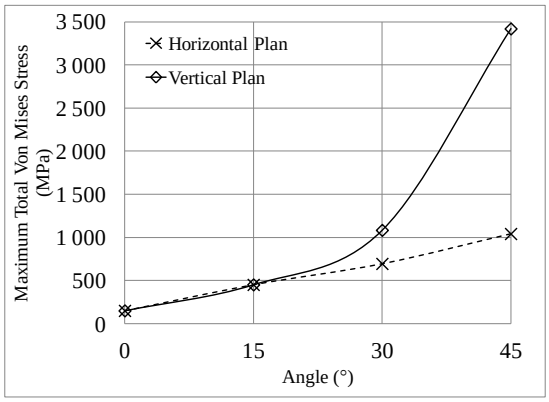

Figure 7. 20 - Effect of horizontal and vertical bend angles for Total von-Mises Stresses

7.8 Conclusion

Chapter 7 presented a comparative study on horizontal and vertical bend angles and quantified on their influence on the internal pressure and velocity fields as well as the von-Mises stresses.

1. The analysis indicates that horizontal and vertical bend angles have a negligible influence on the transient pressure and a moderate influence on the velocity.
2. Conversely, the presence of bends is observed to cause a sharp increase in the transient and total von-Mises stresses, showing the necessity of providing proper anchoring details at the bend location.
3. The vertical bend angle is observed to cause an increase in the von-Mises stresses that is more significant than the horizontal bend angle of the same magnitude.

CHAPTER 8 – COMPARATIVE STUDY OF BURIED HORIZONTALLY BENT PENSTOCKS

8.1 Objectives

This chapter presents a comparative study based on the model developed in Chapter 4 for an additional design parameter: the subgrade modulus. Towards this goal, the elevated penstock with 30° horizontal bend introduced in Run 3 of Chapter 7 is considered as a reference case in this chapter and various scenarios of modulus subgrade reactions are investigated and comparisons are made with the results based on the reference case.

8.2 Description of Parametric Runs

The diameter is 1.067 m, thickness is 19.05 mm and the total span of the pipe including the bent segment is 15.384 m. Boundary conditions at pipe ends are identical to those defined in Section 4.5. Three additional scenarios are considered for a subgrade modulus K_s of 20, 50, 100 MN/m³. In all runs straight spans L_1 at the inlet and L_3 at the outlet are equal to 6.776 m, while the middle span of the curved segment L_2 is equal to 1.833 m. Table 8.1 associates the value of each subgrade modulus K_s to a corresponding soil type for all fours runs conducted in this chapter.

Table 8. 1 - Design parameter value changes in the comparative study

Parametric Run	Horizontal Bend Angle β (Degrees)	Subgrade Modulus K_s (MN/m³)	Type of Soil Bowles,J. (1996)	Span L_1 (m)	Span L_2 (m)	Span L_3 (m)
1 (Reference Case)	30	0	-	6.776	1.833	6.776
2	30	20	Loose Sand (4.8-16 MN/m³)	6.776	1.833	6.776
3	30	50	Medium Dense Sand (9.6-80 MN/m³) Clayey medium dense sand (32 -80 MN/m³)	6.776	1.833	6.776
4	30	100	Dense Sand (64-128 MN/m³)	6.776	1.833	6.776

8.3 Modelling Considerations

The buried horizontal bend model in Fig. 8.1 includes gravity forces. The soil behavior is modeled by an elastic foundation normal to the pipe outside surface. The structural mesh

is taken as described in Section 4.5.1.3. The fluid mesh for subgrade variations (0 MN/m³, 20 MN/m³, 50 MN/m³, 100 MN/m³) is modified to achieve convergence by reducing the longitudinal dimension of the fluid element from 170 mm to 85 mm. The fluid mesh in the radial and circumferential directions is kept as defined in Section 4.5.2.2

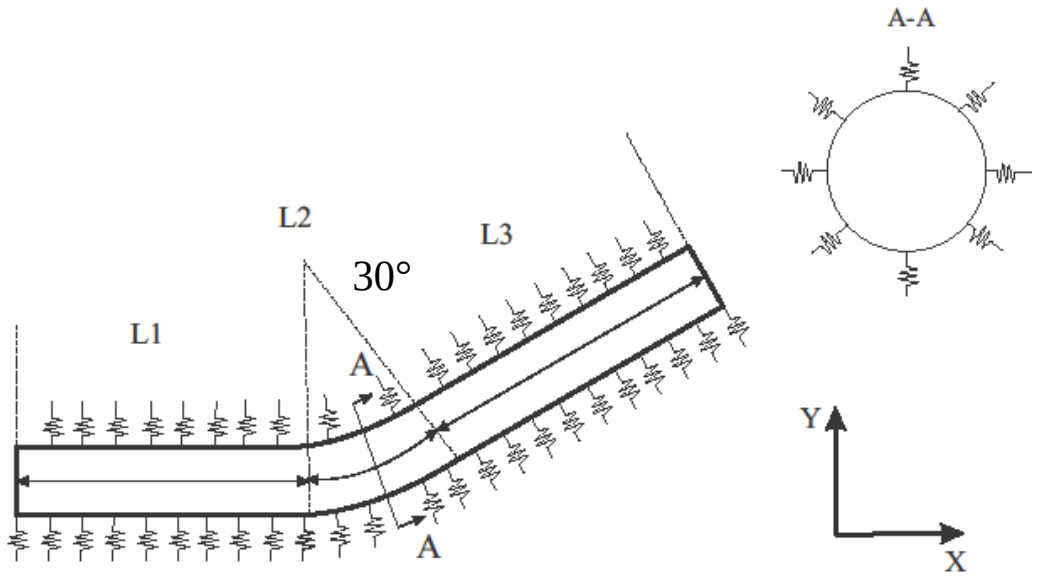

Figure 8. 1 - Geometry of the 30° buried horizontal bend

8.4 Interpretation of Results

When comparing results, the magnitude of a fluid and structural output fields O corresponding to variation input design parameter I (subgrade modulus of soil) compared to its value in the reference case R is quantified using the variation criterion $\Psi_R(I,O)$ as defined in Eq.6.1. The output variables O of interest in this chapter are the pressure (p) and the von-Mises stress (σ_{vm}).

8.5 Results for Parametric Runs related to Subgrade Modulus

Section 8.5 presents the effect of the soil on the fluid and structural fields between 0.00 and 0.07 seconds. Results based on the reference model (with K_s=0 MN/m³) are compared with those based on the three subgrade moduli of (20 MN/ m³, 50 MN/m³, and 100 MN/ m³).

8.5.1 Results and discussion

Figures 8.2 and 8.3 indicate that the subgrade modulus has no effect on the fluid steady-state results. For comparison, the dynamic pressure scale on the contour plot is kept constant within -10 kPa and -5.0 kPa. Also, the velocity scale is kept constant within 2.9 m/s and 4.4 m/s. Figure 8.2 shows that dynamic pressure on the inside of the bend stays constant at -9.5 kPa for each subgrade modulus. It also shows that dynamic pressure on the outside of the bend stays constant at -5.5 kPa. Figure 8.3 shows that velocity on the inside of the bend stays constant at 4.25 m/s. It also shows that velocity on the outside of the bend stays constant at 3.35 m/s.

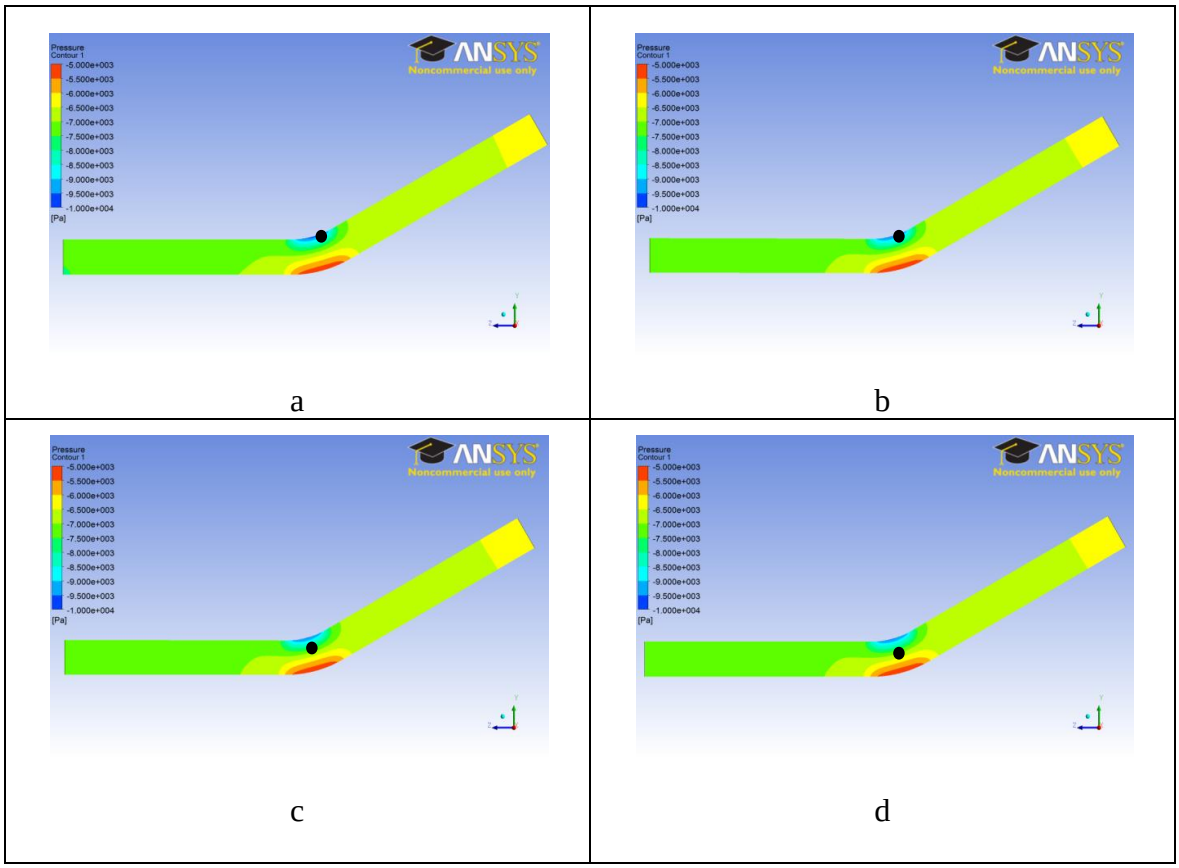

Figure 8. 2 - Dynamic Pressure Contours for various Subgrade Modulus K_s values (a) K_s=0 MN/m³ (b) K_s=20 MN/m³ (c) K_s=50 MN/m³ (d) K_s=100 MN/m³

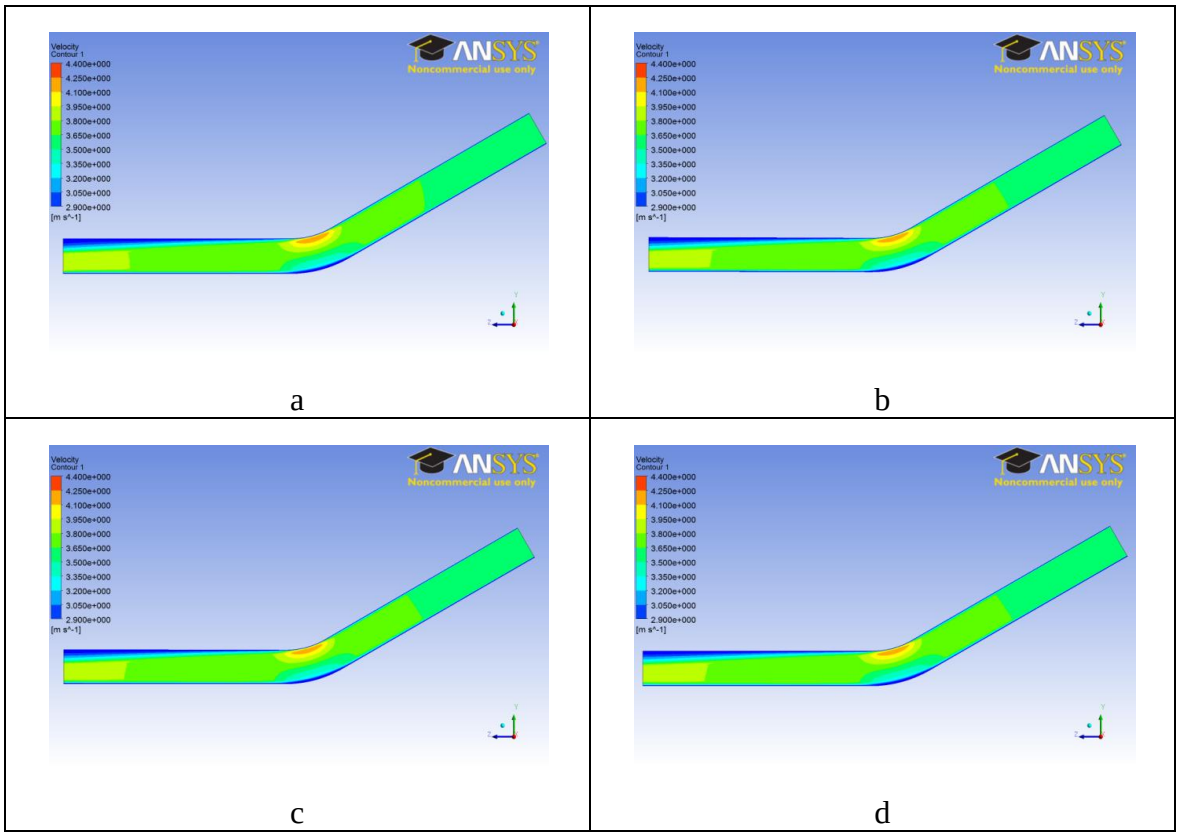

Figure 8. 3 - Velocity Contours for various Subgrade Modulus K_s values (a) K_s=0 MN/m³ (b) K_s=20 MN/m³ (c) K_s=50 MN/m³ (d) K_s=100 MN/m³

Figures 8.4-8.6 show that the subgrade modulus has an effect on the structural steady-state results. Figure 8.4 shows the deformed configuration of the bend using a magnification factor of 10. As expected, the presence of the soil significantly reduces the displacements induced at the bends due to change in momentum of the fluid.

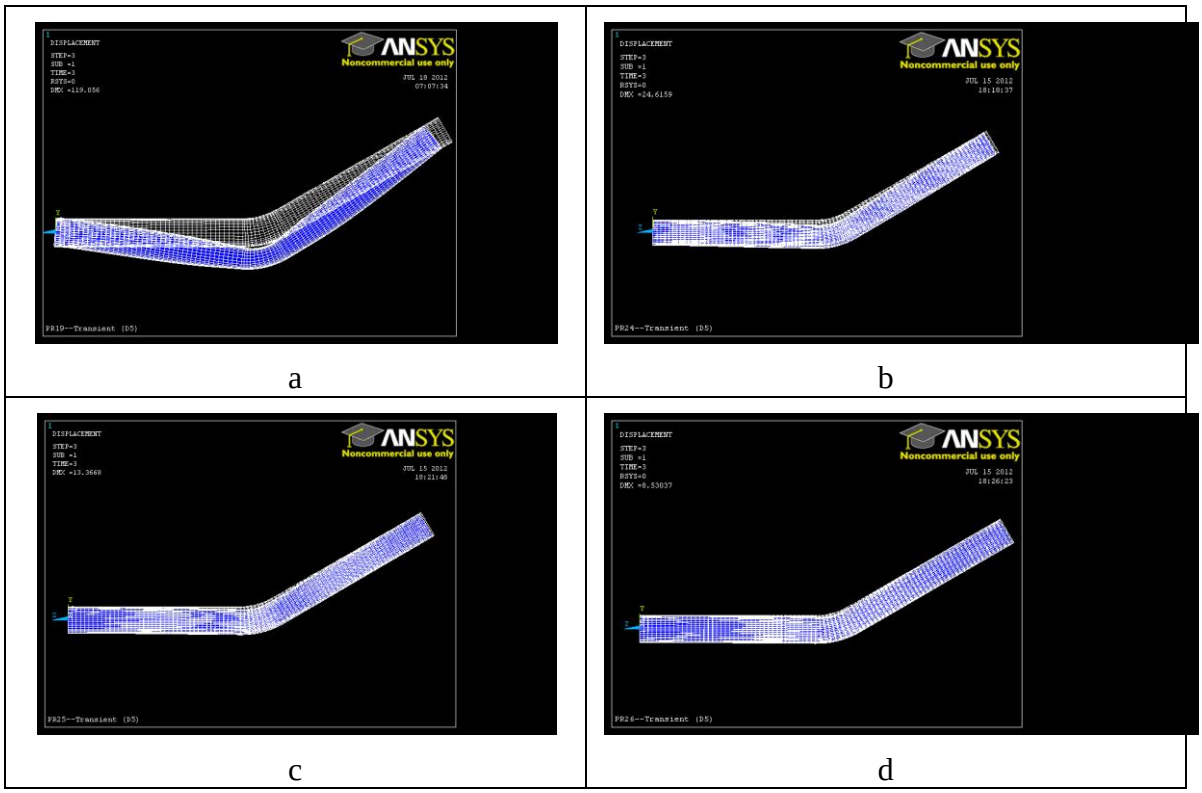

Figure 8. 4 - Deformed Configurations for various Subgrade Modulus K_s values (a) K_s=0 MN/m³ (b) K_s=20 MN/m³ (c) K_s=50 MN/m³ (d) K_s=100 MN/m³

Figures 8.5 and 8.6 show the von-Mises stress values as a function of the subgrade modulus. For comparison, von-Mises stresses contour scale is kept constant within 0 MPa and 600 MPa. Table 8.2 gives the maximum von-Mises stress value for each subgrade modulus shown in Figs. 8.5 and 8.6. The maximum von-Mises stress value sharply decreases from 628.3 MPa for K_s=0 MN/m³ to 243 MPa for the modulus value K_s=20 MN/m³, but then drops gradually to 205.3 MPa for K_s=50 MN/m³ and 188.2 MPa for K_s=100 MN/m³. The comparison illustrates the rather beneficial effect of burying the pipe in the soil.

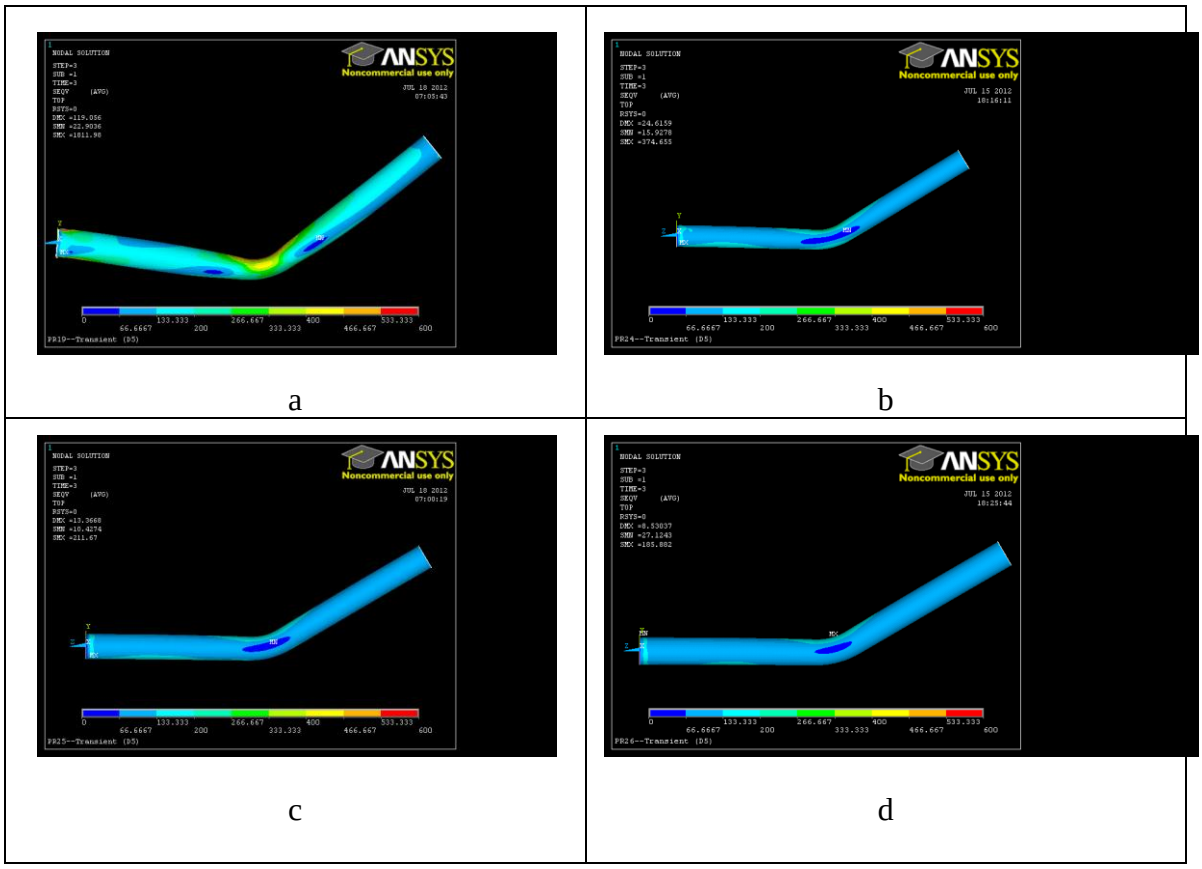

Figure 8. 5 - Plan View for various subgrade modulus K_s values (a) K_s=0 MN/m³ (b) K_s=20 MN/m³ (c) K_s=50 MN/m³ (d) K_s=100 MN/m³

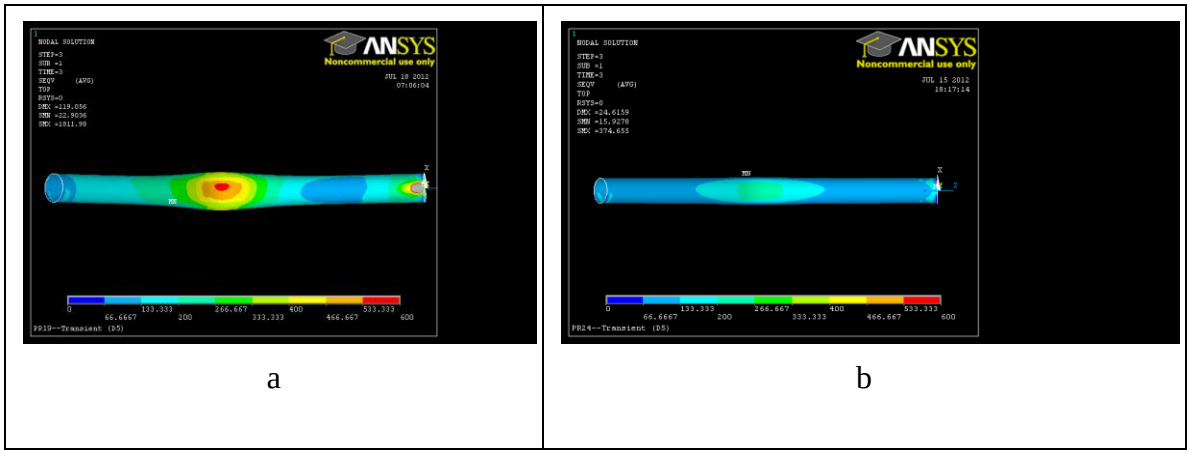

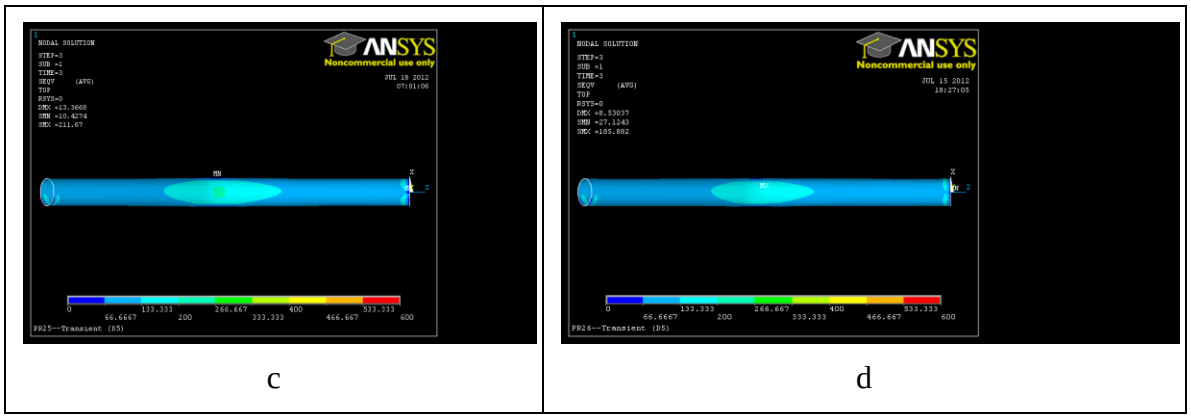

c d

Figure 8. 6 - Elevation View for various subgrade modulus K_s values (a) K_s=0 MN/m³ (b) K_s=20 MN/m³ (c) K_s=50 MN/m³ (d) K_s=100 MN/m³

Table 8. 2 - Maximum von-Mises steady-state stress for the subgrade modulus

Subgrade Modulus K_s (MN/m³)	von Mises Stress σ_{vm} (MPa)
0	628.3
20	243.0
50	205.3
100	188.2

Fluid field results from transient regime in Fig. 8.7 were extracted at the black dot location marked in Figs. 8.2. In the longitudinal direction, this point is located at pipe mid-span. In the radial direction, it is located at the centre of the pipe. Figure 8.7b shows that the transient pressure peaks at a maximum pressure of 412.3 kPa for a subgrade modulus of 0 MN/m³. The peak value increases to 437.1 kPa for 20 MN/m³ , to 459.6 kPa for 50 MN/m³ and reaches a value of 474.1 kPa for a subgrade modulus of 100 MN/m³. This trend is comparable to the one found on the variable thickness in Fig. 6.1 a-b and Table 6.6. The transient pressure increases as the rigidity of the structure increases.

Also, Fig. 8.7d shows that as the subgrade modulus increases, the magnitude of the relative velocity increases. When superimposed on the steady state velocity, the difference between the resulting absolute velocities is observed to be negligible as depicted in Fig. 8.7c.

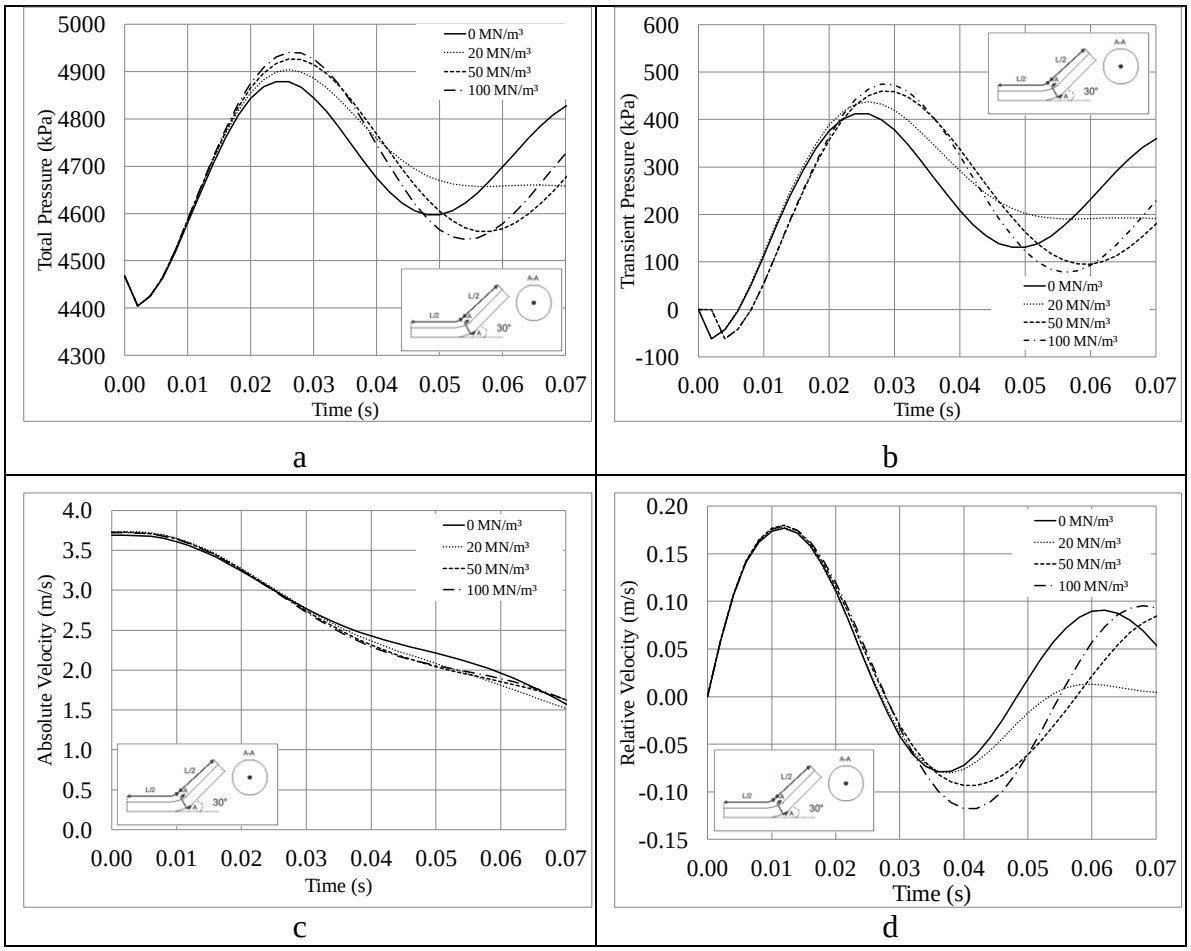

Figure 8. 7 - Effect of Subgrade Modulus on (a) Total Pressure, (b) Transient Pressure, (c) Absolute Velocity, (d) Relative Velocity

The maximum von-Mises stresses within the pipe wall are extracted from transient regime, and its history plotted in Figs. 8.8 a-b. It is observed that the maximum transient von-Mises stresses decrease with the subgrade modulus. The total von-Mises for modulus values of 20 MN/m³, 50 MN/m³, and 100 MN/m³ subgrade moduli slightly exceed the allowable stress for the steady and transient states as given by Eq. 3.9 for ASTM A1018 steel grade, but remain significantly lower than the case of elevated pipe.

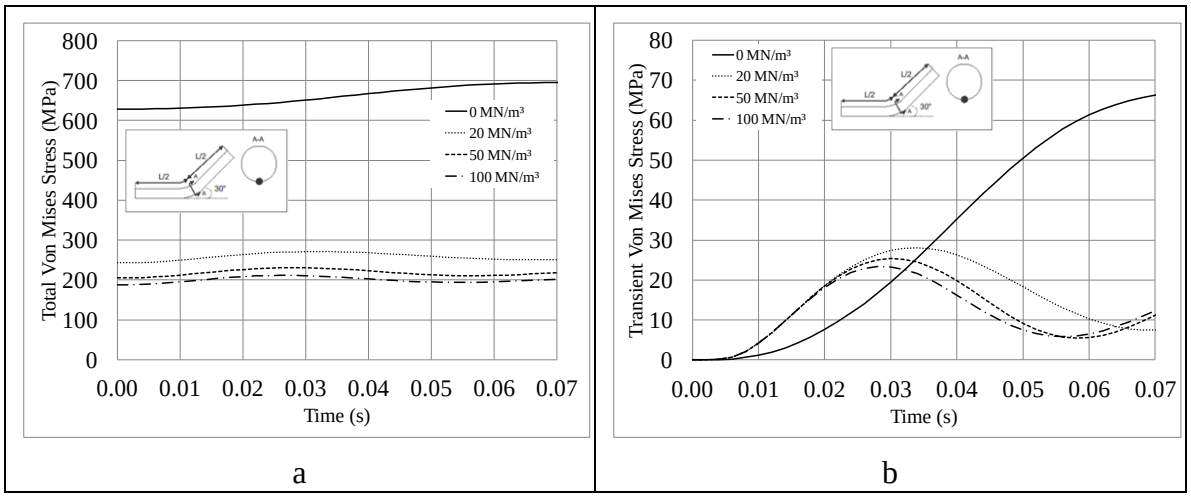

Figure 8. 8 - Effect of Subgrade Modulus on (a) Maximum Total von-Mises Stress, (b) Maximum Transient von-Mises Stress

8.5.2 Sensitivity of Results to the Subgrade modulus

Tables 8.3 and 8.4 respectively present the sensitivity of the pressure and von-Mises stress values to the subgrade modulus value. The sensitivity is assessed based on the variation parameter Ψ_R introduced in Eq. 6.1 from their value in the reference case.

The steady state pressure is observed to be insensitive to the subgrade modulus value. In the transient state, the static pressure is observed to be slightly influenced by the subgrade modulus. As shown on Fig. 8.9, as the subgrade modulus increases, the amplitude of transient pressure is observed to increase.

The von-Mises stress is observed to be greatly impacted by the subgrade modulus, both in the steady state and transient regimes. Figures 8.10 a-b show the total and transient von-Mises stresses as a function of subgrade moduli.

Table 8. 3 - Sensitivity of Pressure on Subgrade Modulus

	Steady-State		Transient State		Total	
	Pressure p (kPa)	$\Psi_R(K_s,p)$	Pressure p (kPa)	$\Psi_R(K_s,p)$	Pressure p (kPa)	$\Psi_R(K_s,p)$
0 N/m²	4467	-	412.3	-	4879	-
20 N/m²	4467	0.00%	437.1	6.02%	4904	0.51%
50 N/m²	4467	0.00%	459.6	11.5%	4927	0.97%
100 N/m²	4467	0.00%	474.1	15.0%	4941	1.27%

Table 8. 4 - Sensitivity of von-Mises Stress on Subgrade Modulus

	Steady-State		Transient State		Total	
	von Mises Stress σ_{vm} (MPa)	$\Psi_R(K_s,\sigma_{vm})$	von Mises Stress σ_{vm} (MPa)	$\Psi_R(K_s,\sigma_{vm})$	von Mises Stress σ_{vm} (MPa)	$\Psi_R(K_s,\sigma_{vm})$
0 N/m²	628.3	-	66.83	-	695.1	-
20 N/m²	243.0	-61.3%	28.09	-58.0%	271.1	-61.0%
50 N/m²	205.3	-67.3%	25.37	-62.0%	230.7	-66.8%
100 N/m²	188.2	-70.0%	23.38	-65.0%	211.6	-69.6%

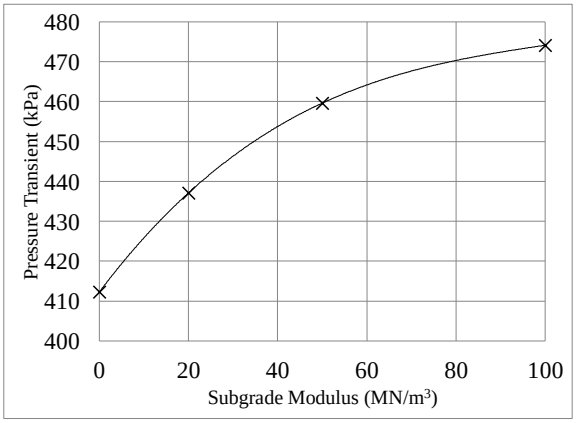

Figure 8. 9 - Effect of Subgrade modulus on transient Pressure

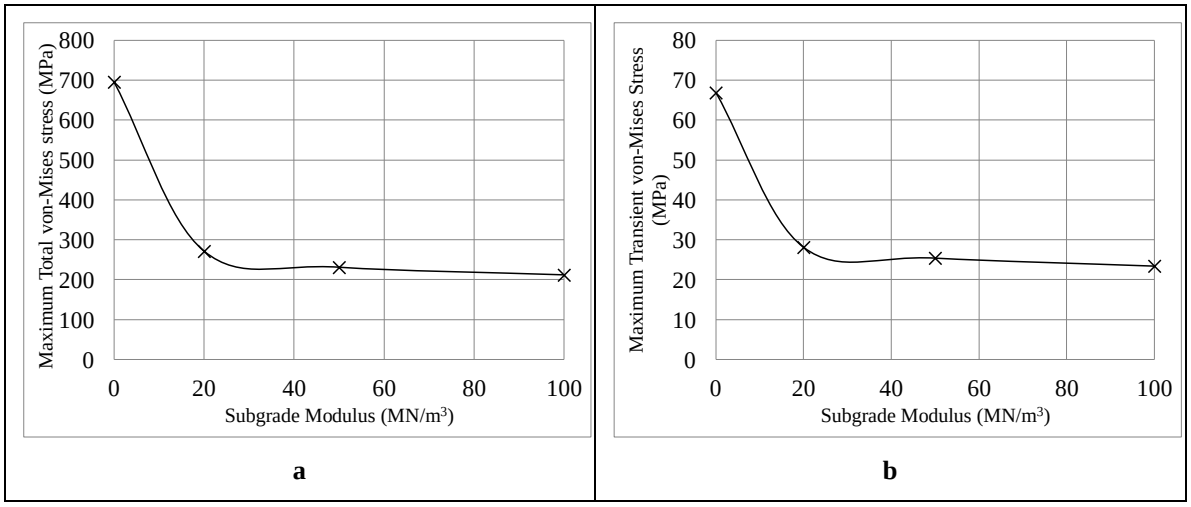

Figure 8. 10 - Effect of Subgrade modulus on von-Mises a) Total Stress, b) Transient Component of the Stress

8.6 Conclusion

Chapter 8 presented a comparative study on the effect of subgrade modulus of the soil on a horizontally bent penstock and quantified on its influence on the internal pressure, velocity fields, and the von-Mises stresses.

1. The analysis indicates that the subgrade modulus has little influence on the transient pressure and a moderate influence on the velocity.
2. Conversely, the presence of soil is observed to cause a significant beneficial effect in decreasing the transient and total von-Mises stresses.

CHAPTER 9 – SUMMARY, CONCLUSIONS AND RECOMMANDATIONS

9.1 Summary

A numerical model of a water hammer caused gate closure for straight elevated penstocks was developed under ANSYS-CFX. The model is based on real design scenario located at the Bear Creek Hydro Project, BC and captures Fluid-Structure Interaction (FSI). The FSI was performed according to an iteration process between a fluid and a structural solver. Navier-Stokes equations were discretized according to the Finite Volume Method (FVM) in the fluid solver and Equilibrium equations were discretized according to the Finite-Element Method (FEM) in the structural solver.

Rapid and slow gate closure events were simulated in the model for different timesteps and compared to analytical solutions. Structural and fluid data from slow gate closure events were taken as reference case.

A parametric study based on the reference case was performed on six different design parameters (pipe thickness, span, initial velocity, damping ratio, closure time and angle of inclination). A sensitivity analysis based on a defined dimensionless index provided an indication of output field sensitivity to input design parameters and the degree of importance of various design parameters was assessed.

A comparative study was then performed to analyze the influence of the horizontal and vertical bend angles on the output fields (pressure, velocity and von-Mises Stress).

Another comparative study was conducted to investigate the effect of the modulus of subgrade reaction on the pressure, velocity and von-Mises Stresses

9.2 Conclusions

Parametric and comparative studies have investigated the effect of certain parameters on determined output fields. Following is an outline of the major findings of these studies.

1. The pipe thickness was found to have a significant influence on the transient and steady hoop stress, making it an essential parameter to take into consideration in the design phase.
2. The span had an influence on many outputs: transient pressure, steady longitudinal stress and displacement, steady radial displacement. Its important influence on the transient pressure makes it a crucial parameter in a water hammer analysis.
3. The initial velocity was also found to have an important effect on the transient pressure, making it another essential parameter in a water hammer analysis.
4. The angle of inclination and damping parameters were found to have a negligible influence on every output field.
5. It was observed that presence of bends causes a sharp increase in both the transient and total von-Mises stresses, demonstrating the necessity of providing proper anchoring details at the bend location.
6. It was observed that the presence of soil has the significant benefit of decreasing the transient and total von-Mises stresses.
7. The fluid-structure interaction effect has been demonstrated for a water hammer caused by a slow gate closure in a simply supported penstock. However, given its minor influence on each output, the effect could be disregarded in penstock design.

9.3 Recommendations for future work

The methodology developed in the present research leads the way to several possibilities for future research, including the following related subjects of practical engineering experience:

1. Structural and fluid analysis of wyes branches, tees branches and manifolds under water hammer loading.
2. Structural and fluid analysis of non-prismatic and non-circular conduits under water hammer loading.
3. Water hammer loading caused by variable gate closure rates.
4. Penstocks under different boundary conditions (Anchored-anchored, Anchored-Simply Supported), and
5. Capturing soil material non-linear effect for buried penstocks.

REFERENCES

Allievi, L. (1902), General theory of the variable motion of water in pressure conduits, Annali della Società degli Ingegneri ed Architetti Italiani, 17(5), 285-325, Milan, Italy

Allievi, L. (1913), Teoria del colpo d'ariete (Theory of water-hammer.) Atti del Collegio degli Ingegneri ed Architetti Italiani, Milan, Italy

Allievi, L. (1925), Theory of water hammer, Translated in English by Mr. Eugène E. Halmos, Typography Riccardo Garroni, Rome

Altstadt, E., Carl, H., Weiss, R. (2003), FSI during artificially induced water hammer in a tube with a bend experiments and analyses, Wissenschaftlich-Techniste Berichte / Forschungszentrum Rossendorf, FZR-393

ASCE (1994), Steel Penstocks, ASCE Manuals and Reports on Engineering Practice No.79, Published by ASCE, USA

AWWA (2004), Steel Water Pipe: A Guide for Design and Installation, Manual of Water Supply and Practices M11, Published by AWWA, Denver, CO

Bergant, A., Simpson, A.R. (1994), Estimating unsteady friction in transient cavitating pipe flow, Proc. Second Int. Conference on Water Pipeline Systems, Edinburgh, Scotland, May, pp.3-15

Bergant, A., Simpson, A.R. (1999a), Pipeline column separation flow regimes, J. Hydraulic Eng., Vol.125(8), pp.835-848

Bergant, A., Simpson, A.R., Vitkowsky, J. (1999b), Review of unsteady friction models in transient pipe flow, IAHR, 9th Int. Meeting of the Work Group on the behaviour of hydraulic machinery under steady oscillatory conditions, Brno, Czech Republic

Bergant, A. Vitkovsky, J., Simpson, A., Lambert, M. (2002a), Performance of instantaneous accelerations models of unsteady skin friction in practical applications, 3rd unsteady friction group meeting, University of Dundee, UK,

Bergant, A., Vitkovsky J., Simpson, A. Lambert, M. (2002b), Behavior of unsteady pipe flow friction models in the case of valve opening, Proceedings of the 21st IAHR Symposium on Hydraulic Machinery and Systems, Lausanne

Bergant, A., Simpson, A.R., Tijsseling, A.S. (2006), Water hammer with column separation: A historical review, J. of Fluids and Structures, Vol.22, pp.135-171

Bergant, A., Tijsseling, A.S., Vitkovsky, J.P., Covas, D.I.C, Simpson, A.R., Lambert, M.F. (2008a), Parameters affecting water-hammer wave attenuation, shape and timing – Part 1: Mathematical Tools, Journal of Hydraulic Research, IAHR, Vol.46 no3, pp. 382-391

Bergant, A., Tijsseling, A.S., Vitkovsky, J.P., Covas, D.I.C, Simpson, A.R., Lambert, M.F. (2008b), Parameters affecting water-hammer wave attenuation, shape and timing – Part 2: Case Studies, Journal of Hydraulic Research, IAHR, Vol.46 no3, pp. 382-391

Bergeron, L. (1935), Études de variations de régimes dans les conduites d'eau : Solution graphique générale, Revue Générale de l'Hydraulique, Paris, Vol.1,1935, pp.12-60

Bowles, J.E. (1997), Foundation analysis and design (Fifth Edition), The McGraw-Hill Companies, Singapore

Brunone,B., Golia, U.M., Greco, M (1991), Some remarks on the momentum equation for fast transients, Proc., Int. Meeting on Hydraulic Transients and water column separation, pp.201-209

Bürmann, W., Janson, H., Thielen, H. (1979a), Water hammer theory for non-axisymmetrically deformed pipes, Universität Karlsruhe, Institüt fûr Hydromechanik, Bericht Nr. 614, Karlsruhe, Germany

Bürmann, W., Janson, H., Thielen, H. (1979b), Motion of pipelines due to water hammer, Universität Karlsruhe, Institüt fûr Hydromechanik, Bericht Nr. 617, Karlsruhe, Germany

Bürmann, W., Janson, H., Thielen, H. (1980), Pipeline motion due to water hammer, Universität Karlsruhe, Institüt fûr Hydromechanik, Bericht Nr. 618, Karlsruhe, Germany

Chaudry M.H, (1979), Applied Hydraulic Transients, Published by Van Nostrand Reinhold Company, NY, USA.

Chaudhry, M.H. (1985), Second-Order accurate explicit finite-difference schemes for waterhammer analysis, J. Fluids Eng., Vol.107(4), pp.523-530

Covas, D., Stoianov, I., Mano, J.F., Ramos, H., Graham, N., Maksimovic, C. (2004), The dynamic effect of pipe-wall viscoelasticity in hydraulic transients Part I – Experimental analysis and creep characterization. J. Hydraulic. Res., IAHR, Vol. 42(5), pp.516-530

Covas, D., Stoianov, I., Mano, J.F., Ramos, H., Graham, N., Maksimovic, C. (2005), The dynamic effect of pipe-wall viscoelasticity in hydraulic transients Part II – Model development, calibration and verification. J. Hydraulic. Res., IAHR, Vol. 43(1), pp.56-70

Daily, J.W., Hankey, W.L., Olive, R.W., Jordaan, J.M. (1956), Resistance coefficients for accelerated and decelerated flows through smooth tubes and orifices, Trans. ASME, Vol.(78), pp.1071-1077

Duan, H.F., Ghidahoui, M.S, Lee, P.J., Tung, Y.K (2012), Relevance of unsteady friction to pipe size and length in pipe fluid transients, J. Hydraulic Eng., Vol.138(2), pp.154-166

Ellis, J. (2008), Pressure transients in water engineering, published by Thomas Telford, London, UK.

Evangelisti, G. (1966), On the Numerical Solution of the Equations of Propagation by the Method of Characteristics, Meccanica, vol. 1, No 1/2, pp. 29-36.

Evangelisti, G., (1969), Waterhammer analysis by the method of characteristics, L'Energie Elettrica, Nos 10-12, pp.673-692,759-770,839-858

Fanelli, M. (2000), Hydraulic Transients with water column separation, IAHR Working Group 1971-1991, Synthesis Report, Delft:IAHR and Milan:ENEL-CRIS

Gally, M., Güney, M., Rieutord, E. (1979), An investigation of pressure transients in viscoelastic pipes, J. Fluids Eng., ASME, Vol.101(4), pp.495-499

Gersten, K., Härten, A., and Pagendarm, H.G. (1987), Optimierung, von Diffusoren, bezüglich der Diffusorströmung und der Diffusorwände, VDI-Verlag Düsseldorf,

Ghidaoui, M.S., Karney, B.W., McInnis, D.A. (1998), Energy estimates for discretization errors in water hammer problems, J. Hydraulic Eng., ASCE, 124, pp.384-393

Ghidahoui, M.S., Mansour, S. (2002), Efficient treatment of the Vardy-Brown unsteady shear in pipe transients, J. Hydraulic Eng., Vol.128, pp.102-112

Ghidahoui, M.S, Zhao, M., Duncan, A.M., Axworthy, D.H. (2005), A review of water hammer theory and practice, ASME, Vol.(58), pp.49-76

Gibson, N.R. (1920), Pressures in penstocks caused by gradual closing of turbine gates, ASCE, no 1439, pp. 707-775

Golberg, D.E., Wylie, E.B.(1983), Characteristics method using time-line interpolation, J.Hydraul, Eng., 109(5), 670-683

Gray, C.A.M (1953), The Analysis of the Dissipation of Energy in Water Hammer, Proc. ASCE,79, 1176

Guinot, V. (2000), Riemann solvers for water hammer simulations by Godunov method, International Journal for numerical methods in Engineering, Vol.49(7), pp.8851-870

Heinsbroek, A.G.T.J., Kruisbrink, A.C.H. (1993), Fluid-Structure interaction in non rigid pipeline systems large scale validation experiments, Elsevier Science Publishers

Heinsbroek, A.G.T.J, Tijsseling, A.S. (1994), The influence of support rigidity on waterhammer pressures and pipe stresses, Proceedings of the 3rd ASME/JSME Joint Fluids Engineering Conference

Hu, C.K., Phillips, J.W. (1981), Pulse propagation in fluid-filled elastic curved tubes, ASME, J. of Pressure Vessel Technology, Vol.103, pp.43-49

Jaeger, C. (1933), Théorie Générale du coup de bélier, École Polytechnique Fédérale de Zurich, Dunod, Paris

Joukowski N (1900), On the hydraulic hammer in water supply pipes, Mémoires de l'Académie Impériale des Sciences de St-Petersbourg, 1900

Joung, I. Shin. Y. (1985), A new model on transient wave propagation in fluid-filled tubes, ASME-PVP, Vol.98(7),pp.275-281

Kanyanta, V, Ivankovic, A., Karac, A. (2009), Validation of a fluid-structure interaction numerical model for predicting flow transients in arteries, Elsevier, J. of Biomechanics, Vol.42, pp.1705-1712

Keramat, A., Tijsseling, A.S., Hou, Q., Ahmadi, A. (2012), Fluid-structure interaction with pipe-wall viscoelasticity during water hammer, J. of fluids and structures, Vol.(28), pp.434-455

King, W.W., Frederick, D. (1968), Transient elastic waves in a fluid-filled cylinder, ASCE, J. of the Sanitary Eng. Mechanics Division, Vol. 94, pp.1215-1230

Korteweg, D.J. (1878), On the velocity of propagation of sound in elastic tubes, Annalen der Physik und Chemie, New Series 5, 525-542

Kries, J von, (1883), On the relations between pressure and velocity which exist in the wave-like motion in elastic tubes, Festschrift der 56. Versammlung deutsher Naturforscher und Ärzte [gewidmet von der Naturforschenden Gesellschaft zu Freiburg i. B., Supplement zu Band VIII der Berichte über die Verhandlungen der

Naturforschenden Gesellschaft zu Freiburg i. B.],67-88. [Akademische Verlagbuchhandlung von] JCB Mohr (Paul Siebeck), Freiburg im Breisgau und Tübingen, Germany.

Lai, C. (1961), A study of waterhammer including effect of hydraulic losses, PhD Thesis, The University of Michigan, Ann Arbor, Michigan, USA

Lavooij, C.S.W., Tijsseling, A.S. (1990), Waterhammer with fluid-structure interaction, Applied Scientific Research, Vol.47, pp.273-285

Lister, M. (1960), The numerical solutions of hyperbolic partial differiential equations by the method of characteristics, in Mathermatical methods for digital computers, A. Ralston and H.S. Wild, eds. New-York, John Wiley, p. 165-179

Lin, T.C., Morgan, G.W. (1956), A study of axisymmetric vibrations of cylindrical shells as affected by rotatory inertia and tranverse shear, J. of applied mechanics, Vol. 23, pp.255-261

Otwell, S.R. (1984), The effect of elbow restraint on pressure transients, Michigan State University, Ann Arbor (MI), USA

Parmakian, J. (1963), Waterhammer analysis, Dover Publications, New York

Perkins, F.E, Tedro, A.C, Eagleson, P.S, and Ippen, A.T. (1964), Hydro Power Plant Transient, Part II, Dept. of Civil Engineering, Hydrodynamics, Lab. Report N°71, Massachussetts Institute of Technology

Phillips, J., Valentin, R.A (1978), Reflection and transmission of fluid transients at elbows, University of Illinois, Urbana (IL), USA,

RETSCREEN INTERNATIONAL (2001), Small Hydro Project Analysis, Published by Minister of Natural Resources Canada, Ottawa, Canada

Schnyder, O. (1936), Considération sur le coup de bélier, Bulletin Technique de la Suisse Romande, 6^{ième} année, N°12.

Silva-Araya, W.F., Chaudhry, M.H. (2001), Unsteady friction in rough pipes, J. Hydraulic Eng., Vol.(127), pp.607-618

Shalaby, M.A., Younan, M.Y.A. (1999), Effects of internal pressure on elastic plastic behavior of pipe elbows under in plane bending, ASME, J. Pressure Vessel Technol, Vol. 121(4), pp. 400-406

Shimada, M., Brown J., Leslie, D., Vardy, A., (2006), Time-line Interpolation errors in pipe networks, J. Hydraulic Eng, ASCE, 132, pp.294-306

Shimada, M., Brown, J.M.B., Vardy, A.E. (2007), Estimating friction errors in MOC analysis of unsteady pipe flows, Elsevier, Computer and Fluids, 36, pp. 1235-1246

Shimada, M., Brown J.M.B., Vardy A.E. (2008), Interpolation errors in rectangular and diamond characteristic grids, J. Hydraulics Eng., ASCE, 134, pp.1480-1490

Skalak, R. (1956), An extension of the theory of waterhammer, Transactions of the ASME, Vol.78, pp.105-116

Streeter, V.L. (1962), Valve stroking to control waterhammer, The University of Michigan, Ann Arbor, Michigan, USA

Streeter, V.L. and Lai, C. (1963), Water hammer analysis including fluid friction, Proc. ASCE, 88, pp.79-112

Streeter, V.L. Wylie, E.B., (1967), Hydraulic Transients, McGraw-Hill Book Co., New-York

Streeter, V.L., Wylie, E.B (1985), Fluid Mechanics, Mc-Graw-Hill, New-York

Thorley, A.R.D. (2004), Fluid transients in pipeline systems, Professional Engineering Publishing Limited, UK

Tijsseling, A.S., Heinsbroek, A.G.T.J. (1999), The influence of bend motion on waterhammer pressures and pipe stresses, Proceedings of the 3rd ASME/JSME Joint Fluids Engineering Conf., San Francisco, California

Tijsseling, A.S, Vaugrante, P. (2001), FSI in L-Shaped and T-Shaped pipe systems, Eindoven University of Technology, Netherlands

Tijsseling A.S, Bergant A. (2007), Meshless computation of water hammer, Proceedings of the 2nd IAHR International meeting of the workgroup on cavitation and dynamic problems in hydraulic machinery and systems, pp. 65-76

Tijsseling, A.S, Anderson, A. (2007), Johannes von Kries and the History of Water Hammer, Journal of Hydraulic Engineering, ASCE, January, pp. 1-8

Tijsseling, A., Vardy, A.E. (2008), Time scales and FSI in unsteady liquid-filled pipe flow, BHR Group, Proc. Of the 10th Int. Conf. on Pressure Surges, Edinburgh, UK, pp.553-568

Valentin, R. A., Phillips, J.W., Walker, J.S. (1979), Reflection and transmission of fluid transients at an elbow, Transactions of SMiRT5, Berlin, Germany

Vardy, A.E. (1976), On the use of the method of characteristic for the solution of unsteady flows in networks, Proceedings, Second International conference on pressure surges, Sept. 22-24, BHRA

Vardy, A.E., Fan, D. (1986), Water hammer in close tube, Proceedings 5th Conf. on Pressure Surges, BHRA, Hanover, Germany, pp. 123-137

Vardy, A.E, and Hwang, K-L. (1991), A characteristics model of transient friction in pipes, J. Hydraulic Res., Vol.29(5), pp.669-684

Vardy, A.E., Brown, J.M.B. (1995), Transient, turbulent, smooth pipe friction, J. Of Hydraulic Research, Vol.33(4), pp. 435-456

Vardy, A.E., Brown, J.M.B. (1996), On turbulent, unsteady smooth-pipe friction, pressure surges and fluid transient, BHR Group, London, pp. 289-311

Vitkovsky, J.P., Lambert, M.F., Simpson, A.R., Bergant, A. (2000), Advances in unsteady friction modeling in transient pipe flow, 8th Int. Conf. on Pressure Surges, The Hague, The Netherlands

Vitkovsky,J., Stephens, M., Bergant, A., Lambert, M., Simpson, A. (2004), Efficient and accurate calculation of Zielke and Vardy-Brown unsteady friction in pipe transients, Proc., 9th Int. conference on pressure surges, BHR Group

Vitkovsky, J., Bergant, A., Simpson, A.R., Lambert, M.F. (2006), Systematic evaluation of one-dimensional unsteady friction models in simple pipelines, J. Hydraulic Eng., Vol.132, pp.696-708

Vardy, A.E., Brown, J.M.B. (2007), Approximation of turbulent wall shear stresses in highly transient pipe flows, J. Hydraulic Eng., ASCE, Vol.133(11), pp. 1219-1228

Walker, J.S, Phillips, J.W. (1977), Pulse propagation in fluid-filled tubes, J. of applied Mechanis, Vol. 44, pp. 31-35

Wallis, G.B. (1969), One-dimensional Two-phase flow, McGraw-Hill, New-York

Wiggert, D.C., Otwell, R.S., Hatfield, F.J. (1985a), The effect of elbow restraint on pressure transients, ASME, J. of Fluids Eng. Vol.107, pp. 402-406

Wiggert, D.C., Otwell, R.S., Hatfield, F.J. (1985b), Analysis of liquid and structural transients in piping by the method of characteristics, ASME-FED, Fluid Transients in Fluid-Structure Interaction, Vol.30, pp.97-102

Wiggert, D.C. (1986), Coupled transient flow and structural motion in liquid-filled piping systems: a survey, ASME, Pressure Vessels and piping conference, Chicago, USA, Paper 86

Wiggert, D.C., Otwell, R.S., Hatfield, F.J. (1987), Analysis of liquid and structural transients by the method of characteristics, ASME, J. of Fluids Eng., Vol.109, pp.161-165

Wiggert, D.C, Lesmez, M.L., Hatfield, F.J. (1990), Modal analysis of vibrations in liquid-filled piping systems, ASME-FED, Fluid Transients in Fluid-Structure Interaction Vol.56, pp.107-113

Wiggert, D.C, Tijsseling, A.S. (2001), Fluid transients and fluid-structure interaction in flexible liquid-filled piping, Appl. Mech., ASME, Vol. 54(5), pp. 455-481

Wilkinson, D.H. (1978), Acoustic and mechanical vibrations in liquid-filled pipework systems, Proceedings of the BNES Int. Conf. on vibration in nuclear plant, Keswick, UK, Paper 8.5, pp.863-878

Wilkinson, D.H. (1980), Dynamic response of pipework systems to waterhammer, Proceedings of the 3rd Int. Conf. on Pressure Surge, BHRA, Canterbury, UK, pp.221-240

Wood, D.J., Dorsch, R.G., Lightner, C. (1966), Wave plan analysis of unsteady flow in close conduits, J. Hydraulic Division, ASCE, 92(2), pp.83-110

Wood, D.J. (2005), Waterhammer analysis, essential and easy (and efficient), J. of Environmental Eng., ASCE, Vol.131(8), pp.1123-1131

Wylie, E.B, Streeter, V.L. (1978), Fluid transients, McGraw-Hill, New-York

Wylie, E.B., Streeter, V.L. (1993), Fluid transients in systems, Prentice Hall

Zielke, W. (1969), Frequency-dependant friction in transient pipe flow, J.Basic Eng., 90(1), pp. 109-115

Zhao, M. (2004), Godunov-Type Solutions for water hammer flows, J.Hydraulic Eng., Vol.130, pp.341-348

BIBLIOGRAPHY

Ahamadi, A., Keramat, A. (2010), Investigation of fluid-structure interaction with various types of junction couplings, Journal of fluids and structures, 26, pp. 1123-1141

Alawadhin, M. E. (2010), Finite Element Simulations Using ANSYS, Taylor and Francis, USA

American Iron and Steel Institute (1998), Buried Steel Penstocks, Second Edition, Steel Plate Engineering Data, Volume 4, Published by AISI, Washington, DC

American Lifelines Alliance (2005), Guidelines for the Design of Buried Steel Pipe, Published by ASCE,USA

ANSYS (2010), DesignModeler, Published by ANSYS, U.S.A

ANSYS (2010), ANSYS Mechanical APDL Coupled-Field Analysis Guide, Published by ANSYS, U.S.A

ANSYS (2010), ANSYS Mechanical APDL Element Reference, Published by ANSYS, U.S.A

ANSYS (2010), ANSYS Mechanical APDL and Mechanical Applications Theory Reference, Published by ANSYS, U.S.A

ANSYS (2010), ANSYS Mechanical Application User's Guide, Published by ANSYS, U.S.A

ANSYS (2010), ANSYS CFX-Pre User's Guide, Published by ANSYS, U.S.A

ANSYS (2010), ANSYS CFX-Solver Theory Guide, Published by ANSYS, U.S.A

ANSYS (2010), ANSYS CFX-Solver Manager User's Guide, Published by ANSYS, U.S.A

ANSYS (2010), ANSYS CFX-Solver Modeling Guide, Published by ANSYS, U.S.A

ANSYS (2010), ANSYS CFX Reference Guide, Published by ANSYS, U.S.A

ANSYS (2010), ANSYS CFD-Post User's Guide, Published by ANSYS, U.S.A

AWWA (2009), Ductile-Iron Pipe and Fittings, Manual of Water Supply and Practices M49, Published by AWWA, Denver, CO

Bergeron, L. (1950), Du coup de bélier en hydraulique au coup de foudre en électricité, Published by Dunod, France

Blade, R., Lewis, W., Goodykoontz, J.H. (1962), Study of a sinusoidally perturbed flow in a line including a 90° elbow with flexible supports, NASA Technical Note D-1216, Lewis Research Center, Cleveland, Ohio

Bureau of Reclamation (1986), Welded Steel Penstock, A Water Resources Technical Publication, Engineering Monograph No.3, Published by US Government, Washington, DC

DIPRA (2006), Thrust Restraint Design For Ductile Iron Pipe, Sixth Edition, Published by DIPRA, Birmingham, AL

ESHA (2005), Petite hydroélectricité Guide technique pour la réalisation de projet, Published by ESHA, Bruxelles, Belgium

Gale, J. (2008), Fluid-Structure Interaction for simulations of fast transients, Doctoral Thesis, University of Ljubljana, Slovenia

Madenci, E., Guven, I. (2006), The Finite Element Method and Application in Engineering Using ANSYS, Springer, USA

Moaveni, S. (2008), Finite Element Analysis : Theory and Application with ANSYS Third Edition, Pearson Education, USA

Moser, A.P.,Folkman S. (2008), Buried Pipe Design (Third Edition), Published by McGraw Hill, USA

Ouyang, X.P., Gao, F., Yang, H.Y., Wang, H.X. (2011), Two dimensional stress analysis of the aircraft hydraulic system pipeline, Proceeding of IMechE, Vol. 000, Part G: J. Aerospace Engineering

Streeter, V.L. (1966), Fluid Mechanics Fourth Edition, Published by McGraw-Hill Book Company, New-York, U.S.A

Tijsseling, A.S. (1996), Fluid-Structure Interaction in liquid filled pipe systems: a review, Journal of Fluid and Structures , 10, pp.109-146

Tijsseling, A.S., Vardy, A.E. (1996), Fluid-Structure interaction and cavitation in a single-elbow pipe system, Journal of fluid and structure, Academic Press, 10, pp. 395-420

Tijsseling, A.S. (1997), Poisson-Coupling beat in extended waterhammer theory, ASME, J. FSI, Aeroelasticity, Flow-induced vibration and noise, Vol. 53(2), pp. 529-532

Tijsseling, A.S. (2003), Exact solution of linear hyperbolic four-equation system in axial liquid-pipe vibration, J. of Fluids and Structure, Vol.18, pp.179-196

Tijsseling A.S, Lambert, M.F., Simpon, A.R., Stephens, M.L., Vitkowsky, J.P., Bergant, A., (2007), Skalak's extended theory of water hammer, Journal of sound and vibration, 310, pp. 718-728

Vardy, A.E, Fan, D., Tijsseling, A.S. (1996), Fluid-Structure Interaction in a T-Piece pipe, J. Of Fluids and Structures, Vol. 10, pp. 763-786

Watkins, R.K., Anderson L.R., (2000), Structural Mechanics of Buried Pipes, Published by CRC Press, Boca Raton, FL

Zhang, L, Tijsseling, A.S., Vardy, A.E, (1999), FSI Analysis of liquid-filled pipes, Journal and sound and vibration, 224, pp. 69-99